Time-Resolved Spectroscopy of Non-Volatile Biomolecule Analogues

Author:
Stuart William Crane

Supervisor:
Dr Dave Townsend

Thesis to fulfil the requirements for the degree of Doctor of Philosophy

Ultrafast Molecular Dynamics Group
Institute of Photonics and Quantum Sciences,
School of Engineering and Physical Sciences,
Heriot-Watt University
16th September 2018

Abstract

A time-resolved photoion yield spectrometer, employing a soft thermal desorption source for low vapour pressure sample volatilisation, has been constructed, benchmarked and used to discern the non-adibatic dynamics of biologically relevant molecules. Extensive time-resolved photoion yield data collection and analysis software has also been developed and will be of use to the group for many years to come.

The dynamics of the the RNA base uracil and its sulphur containing analogue 2-thiouracil have been investigated at an excitation wavelength of 267 nm. These results are compared to molecular beam studies employing similar excitation/ionisation schemes in order to benchmark the new spectrometer. Additional studies of uracil at pump wavelengths of 220 nm and 200 nm are the first reported for uracil < 250 nm. This study also looked for evidence of a theoretically predicted ultrafast ring-opening mechanism, however signatures of this process were not observed within the time window investigated

The non-adibatic dynamics operating in 5,6-dihydroxyindole, a sub-unit of the skin pigment eumelanin, have been studied in the gas-phase for the first time employing excitation wavelengths between 241 nm - 296 nm. This investigation revealed a significant change in dynamical behaviour when compared to the related indole and 5-hydorxyindole systems, with the molecule displaying dynamics more akin to phenol/catechol. The addition of a hydroxyl group at the O_6H position opens an energy dissipation mechanism via H-atom barrier tunnelling along the O_5H coordinate, considered as a spectator in the 5-HI system.

Overall, the new spectroscopic instrument developed facilitates the study of low-vapour pressure molecular species in ultrafast dynamics experiments, broadening the range of molecules which may be investigated in the gas-phase. This allows for the study of structure-dynamics-function relationships to be extended to more complex and challenging systems.

Acknowledgements

First and foremost, I would like to thank my supervisor Dr Dave Townsend for the years of support and guidance he has provided from undergraduate studies to the completion of this thesis. His door was always open to discuss any matter large or small and would always make time to help wherever he could. If any who are reading this become interested in pursuing a PhD in this field, you could not ask for a better boss than Dave.

Secondly I would like to thank Dr Omair Ghafur for his tireless efforts in designing the new spectrometer and his guidance with characterising the set-up. Although we did not see eye-to-eye on every occasion, Omair played a huge role in progressing this project and was key to the data acquired for this thesis.

Next I would like to acknowledge the other past and present members of the 'ultrafast molecular dynamics' group for their support over the last four years. Firstly, Dr Nikoleta Kotsina has been a true friend to me through the hard times and the good since joining the group two years ago. As a work colleague, she has provided support and useful discussions and as a friend she has made me laugh and enjoy life and this I thank you for. Next, I would like to thank Ms Lisa Saalbach for the provision of many gummy sweets, which kept my sugar levels sufficiently peaked throughout the writing process. Her friendship over the past six years has meant a lot to me and will miss the fun times we have shared in the lab. Of previous group members, I would like to thank Dr James Thompson and Dr Marco Candelaresi for their help and guidance upon joining the group as a masters student and through the first few years of my PhD, as well as for the impromptu lessons on Italian curse words. I would also like to thank Dr Magdelena Zawadzki for the many useful conversations throughout my studies. In addition, my thanks go to the many project and summer students I had the fortune to supervise over the past four years, providing me with happy distractions and friendly conversation.

Furthermore, my thanks go to Dr Ashley Lyons for his guidance in the use of Latex to write this thesis and to Dave, Nikoleta, Lisa and Dr Federico Belli for reading the various sections and advising me on improvements.

After nine years at Heriot-Watt University, I must thank the various staff and students within the the IPaQS and ICS departments who have enriched my study experience, as well as the university itself for financial support to pursue this doctorate.

Finally, I would like to thank my family for all the financial and emotional support over the years, in particular my parents Yvonne and Gary Crane who could not have done more to help me.

Contributions

This document is included to state the specific contributions of myself and others to the work produced and discussed within this thesis. Unless otherwise stated here, all experiments performed, data collected and analysis have been performed by myself.

Within Chapter 2, the design of the new laser desorption time-of-flight spectrometer was performed by Dr Omair Ghafur, with construction and characterisation of the chamber performed in conjunction with him. Simulations of the effects of a mu-metal shield performed in SIMION are also the work of Dr Gafur. Furthermore, the various beamlines constructed through a combined effort of myself and Dr Ghafur. All data collection and analysis code discussed within Chapter 3 has been developed and tested by myself. In Chapter 4, the 220 nm and 200 nm pump time-resolved data on the uracil molecule were collected with assistance from Dr Ghafur and Dr Michal Ryszka, with data collected with a 267 nm pump for uracil and 2-thiouracil performed solo. Additionally, foil temperature measurements were performed by myself. Nanosecond REMPI studies discussed within this chapter were performed by Andre Rebelo and Jana Bockova at the Open University. Synthesis of both 5,6-dihydroxyindole and its deuterated equivalent, discussed in Chapter 5, was performed by Thomas Cowie of Heriot-Watt University. UV-visible spectra of 5,6-DHI, the mono-hydroxyindoles, 4-HI, 5-HI and 6-HI, as well as indole, were performed by Dr James Thompson. Time-resolved data of 5,6-DHI were performed in conjunction with Dr Ghafur, with data analysed by myself. The idea of producing a molecular nozzle for increasing sample density, as discussed in Chapter 6, was that of Dr Ghafur, with design, simulation and construction of this nozzle performed by myself. Photoelectron images produced in this chapter were also performed in conjunction with Dr Ghafur.

Links To Publications

- **Publication** (Third author)**:** Ultraviolet relaxation dynamics of aniline, N, N-dimethylaniline and 3, 5-dimethylaniline at 250 nm:
  https://doi.org/10.1063/1.4914330
  - Collection of gas-phase UV-absorption spectra of aniline, 3,5-dimethylaniline and N,N-dimethylaniline.

- **Publication** (Third author)**:** Ultrafast relaxation dynamics of electronically excited piperidine: ionization signatures of Rydberg/valence evolution:
  https://doi.org/10.1039/C6CP04494H
  - Development of code for temporal and angular analysis of time-resolved photoelectron imaging data on piperidine.

- **Publication** (Fourth author)**:** Observation of multi-channel non-adiabatic dynamics in aniline derivatives using time-resolved photoelectron imaging:
  https://doi.org/10.1039/C6FD00092D
  - Development of code for temporal analysis of time-resolved photoelectron imaging data on aniline.

- **Publication** (First author)**:** Caveats in the interpretation of time-resolved photoionization measurements: A photoelectron imaging study of pyrrole:
  https://doi.org/10.1063/1.4972096
  - Extensive analysis of previously collected time-resolved photoelectron imaging data on pyrrole in addition performing and analysing time-resolved photoion yield studies of the molecule.

- **Publication** (Fifth author)**:** A new technique for probing chirality via photoelectron circular dichroism:
  https://doi.org/10.1016/j.aca.2017.06.051
  - Contributed to the initial testing of the new photoelectron circular dichroism spectrometer.

- **Publication** (Joint first author)**:** Ultraviolet relaxation dynamics in uracil: Time-resolved photoion yield studies using a laser-based thermal desorption source:
  https://doi.org/10.1063/1.5034419
  - Extensively involved in all time-resolved data collected and performed all data analysis. Also performed temperature characterisation of the desorption source.

- **Publication** (First author)**:** Wavelength-dependent ultrafast relaxation dynamics in 5,6-dihydroxyindole: A key chromophore in eumelanin pigments: *In preparation*
  - Extensively involved in all time-resolved data collected and performed all data analysis.

ACADEMIC REGISTRY
Research Thesis Submission

Name*:*	Stuart William Crane		
School:	EPS/IPaQS		
Version: *(i.e. First, Resubmission, Final)*	Final	Degree Sought:	Doctor of Philosophy in Physics

Declaration

In accordance with the appropriate regulations I hereby submit my thesis and I declare that:

1) the thesis embodies the results of my own work and has been composed by myself
2) where appropriate, I have made acknowledgement of the work of others and have made reference to work carried out in collaboration with other persons
3) the thesis is the correct version of the thesis for submission and is the same version as any electronic versions submitted*.
4) my thesis for the award referred to, deposited in the Heriot-Watt University Library, should be made available for loan or photocopying and be available via the Institutional Repository, subject to such conditions as the Librarian may require
5) I understand that as a student of the University I am required to abide by the Regulations of the University and to conform to its discipline.
6) I confirm that the thesis has been verified against plagiarism via an approved plagiarism detection application e.g. Turnitin.

* *Please note that it is the responsibility of the candidate to ensure that the correct version of the thesis is submitted.*

Signature of Candidate*:*		Date:	

Submission

Submitted By *(name in capitals):*	
Signature of Individual Submitting:	
Date Submitted:	

For Completion in the Student Service Centre (SSC)

Received in the SSC by *(name in capitals):*			
Method of Submission *(Handed in to SSC; posted through internal/external mail):*			
*E-thesis Submitted (**mandatory for final theses)***			
Signature:		Date:	

Please note this form should be bound into the submitted thesis.

Contents

CHAPTER 1

Introduction:

Investigating Neutral Molecules in the Gas-Phase

Within the discipline of physical chemistry, there are a number of fundamental questions which permeate across the numerous experimental and theoretical fields. One question of particular interest is that of how chemical or molecular substances change under various conditions. This may be represented by the 'arrow of chemistry', whereby initial reactants undergo some process to become products. A representation of the arrow of chemistry may be seen in Figure 1.1.

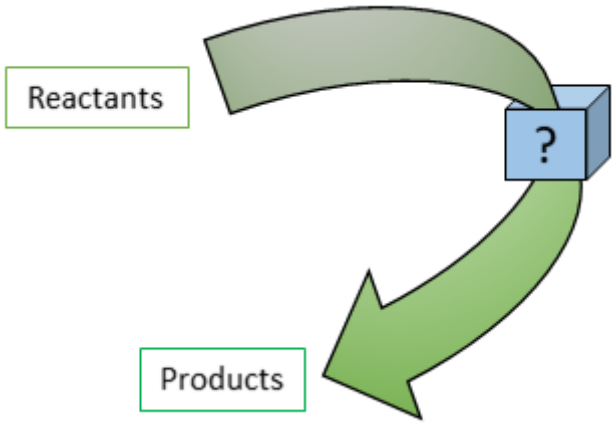

Fig. 1.1: A pictorial representation of the arrow of chemistry.

For the case of a molecule following photoexcitation, electrostatic forces, potentials and charges play a key role in driving dynamical processes such as bond formation and breaking, ionisation and energy and charge redistribution. By ascertaining the molecular structure and dynamical reactions of these systems, there is potential to gain a valuable insight into the functionality of the molecules.

The primary focus of this thesis is to investigate the dynamical processes which dictate energy redistribution within naturally-occurring biological molecules, such as the DNA and RNA bases (cytosine, guanine, adenine, thymine and uracil) and eumelanin (a constituent of skin pigmentation), following the absorption of ultraviolet (UV) radiation. Prior to the formation of the ozone layer, the Earth's surface was irra-

diated with far greater levels of UV light than at present, with molecules of biological interest having to withstand these harsher conditions. A key question to consider here is 'why, over millions of years of evolution, has nature chosen but a few molecules to genetically code all life on Earth?'. There are alternative combinations of naturally occurring nucelobases which form similar hydrogen bonded base-pairings[1]. These candidates for alternative genetic building blocks, however, have not been employed in biologically relevant roles. An example is that of 2,6-diaminopurine and uracil as replacements for guanine and cytosine, schematics of which may be seen in Figure 1.2.

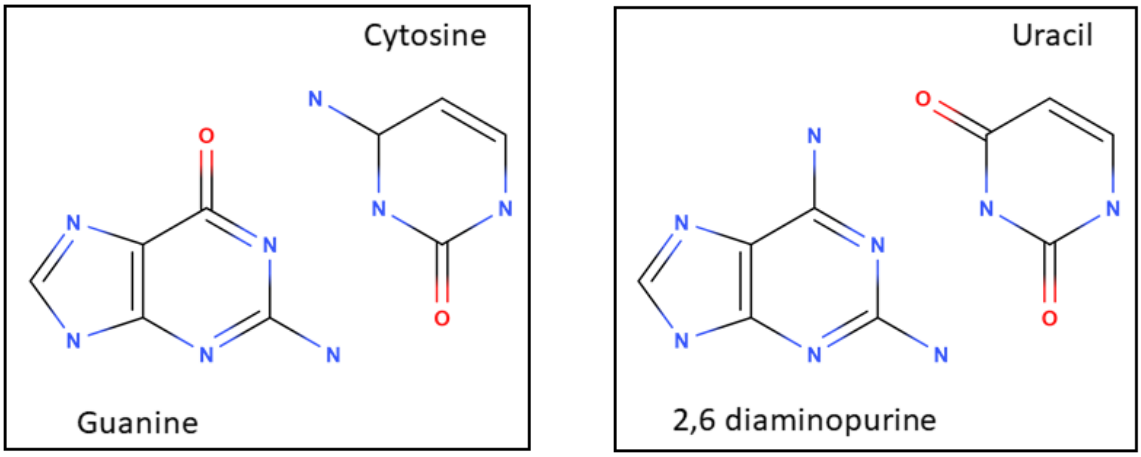

Fig. 1.2: Schematics of the DNA nucleobase pair guanine and cytosine, as well as the alternative candidate nucleobase pairing 2,6-diaminopurine and uracil.

One notable reason to consider is that of the photoresistance of these molecules, and how they dissipate excess energy through non-destructive methods (i.e. without bond breaking or fragmentation). This could be achieved through fluorescence, whereby energy is dissipated from a system via emission of a photon, however, it is evident that this is not the process occurring in the systems described due to low fluorescence yields[2]. A more likely scheme is that of non-adiabatic dynamics, whereby systems undergo non-radiative energy transfer between electronic states[3] and vibrational degrees of freedom, with excess energy then dissipated as heat to the surroundings[4]. This process, in which there is a breakdown of the Born-Oppenheimer approximation, may be used to explain how molecules redistribute surplus energy in a stable manner as a form of photoprotection[5;6]. Experimentally investigating the temporal response of a molecule following UV absorption, however, is by no means a trivial matter; it has been found that these processes often occur on an ultrafast timescale and, thus, in order to observe the real-time molecular dynamics experimentally, one requires an acquisition method on a comparable timescale.

The field of molecular dynamics was revolutionised upon advent of the femtosecond laser[7], making it possible to investigate molecular systems with sub-picosecond resolution. The use of femtosecond lasers to interrogate the molecular dynamics of a molecule in real time was pioneered by Prof. Ahmed Zewail in the 1980s and 1990s[8], leading to the Nobel Prize in chemistry in 1999[9]. Interrogating molecular dynamics may be achieved through utilising the 'pump-probe' technique[10]; 'pump' photons provide an initial excitation to the molecule under test, whilst 'probe' photons interrogate the system a controlled time later, Δt, sampling the dynamical excitation processes. This allows one to interrogate the transitory behaviour of a system as photoreactants transition to photoproducts.

In this thesis, spectroscopic information will be attained through use of the time-resolved photoion-yield technique, whereby parent ion and mass fragment yields are monitored with respect to pump-probe separation. This is used in conjunction with a new soft thermal desorption for volatilisation of low vapour pressure samples. Chapter 1 will provide a background to molecular dynamics and energy dissipation mechanisms, as well as extensive literature reviews on spectroscopic techniques and molecular sample volatilisation. Chapter 2 will provide an understanding of the newly commissioned time-resolved photoion-yield mass spectrometer and aspects of the experimental set-up utilised, while Chapter 3 will discuss the extensive computer code development for experimental automation and analysis. Chapter 4 will discuss spectroscopic studies of the RNA base uracil and its sulfated equivalent 2-thiouracil following excitation across the 200 - 267 nm region and Chapter 5 will present the dynamical behaviour of the molecule 5,6-dihydroxyiodole following excitation at wavelengths between 241 - 296 nm. Finally, Chapter 6 will discuss the various avenues of future work intended for this project, as well as present a final conclusion to the work undertaken.

1.1 Molecular Dynamics Theory

Prior to the experimental study of molecular dynamics, it is important to first consider theoretically how molecules and electrons interact upon photonic excitation. This section will provide a basic theoretical background to non-adiabatic dynamics and discuss many of the principles and approximations which are assumed in spectroscopic studies.

1.1.1 The Time-Independent Schrödinger Equation

In order to investigate energy and charge redistribution in a molecular system due to the absorption of an energetic photon, it is imperative to first consider the initial and prepared wavefunctions of the molecule of interest and, concurrently, the energies of these states. An undertaking such as this requires an understanding of the underlying quantum mechanical nature and, thus, may be interrogated through use of the time-independent Schrödinger equation[11], presented in Equation (1.1).

$$\frac{-\hbar^2}{2m}\nabla^2_{\vec{r},\vec{R}}\Psi(\vec{r},\vec{R}) + \hat{V}(\vec{r},\vec{R})\Psi(\vec{r},\vec{R}) = \hat{H}\Psi(\vec{r},\vec{R}) = E\Psi(\vec{r},\vec{R}) \tag{1.1}$$

Here $\hat{V}(\vec{r},\vec{R})$ is the potential energy, $\hat{H}$ is the time-independent Hamiltonian operator, $\hbar$ is Planck's constant didided by 2π and E is the resultant energy eigenvalue. The wavefunction investigated is represented by $\Psi(\vec{r},\vec{R})$ and is a function of both the electronic, $\vec{r}$, and nuclear, $\vec{R}$, coordinates in a system of interest and the operator $\nabla^2_{\vec{r},\vec{R}}$ may be presented as Equation (1.2) for a one electron system.

$$\nabla^2_{\vec{r},\vec{R}} = \frac{\partial^2}{\partial\vec{r}^2} + \frac{\partial^2}{\partial\vec{R}^2} \tag{1.2}$$

The Hamiltonian may also be considered as a summation of kinetic, $\hat{T}$, and potential energies, $\hat{V}$, of a molecule as shown in Equation (1.3).

$$\hat{H} = \hat{T}_{elec} + \hat{T}_{nuc} + \hat{V}_{elecnuc} + \hat{V}_{elecelec} + \hat{V}_{nucnuc} \tag{1.3}$$

Where $\hat{T}_{elec}$ and $\hat{T}_{nuc}$ are the electronic and nuclear motions respectively, $\hat{V}_{elecelec}$ and $\hat{V}_{nucnuc}$ represent coulombic repulsion from electron-electron and nuclei-nuclei interactions and $\hat{V}_{elecnuc}$ accounts for an attractive potential between electrons and nuclei. To solve Equation (1.1) analytically for a molecule or a multi-electron system becomes impossible, thus approximations must be introduced so as to quantitatively analyse these systems.

1.1.2 The Born-Oppenheimer Approximation

The wavefunction of a system may be further expanded when one considers the relevant timescales of its constituents. Within a molecular system, one can consider the electronic motion to be on a far shorter timescale (attoseconds) than that of nucleic motion (femtoseconds-picoseconds), thus, one can decouple the respective components within the wavefunction; this is known as the Born-Oppenheimer approximation [12] and is expressed by Equation (1.4) below.

$$\Psi_{TOT}(x) = \Psi_{elec}(\vec{r};\vec{R})\Psi_{nuc}(\vec{R})\Psi_s(s) \tag{1.4}$$

Where $x = (\vec{r},s)$ denotes the full collection of electron position, $\vec{r}$, and spin, s, variables and Ψ_{elec}, Ψ_{nuc} and Ψ_s are the individual electronic, nucleic and spin components of the total wavefunction Ψ. A similar argument may be presented when considering vibrational and rotational motion of the nuclei, occurring on the femtosecond and picosecond timescales respectively, which may too be decoupled and is known as the 'rigid rotor' approximation as seen in Equation (1.5).

$$\Psi_{nuc}(R,\theta,\phi) = \Psi_{vib}(R)\Psi_{rot}(\theta,\phi) \tag{1.5}$$

Where Ψ_{vib} and Ψ_{rot} are the individual vibrational and rotational components of the nucleic wavefunction Ψ_{nuc}. The total wavefunction, therefore, may be presented as a product of the electronic, vibrational, rotational and spin wavefunctions and the total energy a summation of these constituent energies as shown in Equation (1.6) and Equation (1.7) below.

$$\Psi_{TOT} = \Psi_{elec}(\vec{r};\vec{R})\Psi_{nuc}(R,\theta,\phi)\Psi_s(s) = \Psi_{elec}(\vec{r};\vec{R})\Psi_{vib}(R)\Psi_{rot}(\theta,\phi)\Psi_s(s) \tag{1.6}$$

$$E = E_{elec} + E_{vib} + E_{rot} + E_s \tag{1.7}$$

By means of the above approximation, it is possible to simplify the Schrödinger equation by expressing the electronic wavefunction as a function of the coulombic field created by the nuclei.

$$(\hat{T}_{elec} + \hat{V}_{elecnuc} + \hat{V}_{elecelec})\Psi_{elec} = \hat{H}_{elec}\Psi_{elec} = E_{elec}\Psi_{elec} \tag{1.8}$$

This decoupling of motions may be considered as an adiabatic framework, which one can utilise to deduce the potential energy surfaces (PES) of a non-linear poly-

atomic system, a mathematical function which gives the energy of a molecule with respect to its geometry[13–15]. For the instance of a diatomic or linear molecule, the potential energy of the system may only be varied through extension and compression of internuclear distance (R), meaning it is possible to accurately simulate this through simple theoretical models. However, for the case of non-linear polyatomic molecules, the PES is far more complex with a larger number of coordinates, n, due to the increased degrees of freedom associated with higher numbers of atoms, N. A summary of the vibrational degrees of freedom for such linear and polyatomic molecules is presented in Equation (1.9)

$$n = \begin{cases} 3N - 5, & \text{N} = 2 \text{ or linear} \\ 3N - 6, & \text{N} > 2 \text{ and non-linear} \end{cases} \tag{1.9}$$

Here a factor of three is utilised as the atoms' positions are considered in a three-dimensional coordinate system, with the removal of six (five in linear or diatomic molecules) to account for centre-of-mass motion. This results in complicated multi-dimensional PESs which are impossible to construct due to the large number of degrees of freedom. An alternative is to investigate a coordinate of interest, such as a particular torsional angle or bond extension, in a one-dimensional framework. This is of significant interest as it allows one to determine the motions that are key or spectator in decay dynamics and is a benefit to systematic studies. Furthermore, this one-dimensional cut through the multidimensional PES, known as a potential energy cut, is far less expensive to compute and provides a valuable insight into the excited state topography. An example of a potential energy cut is presented in Figure 1.3.

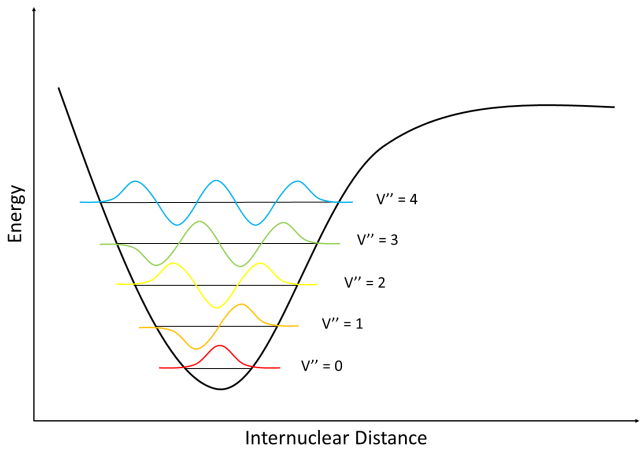

Fig. 1.3: A schematic of a potential energy cut, plotting internuclear distance against energy. V = 0-4 represent the first five vibrational levels for the particular electronic state shown.

1.1.3 The Franck-Condon Principle

The Franck-Condon principle[16;17] is a rule which dictates the intensity of vibronic transitions following the absorption or emission of a photon. The principle states that during an electronic transition, a change from one vibrational state to another will occur with a higher propensity if there is a significant wavefunction overlap between the two vibrational states.

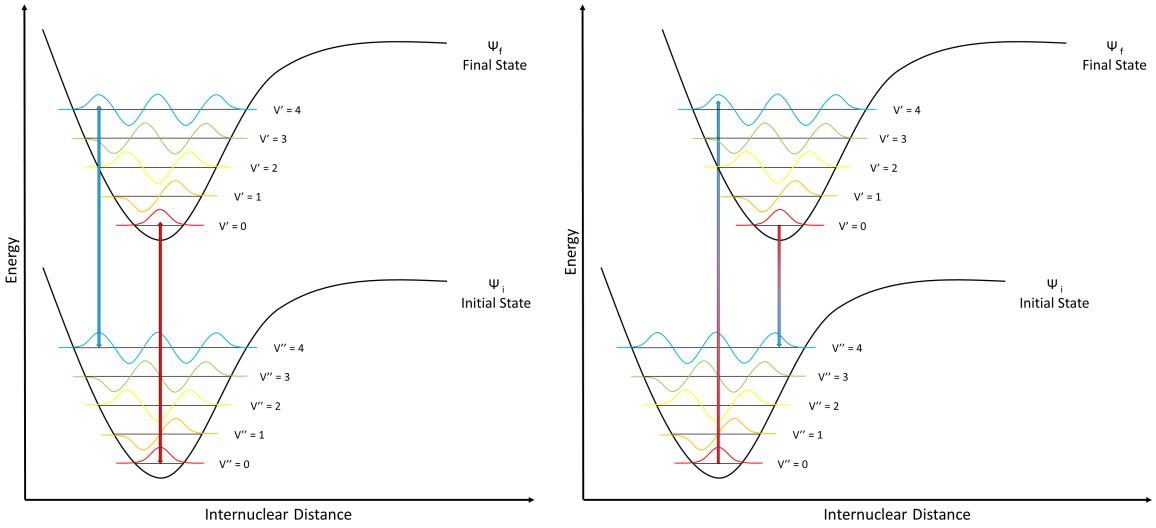

Fig. 1.4: Schematics of the Franck-Condon Principle: Transitions occur from the ground vibrational state to an excited state with the largest overlap of vibrational wavefunctions. Arrows between vibrational levels represent a favoured vertical transition with good overlap.

This is dictated by the transition dipole moment, $d_{i\rightarrow f}$ expressed mathematically in Equation (1.10).

$$d_{i\rightarrow f} = \int {\Psi_{felec}}^* {\Psi_{fvib}}^* {\Psi_{fspin}}^* (\vec{\mu}_e \vec{E} + \vec{\mu}_n \vec{E}) \Psi_{ielec} \Psi_{ivib} \Psi_{ispin} d\tau \tag{1.10}$$

Where Ψ_i and Ψ_f represent the initial and final wavefunctions, $\vec{\mu}_e$ and $\vec{\mu}_n$ are the electronic and nucleic transition moment operators, $\vec{E}$ is the electric field and subscripts *elec*, *vib* and *spin* represent, electronic, vibrational and spin components respectively. This may be further expanded and simplified when considering the orthogonality of the electronic wavefunctions[18], producing a final transition probability Equation (1.11).

$$d_{i\rightarrow f} = \int {\Psi_{fvib}}^* \Psi_{ivib} d\tau_n \int {\Psi_{felec}}^* \vec{\mu}_e \vec{E} \Psi_{ielec} d\tau_e \int {\Psi_{fspin}}^* \Psi_{ispin} d\tau_s \tag{1.11}$$

The square of the first integral represents the Franck-Condon factor (FC), the second the origin of orbital selection rules and the third presents the spin selection rules. If all three of these integrals are non-zero, the transition is formally allowed, with an intensity proportional to the square of the wavefunction overlap integral, as shown in Equation (1.12).

$$(d_{i\to f})^2 = \left[\int \Psi_{fvib}{}^* \Psi_{ivib} d\tau_n \int \Psi_{felec}{}^* \vec{\mu}_e \vec{E} \Psi_{ielec} d\tau_e \int \Psi_{fspin}{}^* \Psi_{ispin} d\tau_s\right]^2 \qquad (1.12)$$

The highest probability ground-state electronic transitions, assuming v = 0, occur when potential energy cuts have minima at the same reaction coordinate, as in the left plot in Figure 1.4, whereas transitions to higher vibrational states($\Delta v \neq 0$) are favoured for systems where electronic state-minima are offset, as displayed in the right plot of Figure 1.4.

1.1.4 Wavepacket Dynamics and Conical Intersections

When considering non-adiabatic dynamics of a molecule, in cases such as in avoided crossings in diatomic molecules or at conical intersections in polyatomic molecules when the PES become degenerate, the Born-Oppenheimer approximation breaks down[19–21]. Examples of these processes may be seen in Figure 1.5.

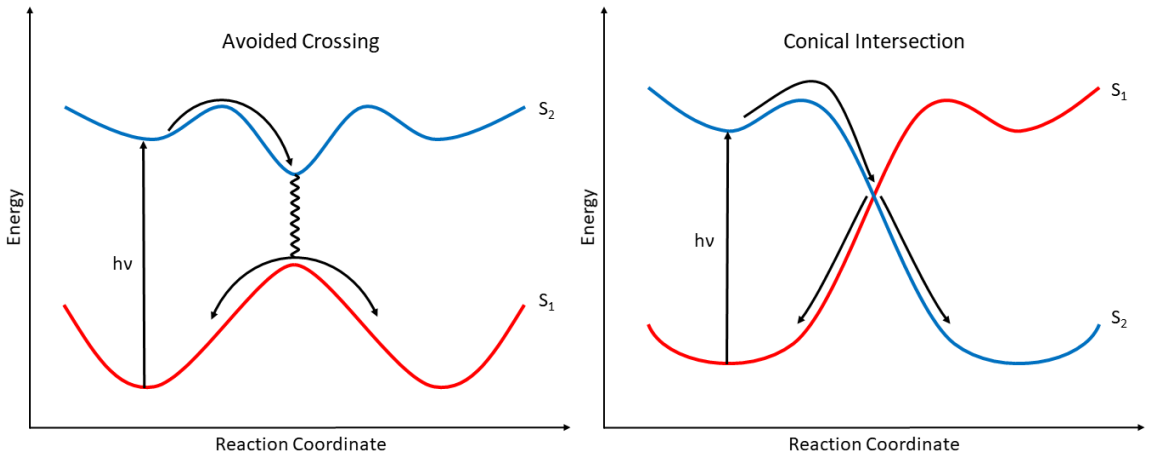

Fig. 1.5: Potential energy profiles of ground and excited states illustrating an avoided crossing and a conical intersection.

Vibronic coupling between two PES's allows the dissipation of energy from an energetically higher electronic state to another lower-lying electronic state through

a non-radiative decay process. When a broadband pulse excites a molecule into a higher electronic state, a wavepacket, $\Psi(t)$, is formed which may propagate over a PES, shown mathematically in Equation (1.13)

$$|\Psi(t)\rangle = \sum_n A_n e^{\left(-i\left[\frac{E_n t}{\hbar}+\phi_n\right]\right)} |\Psi_n\rangle \tag{1.13}$$

The wavepacket is a superposition of the time-independent eigenstates, Ψ_n, of the Hamiltonian with energy E_n. A_n and ϕ_n are the amplitude and phase of the individual modes that contribute to the overall wavepacket respectively. In the adiabatic framework, the temporal evolution of the wavepacket is dictated by the dimensions of the potential energy surface (PES) and the initial excitation conditions, with the vibrational wavepacket able to evolve adiabatically on a single PES, as given by the Born-Oppenheimer approximation. Under non-adiabatic conditions, such as at the point of a conical intersection, the amplitude of a wavepacket will decrease as strong interactions between the electronic states result in population transfer and relaxation to a lower energy state. To understand this phenomena, one must first consider the wavefunction as a linear combination of atomic orbitals (LCAO) as in Equation (1.14)[22].

$$\Psi = \sum_{i=1}^{N} c_i \phi_i \tag{1.14}$$

Where c_i is the contribution to the molecular wavefunction, Ψ, and ϕ_i is the atomic wavefunction. It is pertinent at this point to discuss what are atomic orbitals and the manner in which they may combine in order to produce molecular orbitals.

Atomic wavefunctions, often referred to as orbitals[23], are solutions of the previously discussed Schrödinger equation[24] (Section 1.1.1). These solutions may be separated into radial ($R_{nl}(r)$) and angular ($Y_{lm}(\theta,\phi)$) components, as shown in Equation (1.15)

$$\phi_{nlm} = R_{nl}(r) Y_{lm}(\theta, \phi) \tag{1.15}$$

Here, ϕ_{nlm} is the overall atomic wavefunction and the radial ($R_{nl}(r)$) and angular ($Y_{lm}(\theta,\phi)$) wavefunctions are associated Laguerre and spherical harmonic functions respectively. Furthermore, n, l and m correspond to the energy, angular momentum, and the angular momentum vector component (the magnetic quantum number) of each atomic wavefunction. The square modulus of this solution provides the probability distribution function, which describes the likelihood of finding an electron at a particular position around the atomic nucleus. A further note is that no two electrons

can occupy the same quantum state, given the fact that an electron is a fermionic particle. In accordance with the Pauli exclusion principle[25], each orbital can therefore only be occupied by a maximum of two electrons, with each electron having its own spin quantum number ($s = \pm\frac{1}{2}$). A graphical representation of hydrogen-like atomic orbitals of s, p and d character ($l = 0$, 1 and 2 respectively) may be seen in Figure 1.6

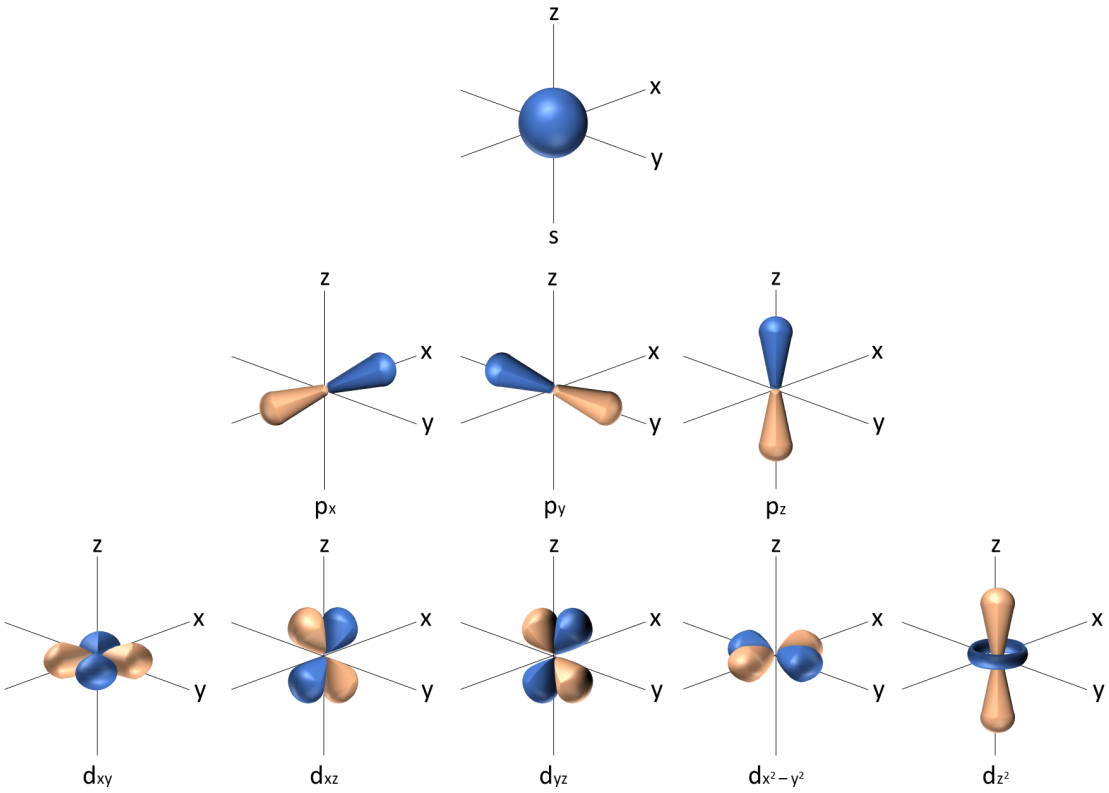

Fig. 1.6: Graphical representations of hydrogen-like atomic orbitals of s, p and d character. Orbital colours are used to depict relative phase.

When two atomic species are brought together, it is possible for their respective orbital wavefunctions to overlap and interfere to form a molecular orbital[19;23;26–28]. If the two electronic wavefunctions are in phase, it is possible for the orbitals to interfere constructively, leading to an accumulation of electron density within the internuclear space. This results in the formation of a bonding molecular orbital of σ or π character. Should the orbitals be out of phase with respect to each other, the two electronic wavefunctions will interfere destructively, resulting in a deficit of electron density within the internuclear space. This leads to the formation of an antibonding molecular orbital of σ^* or π^* character and repulsion between the nuclei. A bonding orbital sits energetically lower than the individual atomic orbitals, whereas an antibonding orbital lies energetically higher. If the overlapping atomic wavefunctions

have a net phase difference of zero, this results in the production of a non-bonding molecular orbital. Graphical representations of various bonding and anti-bonding orbitals may be seen in Figure 1.7.

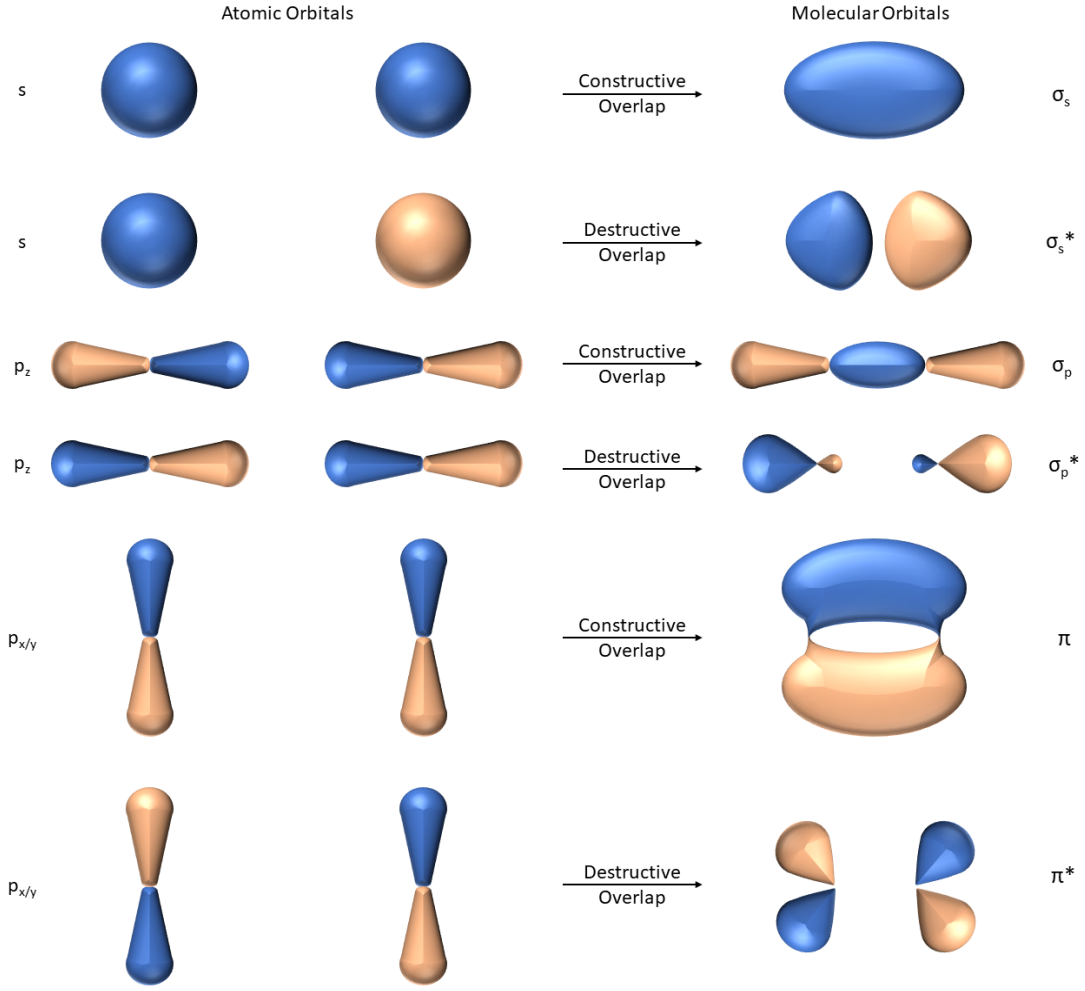

Fig. 1.7: Graphical representations of bonding and anti-bonding molecular orbitals formed from a linear combination of atomic orbitals.

Upon absorption of a UV photon, electrons transition from lower lying molecular orbitals to those that are energetically higher. For instance, an electron may originally lie in a π orbital but may be excited to an orbital of π^* or σ^* character. These transitions are denoted as $\pi\pi^*$ or $\pi\sigma^*$ respectively, with this notation employed throughout this thesis.

Returning to Equation (1.14), if all but two of the electronic wave equation solutions have been found, with solutions of the functions ϕ_1 and ϕ_2 forming a complete

orthonormal set, the final two wavefunctions may be presented as in Equation (1.16).

$$\Psi = c_1\phi_1 + c_2\phi_2 \tag{1.16}$$

With considerations of the time-independent Schrödinger equation presented previously in Equation (1.2), one can deduce that molecular energy levels, or orbital energies, are eigenvalues of the molecular Hamiltonian $\hat{H}$ as shown in Equation (1.17).

$$\begin{aligned} E &= \frac{\langle\Psi|\,\hat{H}\,|\Psi\rangle}{\langle\Psi|\Psi\rangle} \\ &= \frac{\langle c_1^*\phi_1 + c_2^*\phi_2|\,\hat{H}\,|c_1\phi_1 + c_2\phi_2\rangle}{\langle c_1^*\phi_1 + c_2^*\phi_2|c_1\phi_1 + c_2\phi_2\rangle} \\ &= \frac{{c_1}^2\langle\phi_1|\,\hat{H}\,|\phi_1\rangle + c_1^*c_2\langle\phi_1|\,\hat{H}\,|\phi_2\rangle + c_2^*c_1\langle\phi_2|\,\hat{H}\,|\phi_1\rangle + {c_2}^2\langle\phi_2|\,\hat{H}\,|\phi_2\rangle}{{c_1}^2\langle\phi_1|\phi_1\rangle + c_1^*c_2\langle\phi_1|\phi_2\rangle + c_2^*c_1\langle\phi_2|\phi_1\rangle + {c_2}^2\langle\phi_2|\phi_2\rangle} \end{aligned} \tag{1.17}$$

If the Hamiltonian matrix element $\langle\phi_i|\,\hat{H}\,|\phi_j\rangle$ is now defined as H_{ij} and the overlap integral $\langle\phi_i|\phi_j\rangle$ as S_{ij} and note that $H_{ij} = H_{ji}$ and $S_{ij} = S_{ji}$ respectively, Equation (1.17) simplifies to Equation (1.18), assuming $c_{1,2}$ are real numbers.

$$E\left({c_1}^2S_{11} + 2c_1c_2S_{12} + {c_2}^2S_{22}\right) = {c_1}^2H_{11} + 2c_1c_2H_{12} + {c_2}^2H_{22} \tag{1.18}$$

Employing the variational principle, differentiating Equation (1.18) with respect to c_1 and c_2 yields two equations with the two unknowns c_1 and c_2, which can be solved to determine the coefficients and the energy. These are known as secular equations and may be seen in Equation (1.19)[29].

$$\begin{aligned} c_1\left(H_{11} - ES_{11}\right) + c_2\left(H_{12} - ES_{12}\right) &= 0 \\ c_1\left(H_{12} - ES_{12}\right) + c_2\left(H_{22} - ES_{22}\right) &= 0 \end{aligned} \tag{1.19}$$

The energies of the PES may be found by solving for the eigenvalues of Equation (1.19), the results of which may be seen in Equation (1.20).

$$\begin{aligned} E_1 &= \frac{1}{2}\left[\left(H_{11} + H_{22}\right) + \sqrt{\left(H_{11} - H_{22}\right)^2 + 4{H_{21}}^2}\right] \\ E_2 &= \frac{1}{2}\left[\left(H_{11} + H_{22}\right) - \sqrt{\left(H_{11} - H_{22}\right)^2 + 4{H_{12}}^2}\right] \end{aligned} \tag{1.20}$$

Here $S_{11} = S_{22} = 1$ through normalisation and S_{12} is assumed 0 for simplification.

To this level of approximation, the energy of the two molecular orbitals are displaced with respect to the individual atomic orbitals (H_{11} and H_{22} respectively) by a factor of $\pm\sqrt{(H_{11}-H_{22})^2+4{H_{21}}^2}$. In the case of diatomic hydrogen, this is representative of 1s σ and σ^* molecular orbitals, as depicted in Figure 1.8.

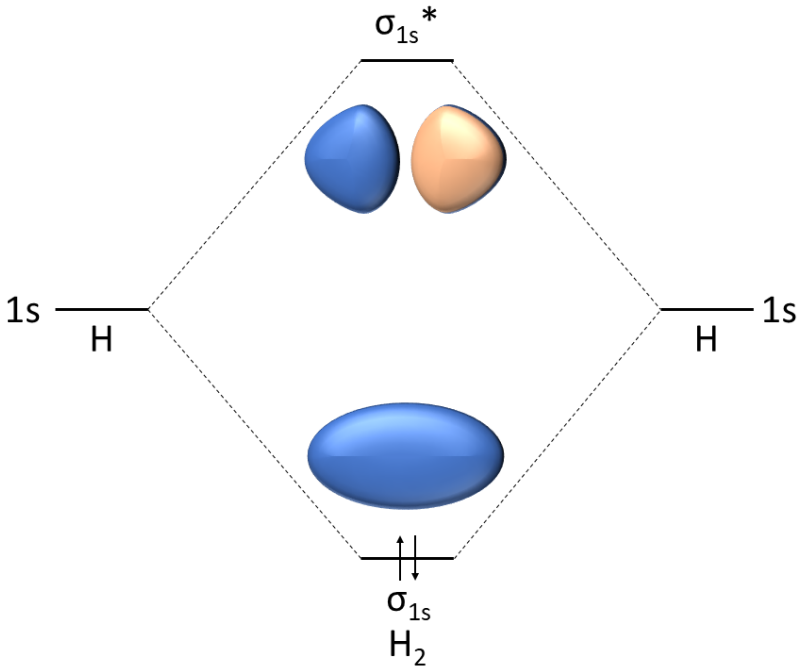

Fig. 1.8: Depictions of the σ and σ^* orbitals of the H_2 diatomic molecule.

For a conical intersection to occur between two potential energy surfaces, the two eigenvalues in Equation (1.20) must be equivalent, satisfying the conditions H_{11}=H_{22} and H_{12}=H_{21}=0 respectively. To solve for two conditions, two independent degrees of freedom are required, thus only molecules of three or more atoms may have a conical intersection. If two of the 3N-6 coordinates are chosen, $\mathbf{x}$ and $\mathbf{y}$, with the origin at W=H_{11}=H_{22} the secular equations may now be considered as either Equation (1.21) or Equation (1.22) .

$$\begin{bmatrix} W+h_1\mathbf{x}-E & l\mathbf{y} \\ l\mathbf{y} & W+h_2\mathbf{x}-E \end{bmatrix}\begin{bmatrix} c_1 \\ c_2 \end{bmatrix}=0 \tag{1.21}$$

$$\begin{bmatrix} W+(m+k)\mathbf{x}-E & l\mathbf{y} \\ l\mathbf{y} & W+(m-k)\mathbf{x}-E \end{bmatrix}\begin{bmatrix} c_1 \\ c_2 \end{bmatrix}=0 \tag{1.22}$$

Where the conditions presented in Equation (1.23) hold.

$$\begin{aligned} m &= \frac{1}{2}(h_1 + h_2) \\ k &= \frac{1}{2}(h_1 - h_2) \end{aligned} \tag{1.23}$$

The eigenvalues of this second set of secular equations may then be presented as in Equation (1.24).

$$E = W + m\mathbf{x} \pm \sqrt{k^2\mathbf{x}^2 + l^2\mathbf{y}^2} \tag{1.24}$$

This is the equation of a cone, giving rise to the name conical intersection. A 3D representation of a conical intersection may be seen in Figure 1.9.

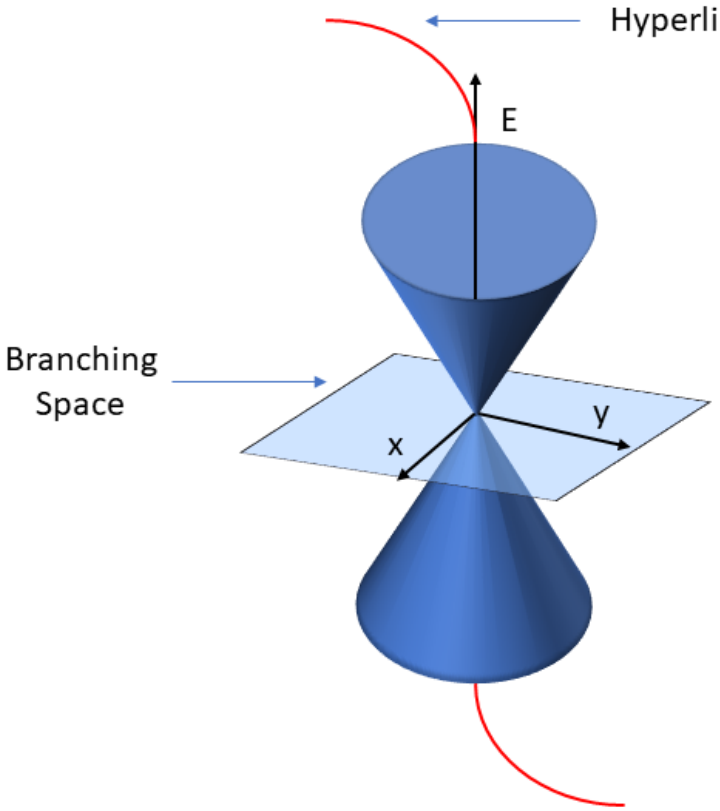

Fig. 1.9: A 3D representation of a conical intersection.

If one were to travel in the plane spanned by these **x** and **y** coordinates, known as the 'branching space', the degeneracy of the PES would breakdown, whereas if one were to move along any of the other n-2 degrees of freedom, the degeneracy would be held. This space is known as a 'hyperline' consisting of an infinite number of conical

intersection points. The two directions which breakdown this degeneracy are known as the gradient difference vector, $\vec{g}$, and the gradient of the interstate coupling vector, $\vec{h}$, which may be seen in Equation (1.25) and Equation (1.26) respectively

$$\vec{g} = \frac{\partial \left(E_1 - E_2\right)}{\partial \vec{R}} \tag{1.25}$$

$$\vec{h} = \langle \Psi_1 | \frac{\partial \hat{H}^{el}}{\partial \vec{R}} | \Psi_2 \rangle \tag{1.26}$$

Where E_1 and E_2 are the energy eigenvalues found in Equation (1.24), $\vec{R}$ is the nuclear configuration vector, $\hat{H}^{\text{el}}$ is the conical intersection Hamiltonian, and Ψ_1 and Ψ_2 are the adiabatic wavefunctions.

Conical intersections, also known as photochemical funnels, have been found to be extremely efficient at non-radiatively transfering population between vibronic states and are attributed as a major relaxation pathway to photostability. A key example is that of the DNA bases, where conical intersections play a leading role in non-destructively dissipating excess energy on an ultrafast timescale, preventing chemical damage. A key example of this is a comparison of two of the nucelobases presented previously in Figure 1.2, 2,6-diaminopurine and cytosine. Utilising similar pump wavelengths across 280-290 nm region, 2,6-diaminopurine displays a much more extended lifetime (6 - 9 ns)[30] than that of cytosine (55 - 150 ps)[31] which may partially explain nature's selectivity.

1.2 Molecular Relaxation Processes

Having provided a theoretical understanding of the assumptions and approximations required for spectroscopic analysis, an understanding of how molecules and electrons dissipate excess energy upon photonic excitation is now required. This section will provide an overview of the various radiative and non-radiative energy dissipation mechanisms one can observe when a molecule redistributes excess energy. A summary of these various mechanisms is provided in the Jablonski diagram [32] in Figure 1.10.

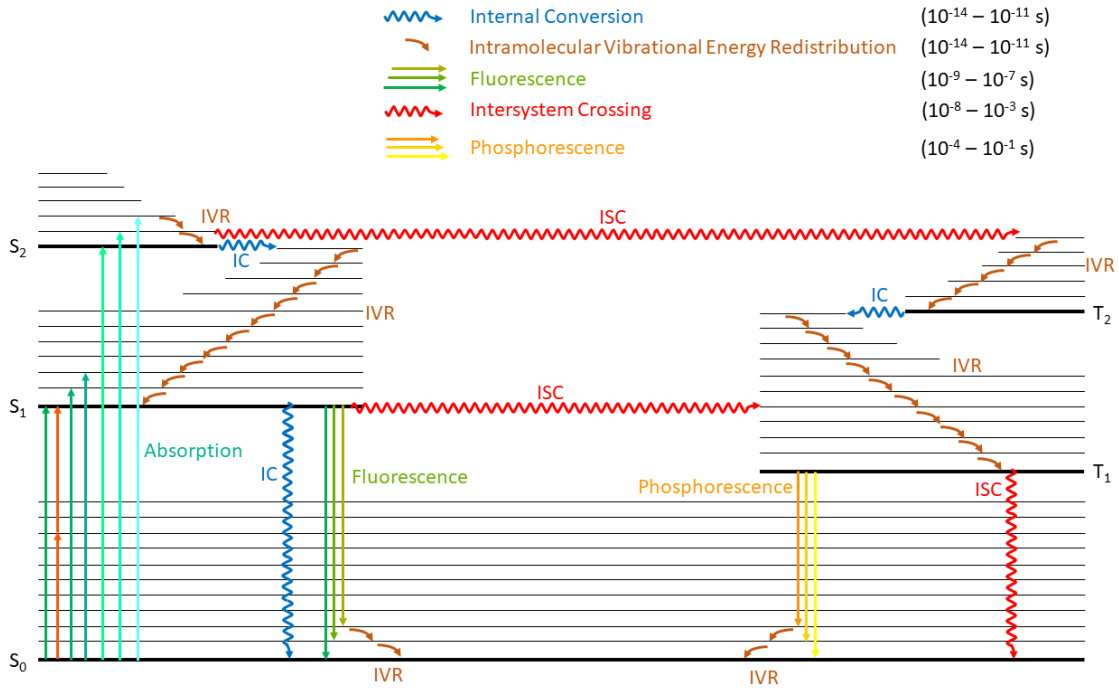

Fig. 1.10: A Jablonski diagram presenting the various radiative and non-radiative photophysical processes a molecule may undergo to non-destructively release excess energy.

1.2.1 Non-Radiative Decay

Intramolecular Vibrational Energy Redistribution

Intramolecular vibrational energy redistribution [4;15;33] (IVR) is a non-radiative energy redistribution process which occurs on ultrafast timescales (10^{-14} - 10^{-11} s). The principle of IVR is that the few vibrational modes populated in an initially excited state may disperse energy between a larger number of vibrational modes within the particular electronic state. Due to energy conservation considerations, energy dissipated via IVR must be considered as a redistribution across the vibrational modes

along a particular reaction coordinate and not an energy release mechanism. When in the condensed phase, vibrational modes may couple to the surrounding environment, with excess energy then dissipated safely in the from of heat. An example of intramolecular vibrational energy redistribution may be seen in Figure 1.10.

Internal Conversion

Internal conversion (IC) is a non-radiative decay mechanism based on the principle of coupling between vibronic levels, to perform radiationless population and energy transfer from one excited electronic state to an energetically lower electronic state[19–21]. Internal conversion is termed when the transition occurs between states of equivalent spin ($S_2 \rightarrow S_1$, $T_2 \rightarrow T_1$) and occurs on an ultrafast timescale (10^{-14} - 10^{-11} s). The probability of a non-adiabatic event such as this occurring is dictated by the energy separation between the vibronic states, with probability highest as the energy between states becomes degenerate ($\Delta E = 0$)[21]. These points of degeneracy are known as conical intersections, as previously discussed in Section 1.1.4. An example of internal conversion may be seen in Figure 1.10

Intersystem Crossing

Intersystem crossing is an example of a non-radiative energy and population transfer between two electronic states of different spin multiplicity ($S_1 \rightarrow T_1$, $T_2 \rightarrow S_1$). Although formally forbidden due to conservation of angular momentum, a rule first stated by Mostafa El-Sayed[34] says that the rate of intersystem crossing is relatively large if the radiationless transition involves a change of molecular orbital type. Intersystem crossing thus becomes a competitive energy dissipation pathway through molecular spin-orbit coupling. Furthermore, intersystem crossing is prevalent in systems which display substantial spin/orbital interactions, where a change of spin is more favourable, and so is commonly found in molecules containing heavy atoms[35]. These population transfers occur on a nanosecond to millisecond (10^{-8} - 10^{-3} s) timescale, although there is also a growing body of evidence for ultrafast intersystem crossing[36–38]. An example of intersystem crossing may be seen in Figure 1.10.

Photodissociation

Photodissociation is a destructive energy release mechanism of molecules upon absorption of one or more photons. In this process excess energy is released through the breaking of bonds between nuclei, with any remaining excess energy converted into

translational energy in the products. A schematic of a photodissociation process may be seen in Figure 1.11.

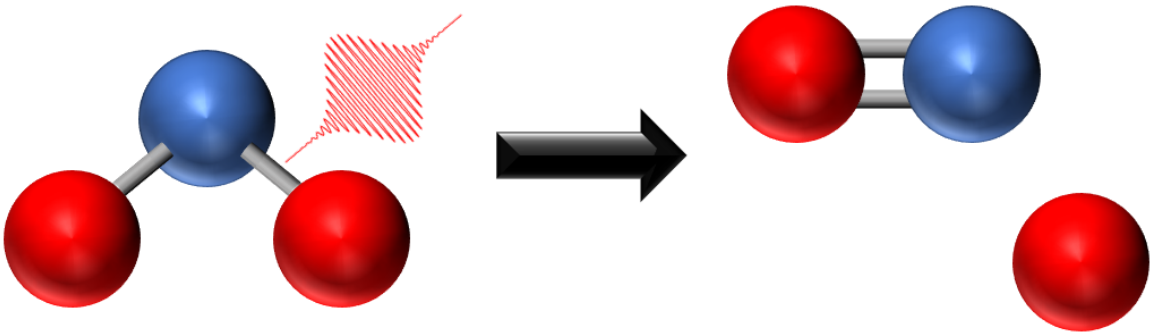

Fig. 1.11: A schematic of an example photodissociation event. Upon absorption of a photon hν, energy is released from the molecule through bond-breaking.

When a molecule is excited with low energy photons, such as those in the infrared region of the spectrum, a high-photon order absorption is required for photodissociation. For efficient photodissociation in this regime, fast photon absorption must out-compete energy dissipation mechanisms such as IVR and collisional cooling[39]. When utilising high energy photons in the UV and VUV region it is possible to induce fragmentation with far fewer photons, even single photon fragmentation, due to the rapidity and magnitude of the energy deposition[40].

1.2.2 Radiative Decay

Radiative decay processes are those in which an excited state molecule emits a photon in order to release excess energy. There are two main forms of radiative processes in molecular dynamics, fluorescence[41] and phosphorescence[42], which will be discussed presently.

Fluorescence and phosphorescence are radiative decay processes which occur on the nanosecond (10^{-9} - 10^{-7} s) and millisecond ($>10^{-3}$ s) timescales respectively. In fluorescence, excitation is achieved through absorption of a photon from the molecular ground state to an excited singlet state, prior to the emission of a photon of equal or lower energy[41] as a result of IVR, as previously discussed in Section 1.2.1[43]. Phosphorescence, however, undergoes a further non-radiative relaxation process known as intersystem crossing, as explained in Section 1.2.1, transitioning from the excited singlet state to an energetically lower, longer lived triplet state prior to radiative decay[43]. These processes may be either spontaneous, where the photon is emitted at random from the molecule, or stimulated, whereby a molecule already in an excited

state absorbs a further photon inducing the emission of a fluorescence or phosphorescence photon. A photon emitted due to stimulated emission will have identical polarisation, frequency, phase and propagation vector to the photon which caused stimulation. Examples of fluorescence and phosphorescence decays may be seen in Figure 1.10.

1.3 Experimental Molecular Dynamics

Thus far this thesis has provided an understanding of the basic background to non-adiabatic dynamics and the various energy dissipation mechanisms which dictate radiative and non-radiative decay. In order to study these processes in detail, various spectroscopic techniques may be employed to observe and follow the dynamics of a photoexcited molecule. This section aims to discuss the various spectroscopic tools which may be utilised to unravel these molecular dynamics, as well as the observables which may be obtained from these various methods.

1.3.1 Spectroscopic Techniques

Broadly, spectroscopic techniques may be divided into two complementary categories, frequency-resolved techniques and time-resolved techniques. Due to the inherent nature of a laser pulse, as the temporal duration of a pulse becomes shorter, the bandwidth broadens, and thus the frequency of a photon within the pulse becomes more uncertain. Conversely, as the frequency of a laser pulse is known to a greater precision, the temporal nature of the pulse becomes elongated. A wealth of molecular spectroscopic information may be gleaned from utilisation of both temporal and frequency resolved methods, with a subset described in the following section.

Direct and Multiphoton Ionisation

One of the simplest frequency-resolved measurements one may consider is that of direct photoionisation of a molecule or atom with UV light [44]. This is a process by which a single photon of UV radiation is absorbed by an atom or molecule to promote an electron to the ionisation continuum. A high-energy UV-photon source is utilised so as to determine the precise frequency at which an ionisation event occurs, through observation of the kinetic energy of photoproducts, and thus discover the ionisation potential of a molecular species. The development of highly tunable synchrotron sources has expanded this technique into both the vacuum and extreme ultraviolet regions of the electromagnetic spectrum, extending the range of molecules which may be investigated [45] as well as allowing for the determination of multi-ionisation potentials [46].

In order to obtain frequency resolved data utilising commercially available table-top laser systems, many molecular species require a multiphoton ionisation [47;48] scheme. In this case, two or more photons below the ionisation threshold are simultaneously absorbed by the molecule under investigation in order to achieve ionisation. If one knows

the photon order involved during ionisation, it is possible to deduce the molecule's ionisation potential. The multiphoton process does not require that the photon energies involved summate to one of the excited states intrinsic to the molecule, however, should the first photon absorbed during multiphoton ionisation correlate with one of these states, the propensity for ionisation significantly increases. This phenomenon is known as resonantly enhanced multiphoton ionisation[49;50] (REMPI) and is a useful tool in elucidating the excited states of a molecule. Schematics of both direct and multiphoton ionisation are presented in Figure 1.12.

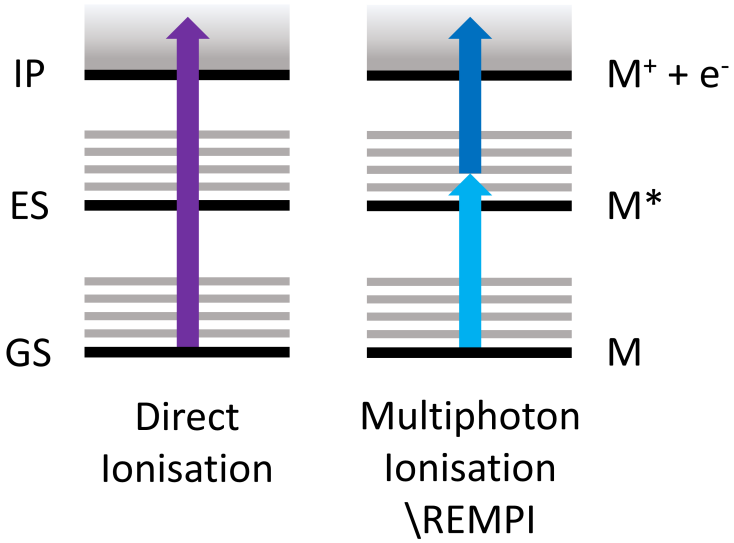

Fig. 1.12: Jablonski diagrams presenting direct ionisation and multiphoton/REMPI ionisation schemes.

ZEKE and MATI

There are numerous extensions to the REMPI technique within frequency resolved spectroscopy, however one of particular interest in this field is the so-called zero electron kinetic energy[51] (ZEKE) spectroscopy. A pump-probe REMPI scheme is utilised such that a molecule is first promoted to an excited state by a photon of fixed-wavelength, prior to an excitation to a high lying Rydberg state by a photon of tunable energy. The ZEKE technique consists of molecular excitation via the aforementioned REMPI scheme, prior to a delay, on the order of 1 μs, to allow for the dispersion of any low energy photoelectrons produced. A pulsed electric field is then applied to the molecules, with excited Rydberg states close to the ionisation threshold then capable of releasing an electron in an autoionisation event. Electrons emitted may then be detected through standard time-of-flight techniques. Through tuning of

the Rydberg excitation wavelength, it is possible to attain excited state spectra for the molecule with resolution on the order of 1 cm^{-1} [52].

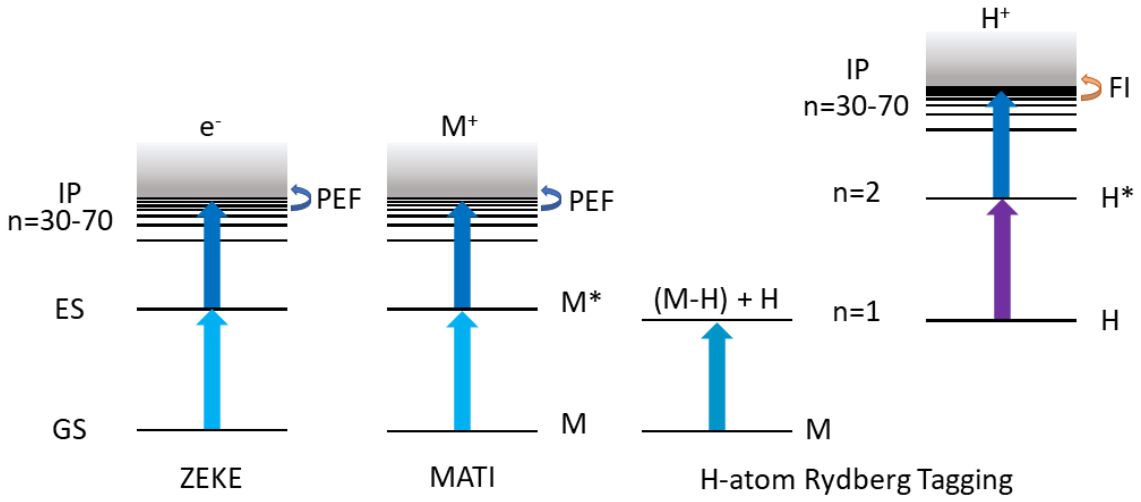

Fig. 1.13: Jablonski diagrams presenting ZEKE and MATI ionisation schemes, as well as a depiction of the H-atom Rydberg tagging technique. ZEKE and MATI are excited to high lying Rydberg states prior to ionisation with a pulsed electic field. H-atom Rydberg tagging requires a photodissociation event for the release of H-atoms prior to field ionisation and detection.

A limitation of the ZEKE technique is that there is no information with regard to the origin of the emitted electron, whether it was produced by the parent molecule or a neutral fragment. This information may be attained through use of a mass selective alternative to ZEKE known as mass analysed threshold ionisation [53] (MATI). The MATI technique consists of the same REMPI excitation scheme to a high lying Rydberg state, with ionisation again achieved through use of a pulsed electric field, however the frequency resolved analysis is performed on the produced ions rather than electrons. Post Rydberg-excitation, a small electric field (<1 V/cm) is applied to the molecules in order to spatially separate any photoions from excited state neutrals. Field ionisation of the neutral Rydberg atoms/molecules then allows for a mass selective analysis of a molecule's rovibronic structure. MATI has an equivalent frequency resolution to ZEKE spectroscopy, however the advantage of mass selection allows for the observation of additional processes such as molecular fragmentation [54]. Examples of ZEKE and MATI ionisation schemes can be seen in Figure 1.13.

H Atom Rydberg Tagging

In order to investigate the translational energy of photofragments after a photodissociation process, a similar technique one may utilise is that of H atom Rydberg tag-

ging[55;56]. The technique consists of a gas-phase molecular sample of interest first undergoing photolysis, producing rotationally and vibrationally excited H atoms as well as an additional excited photoproduct. A multiphoton $(1 + 1')$ excitation process (one photon VUV and one photon UV) excites the H atoms to a high-lying Rydberg state (n=30-90), whilst in the presence of a weak electric field (20 V/cm)[57]. The role of the electric field is to remove any photoions produced during the excitation process, as well as to stabilise the Rydberg states and extend their lifetime[58]. H atoms then propagate along a time-of-flight tube and are field-ionised momentarily before detection. Field-ionisation post time-of-flight increases detection resolution as it negates the effects of space-charge repulsion induced in ionised samples over long flight distances. High resolution Total Kinetic Energy Release (TKER) spectra may then be obtained through analysis of the H atom TOF profile[59], with anisotropic studies also possible through variation of the dissociation laser polarisation[60]. It is also possible to utilise alternative atomic species for Rydberg tagging studies, including oxygen[61] and sulphur[62], broadening the applicability of the technique.

Hole-burning Spectroscopy

If one wishes to obtain conformer-specific frequency-resolved spectra, an alternative REMPI technique which may be considered is that of hole-burning spectroscopy[63]. Within the hole-burning excitation method, the REMPI scheme is utilised as a conformer-specific probe to excite and ionise the molecule directly from the ground state. By either exciting the molecule of interest vibrationally[64;65] (IR-UV) or electronically[66;67] (UV-UV) prior to the REMPI probing scheme, it is possible to observe the change in ground state population in the produced parent ions. Thus, through variation of the excitation wavelength, it is possible to obtain conformer-specific frequency-resolved molecular spectra through monitoring the 'ion-dips' in parent ion production. It is possible to use hole-burning spectroscopy in conjunction with another frequency-resolved technique, laser induced fluorescence, allowing for confidence in conformer specificity in the latter technique[68;69]. Example Jablonski diagrams of IR-UV and UV-UV hole-burning spectroscopy may be seen in Figure 1.14.

Laser Induced Fluorescence

Laser induced fluorescence[70;71] (LIF) is a versatile spectroscopic technique which may be utilised both in the time- and frequency-domain. The LIF process consists of an incident photon first being absorbed by a molecule, promoting the molecule from the ground state to a vibrationally excited electronic state. The vibrationally

excited molecule then undergoes non-radiative energy dissipation, relaxing to the lowest vibrational level of the electronic state, prior to the spontaneous emission of a fluorescence photon, relaxing the molecule to a vibrational level within the ground state.

In the case of frequency-resolved studies, there are two main LIF measurements used to attain the vibrational structure of a molecule, disperse spectra[72;73] and excitation spectra[74;75]. To attain an excitation spectrum, the fluorescence yield at a fixed wavelength is observed for a range of excitation wavelengths. Conversely, for a dispersion spectrum a fixed wavelength excitation laser is utilised to observe the wavelength dependent fluorescence yield which is spontaneously emitted by a molecule. A combination of both techniques is often used to attain the full vibrational spectrum of a fluorescing molecule[76–79].

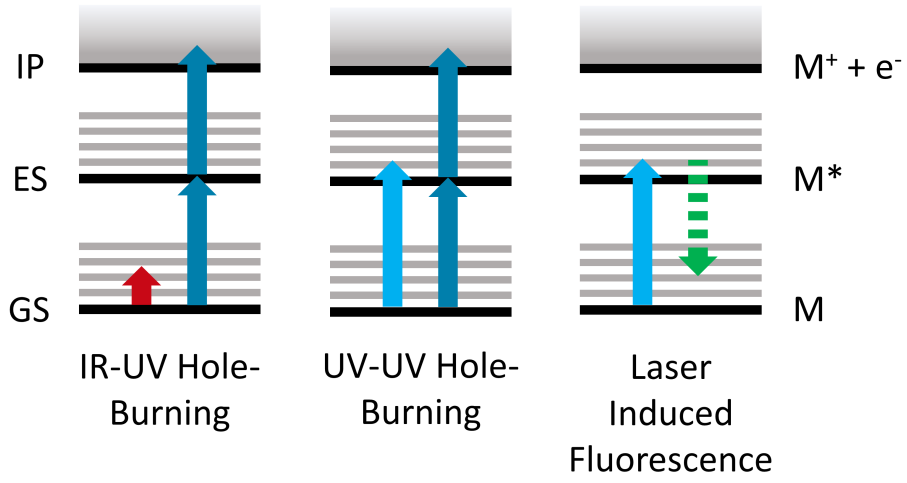

Fig. 1.14: Jablonski diagrams presenting IR-UV and UV-UV holeburning spectroscopy techniques, in addition to a schematic of the laser induced fluorescence principle.

Temporal spectroscopic information may also be obtained through investigating gas-phase molecular fluorescence[80–82]. A molecule of interest may be excited to a particular electronic or vibrational state through absorption of a photon, before spontaneously emitting a secondary photon of equal or lower energy. Observation of the flux of photons spontaneously emitted by the molecule, achieved through single-photon counting[83], provides an insight to the lifetime of a particular state of the molecule on the picosecond to nanosecond timescale.

Although a useful spectroscopic technique, one of the major limitations of fluorescence spectroscopy is that it may only probe molecular decay mechanisms with a

significant fluorescence yield. Fluorescence spectroscopy is effectively blind to non-radiative decay mechanisms, such as bond-breaking and non-adiabatic energy redistribution mechanisms, and thus is restricted to molecules with a propensity for radiative energy dissipation[84]. An example Jablonski diagram of laser induced fluorescence may be seen in Figure 1.14.

Transient Absorption Spectroscopy

An alternative technique one may consider to provide both frequency- and time-resolved spectroscopic information is that of transient absorption spectroscopy[85–89]. The technique consists of a sample of interest first being excited by an ultrafast pump pulse, prior to being probed by a chirped (stretched temporally and spectrally) supercontinuum pulse at a controlled and known time later. The observable monitored in this experiment is the supercontinuum spectrum post sample interaction, with a difference absorption spectrum between ground and excited state molecules recorded[90]. Through careful control of the pump-probe separation, a wealth of spectroscopic information may be gleaned from the transient absorption spectrum, with it possible to observe processes including electron/proton transfer[91;92], intersystem crossing[93], energy migration[94] and isomerisation[95]. Although some gas-phase measurements have previously been reported[96;97], transient absorption spectroscopy is more customarily utilised as a solution-phase technique with resolution down to the attosecond regime possible[98–100].

2D-Spectroscopy

A limitation of the transient absorption technique is an inability to distinguish the origin of coupled vibrational or electronic peaks; whether signals arise from different species with individual optical excitation frequencies, or from coupled systems, with energy levels split only by coupling constants. 2D spectroscopy[101–103] may be utilised to interrogate both coupled vibrational modes (2DIR)[104] as well as coupled electronic transitions (2DES)[105]. There are two main methods for obtaining a 2D-spectrum, one in the frequency domain (2D double-resonance spectroscopy)[106] and one in the time domain (2D Fourier transform spectroscopy)[107], each with a respective transient equivalent[108;109].

The experimental principle behind both 2D methods is similar, with spectral analysis following three laser field-molecule interactions. The first field interaction creates a coherence between the excited vibrational level or electronic state with the molecular ground state, whilst the second field interaction creates a population in the excited or

ground states[110], with temporal separation between these two interactions known as the coherence time, τ. When the molecules are probed by a third laser field, following waiting time T, an electronic coherence is again created within the molecule, creating singly and doubly excited electronic or vibrational states. This induces a third-order polarisation response from the molecule and, after a detection time t, a radiating signal field response. An interferometric response between the radiating field signal and part of the original excitation beam allows for complete analysis of the resultant field amplitude and phase. This principle pulse sequence is presented pictorially in Figure 1.15.

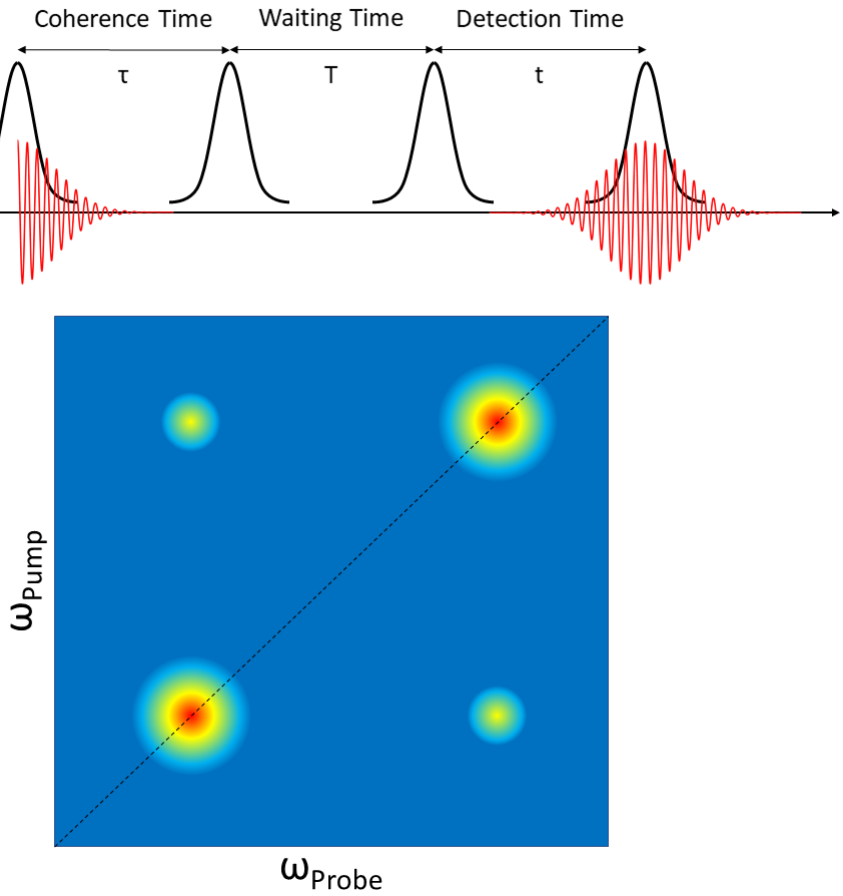

Fig. 1.15: A pictorial representation of the excitation scheme utilised in a 2DIR or 2DES experiment, as well as a representation of a 2D-spectrum demonstrating ground-state vibrational coupling.

A 2D double-resonance spectroscopy experiment consists of a sample being interrogated by two laser pulses in a crossed beam configuration. The pump pulse is spectrally filtered to form a narrow-band pulse, whilst the probe pulse is maintained temporally short[111]. The pump-probe waiting time in these experiments is typically on the order of 2 ps, so as to minimise temporal overlap between pump and probe

pulses. The first two laser-molecule interactions occur within the temporal duration of the pump pulse, however within the bounds of this set-up it is not possible to control laser-molecule interaction separation time, nor the order in which these two field interactions occur[112]. This results in the third order response obtained containing both rephasing and non-rephasing components of the wavevector architecture[113].

In the time-domain, a 2D Fourier-transform spectroscopy experiment consists of a sample being interrogated by three broadband and ultrafast laser pulses in either a crossed beam[114] or box configuration[115;116]. In a crossed beam allignment, the emitted field emission pulse is heterodyned with the residual pump beam, whilst in a box geometry an additional local oscillator pulse is required, positioned as the fourth corner of the square layout[117]. The second frequency axis is generated through Fourier transformation with respect to the change in coherence time τ. As the order in which the first and second laser-field interact with the molecule is known in this set-up[113], the first laser-field pulse must be temporally scanned equidistantly through the second laser-field pulse in order to collect equally-weighted rephasing and non-rephasing components of the wavevector architecture[118]. A transient variation of this experiment may again be achieved through variation of the waiting time T, with temporal resolution in the femtosecond regime accessible[119].

Both of these methods produce broadly equivalent equilibria spectra[112], however a description of the benefits of utilising each technique is outwith the scope of this thesis. The layout of an equilibria 2D spectrum consists of a plot comparing excitation wavenumbers with emission wavenumbers of the sample under investigation. Peaks appearing along the diagonal of the plot with equivalent wavenumber are known as the autopeaks with the line representative of a standard 1D absorption spectrum. Peaks arising away from this diagonal line may be considered as crosspeaks, a signature of vibrational or electronic coupling between two states. A pictorial representation of a 2D-spectrum may be seen in Figure 1.15.

With the inclusion of transient measurements, it is possible to follow the temporal evolution of these excited couplings to follow the folding of peptides[120;121] and structural rearrangements in catalytic complexes[122], as well as tautomerisation of organic compounds[123]. Although some measurements have been performed in the gas phase[124], 2D spectroscopy of this form is still mainly utilised as a solution-phase technique.

Gas-Phase Electron Diffraction

It should be noted that the excited-state dynamics of a molecule are not the only important time-resolved measurement that needs to be considered, the intermittent

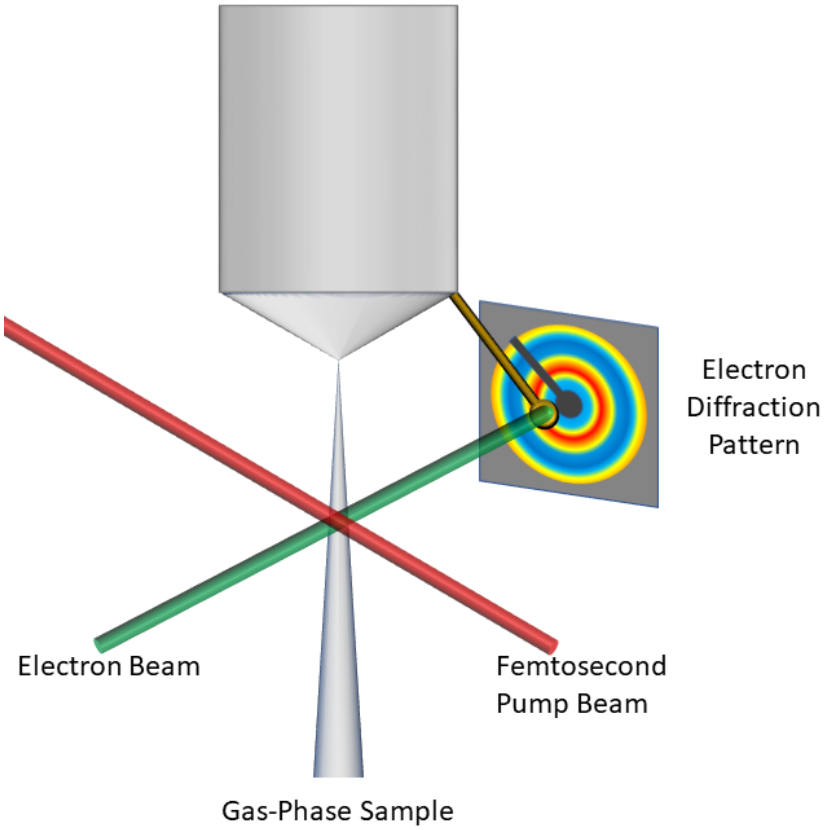

Fig. 1.16: An example time-resolved gas-phase electron diffraction experimental scheme. Femtosecond pump pulses excite the molecule of interest prior to an electron beam probe to interrogate molecular structure.

structures which form during energy redistribution are also of vital importance in understanding the structure-function-dynamics relationship of any molecule. Traditionally, gas-phase electron diffraction has been a conventional technique in the determination of equilibria molecular structures[125–130]. When an accelerated beam of electrons is incident on a gaseous molecular sample, the probing electrons are scattered upon interaction with the charge gradients of the molecule's nuclei onto a 2D detector. If no alignment of the molecules within the molecular beam has been performed[131], the resulting diffraction pattern produced from the sample will consist of a series of concentric rings and may be interpreted as a convolution of sinusoidal functions dependent upon the interatomic distances of the molecule and scatter intensity. A Fourier transform of the data provides radial distribution curves, peaking at the average interatomic distances within the molecule[132].

To perform ultrafast gas-phase electron diffraction, the electron beam used must be pulsed and utilised as a probe after laser excitation of the molecular sample[133–135].

Temporal separation between laser pump and electron probe pulses allow for time-resolved measurements of a molecule's excited-state structure. Although previously limited to picosecond timescales due to difficulties including space-charge repulsion between electrons[136] and velocity mismatch between electron and laser pulses[137], recent developments have allowed for femtosecond resolution to be achieved at both accelerator facilities[138;139] and with table-top devices[140].

2D Imaging Techniques

2D-imaging spectroscopic techniques[141] are also vital in the analysis of a molecule's dynamical behaviour. The use of a 2D array as a detector allows one to obtain measurements of a molecule or fragment's internal energy and velocity simultaneously. Alternatively, one can equally measure the electron emissions post molecular ionisation, providing an energy- and angular-resolved measurement of the photoemission process. The techniques described here are known as photoion imaging spectroscopy[142] and photoelectron imaging spectroscopy[143] respectively, with a brief description of the methods explained presently.

The technique consists of a sample of interest first being seeded in a molecular beam. Through irradiation with a laser pulse, one may electronically excite a molecule and/or induce dissociation. If single or muti-photon absorption from a photolysis laser is in excess of the molecule's dissociation threshold, surplus energy is partitioned between the internal and kinetic energies of the photoproducts. Through ionisation a controlled time later, and due to momentum conservation during the photodissociation process, photoproducts expand on a Newton sphere and are directed towards an array detector by an electrode assembly.

Initial molecular imaging studies utilised a repeller plate and grounded grid pair[144;145], with photoions born in the middle of this assembly. It was later discovered that by replacing the grid pair with open extractor and grounding electrodes in an Einzel lens configuration, it is possible to map the velocity of photoions or photoelectrons on the 2D detector, independent of their initial starting positions, in a technique known as velocity map imaging[146;147]. The polarity of the voltages applied to a repeller, extractor and ground plate dictate whether one investigates the electronic or ionic distribution post-ionisation, with a positive repeller voltage and negative electrode voltage for ion detection and an opposite voltage configuration for electron detection.

When the ionic or electronic expansion is projected onto a 2D detector, such as a microchannel plate/phosphor screen assembly, circular images may be collected on a camera. The attained images must be processed so that it is possible to effectively retrieve the central slice of the projected Newton sphere, containing the energy and

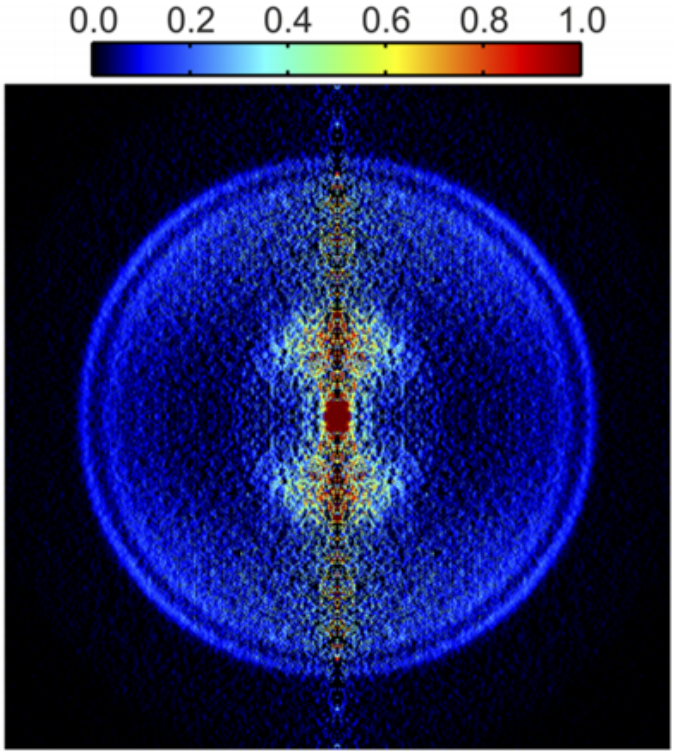

Fig. 1.17: An example of an abel transformed photoelectron image of pyrrole following excitation at 267 nm and probe at 300 nm. Noise along the central aixs is a reult of the abel inversion method. Image taken from Crane et al.[148].

angle-resolved spectroscopic information of the photoproducts, with various methods available to do so[149–155]. The radius of the image produced determines the kinetic energy of the photoproduct and, due to the use of the 2D detector, the angular distribution[156] of photoproducts is also attained. If observing a particular photodissociation product, mass selectivity may be achieved through gating of the 2D detector, only acquiring data within the fragment's time-of-flight window[157;158]. An example of an abel-transformed 2D-photoelectron image may be seen in Figure 1.17

If one wishes to monitor multiple mass channels in a spectroscopic imaging experiment, there are a number of methods by which one may do so. The simplest technique to implement is to gate the detector for the time-of-flight of each individual mass fragment in the ion imaging set-up previously described, building a multi-mass image spectrum over multiple data acquisition periods[159–162]. This, however, can become a time-consuming technique if the molecule under investigation has multiple fragmentation pathways, leading to a large variety of molecular photoproducts and a full fragment analysis is unreasonable.

An alternative method of multi-mass ion imaging which allows for detection of mul-

tiple photofragment translational energies simultaneously may be achieved through use of a constant momentum mass spectrometer[163–165]. The technique itself consists of a sample in a molecular beam first interacting with a photolysis laser, leading to photodissociation and a spherical expansion of the photoproducts due to the fragments' recoil velocities. A controlled time later, a VUV probe beam interacts across the centre of the spherical photoproduct distribution, ionising the photodissociation products and creating a velocity distribution in the centre-of-mass frame. A pulsed electric field may then be utilised for ion extraction prior to entry into a radial cylindrical energy analyser for mass selectivity and translational energy analysis. Data collection on a 2D ion detector allows for mass and energy resolved analysis of the photoproducts present, with it also possible to discern between dissociative products of neutral molecules and ionisation dissociation products by their image distributions. This technique, however, loses the angle-resolved aspect gained from a velocity map imaging experiment and thus limits the spectroscopic data which may be attained.

A final multi-mass imaging technique of note has been recently developed due to technological advances in ultrafast imaging[167;168]. By utilising the same VMI set-up as described previously for photoproduct imaging, but replacing the camera with a PImMs camera[169;170], one is able to image multiple fragments within a single measurement. The most recently developed PImMs camera, the PImMs2[171], consists of a 324 by 324 CMOS array, with each individual pixel capable of recording the presence and time of arrival of a charged particle four times per millisecond with a temporal resolution of 12.5 ns. If molecular flux is maintained low, it is possible to collect ion images for multiple mass fragments simultaneously and generate a complete picture of the photoproduct emissions in a single experiment. It should also be noted at this point that the PImMs camera may be utilised for various other applications, with examples including coulomb explosion imaging for structure determination[172–175] and neutron imaging[176]. An example PIMMS imaging spectrum may be seen in Figure 1.18.

An important dynamical extension to the imaging methods discussed previously is the ability to perform time-resolved measurements[166;177–183]. This is achieved through careful timing variation between the arrival of the photolysis/ electronic excitation pulse (pump pulse) and the ionisation pulse (probe pulse). One is then able to perform an extremely differential measurement, with time-, energy- and angle-resolved data capable of being collected simultaneously, with resolution possible down to the attosecond regime[184–186]. It should also be noted that femtosecond time-resolved photoelectron spectroscopy[187;188] is an established technique within the Townsend group, utilised within a wide variety of studies[148;189–196].

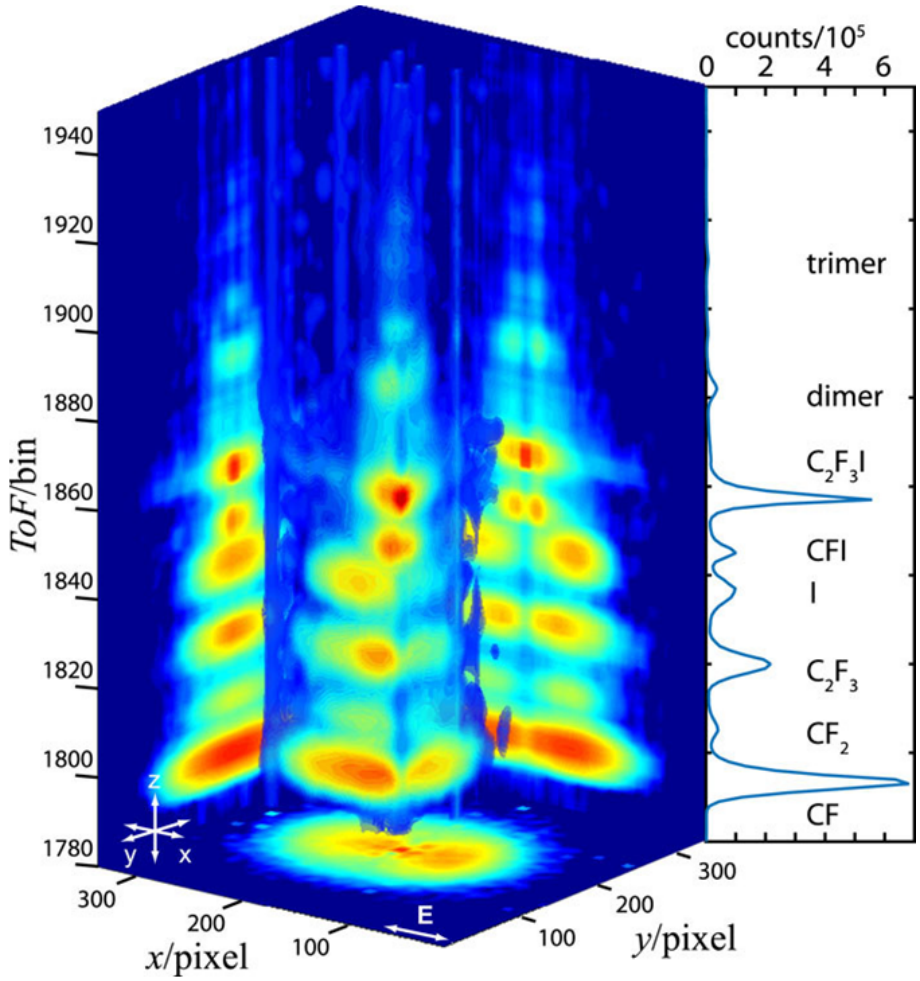

Fig. 1.18: An example PImMS spectrum of the molecule C_2F_2I following VUV-UV pump-probe excitation. The fast response of the PImMs cammera allows for 2D-imaging of multiple mass fragments within a single measurement. Image taken from Forbes et al.[166].

1.3.2 Time-Resolved Photoion-Yield Spectroscopy

Time-resolved photoion yield spectroscopy[10;197;198] is a simple yet effective technique for the study of molecular dynamics. Although not as differential a measurement as some of the others discussed in Section 1.3.1, it is sufficient for the spectroscopic applications pursued within this thesis. An example time-resolved ion-yield set-up may be seen in Figure 1.19.

The technique itself consists of a molecular gaseous sample being intercepted by femtosecond laser pulses in the center of a time-of-flight mass spectrometer. The first femtosecond pulse initiates an excited state process, acting as the pump pulse, with a second femtosecond pulse utilised to probe the excited state population a controlled time later through ionisation. By monitoring the yield of the ionised parent with

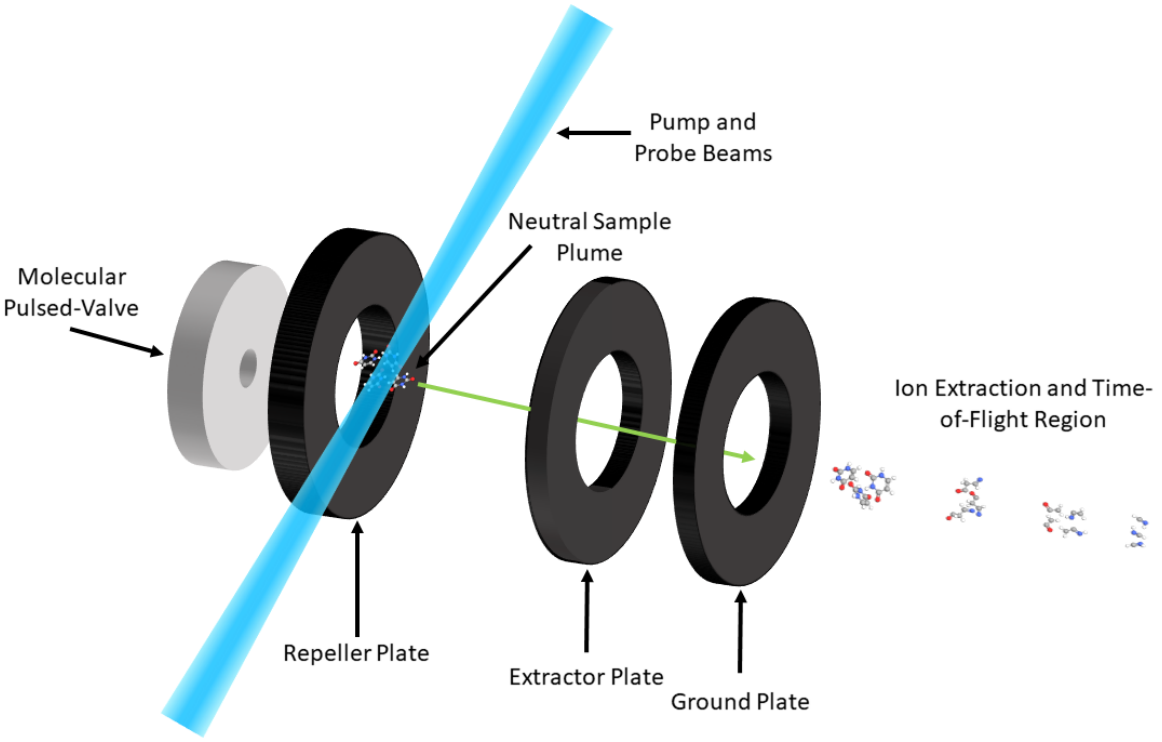

Fig. 1.19: A schematic diagram of a time-resolved ion-yield set-up.

respect to the time delay between pump and probe beams, Δt, it is possible to observe the dynamical changes in parent lifetime. Temporal resolution of the experiment is typically limited by the convoluted width of the pump and probe pulses utilised.

A further caveat to the time-resolved photoion yield technique is that one is able to also monitor the appearance of photofragments, which are distinguishable from the parent ion due to spatial separation within the time-of-flight set-up. Due to neutral photofragments typically having a much higher ionisation potential than the photon energy within the probe pulse, REMPI schemes are commonly utilised for photoproduct detection. Key examples include the detection of methyl radicals[199], iodine atoms[200] and hydrogen atoms[201;202].

Time-resolved photoion yield measurements are an important spectroscopic tool and have been utilised on the nanosecond[203], picosecond[204], femtosecond[205;206] and attosecond[207] timescales. The technique has been used extensively in a wide variety of studies, providing insights into vibrational wave-packet motions[208–211], photodissociation dynamics[212–214], excited state lifetimes[203–207] and electron relaxation dynamics[215;216]. In this thesis, the technique has been utilised to study the excited-state lifetime of various molecular species, with a description of the experimental set-up and implementation described in Chapter 2.

1.4 Producing Gas-Phase Molecules

When considering the various methods used to obtain a sample for molecular spectroscopic interrogation, one can broadly consider the techniques split into two categories, those used for volatile molecules and those used for non-volatile molecules.

If a molecule is considered volatile, samples for spectroscopic study may be obtained by utilising the naturally high vapour pressure of the molecule. The propensity for samples to already have a significant vapour form means they may be utilised as a neat source or in conjunction with a rare gas carrier such as helium or argon which provides additional molecular cooling. Further molecules may be volatilised through controlling sample temperature; by heating a molecular sample it is possible to increase its vapour pressure to a reasonable level for gas-phase analysis, however additional complications may occur due to some molecules undergoing thermal decomposition on heating. A volatilised sample may then be injected into a laser interaction region through either bleeding gas into the system, by generating an effusive jet or creating a pulsed molecular beam. A final consideration is that the molecules may form clusters due to intermolecular forces, such as hydrogen bonding and van der Waals forces. These issues may be mediated through careful consideration of the sample's temperature and pressure when being introduced to the laser interaction region.

1.4.1 Non-Volatile Molecules in the Gas-Phase

There are numerous methods which one may utilise to volatilise low vapour pressure molecules. This subsection will summarise some of the most commonly used techniques to facilitate this aim, as well as discussing the benefits and detriments of each for the study of neutral gas-phase molecules.

Direct Laser Desorption and MALDI

The simplest method one may utilise to put non-volatile molecules into the gas phase is that of direct laser desorption[217;218]. The technique itself consists of a sample of interest being irradiated by a laser, resulting in a direct volatilisation of the molecules and has been utilised to study the spectroscopic signatures of various neutral biomolecules[219–222]. This method, however, has significant drawbacks for investigating the neutral dynamics of molecules. The laser desorption process results in the formation of not only neutral parent molecules, but additional ionised parents, as well as neutral and ionised fragments[223] which is not ideal when one wishes to investigate the dynamics of the neutral parent molecule.

An extension to the laser desorption technique that has been developed to facilitate the volatilisation of solely parent molecules without fragmentation is that of matrix-assisted laser desorption/ionisation (MALDI)[224–227]. When utilising this method, the sample is prepared within an excess of matrix forming a matrix-sample crystalline structure. When irradiated with a pulsed laser, the matrix molecules and sample of interest are vaporised creating a volatilised sample. A schematic of the MALDI technique may be seen in Figure 1.20.

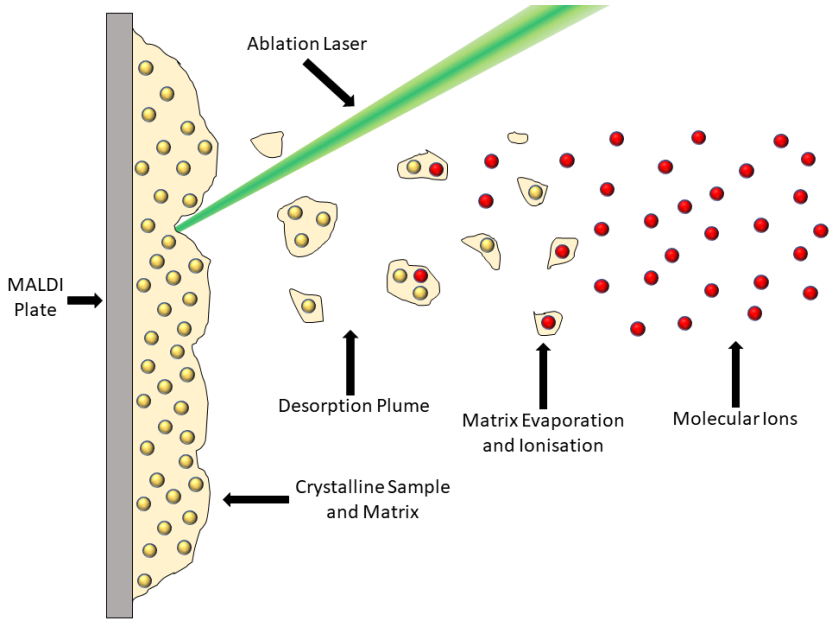

Fig. 1.20: A schematic diagram of a MALDI desorption scheme.

However, again there are drawbacks to this technique for investigating neutral dynamics as many of the sample molecules become ionised during the volatilisation process due to interactions with the matrix used[228] (although the exact mechanism with which this occurs is not fully understood)[229]. Furthermore, the matrix molecules used in this technique are not universal, with various studies performed to find suitable candidates for volatilisation of different sample types[230–232]. Examples of common matrix molecules include 3,5-dimethoxy-4-hydroxycinnamic acid[230;233], α-Cyano-4-hydroxycinnamic acid[230;233] and 2,5-dihydroxy benzoic acid[234]. A final complication introduced through the use of a matrix is the fact that the presence of the matrix molecules will need to be accounted for in data analysis. Minimal studies on neutral molecules utilising the laser desorption or MALDI techniques have been previously reported[235;236], however a number of pump-probe experiments have investigated the ion desorption yields produced during the laser-desorption process[237–242].

Electrospray Ionisation

An alternative approach to laser desorption methods for attaining gas-phase samples of non-volatile molecules is that of electrospray ionisation [243–245]. The technique itself consists of a sample of interest first being dissolved in a volatile, polar solvent before flowing through a fine capillary at a rate of the order 1 μL/min. A high potential difference is applied between the capillary tip and an extraction electrode (on the order of 2.5 - 5 kV), resulting in the formation of a Taylor cone and a cone-jet. The jet-flow undergoes nebulisation into a fine, highly-charged aerosol mist, often facilitated through use of a nitrogen or carbon dioxide counter-flow [246]. As the solvent evaporates from the aerosol droplets, charges within the droplet become more spatially confined to the point at which the Rayleigh limit is surpassed and coulomb fission occurs, with the process repeating as desolvation continues [247].

Gas-phase singly- and multiply-charged ion samples of interest are generated from the desolvated aerosol droplets, however the mechanism for ion production is not yet fully understood with two main competing theories as to their origination. One theory is the 'ion-evaporation model' [248], in which an aerosol droplet desolvates and reaches a radial limit where by the electric field strength at the surface of the droplet is large enough to facilitate the desorption of molecular ions from within. The alternative theory is the 'charged-residue model' [243;249], in which continuous evaporation and fission cycles lead to aerosol droplets with an average of one sample ion or less, with eventual solvent evaporation leading to a gaseous ionic sample. An example of an elecrospray ionisation set-up is depicted in Figure 1.21.

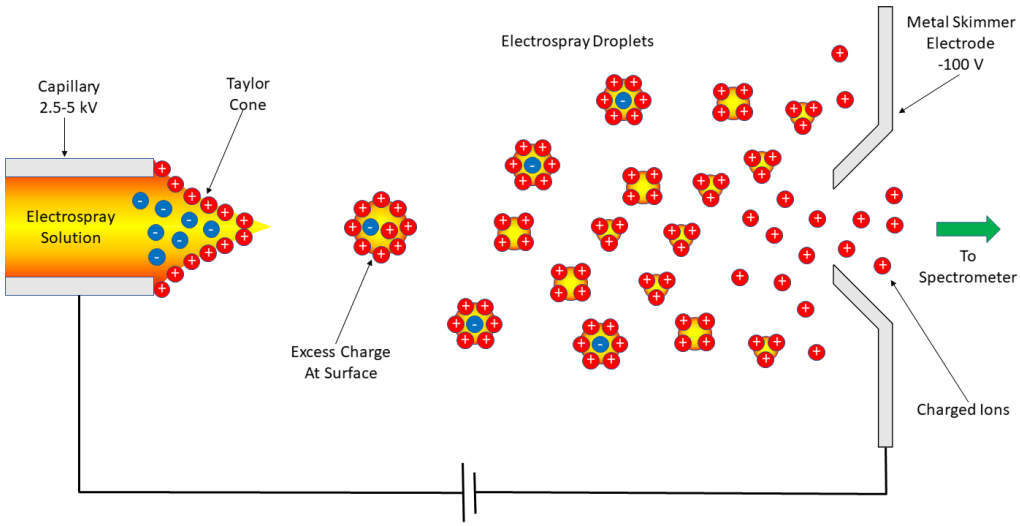

Fig. 1.21: A schematic diagram of an electrospray ionisation set-up for the volatilisation of low vapour-pressure molecules.

Although electrospray ionisation is a useful technique to facilitate gas phase studies, again it is unsuitable for the investigation of neutral molecular dynamics due to molecules being singly- or multiply-charged during the volatilisation mechanism. However, time-resolved spectroscopic studies have been shown to be possible utilising an electrospray ionisation set-up for the interrogation of anions, with numerous such studies having been reported in recent years[250–258].

Blister-Based Laser-Induced Forward Transfer

Blister-based laser-induced forward transfer (BB-LIFT) is a recently developed technique which shows significant promise for the production of neutral molecules in the gas phase[259;260].The technique consists of depositing a thin film of either metal[259–264] or polymer[265;266] on a glass substrate, prior to the deposition of the sample of interest above. The thin film between the glass and sample layers is utilised to absorb the energy from a laser pulse incident upon the glass substrate, leading to blister formation. This deformation process does not destroy or remove the film, however it imparts momentum to the sample layer above leading to a desorbed neutral sample. A schematic of the BB-LIFT sample volatilisation process may be seen along the top of Figure 1.22

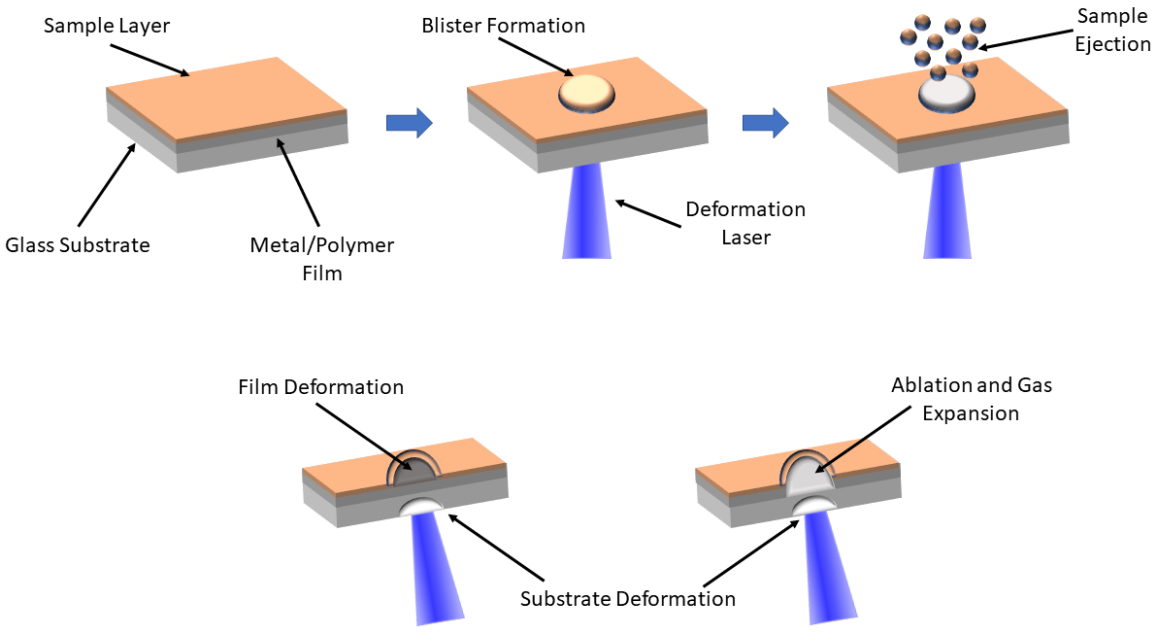

Fig. 1.22: A schematic of the BB-LIFT process. Top: process by which blister formation occurs and sample ejection. Bottom: Examples of the two theorised mechanisms for blister formation.

There are presently two accepted mechanisms for blister formation in BB-LIFT, with each dependant on the use of either a metal or polymer thin film. When utilising a polymer layer, the blister formation process is a result of localised ablation at the interface between polymer and glass layers, resulting in a gas expansion and film deformation[260;266]. Alternatively, when a metal film is used, the deformation process results from the differing thermal expansion coefficients of the metal film and the underlying glass substrate[259;260]. Schematics of both these processes may be seen along the bottom of Figure 1.22.

An initial concern with the BB-LIFT method, however, was evidence of possible sample degradation due to thermal effects when utilising a nanosecond deformation laser in both polymer and metal films[259;260;265], however a recent publication by Goodfriend *et al.*[267] investigating the thermal velocities of the desorbed particles found no evidence of thermal damage.

1.4.2 Laser Induced Acoustic Desorption

A final technique which shows promise for the production of neutral plumes of gas-phase sample is that a laser induced acoustic desorption (LIAD)[268] and is the source of sample volatilisation for the work carried out within this thesis. A sample for this technique is prepared by depositing a crystalline species of interest onto a thin metal foil (10 - 20 μm). This foil is then back irradiated with a continuous wave or pulsed laser, producing a neutral gaseous plume of sample from the front surface. Although an established volatilisation technique, the process by which this plume is produced is still not well understood. The initial hypothesis was that use of a nanosecond laser resulted in acoustic waves propagating through the sample foil, with sample volatilised through a 'shake-off' mechanism[269]. Further investigations, such as measurements of the desorbed molecules velocity, have however indicated that this cannot be the primary mechanism of desorption[270–273]. A recent publication by Huang *et al.*[274] suggests the desorption mechanism may be the result of a surface-stress between the metal foil substrate and sample layer. It is theorised that laser back-irradiation of the sample foil forms islands of sample on the substrate, with further irradiation leading to deformation, decomposition, and cracking of sample islands until a molecular sample is desorbed. A schematic of a LIAD desorption set-up may be seen in Figure 1.23.

Nonetheless, LIAD has been extensively used in the field of mass spectromety[270;275;276] and has been utilised in conjunction with quadrupole linear time-of-flight mass spectrometers[277;278] and Fourier transform ion cyclotron mass spectrometers[271;279;280].These studies showed it was possible to volatise large neutral molecules, with atomic weights

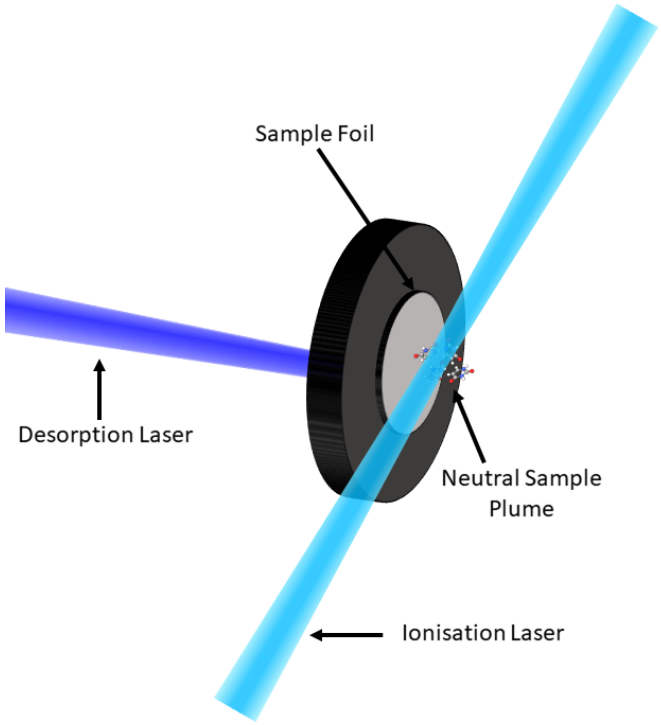

Fig. 1.23: A schematic diagram of a laser induced acoustic desorption source for neutral sample volatilisation. A neutral plume is produced through back irradiation of a thin foil with a sample of interest deposited on the opposite side. Ionisation of products is achieved through use of an additional laser source.

up to 500 u. Furthermore, LIAD has been shown to be applicable to volatilisation of much larger molecules[281] and biological systems, such as cells, bacteria and viruses, with precise mass analysis possible through use of quadrupole ion traps[282;283].

LIAD has the potential to become the leading method of producing non-volatile gas phase samples for time-resolved photoelectron/photoion-yield spectroscopy. The ability to produce neutral plumes of solvent and matrix-free, nonfragmented samples means that one may now interrogate a range of molecules that would not volatilise when utilising other methods. This technique presents the opportunity to investigate the molecular dynamics of both small and macro molecules in the gas-phase, as well as mixtures of samples simultaneously. This process is, therefore, of great interest in the field of molecular dynamics of large non-volatile molecules. Further to this, the LIAD technique has already previously been utilised for time-resolved studies of biologically relevant molecules on the femtosecond and attosecond timescale, investigating both photoelectrons and photoions. Of particular note is the works of Jason Greenwood and Mauro Nisoli[284–289] who have helped pioneer this technique for dynamical studies with further examples presented in the forthcoming chapters.

1.5 Conclusion

This chapter has provided an extensive review of spectroscopic techniques in the frequency- and time-domain, as well as a review of the various volatilisation methods to produce gas-phase samples of low vapour pressure molecules of interest in this work . Furthermore, an overview of the various radiative and non-radiative energy dissipation mechanisms for molecular relaxation are introduced as well as a discussion of the various principles and approximations which are assumed in spectroscopic studies.

Chapter 2 will discuss the design and commission of a new mass spectrometer for study of non-volatile UV chromophores, using a LIAD-style desorption source for sample volatilisation, as well as a thorough description of the optical set-up employed. In light of the recent studies discussed in Section 1.4.2, the LIAD source has been shown to not be acoustic in nature and thus will be referred to as a soft thermal desorption source in the proceeding chapters.

CHAPTER 2

Experimental:

Theory and Set-Up

In order to perform a time-resolved spectroscopic measurement, there are various key tools one must utilise, such as lasers, vacuum systems and detectors. It is important, therefore, to understand the underlying theory and principles of operation of these experimental components. Furthermore, in the case of obtaining UV pulses from an infra-red laser system, one requires a working understanding of non-linear optics within birefringent crystals. This chapter will describe the main aspects of the experimental set-up required for time-resolved photoion-yield spectroscopy measurements, as well as providing a theoretical background to many of the key components discussed.

2.1 The Laser System

2.1.1 Making Femtosecond Laser Pulses

Since the invention of the first laser in the 1960s[290], scientists have strived to produce pulses of increasingly shorter temporal duration, with the current reported record set at 53 attoseconds[291].

Limitations in minimising the temporal duration of a laser pulse may be attributed to the time-bandwidth product, whereby the product of a pulse's temporal duration and spectral width (in frequency space) result in a fundamental limit of 0.441[292] for a Gaussian pulse. This may be shown by considering the electric field of a Gaussian laser pulse, $\varepsilon(t)$, in Equation (2.1) and its Fourier transform, $\tilde{E}(\omega)$, in Equation (2.2)[293].

$$\vec{\varepsilon}(t) = \epsilon_0 \hat{n} exp(-at^2) exp(i\omega_0 t + ibt^2) \tag{2.1}$$

$$\tilde{E}(\omega) = \epsilon_0 exp\left[-\frac{1}{4}\left(\frac{a}{a^2+b^2}\right)(\omega-\omega_0)^2 - i\frac{1}{4}\left(\frac{b}{a^2+b^2}\right)(\omega-\omega_0)^2\right] \tag{2.2}$$

Here a and b represent the real and imaginary components of the Gaussian envelope, ϵ_0 is the amplitude of the electric field, $\hat{n}$ is an arbitrary unit vector, ω_0 is the carrier frequency of the optical wave and ω is angular frequency. The pulse width, τ_p, may be obtained by considering the pulse's instantaneous intensity, $I(t)$ in Equation (2.3), resulting in the solution presented in Equation (2.4).

$$I(t) = \left\langle \mid \varepsilon(t) \mid^2 \right\rangle_t \simeq exp(-2at^2) = exp\left[-(4ln2)\left(\frac{t}{\tau_p}\right)^2\right] \tag{2.3}$$

$$\tau_p = \sqrt{\frac{2ln2}{a}} \tag{2.4}$$

The pulse bandwidth, Δf_p, may be obtained similarly by considering the Fourier transformed Gaussian envelope, Equation (2.2). One can calculate the power spectral density of the pulse, $|\tilde{E}|$ (Equation (2.5)), before solving for the full width at half maximum (FWHM) spectral width, $\Delta\omega_p$ in Equation (2.6). The pulse bandwidth, Δf_p, may then be found by the simple relation shown in Equation (2.7).

$$\mid \tilde{E}(\omega) \mid^2 \simeq exp\left[-\frac{1}{2}\left(\frac{a}{a^2+b^2}\right)(\omega-\omega_0)^2\right] = exp\left[-(4ln2)\left(\frac{\omega-\omega_0}{\Delta\omega_p}\right)^2\right] \tag{2.5}$$

$$\Delta\omega_p = 2\sqrt{2ln2}\sqrt{a\left(1+\frac{b^2}{a^2}\right)} \tag{2.6}$$

$$\Delta f_p = \frac{\Delta\omega_p}{2\pi} = \frac{\sqrt{2ln2}}{\pi}\sqrt{a\left(1+\frac{b^2}{a^2}\right)} \tag{2.7}$$

The time-bandwidth product may then be solved by utilising solutions from Equation (2.4) and Equation (2.7)

$$\Delta f_p \tau_p = \frac{2ln2}{\pi}\sqrt{\left(1+\frac{b^2}{a^2}\right)} \approx 0.441\sqrt{\left(1+\frac{b^2}{a^2}\right)} \tag{2.8}$$

Thus, a given pulse width is dictated by the real parameter of the Gaussian wavepacket, a, whilst frequency chirp is associated with the imaginary part of the Gaussian wavepacket, ib. Examining Equation (2.8), this leads to the conclusion that a Gaussian pulse is constrained to a minimum time-bandwidth product of 0.441, assuming there is no frequency chirp on the pulse in question. A short laser pulse may only be created from a combination of a large number of frequencies, thus the pulse will have a large bandwidth[294]. The temporal duration of a laser pulse, therefore, is usually constrained by the bandwidth of the laser gain medium used[295].

Inside a laser cavity, only frequencies that are a multiple of the laser cavity length, L, may be amplified, as described in Equation (2.9) below[296].

$$L = \frac{mc}{2f} = \frac{m\lambda}{2}, m = 1, 2, 3, ... \tag{2.9}$$

Where m is an integer. The frequencies that satisfy Equation (2.9) are known as the laser modes and contribute to the temporal duration of the laser pulse. If the laser modes are amplified randomly, the power distribution will be a random fluctuation. If, however, the modes are amplified simultaneously, with the modes 'phase-locked', a temporally short, high peak power pulse may be produced, with near to zero intensity between peaks. This process is known as mode-locking[297;298] with sub-10 fs pulses consisting of >250000 modes. A representation of this may be seen in Figure 2.1.

Production of femtosecond pulses has progressed significantly since the discovery of 'self-mode-locking' in a Ti:sapphire (Ti:Al_2O_3) laser by Spence et al. in 1991[299], a phenomena commonly known as Kerr-lens mode-locking (KLM)[300]. KLM is a passive mode-locking technique and is the result of self-focusing within a laser medium, a consequence of the non-linear intensity-dependent response of the refractive index, n. This is due to the electric displacement field, $\vec{D}$, of a material having a third-order

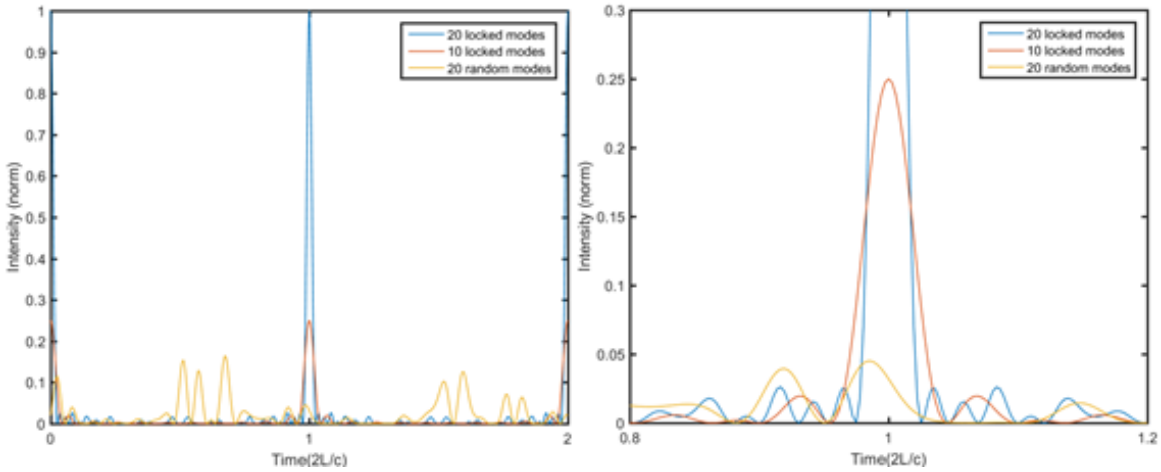

Fig. 2.1: A simplified example of laser modelocking, comparing 10 and 20 in-phase mode summations (pulsed) to a 20 random mode summation (continuous wave). It should also be noted that the temporal duration of the laser pulse decreases with more modes when comparing the 10 and 20 mode examples, shown clearly in the zoomed in right hand plot.

response for high electric fields, $\vec{E}$, as shown in Equation (2.10)[301].

$$\vec{D} = \epsilon_0[1 + \chi_{(1)}]\vec{E} + \chi_{(3)}\vec{E}\vec{E}\vec{E} = \epsilon\vec{E} \tag{2.10}$$

Where ϵ_0 is the vacuum permittivity, $\chi_{(n)}$ is the electric susceptibility for the n$^{\text{th}}$-order and ϵ is the dielectric constant. This dielectric constant may be related to the refractive index of a medium by Equation (2.11)[293].

$$n \simeq \sqrt{\frac{\epsilon}{\epsilon_0}} = \sqrt{\frac{\epsilon_0[1 + \chi_{(1)}] + \chi_{(3)}E^2}{\epsilon_0}} = n_0 + n_2E^2 \tag{2.11}$$

Thus, the refractive index of the material increases as the electric field increases, resulting in a focusing effect at the most intense region of the electric field, the central beam axis. This is a cyclic effect, as higher focusing leads to more intense electric fields and, thus, a higher refractive index and tighter focussing[302].

A hard aperture may be used in conjunction with the lasing medium to induce the mode-locking effect[303], where the lower intensity, continuous wave components of the laser spectrum are physically cut with each round-trip of the cavity. It is also important to note that KLM is not a 'self-starting' process, i.e. in order to produce ultrashort laser pulses, an external stimulus is required. This may be achieved through the use of a vibrating mirror and synchronous pumping.

The laser utilised within the Townsend group is also a femtosecond Ti:sapphire sys-

tem (Spectra-Physics, Tsunami)[304] , synchronously pumped using a 5 W neodymium-doped yttrium orthovanadate (Nd:YVO_4) second-harmonic (λ_c = 532 nm) diode-pumped laser (Spectra-Physics, Millenia Pro)[305], producing a 400 mW, 800 nm output of 50 fs pulses, with a bandwidth of 40 nm and a repetition rate of 80 MHz. This output is used to seed a chirped pulse regeneratively amplified system (Spectra-Physics, Spitfire Pro XP)[306], synchronously pumped using a Q-switched 20 W neodymium-doped yttrium lithium fluoride (Nd:YLF) second-harmonic (λ_c = 527 nm) diode-pumped laser (Spectra-Physics, Empower)[307]. The final output produces 4 W, 70 fs pulses, with a central wavelength of 800 nm, bandwidth of 30 nm and a repetition rate of 1 kHz. A schematic of the femtosecond laser system used for all experiments within this thesis may be seen in Figure 2.2 below.

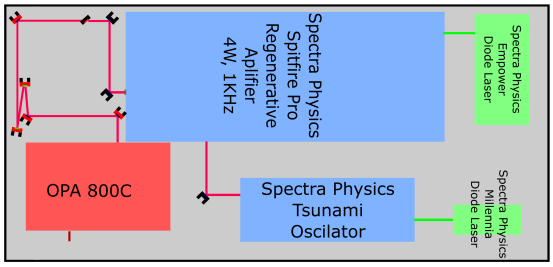

Fig. 2.2: Regeneratively amplified Ti:saphire ($Ti:Al_2O_3$) femtosecond laser system set-up

As previously stated, the regenerative amplification step utilises the chirped-pulse amplification technique (CPA)[308;309] and is performed in three steps, a simple schematic of which may be seen in Figure 2.3.

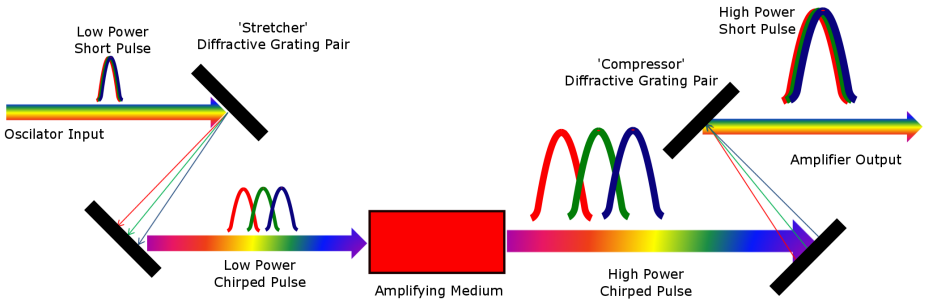

Fig. 2.3: A simplified schematic of the chirped-pulse amplification process. Seed pulses are stretched from the femtosecond to nanosecond regime through use of a grating pair prior to amplification within a Ti:sapphire crystal. Post-amplification, the pulses are recompressed to the femtosecond regime though a second pair of gratings.

The seed pulses are initially stretched from the femtosecond to nanosecond time domain using a grating pair; this is required as the power density of the femtosecond pulses would otherwise damage the optics during the amplification process. The pulse is then amplified by performing multiple propagations through a Ti:sapphire crystal (the gain medium), with input and release controlled using a pair of Pockels cells and a thin film polariser. The Pockels cells are electro-optics components, acting as voltage-dependent $\lambda/4$ waveplates, controlling the input and release of pulses to and from the regenerative amplifier cavity. The final step is to recompress the amplified pulses to the femtosecond time domain, utilising a second pair of gratings. The optical layout of the regenerative amplifier utilised for work within this thesis may be seen in the schematic in Figure 2.4.

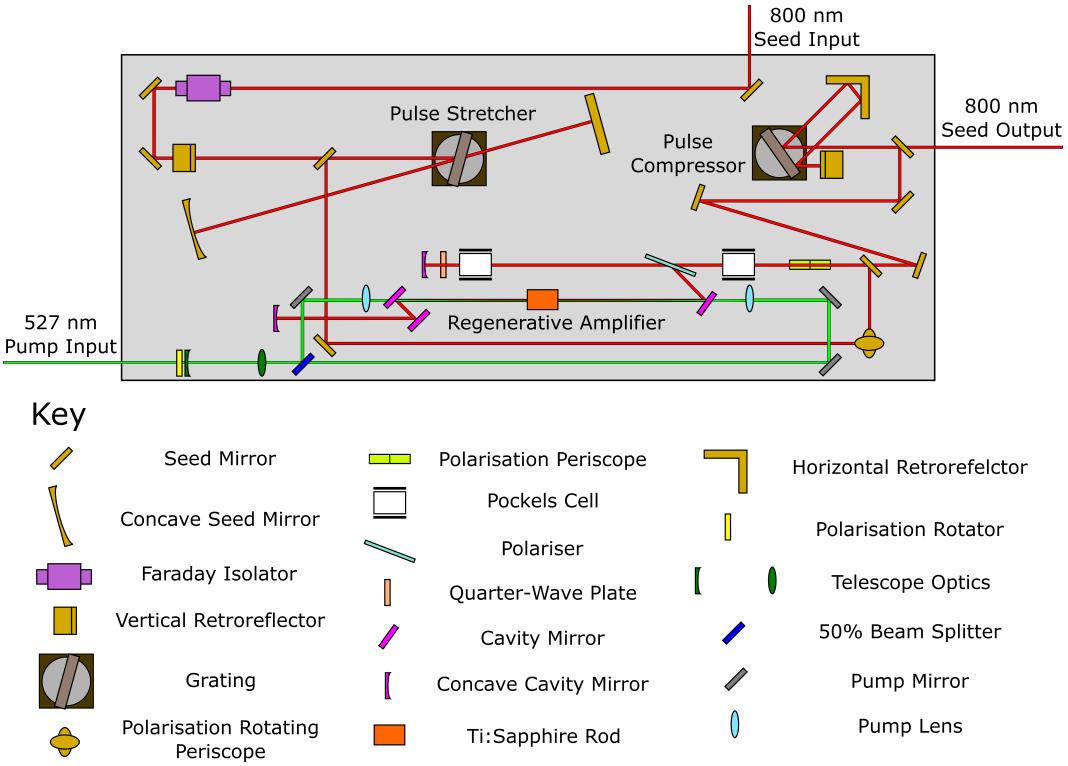

Fig. 2.4: A schematic of the Spectra-Physics, Spitfire Pro XP regenerative amplifier optical layout.

2.2 Non-Linear Optics

In order to investigate the UV self-protection mechanisms of biological analogues, one requires femtosecond laser pulses with a central wavelength, λ_c, <400 nm[310]. To facilitate this through use of the infrared laser system described in Section 2.1.1, one must utilise several non-linear optical techniques including optical parametric generation[311;312] and amplification[313;314], sum-frequency generation (SFG)[315] and second-harmonic generation (SHG)[316]. In this subsection, a theoretical description of these non-linear processes will be provided, as well as a summary of the optical set-up utilising them.

2.2.1 Birefringent Crystals and Phase Matching

The relationship between the electric field, $\vec{E}$, of a light wave propogating through an optical medium with the electric polarisation, $\vec{P}$, of the material may be expressed by Equation (2.12)[317].

$$\vec{P} = \epsilon_0 \chi \vec{E} \tag{2.12}$$

Here χ is the electric susceptibility of the medium. The polarisation, $\vec{P}$, of the material is a direct consequence of electric field applying a force to the medium, resulting in a displacement of the electron cloud and a macroscopic polarisation change. When plotted, $\vec{P}$ versus $\vec{E}$ would show a linear relationship, when $|\vec{E}|$ is small.

As the electric field becomes large, a weakly non-linear structure is formed due to further distortion of the electron cloud within the medium, resulting in a non-linear response in the polarisation observed.[318]

$$\vec{P} = \epsilon_0(\chi_1 \vec{E} + \chi_2 \vec{E}\vec{E} + \chi_3 \vec{E}\vec{E}\vec{E} + ...) = \epsilon_0 \chi \vec{E} \tag{2.13}$$

In isotropic materials, the polarisation is solely an odd function and so the electric polarisation is reversible. By symmetry, one can therefore deduce that there are no even harmonics of the polarisation in these materials. For even harmonics to exist in the electric polarisation, the medium must have a noncentrosymmetric crystal structure, an example of which would be a birefringent crystal[319].

The χ_n terms (where n >1) in Equation (2.13) represent the higher order non-linearity of the electric polarisation, leading to several non-linear effects. Second order non-linearities include sum-frequency generation (SFG)[315], difference-frequency generation (DFG)[320] and second harmonic generation (SHG)[316], a specific form of SFG.

These non-linear effects may be achieved through an interaction between linearly-polarised monchromatic plane waves, of frequency $\omega_{\ 1}$ and ω_2 respectively, within a birefringent crystal structure. The electric field in this case would take the form of Equation (2.14)[321].

$$\vec{E} = [E_1 cos(k_1 z - \omega_1 t + \phi_1) + E_2 cos(k_2 z - \omega_2 t + \phi_2)]\,\hat{z} \tag{2.14}$$

Where k_n is the wavevector, ϕ_n is the phase term and $\hat{z}$ is a unit vector. The polarisation response of the medium to second-order non-linearity may then be represented in the form of Equation (2.15)[322].

$$P_{(2)} = \epsilon_0 \chi_2 \begin{pmatrix} \frac{1}{2}E_1^2 cos[2(k_1 z - \omega_1 t + \phi_1)] \\ +\frac{1}{2}E_2^2 cos[2(k_2 z - \omega_2 t + \phi_2)] \\ +\frac{1}{2}(E_1^2 + E_2^2) \\ +E_1 E_2 cos([k_1 + k_2]z - [\omega_1 + \omega_2]t + [\phi_1 + \phi_2]) \\ +E_1 E_2 cos([k_1 - k_2]z - [\omega_1 - \omega_2]t + [\phi_1 - \phi_2]) \end{pmatrix} \tag{2.15}$$

In Equation (2.15), the processes from top to bottom are the second harmonic of ω_1, the second harmonic of ω_2, the optically rectified field, the sum-frequency generation of ω_1 and ω_2 and the difference-frequency generation of ω_1 and ω_2. Similar expansions of the polarisation to higher-order non-linearity will lead to further terms in the electric polarisation[322].

The efficiency of non-linear optical processes depends critically upon matching the phase velocities of input waves with the noncentrosymmetric crystal axis. Each plane wave input has its own wave vector, $\vec{k_n}$, and angular frequency, ω_n. For a non-linear process to occur efficiently, a summation of the input wave vectors must be equal to that of the output wave vector, with a wave vector mismatch, $\Delta\vec{k}$, equal to zero[323]. 1

$$\vec{k_1} + \vec{k_2} + \Delta\vec{k} = \vec{k_3} \tag{2.16}$$

With the angular frequencies also required to satisfy the conditions of Equation (2.17).

$$\omega_1 + \omega_2 = \omega_3 \tag{2.17}$$

When the conditions for Equation (2.16) and Equation (2.17) are satisfied, both the temporal and spatial phase matching of the three waves is ensured.

There are two main methods of achieving this phase-matched condition temperature tuning[324] and angle tuning[325;326]. Angle tuning is possible due to the birefringence of noncentrosymmetic crystals, which have different refractive indices, for

a single wavelength, along the ordinary, $\hat{o}$, and extraordinary, $\hat{e}$, crystal axes. The k-vector will observe an angle dependent refractive index with respect to crystal orientation[327].

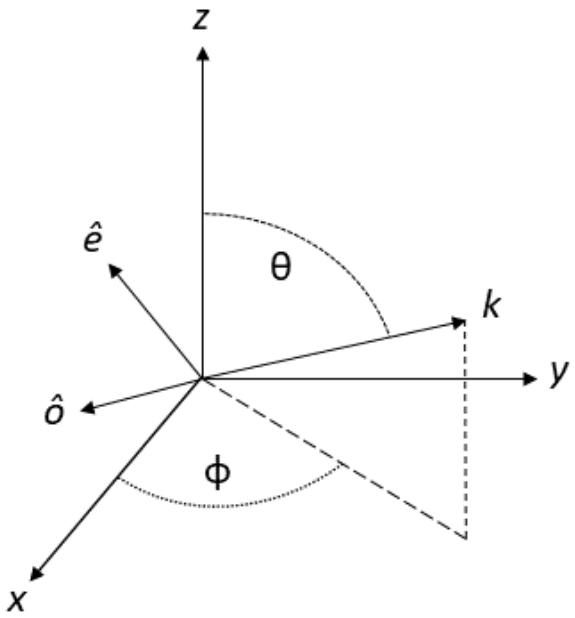

Fig. 2.5: k-vector direction with associated ordinary and extraordinary crystal axis in a birefringent crystal.

The wavenumber of an electromagnetic wave is proportional to the wavelength and refractive index of the propagation material, as shown in Equation (2.18).

$$k_n = \frac{2\pi n}{\lambda_n} \tag{2.18}$$

The wavenumber may then be related to the phase velocity, v_p, of the electromagnetic wave by Equation (2.19).

$$v_p = \frac{\omega}{k} \tag{2.19}$$

2.2.2 Optical Parametric Generation and Amplification

Optical parametric generation[311;312] is a process in which a pump photon, of angular frequency ω_p, interacts with a $\chi_{(2)}$ medium, resulting in the production of two photons of lower frequency known as the 'signal' photon, ω_s, and 'idler' photon, ω_i. Given that this is a parametric process, and thus energy conservation rules must be maintained, the frequencies of the initial and emitted photons must be equal, as shown in

Equation (2.20).

$$\omega_p = \omega_s + \omega_i \tag{2.20}$$

Furthermore, phase matching conditions must also be satisfied, as described in Section 2.2.1. This may be achieved through angle-tuning of the non-linear medium with respect to the input beam.

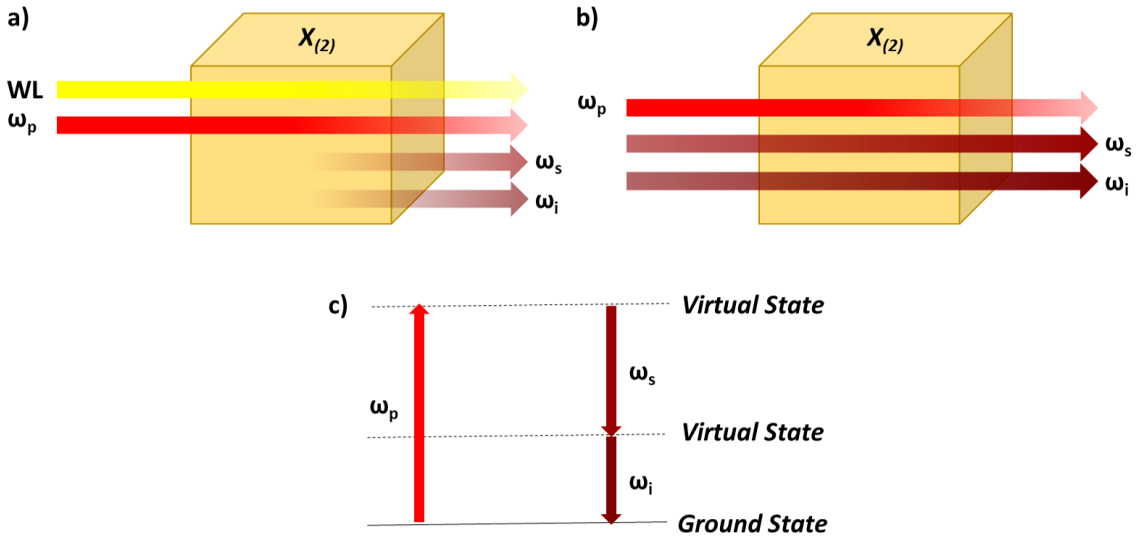

Fig. 2.6: Diagrams showing the production of a signal and idler beam from a white light continuum (WL) seed via optical parametric generation (a)), before undergoing optical parametric amplification upon a second interaction with the $\chi_{(2)}$ medium (b)). A Jablonski diagram representative of this process may also be seen in c).

Through use of a white light continuum or a signal or idler beam as an additional input, it is possible to also amplify the optical parametric signal through a process known as optical parametric amplification[313;314], an illustration of which may be seen in Figure 2.6. In the commercial optical parametric amplifier utilised for work within this thesis (OPA-800CF, Spectra Physics)[328], both of these parametric techniques are employed in order to generate a usable signal or idler beam for further frequency conversion techniques. A 1 W 800 nm input beam is split at a 96:4 ratio to be used as a pump beam and for white light continuum generation respectively. The pump beam is then further split at a 15:85 ratio, so as to create two individual beams for pumping the non-linear medium. The white light continuum is co-propagated through a β-barium borate crystal (BBO) with 15% of the pump beam, with pulses temporally overlapped through use of a manual translation stage. The white light continuum acts

as a seed for the process, with phasematching conditions for production of the signal and idler achieved through angle tuning of the BBO. A depletion of the white light continuum and the pump beams leads to the production of a weak signal and idler beam. By passing the signal and idler beams a second time through the BBO crystal, co-propagating with the 85% pump beam and temporally overlapped via a second manual delay stage, it is possible to amplify the signal and idler beams through depletion of the second pump beam. The OPA-800CF utilises a type I frequency mixing process, producing the signal and idler beams with perpendicular polarisations. This allows for simple separation of the two outputs through use of polarisation dependent mirrors post generation. The wavelength ranges of the signal and idler beam are 1.1-1.6 μm and 1.6-3.0 μm respectively, depending upon the phase matching conditions utilised.

2.2.3 Sum-Frequency Generation

Sum-frequency generation (SFG)[315] is a second-order non-linear process in which a photon, of angular frequency ω_3, is generated via the annihilation of two photons, each with an individual angular frequency ω_1 and ω_2 respectively, upon interaction with a medium with a $\chi_{(2)}$ non-linearity. A simplified picture and Jablonski diagram of this process may be seen in Figure 2.7 a) and b) respectively.

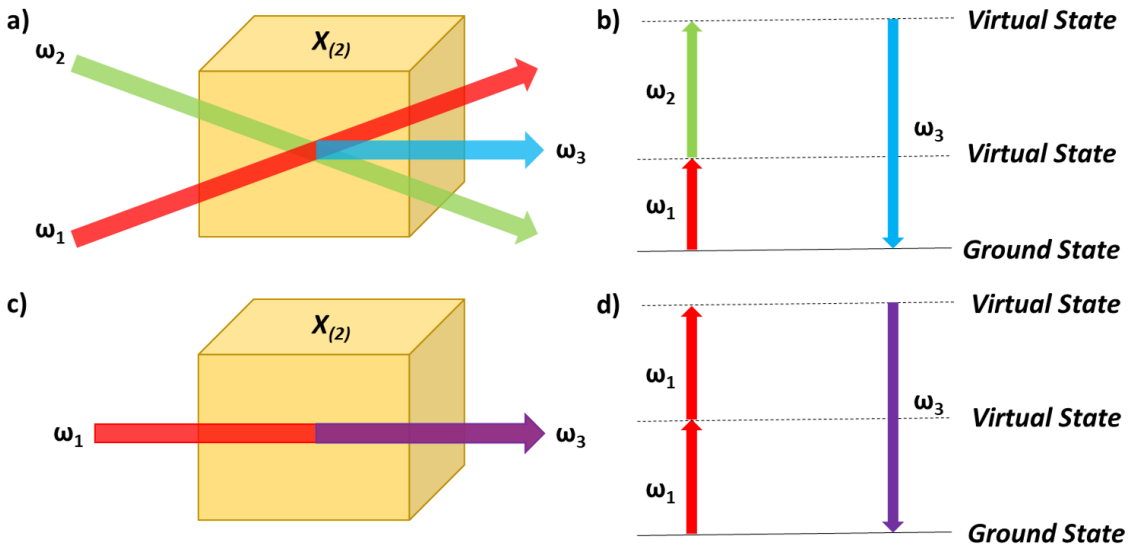

Fig. 2.7: a) a simple pictorial representation of the sum-frequency generation process with an associated Jablonski diagram in b). The equivalent diagrams for second-harmonic generation are represented in c) and d) respectively.

As previously explained in Section 2.2.1, non-linear optical processes depend crit-

ically upon satisfying the phase-matching conditions of the $\chi_{(2)}$ medium utilised. Similarly to processes described in Section 2.2.2, sum frequency generation is a parametric process and thus must satisfy the conditions of Equation (2.17), with the sum of the angular frequencies of the input photons being equivalent to the angular frequency of the photon emitted.

Second-harmonic generation[316] is a particular example of sum-frequency generation in which the angular frequency of the input photons are equivalent, ω_1=ω_2, with the resulting annihilation producing a single photon of twice the angular frequency, ω_3. As only photons of a single angular frequency are required to implement this process, only one beam of light is needed to perform this technique, with the second harmonic co-propagating with the fundamental frequency post generation. An example of second harmonic generation and its' associated Jablonski diagram may be seen in Figure 2.7 c) and d).

Throughout this thesis, the medium used to perform these non-linear optical processes is a β-barium borate (BBO) crystal[329]. In order to generate the various wavelengths utilised in the experiments described, it was necessary to use a selection of BBO crystals cut at a range of angles with respect to the crystal optical axis, with optimisation of the non-linear process achieved through angle tuning.

The wavelengths required may be obtained through various input configurations and combinations of the non-linear techniques described. A key staple in the wavelength production is the utilisation of the harmonics of the laser's fundamental frequency, a summary of which may be seen in Table 2.1.

Input 1 (nm)	Input 2 (nm)	Output (nm)	Crystal Angle (°)
800	800	**400**	29.2
400	800	**267**	44.2
267	800	**200**	64.8

Table 2.1: A tabulation of the BBO crystal angles and input frequencies required for the production of the 2nd, 3rd and 4th harmonic of a Ti:Sapphire laser system centred at λ_c = 800 nm. Bold text represents the produced wavelength of interest.

Harmonics of the laser output are the simplest and most efficient UV wavelengths to generate due to the high input power provided by the laser system and the minimal non-linear processes required for their production. In order to interrogate molecules with a wider range of UV wavelengths, the output of the optical parametric amplifier

is utilised as part of a two-stage sum-frequency mixing set-up, in conjunction with the fundamental or harmonics of the Ti:sapphire laser system used. A summary of some of the wavelengths of interest within this dissertation, as well as the processes involved in their generation, may be seen in Table 2.2.

	Input 1 (nm)	Input 2 (nm)	Output (nm)	Crystal Angle (°)
Stage 1	1257	800	489	23.9
Stage 2	489	400	**220**	66.0
	1238	800	486	24.1
	486	486	**243**	54.9
	1292	800	494	23.7
	494	494	**247**	53.4
	1333	800	500	23.4
	500	500	**250**	52.4
	1392	800	508	23.0
	508	508	**254**	51.1
	1454	800	516	22.7
	516	516	**258**	49.9
	1536	800	526	22.3
	526	526	**263**	48.5
	1720	800	546	21.6
	546	546	**273**	45.9
	1823	800	556	21.3
	556	556	**278**	44.8
	1935	800	566	21.0
	566	566	**283**	43.7
	2032	800	574	20.8
	574	574	**287**	42.9
	2163	800	584	20.6
	584	584	**292**	41.9
	2307	800	594	20.5
	594	594	**297**	41.0

Table 2.2: A tabulation of the BBO crystal angles and input frequencies required as part of a two-stage tunable-UV set-up. The output of an OPA-800CF is utilised as part of a sum-frequency mixing process, with the solid line representing the switch from signal (above line) to idler beam (below line). Produced wavelengths of interest are shown in bold.

Although the non-linear processes described previously are convenient for the generation of UV-pulses, it is also important to consider their implications upon the temporal characteristics of the produced laser pulses and what precautions may be taken to minimise their impact. This will now be discussed in Section 2.2.4

2.2.4 Pulse Dispersion

A complication in the use of non-linear crystals for frequency conversion is the dispersive effect it may have on the temporal duration of a laser pulse. To explain this, one must first consider the phenomena of group delay[330], τ_g, presented in Equation (2.21) below.

$$\tau_g = -\frac{d\phi}{d\omega} = \frac{\omega_0}{v_\phi(\omega_0)} \tag{2.21}$$

Here $d\phi/d\omega$ is the total spectral phase shift with respect to angular frequency and v_ϕ is the wavelength-dependant phase velocity. Equation (2.21) shows how, as a broadband pulse passes through a medium, the constituent frequencies within the pulse will travel at a phase velocity dependent upon their corresponding wavelength and thus will be delayed with respect to one another. The rate of change of this delay, with respect to angular frequency, is known as the group delay dispersion[327], *GDD*, as shown in Equation (2.22) below.

$$GDD = -\frac{d\tau_g}{d\omega} = \frac{d^2\phi}{d\omega^2} = \frac{1}{v_g} \tag{2.22}$$

Here, v_g is group velocity, a wavelength-dependent property which describes the speed of a Gaussian pulse envelope travelling through a particular length of medium. The group delay dispersion, therefore, represents a measure of the chromatic dispersion of a particular optical element of known length.

In order to asses the impact of dispersive media on the temporal duration and shape of a Gaussian pulse, however, one must consider the change in the group velocity with frequency variation. This quantity is known as 'group velocity dispersion'[331], *GVD*, expressed in Equation (2.23).

$$GVD = \frac{d^2\tau_g}{d\omega^2} = \frac{d}{d\omega}\left(\frac{1}{v_g}\right) \tag{2.23}$$

It is often intuitive to consider the group velocity dispersion in terms of the simple experimental variables of refractive index, n, and central wavelength, λ_0. A short

derivation leads to the expression represented in Equation (2.24)[322].

$$GVD = \frac{\lambda_0^3}{2\pi c_0^2}\frac{d^2n}{d\lambda_0^2} \tag{2.24}$$

As is clearly seen in Equation (2.23) and Equation (2.24), the differential frequency imposes variation in the group velocity across the Gaussian pulse envelope. As an ultrashort laser pulse is made from a large combination of frequencies, the Gaussian pulse envelope is prone to elongate, compress and/or change shape depending upon the medium the pulse propagates through.

Throughout the experiments described within this thesis, the effects of GVD have been minimised through pre-chirping the laser pulses, utilising the internal compressor within the Ti:sapphire amplifier described in Section 2.1.1. Pre-chirping is a process by which a negative chirp is purposely applied to a laser pulse, with shorter frequencies of light propagating ahead of longer frequencies. As the pulse passes through various optical components, a positive chirp is applied to the pulse, with longer frequencies propagating through the materials faster than shorter frequencies. The compressor is optimised such that the non-linear processes described in Section 2.2.3 occur with a maximum efficiency. As it is only possible to optimise one of the two optical lines (the pump or probe) utilising this technique at any one time, the second line is optimised by propagating the beam through glass plates, applying chirp to the laser pulse, again achieving optimum compression.

2.2.5 The Beamlines

Schematics of the two main optical beamline set-ups utilised for experiments throughout this thesis are shown in Figure 2.8.

In the 267/200+800 set-up, the initial input beam, of power 2.4 W and central wavelength, λ_c, 800 nm, is split at a 2:1 ratio into two beams of 1.6 W and 0.8 W respectively. The 1.6 W beam is utilised as the pump beam within this set-up, undergoing the various non-linear procedures, whilst the 0.8 W beam acts as the probe.

The pump beam is initially reflected off a hollow gold retroreflector (# 46-188, Edmund Optics) mounted on a computer controlled linear translation stage (M-403.12s, Physik Instrumente). The stage is utilised within the time-resolved experimental set-up to control the temporal separation between the pump and probe beams. Through use of a pair of curved tunable laser line mirrors (TLM1-800-0-1025-3.00CC, CVI Laser Optics and TLM1-800-0-1025-1.00CX, CVI Laser Optics respectively), the pump beam is telescoped down at a ratio of 3:1. This step is taken so as to increase

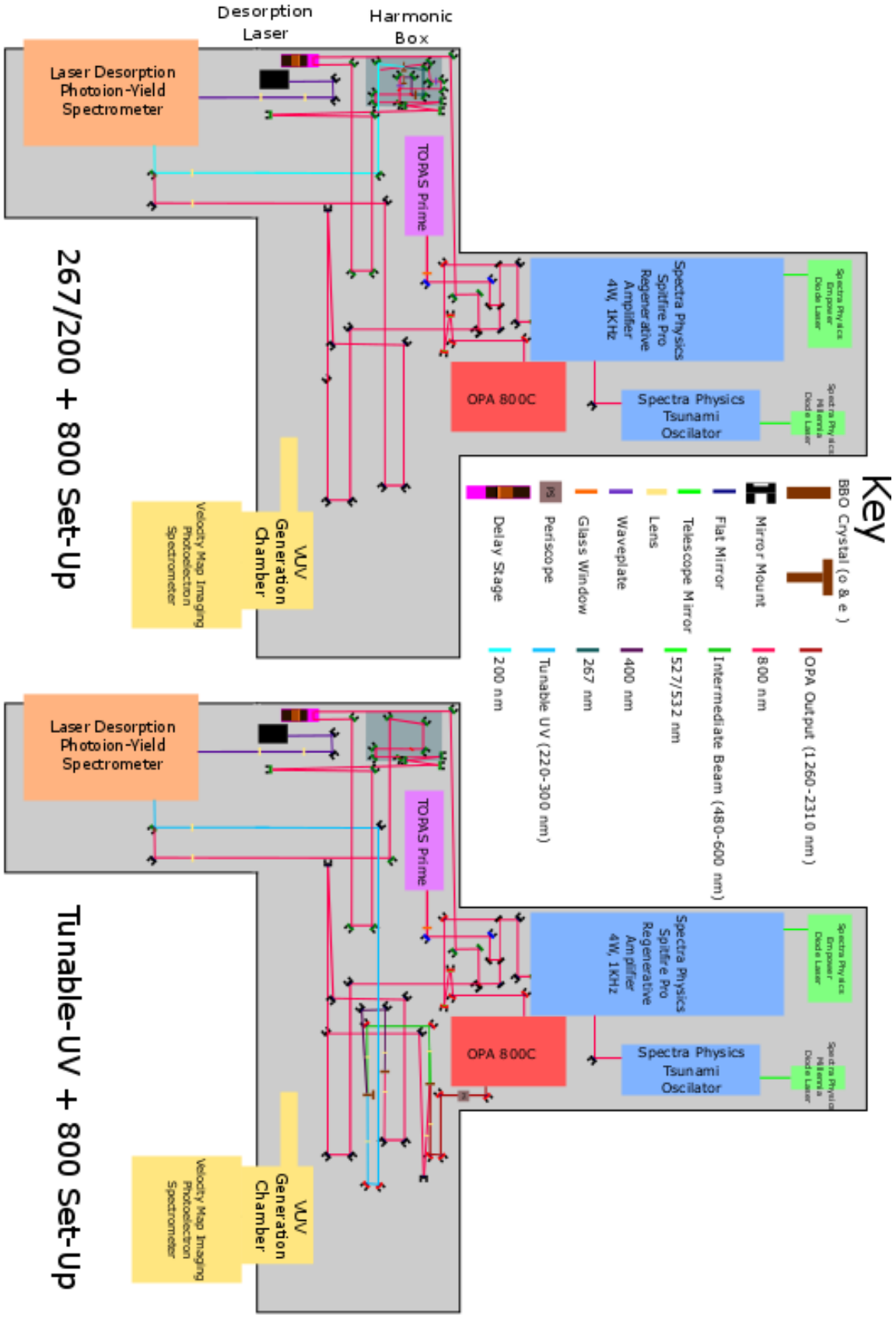

Fig. 2.8: Optical set-up utilised for various time-resolved experiments

the power density of the pump beam as well as to more easily propagate through the BBO crystal apertures without clipping. The required 200 or 267 nm light may then be generated through the use of an in-house built harmonics box. The two configurations for the harmonics production may be seen in Figure 2.9.

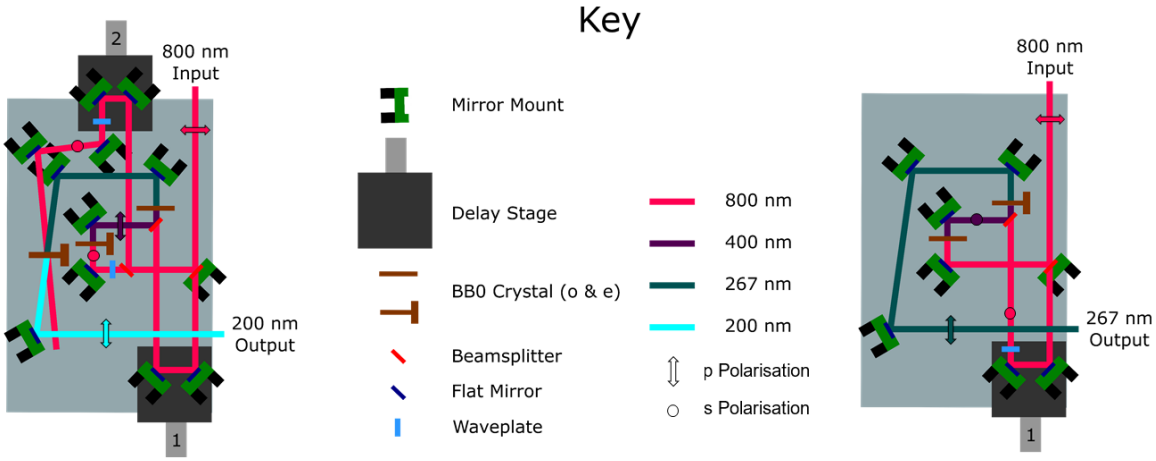

Fig. 2.9: Schematics of the harmonics box orientations utilised for the production of 267 nm and 200 nm pump beams.

For the generation of 267 nm light, as shown on the right of Figure 2.9, the input beam is initially split through use of a 75% reflective beamsplitter. The more intense reflected beam undergoes second-harmonic generation through use of a vertically mounted BBO crystal (0.5 mm thick, 29°), producing vertically-polarised 400 nm pulses through type I phase matching. The less intense transmitted beam is propagated an equivalent path length, with the initial horizontal polarisation rotated to vertical through use of a half waveplate. The two beams are then recombined and co-propagated through use of a combiner optic (106853, Layertec), with fine control of the pulse overlap achieved through use of delay stage 1. The co-propagating beams are then incident upon a horizontally mounted BBO (0.2 mm thick, 45°) producing a sum-frequency generated beam of horizontally-polarised 267 nm pulses. Residual 800 nm and 400 nm beams are separated from the 267 nm pulses through use of 267 nm high reflectors.

For the production of 200 nm pulses, as in the left side of Figure 2.9, further nonlinear processes are required. The input beam is again initially split through use of a 75% reflective beamsplitter, with the more intense reflected beam interacting with a second beamspiltter which is 25% reflecting. This produces 3 beams which are 18.75%, 25% and 56.25% of the initial input respectively. The most intense of these inputs (56.25%) interacts with a half waveplate rotating the initial horizontal polarisation to vertical. This beam then undergoes second-harmonic generation through use of a

horizontally mounted BBO crystal (0.5 mm thick, 29°), producing vertically-polarised 400 nm pulses through type I phase matching. The second most intense beam (25%) is propagated an equivalent distance and overlapped with the 400 beam through use of a beam recombiner, with fine control of the pulse overlap achieved through use of delay stage 1. The co-propagating beams pass through a second BBO crystal (0.2 mm thick, 45°), mounted vertically, producing vertically polarised 267 nm pulses through a sum-frequency generation process. 267 nm pulses are separated from the residual 800 nm and 400 nm beams through use of 267 nm high reflectors. The least intense input beam (18.75%) is propagated along an equal path length to the produced 267 nm pulses and with the beam's polarisation rotated from horizontal to vertical through use of a second half waveplate. This 800 nm beam and the previously produced 267 nm pulses are spatially overlapped in a third BBO crystal (0.1 mm thick, 65°) and temporally overlapped through use of a second manual delay stage. Non-linear interactions with the BBO crystal produce 200 nm pulses again through a sum-frequency generation process, with residual 267 nm, 400 nm and 800 nm pulses separated through use of 200 nm high reflectors.

The produced pump beam (267/200 nm) is focussed through use of a 63 cm focal length lens (630PQ25, Comar Optics), propagated to a combining optic (101343, Layertec or PW1-1012-UV, CVI Laser Optics) and reflected into the time-of-flight mass-spectrometer. The 0.8 W probe beam is propagated an identical distance as the pump beam post separation, focussed through use of a 50 cm focal length lens (LA5464, Thorlabs) and co-propagated through the combiner optic with the 'pump' beam into the time-of-flight mass-spectrometer.

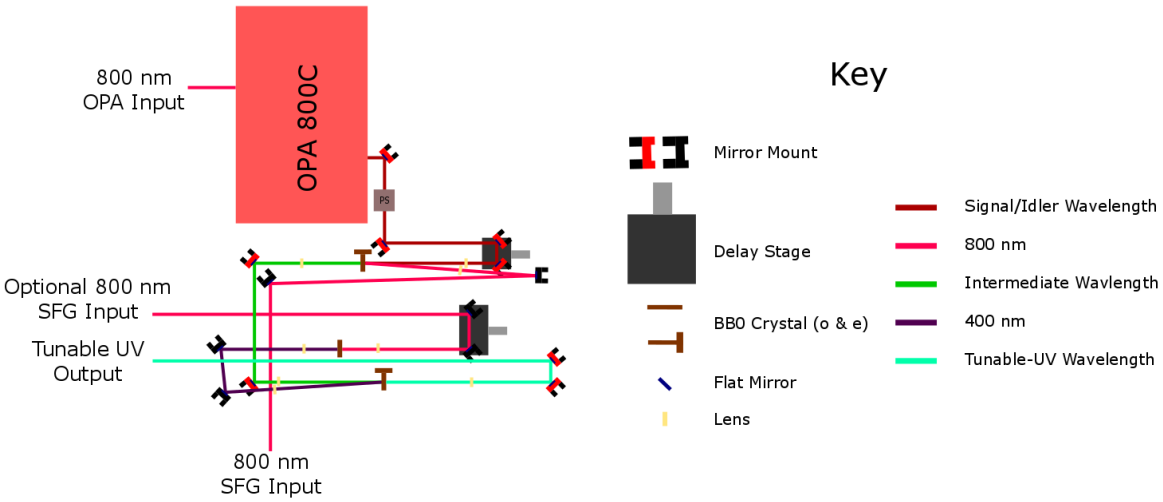

Fig. 2.10: Schematic of a 2-stage tunable-UV set-up

In order to produce more exotic UV-wavelengths for the pump beam, a 2-stage tunable-UV set-up is required, as may be seen in Figure 2.10. 1 W of the initial laser output is split through use of a series of beam splitters and telescoped at a 3:2 ratio (TO-DM2000C8D56, Newport Optic and TO-FM2500C8D56, Newport Optic respectively). The beam then enters an OPA-800CF producing an output of either a signal or idler beam, as described in Section 2.2.2. The produced OPA beam is converted from vertical to horizontal polarisation through use of a periscope, then focussed using a 20 cm focal lens (LA1708-C, Thorlabs) and propagated to a horizontally mounted BBO crystal. A beam of 800 nm pulses is propagated along an equivalent path length to the OPA output, focussed through use of a 30 cm glass lens and spatially overlapped with the OPA output in the BBO crystal. Temporal overlap is achieved through use of a manual translation stage and characteristics of the BBO utilised are determined by the input beams and information found in Table 2.2. A non-colinear sum-frequency generation process occurs between the input beams and BBO producing an intermediate wavelength in the first stage of tunable-UV generation. The intermediate wavelength obtained may be utilised in either a sum-frequency generation set-up or second harmonic generation set-up depending upon the tunable wavelength desired.

In a second-harmonic generation set-up, the intermediate wavelength beam is focussed through use of a 30 cm focal length lens (LA4579-A, Thorlabs) and is propagated through a second BBO crystal. The characteristics of the BBO utilised are determined by input the parameters as shown in Table 2.2. A non-linear interaction between the input beam and BBO crystal ensues, producing second-harmonic UV pulses.

In the case of a sum-frequency generation set-up during this second stage, an additional beamline is required. A further portion of the initial laser output may be utilised and frequency doubled through use of an additional horizontally-mounted BBO crystal (0.5 mm thick, 29°), producing 400 nm pulses. These 400 nm pulses are propagated an identical distance to the produced intermediate wavelength beam, focussed into the same BBO through us of a 20 cm focal length lens (LA1708-A, Thorlabs) and spatially overlapped. Temporal-overlap between the intermediate beam and 400 nm pulses was achieved through use of a manual translation stage. The non-colinear beams interact with the BBO crystal producing a UV beam. A complete list of the various intermediate wavelengths utilised and produced UV beams may be seen in Table 2.2.

The produced tunable-UV may be separated from any residual beams through use of a series of UV high reflectors and is focussed through use of a 63 cm focal

length lens (630PQ25, Comar Optics). The focussed pump beam is then reflected off a combining optic and propagated into the time-of-flight mass-spectrometer. The probe 800 nm beam is propagated an equivalent distance as the tunable-UV pulses, focussed by a 50 cm focal length lens (LA5464, Thorlabs) through the combining optic and co-propagated with the tunable-UV beam into the mass-spectrometer. Timing between the 800 nm probe pulses and tunable-UV pump are controlled via an electronic translation stage in the probe beamline.

2.3 The Spectrometer

The study of gas-phase molecules allows one to distinguish between intrinsic molecular properties and those that are a consequence of the surrounding environment. The fundamental dynamics of a molecule following photoexcitation can be perturbed by intermolecular effects. Background-free study of gas-phase molecules may be achieved through use of vacuum technology, removing extraneous molecules from the sample-laser interaction region.

In this subsection, a thorough description of the vacuum chamber designed and utilised for experiments within this thesis will be given. In addition, an overview of the instruments contained within the vacuum chamber used to produce a neutral sample plume, control the motion of ions and electrons and those utilised for the detection of such particles, will be described at length.

2.3.1 Time-of-Flight Mass-Spectrometer

A newly commissioned time-of-flight mass-spectrometer[332;333] has been utilised for all experiments performed within this thesis. Construction and characterisation of the device formed a considerable part of the work undertaken, with the assistance of Dr Omair Ghafur, while the design of the spectrometer itself was performed by Dr Ghafur. A CAD drawing of the design may be seen in Figure 2.11 with an additional cut-through view available in Appendix A. The ultra-high vacuum spectrometer itself consists of a single chamber evacuated through use of a pair of turbomolecular pumps (STP-ix455C, Edwards Vacuum and EXT75DX, Edwards Vacuum) with pumping speeds 450 l/s and 60 l/s respectively. The turbomolecular pumps may only safely operate in the molecular-flow regime, therefore a pair of backing rotary pumps (nXDS10i, Edwards and XDS35i, Edwards respectively) are required for the transition between viscous and molecular flow. Pressures in the two regimes are measured through use of active pirani (APG100-XLC NW25, Edwards Vacuum) and wide range gauges (WRG-S-NW35, Edwards Vacuum), with a minimum achievable pressure of 10^{-8} mbar.

Within the chamber itself there are various components which are utilised to produce time-resolved photoion-yield data of non-volatile molecular species. These include a soft thermal desorption molecular source used to produce a gas plume of the sample of interest, a velocity map imaging electrostatic lens set-up which controls the motion of ions and electrons post laser interaction and a microchannel plate/ phosphor detector which allows for the detection of charged species. Each of these parts

will be discussed in turn in the proceeding sub-sections.

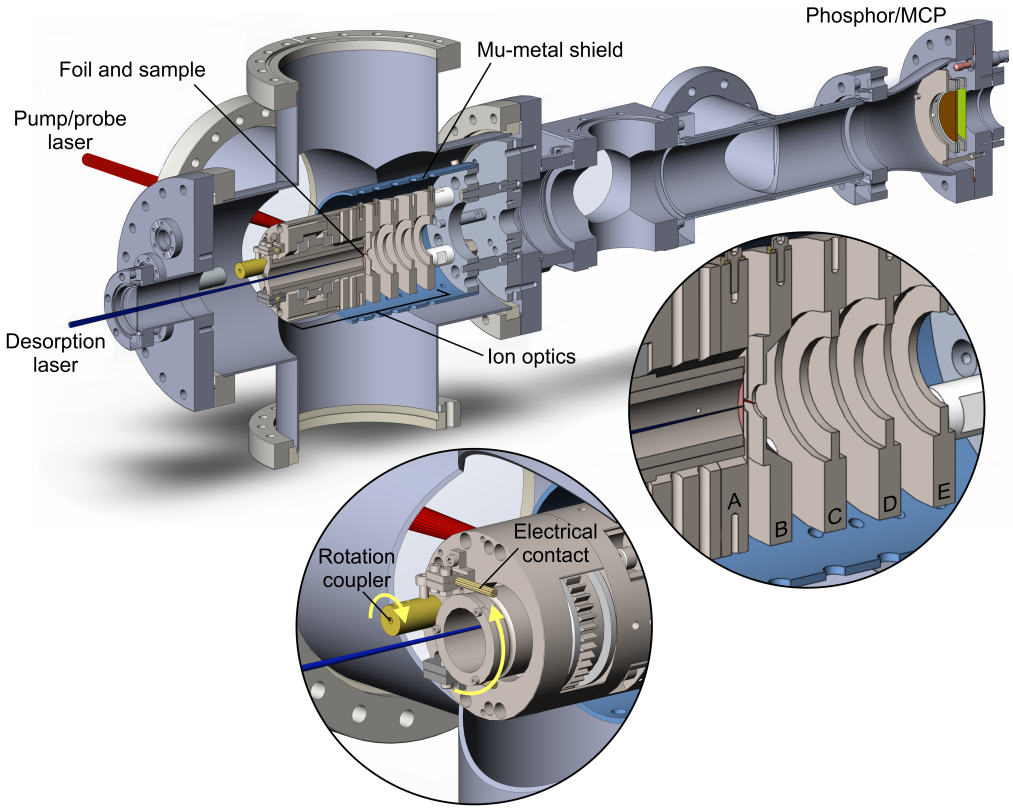

Fig. 2.11: TRIY spectrometer overview. The rear repeller electrode (A) incorporates a clamp holding a 10 mm stainless steel foil on which sample is deposited. The foil clamp is located at one end of a larger cylindrical mount, to facilitate easy installation and removal. Circular motion of the rotation coupler is achieved via a mechanical air-to-vacuum feedthrough (not shown), generating counter-rotation of the foil-plus-cylinder arrangement via a simple gear system. A gold brush contact maintains the electrical connection to the repeller electrode at all times (required as the foil holder rotates on Teflon bearings). The ion optics are 80 mm in diameter, mounted on 4 × 10 mm diameter PEEK support rods. Spacing between the outer edges of the electrodes is 8 mm (A-B) or 12 mm (B-E). The extractor electrode (B) consists of a flat plate (1.5 mm thick) with an 8 mm diameter through hole plus an 8 mm thick aperture with a conical taper (26 to 36 mm diameter). Electrodes C-E are 8 mm wide, have an inner lip thickness of 3 mm and 26 mm diameter clear apertures. The overall distance from the pump/probe laser interaction region to the detector is 97 cm.

2.3.2 Soft Thermal Desorption Molecular Source

Within the 6-way cross depicted in Figure 2.11, one can see the soft thermal desorption set-up utilised to produce a neutral plume of molecules. A solid sample of interest is deposited on a 10 μm thick, 32 mm diameter, circle of stainless steel foil. Deposition

is achieved through simply pressing the sample to a cleaned stainless steel foil, with a small amount of methanol used to help bind to the surface. The foil and sample are then positioned in an in-house built off-axis manual rotation mount, shown in the inset of Figure 2.11. The mount turns via the rotation of a knob external to the chamber, with motion facilitated by a series of stainless steel cogs.

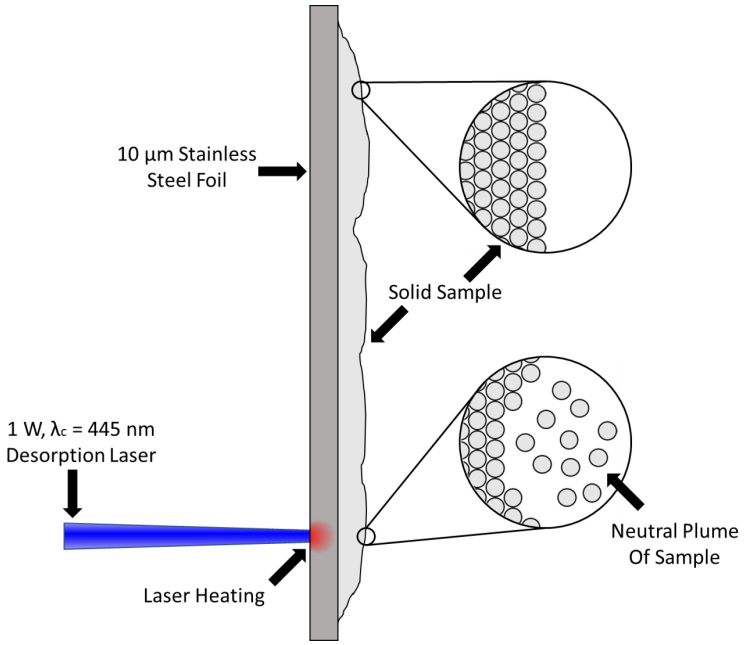

Fig. 2.12: A simplified diagram depicting the soft thermal laser desorption process.

A window positioned behind the sample foil allows access for a 1 W, λ_c= 445 nm, laser (44513FPA5, Kale CNC) to facilitate sample desorption, focussed through use of a pair of lenses of focal lengths 10 cm (LA1509, Thorlabs) and 20 cm (LA4102-A, Thorlabs) respectively. A pair of lenses are utilised so as to first expand the desorption beam, post the focal point of the first lens, and then more tightly focus through use of the second lens. A soft thermal localised heating on the rear side of the foil, provided by the desorption laser beam, produces a neutral plume of molecules of interest propelled from the front side of the foil. The desorption laser could be used in both continuous wave and pulsed operation modes, controlled through the use of an in-house built pulse generator triggered off the output of the regenerative amplifier. This allowed for the production of desorption laser pulses down to 100 ns duration and made it possible to investigate if there is any temporal profile to the generated plume, such as in the laser induced acoustic desorption (LIAD) technique discussed in Section 1.4.2. Subsequent investigations lead to the conclusion that the plume produced no significant temporal nature through use of a pulsed laser and thus the

desorption process is likely thermal in nature. A simplified diagram of the thermal desorption process may be seen in Figure 2.12.

The design of the sample mount also allows for quick sample replenishment; with the foil rotation off-axis with respect to the desorption beam position, turning the external knob between scans provides a fast method for sample renewal.

The rotation mount itself is integrated into the repeller plate of a set of ion optics, the operation of which will be explained in Section 2.3.3. To prevent charge build-up of the solid sample, the foil mount is grounded through the use of gold electrical contacts, as shown in the inset of Figure 2.11.

Post production of the molecular plume, the pump and probe laser beams discussed in Section 2.2.5 are focussed into the gaseous sample, exciting and ionising the molecules of interest. The motion of the charged particles produced is then dictated through use of ion optics, as will be discussed in Section 2.3.3.

2.3.3 Ion Optics and Velocity Map Imaging

Ion optics consist of three principle plates, a repeller plate, an extractor plate and a ground plate. The function of the ion optics is to control the motion of ions produced via laser excitation within the interaction region between the repeller and extractor plates. A simplified diagram showing the operation of the ion optics, in conjunction with the laser desorption source, used within this thesis may be seen in Figure 2.13.

The repeller and extractor plates have voltages applied via in-house built high voltage supply units creating an electrostatic field. In time-resolved photoion-yield spectroscopy, the repeller plate is set to a higher positive voltage than the extractor plate, so as the ions have a net motion away from the repeller and, by consequence, electrons have a net motion towards the repeller plate. The ratio of the voltages between extractor and repeller plates determines the acceleration of the photoions, with photoions separated depending upon their mass-to-charge ratio. Lighter and/or more highly charged ions are accelerated faster than heavier and/or less highly charged ions. This information is extremely important for photoion-yield experiments, where it is essential to relate the arrival times of detected photoions to the ions mass. In the time-resolved experiments presented within this thesis, the optimal voltages for collecting photoion-yield data were found to be 2500 V and 2200 V for the repeller and extractor plates, respectively.

The final plate utilised in the ion optics set-up is a ground plate. The role of the ground plate is to stop further propagation of the electrostatic field produced by the extractor and repeller plates, creating a field-free region for ion propagation known

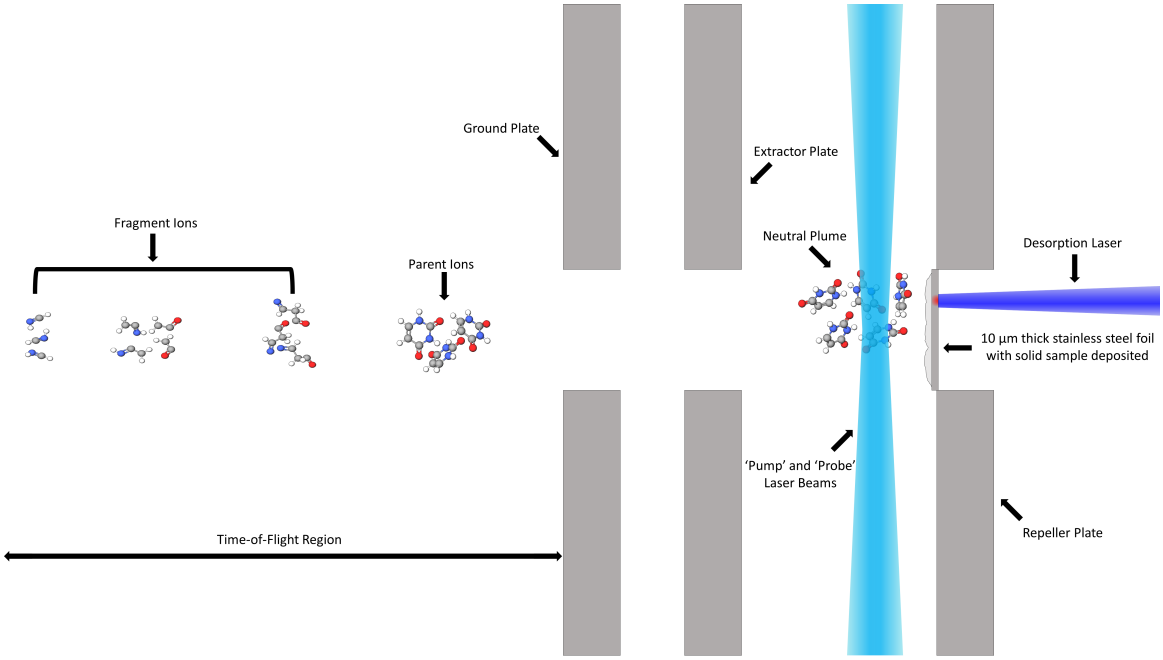

Fig. 2.13: A simplified diagram depicting the ion optics and the time-of-flight mass spectrometry set-up utilised for data collection. The VMI optics consist of a repeller plate, an extractor plate and a ground plate.

as the flight tube. The accelerated ions travel at a constant velocity within the flight tube and spatially separate depending upon their mass-charge ratio. Shielding from external magnetic fields is achieved through use of mu-metal, which surrounds the ion optic set-up. Rather than blocking the external fields, the high permeability of the mu-metal provides an alternate route for the fields to propagate around the shielding, in turn creating a field-free region within the mu-metal shell.

In addition to functioning as standard ion optics, the design was simulated by Dr Omair Ghafur for velocity map imaging capability, with a particular focus on photoelectron spectroscopy. Velocity map imaging for photoelectrons consists of the same ion optics as previously described, except repeller and extractor plates have high negative voltages applied to them. When the ratio between the extractor and repeller voltages is approximately 0.75 (0.7-0.8 depending upon the exact design of the ion optics), an Einzel lens may be created. The inhomogeneous field created by the Einzel lens maps the velocity of the electrons to different locations on a 2D detector, independent of their initial ionisation position. This allows for time-, energy- and angle-resolved data to be obtained in an extremely differential measurement. A diagram of a velocity map imaging photoelectron set-up incorporating a thermal-desorption source may be seen in Figure 2.14.

Dr Omair Ghafur performed simulations for two sample foils offset by 0.1 mm in

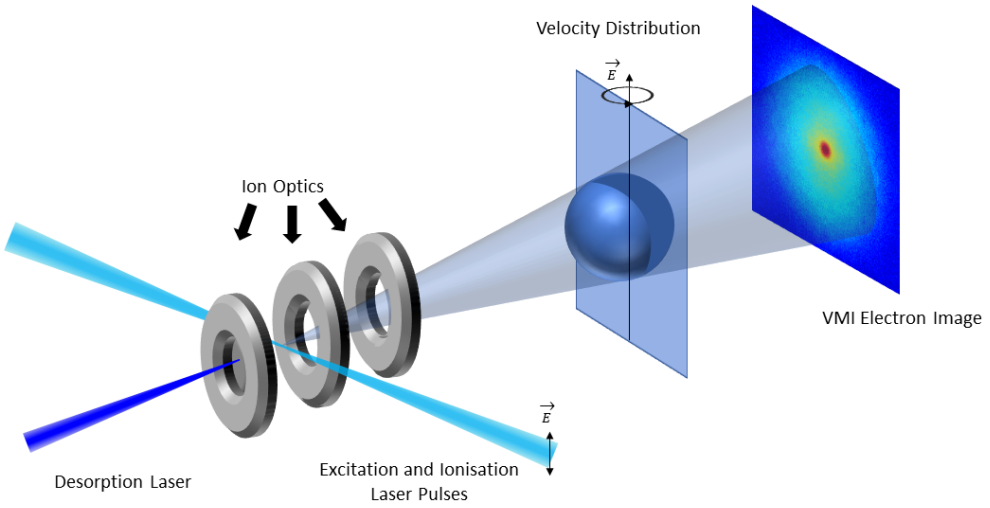

Fig. 2.14: A simplified diagram depicting velocity map imaging time-resolved photoelctron spectroscopy set-up incorporating a soft thermal-desorption source.

both mu-metal shielded and unshielded designs using SIMION 8.0, with a gridstep of 0.025 mm. The repeller voltage was set to 3000 V for the simulation and the source was positioned 3 mm from the repeller plate in the unshielded design and built within the repeller plate for the shielded design. A laser focus of 0.2 by 0.2 mm was assumed with an ionisation length of 2 mm in the laser propagation direction. The electrode design was optimised through use of a simple simplex type downhill iterative optimisation. The resolution is presented as a percentage of radial standard deviation of the hit points/ average radius, with plots shown in Figure 2.15.

As can be seen in Figure 2.15, the inclusion of a mu-metal shield greatly reduces the effects of sample foil offset, obtaining a minimum for an extractor voltage of -2657 V. The unshielded design is far more sensitive to the foil axis position, with a 0.1 mm change resulting in an extractor voltage variation of 15 V. Although the inclusion of the mu-metal shield slightly decreases resolution, the reduced sensitivity to the foil axis position allows for more robust data acquisition.

This short discussion of the velocity map imaging capabilities of the spectrometer has been included due to the initial design brief and the intended future direction of the experimental set-up. No time-resolved photoelectron data will be presented within the results chapters of this thesis, however preliminary results of photoelectron imaging utilising the soft thermal source may be seen in Section 6.1.2.

Once the charged particles of interest have propagated along the flight tube, one must have a method of detecting them. Section 2.3.4 will discuss the use of microchannel plates and phosphor screens to achieve charged particle detection, as well as the instruments required to retrieve the spectroscopic data.

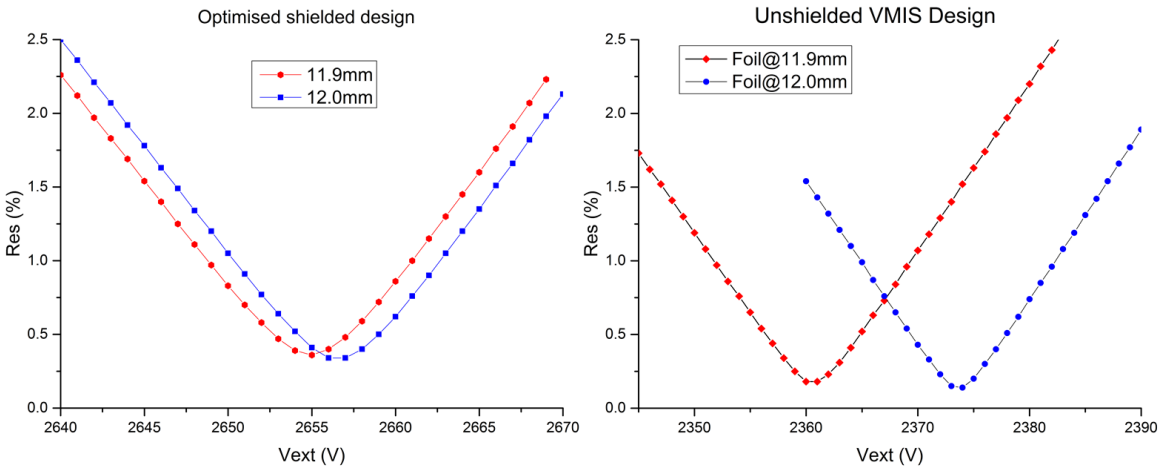

Fig. 2.15: Plots of resolution (%, radial standard deviation of the hit points/ average radius) versus extractor voltage for mu-metal shielded and unshielded VMI optics produced by Dr Omair Ghafur in SIMION 8.0. Sample foils were offset by 0.1 mm to show design sensitivity.

2.3.4 Detection of Ions and Electrons

There are numerous devices which may be used to detect the presence of an electron or an ion, including photomultiplier tubes[334], Faraday cups[335] and Daly detectors[336]. These devices, however, are limited to data acquisition in only a single dimension, providing no spatial information of where the charged particle hit the detector. In order to make the spectrometer multifunctional and allow for imaging capability, the detector utilised within this work is a microchannel plate detector[337], a diagram of which may be seen in Figure 2.16.

A microchannel plate consists of a highly resistive glass material with a regular array of channels passing through, each on the order of 10 μm diameter and displaced by 25 μm. Channels are slightly angled with respect to the incoming charged particles, so as to minimise back scatter and to increase collisions with the channel walls. As the photoion or photoelectron hits a channel wall, secondary electrons are produced due to each channel being coated with a highly resistive semiconductor coating. Each subsequent channel wall hit by a charged particle produces further electrons resulting in an electron cascade effect.

The detector utilised for experiments described within this thesis is a chevron microchannel plate, whereby two microchannel plates are stacked rotated 180° with respect to each other, as shown in Figure 2.17.

The chevron configuration achieves a gain on the order of 10^7 electrons. A phosphor screen (P47) used in conjunction with the chevron MCP converts the produced

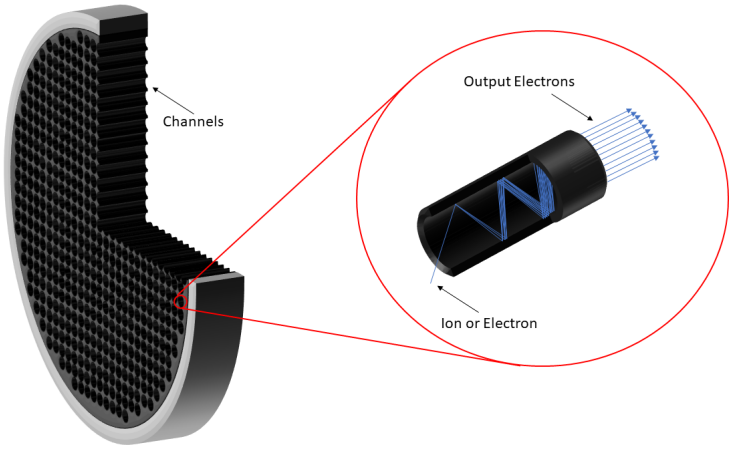

Fig. 2.16: A diagram depicting a microchannel plate detector. Inset shows the electron cascade effect when a charged particle is detected in a channel.

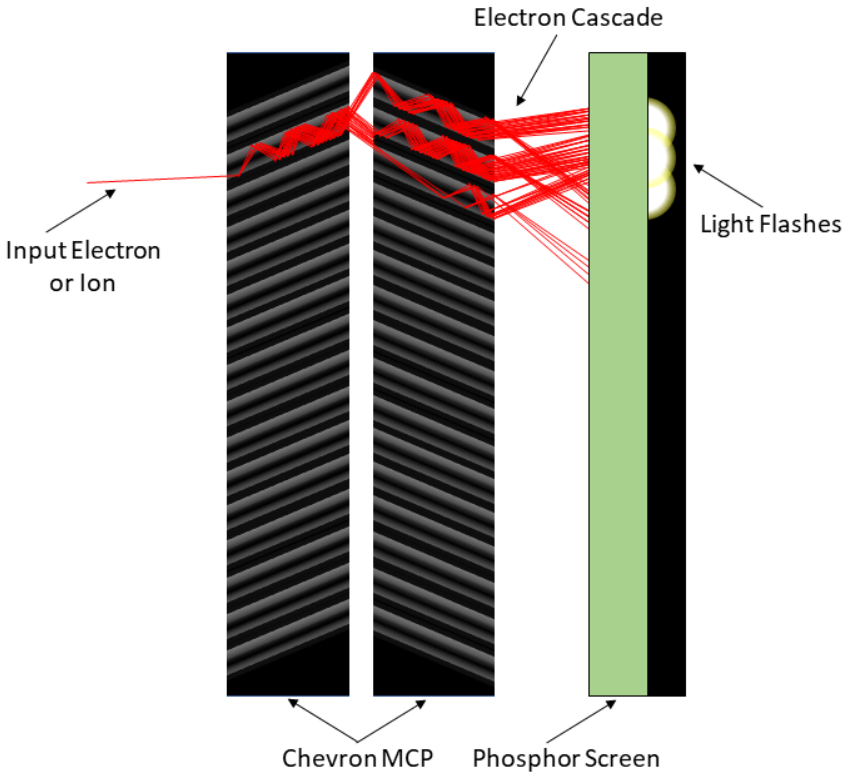

Fig. 2.17: A cut-through diagram of a chevron MCP detector, in conjunction with a phosphor screen, used for the detection of charged particles.

electron cascade into flashes of light, which may then be detected through use of a CCD camera (DMK21BF04, The Imaging Source) or a photomultiplier sensor and oscilloscope combination (MicroFM-10035-X18, Sensl and TDS1002b, Tektronix), for

velocity map imaging and time-of-flight experiments, respectively.

2.3.5 Initial Testing and Results

Initial testing of the chamber and desorption source was performed using time-invariant time-of flight mass spectrometry of various non-volatile molecular species. Test molecules included buckminsterfullerene (C_{60}), 1,4-bis(phenylethynyl)benzene (BPEB) and DL-phenylalanine. BPEB and DL-phenylalanine where interrogated using 267 nm pulses and were utilised for testing due to their extremely low vapour pressures (6 x 10^{-10} mmHg[338] and 2 x 10^{-8}[339] mmHg at 25 °C respectively), whilst 800 nm pulses where used for the interrogation of buckminsterfullerene, which was utilised to test if it were possible to put significantly larger non-volatile molecules (5 x 10^{-6}[340] mmHg at 25 °C) into the gas phase through use of the thermal desorption source. Time-of flight traces obtained for the three molecules may be seen in Figure 2.18 below.

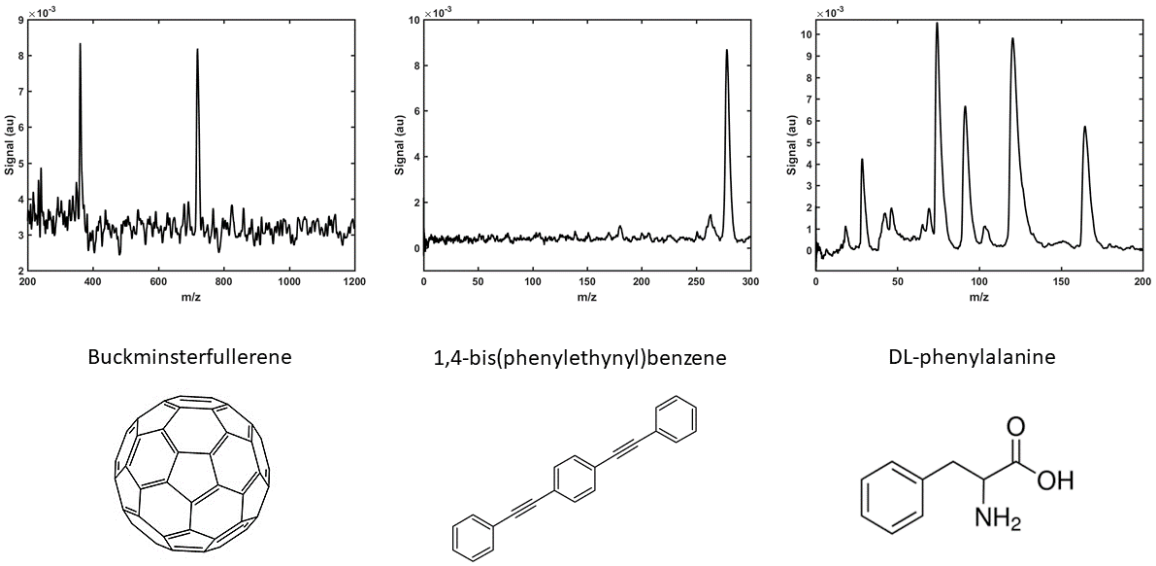

Fig. 2.18: Time-invariant time-of-flight mass spectra of buckminsterfullerene (800 nm), 1,4-bis(phenyletenyl)benzene (267 nm) and DL-phenylalanine (267 nm).

One of the key features of the time-of-flight spectra is a prominent parent peak in each of the three test molecules (720, 278 and 165 mass-to-charge ratio, *m/z*, for buckminsterfullerene, BPEB and DL-phenylalanine respectively). This shows that a portion of the molecules produced through use of the thermal desorption source are the neutral unfragmented parent. Presence of this signal is important for the intended experiments, as it would otherwise not be possible to perform spectroscopic studies of the

neutral molecule. A further observation is that the fragmentation patterns observed in buckminsterfullerene and DL-phenylalanine show many resemblances to those produced via electron impact ionisation experiments (this information is not presently available for BPEB to the best of the authors knowledge). In DL-phenylalanine, peaks observed at m/z = 120, 103, 91, 74, 65, 46, 28 and 18 are consistent with those observed in electron impact measurements[341], with major peaks seen at m/z = 360 and 240 in buckminsterfullerene[342], representing the doubly and triply charged parent ion, further consolidating this notion.

Further testing of the chamber and desorption source were performed using time-of-flight mass spectrometry of uracil, a time-invariant example of which may be seen in Figure 2.19 below.

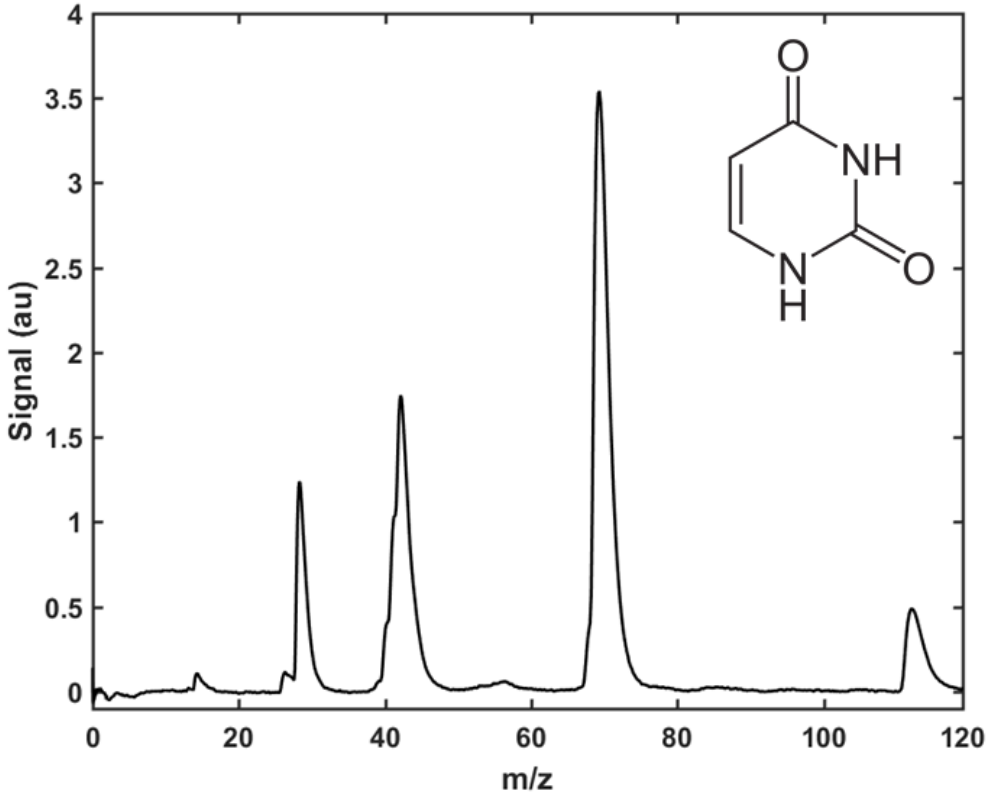

Fig. 2.19: Time-invariant time-of-flight mass spectra of uracil using 267 nm light pulses. Inset is a stick model of the uracil structure.

The mass spectra shows the expected parent peak at m/z = 112 , with significant fragments at m/z = 69, 40, 28 and 14, again consistent with electron impact ionisation measurements[343]. Uracil was then the first molecule used for a time-resolved experiment utilising the thermal desorption source, with an example output shown in Figure 2.20.

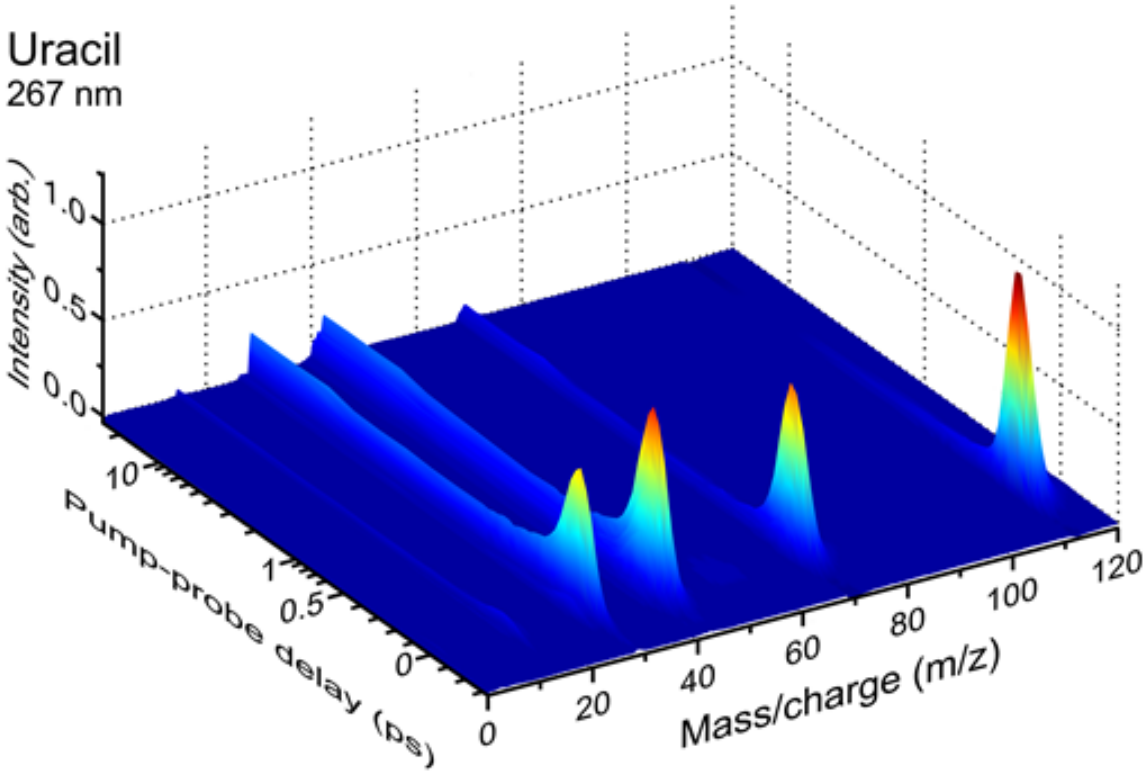

Fig. 2.20: Time-resolved photoion-yield spectrum of Uracil utilising a 267 nm pump and 400 nm multiphoton probe.

Figure 2.20 consists of a three-dimensional plot, with m/z represented on the x-axis, pump-probe separation in femtoseconds on the y-axis and relative signal on the z-axis. The y-axis shows the data plotted on a mixed linear-logarithmic scale, with linear steps of 30 fs from -300 to 600 fs followed by 9 logarithmic steps out to 25 ps. In the example shown, the pump wavelength was 267 nm and the multi-photon probe was 400 nm. As can be seen in Figure 2.20, there is a wealth of dynamical information contained within a single time-resolved spectra, however details will not be provided at this time, with an extended analysis provided later in Chapter 4.

2.4 Conclusion

This chapter has provided a valuable insight into the construction and commissioning of a state-of-the-art time-of-flight mass spectrometer utilising a soft thermal desorption source. Non-volatile model biological chromophores have been interrogated through use of this device using the time-resolved photoion-yield spectroscopy technique. Furthermore, this chapter describes the operation of a femtosecond regeneratively-amplified laser system as well an extensive discussion on non-linear optics, with a particular focus on frequency conversion techniques. The descriptions and knowledge provided within this chapter are central to understanding the concepts discussed in the subsequent chapters to come.

The proceeding chapters will describe much of the practical work undertaken throughout the duration of this PhD. Chapter 3 will discuss the extensive software development undertaken for the collection and analysis of time-resolved photoion-yield data, followed by Chapter 4 which discusses the non-adiabatic dynamics of the the RNA base uracil, as well as complimentary analysis of its' sulfated equivalent 2-thiouracil. Chapter 5 will then proceed to discuss a wavelength-dependent study of the UV chromophore 5,6-dihydroxyindole before Chapter 6 discusses the future outlook of the thermal desorption project as well as providing concluding remarks to the work undertaken.

CHAPTER 3

Spectroscopic Software Development:
The Code

In order to perform a time-resolved measurement to investigate the ultrafast dynamics of a molecular system, one must utilise numerous pieces of hardware; these include translation stages for optical time-delay control, shutter systems to allow for background readings and detection equipment to collect data, such as cameras and oscilloscopes. It is possible to take this data through manually altering these hardware components, however this would be very inefficient and time consuming. It is therefore logical to automate much of this acquisition process, allowing the user to collect data with comparative ease. Furthermore, given that fitting of spectroscopic data is often of a complicated but repetitive nature, development of a graphical user interface (GUI) programme for the analysis of time-resolved ion-yield transients is also highly beneficial. Three extensive GUI programmes, consisting of over 10000 lines of code, have been developed for this purpose. The codes, TOFSET2, TOFRUN2 and TOFANALYSE2, allow one to acquire and analyse time-resolved photoion yield data within user-friendly, self-contained programmes. The GUIs have been developed using MATLAB software due to its ability to handle large quantities of data and due to programmes previously constructed within the Townsend group having utilised this platform. Spectroscopic software development has been a huge part of the work undertaken, and as testament to this the base code for these GUIs is available online (doi 10.5281/zenodo.1419591) and work flow diagrams of its operation may be seen in Appendix B-Appendix E respectively.

3.1 TOFSET2

The first GUI developed was the TOFSET2 programme, designed to allow the user to initially interface with a Tektronix TDS 1002B oscilloscope, dynamically control the oscilloscope settings and record single or multiple time of flight (TOF) spectra from the laser-desorption spectrometer. This was a particularly useful programme as it allowed for on the fly collection of time-invariant mass spectra with relative ease. The graphical user interface of the TOFSET2 programme may be seen in Figure 3.1 below.

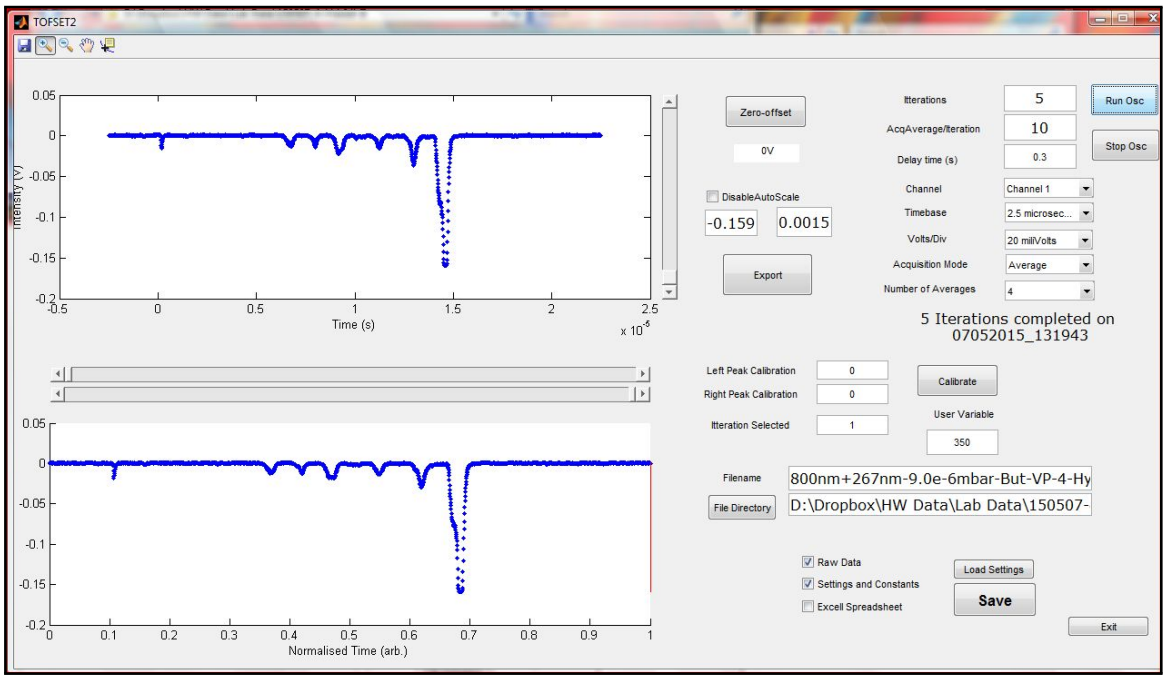

Fig. 3.1: TOFSET2 graphical user interface showing a combined butadiene and 4-hydroxyiondole time-of-flight spectra

Upon initialisation of the GUI, the programme opens communication with the oscilloscope and updates the settings to those of the last closed session, or if these are non-existent, to a set of base parameters. The GUI reacts accordingly, displaying a series of pop-up menus allowing one to alter the timebase, volts per division, averaging, channel number and the acquisition mode. If these parameters are then altered within the GUI environment, the oscilloscope will update to those selected. The user also has the opportunity to load in settings from a previous successful data acquisition. Time-of-flight spectra may then be collected as either a single scan from the oscilloscope, or via series of scan iterations with a user defined delay between readings, plotting each individual trace on acquisition. The data may then be saved to text and/or Excel

format, exported as a parameter file to the next section of the acquisition programme (TOFRUN2), or used to perform a preliminary calibration of the data, changing the time-of-flight axis seen in the raw data to a mass-to-charge (m/z) scale. The data is calibrated through utilisation of two horizontal scroll bars to select two known mass peak positions (or a known mass peak and a zero position) and solving Equation (3.1).

$$m_q = kt^2 + m_0 \tag{3.1}$$

Here m_0 is a mass offset, k is a calibration constant, t is the flight-time of a particular mass peak with respect to the laser trigger and m_q is the calibrated mass for a particular temporal peak. The data is then filtered to only account for masses of $m/z \geq 0$. A final feature of this programme is the ability to apply a voltage offset to the produced spectra, with it possible to scale the base line position through use of an addition vertical scroll bar. This data may then again be saved or exported as a settings file for the collection of time-resolved data in TOFRUN2.

The TOFSET2 programme was generally useful for the collection of time-invariant mass spectra and used extensively throughout the data collected within this thesis. A particular example of its application within the proceeding chapter is for the collection of one-colour ion-yield signals or two-colour mass spectra with a fixed time delay. For uracil and 2-thiouracil, 267 nm and 400 nm one-colour mass spectra, as well as 2-colour signals at fixed time delays of 0 ps and 5 ps, were able to be recorded using this software, as may be seen in Section 4.3.2. Furthermore, this programme facilitated the collection of data for a power-dependence study of uracil, utilising the same excitation conditions and fixed time delays. Relative parent and fragment ion intensities were monitored with respect to the probe power, elucidating the photon order for the formation of each of the peaks, as will be discussed further in Section 4.3.3.

3.2 TOFRUN2

This GUI may be utilised for the acquisition of time-resolved photoion yield data from the laser-desorption set-up, again controlling a Tektronix TDS 1002B oscilloscope, but also a PI M-403.12S linear translation stage and a pair of home built, arduino-controlled beam shutters. The stage is utilised to control the temporal separation between pump and probe pulses, whilst the shutters may be employed for collection of pump-alone or probe-alone data. The interface for the TOFRUN2 programme may be seen in Figure 3.2.

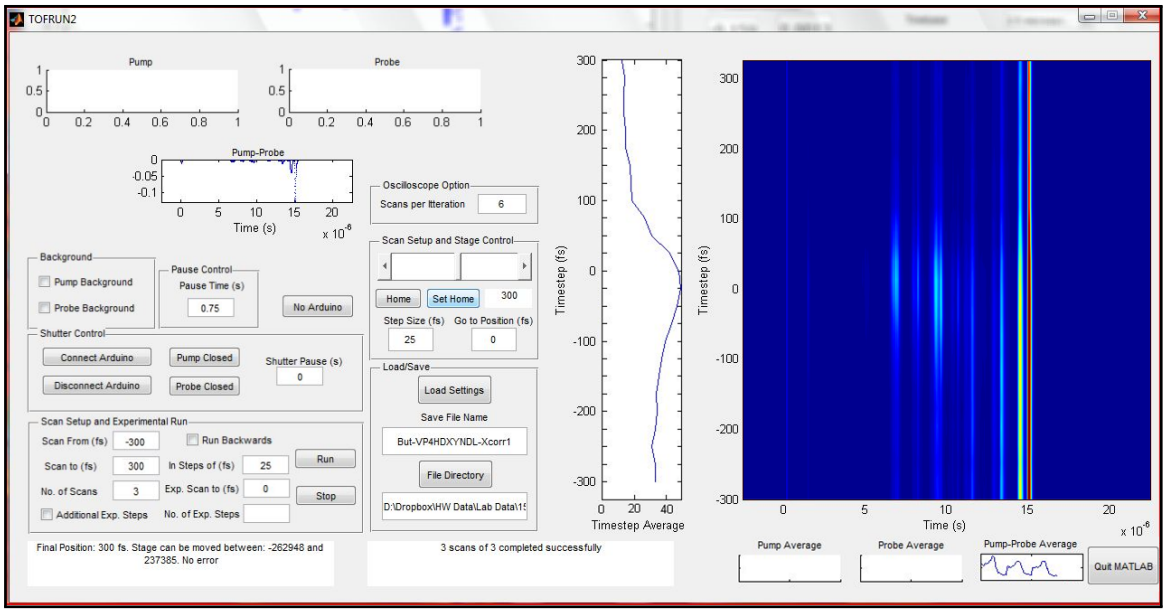

Fig. 3.2: TOFRUN2 graphical user interface displaying a cross-correlation time-resolved ion-yield trace of butadiene and 4-hydroxyiondole. Options within the 'Scan Setup and Experimental Run' submenu allows one to control pump-probe separation and stage position during a scan. The 'Scan Setup and Stage Control' subsection controls the stage position prior to an experimental run, with it possible to set a relative home position. 'Background' and 'Shutter Control' submenus are utilised for arduino shutter control. Individual pump-alone, probe-alone and pump-probe traces can be monitored during data collection in the sub-plots to the left of the GUI interface, whilst the summed average of these traces can be seen in the three sub-plots along the bottom of the GUI.

The TOFRUN2 programme is either opened via exporting data from the TOF-SET2 GUI, as previously explained in Section 3.1, or through running the base code. If the latter method is used, the programme requires the user to load in a previous oscilloscope settings file, so as to provide a clear record of the conditions under which the data was taken.

The first consideration when utilising this GUI is to decide if shutters are required for the intended data acquisition. The arduino-controlled shutters are an optional addition, with the code designed such that it is possible to attain pump-probe spectroscopy data, with options to also record pump-only and/or probe-only background readings. If shutters are connected, one can manually control their positions through the GUI, with a toggle button used to clearly show if each shutter is presently open or closed. If the shutters are not connected or not required for the data acquisition, the 'Shutter Control' and 'Background' menu boxes are hidden from the display.

The next stage of operation is the control of the translation stage, which is required to create a temporal delay between two laser pulses through variation of one's optical path length with respect to the other, as well as for a fast and repeatable method for position control. The user is able to control the position of the translation stage in a number of ways, with the distance travelled represented by the time for light propagation (fs), as given by Equation (3.2) below.

$$t = d/2c \tag{3.2}$$

Here c is the speed of light, d is the relative distance travelled and t is the light propagation time. A factor of two is also required as the retroflector mounted on the translation stage acts as an optical double pass, and thus any distance travelled by the stage is doubled in the beam propagation. A scroll bar is provided within the 'Scan Setup and Stage Control' GUI subsection for one to move the stage either forwards or backwards. A further option provided is to use the 'Go to position' box, which will move the stage to a user-defined point. A text box provides a continuous update of the stage location with reference to a defined 'Home' position. A relative home position is required to allow one to find and record the 'time-zero' position between the pump and probe beam lines, the point at which both have propagated identical distances, prior to starting the experiment. The 'Home' button allows one to return to this defined position, whilst a new home position may be set using the 'Set Home' button. The time-zero position is found by performing a time-resolved ion-yield measurement on a molecule with a Gaussian response for the experimental pump and probe wavelengths utilised. A Gaussian fitting model, which will be discussed further in Section 3.3, provides the Gaussian peak offset with respect to the assigned home position, as well as a measure of the cross-correlation between the pump and probe pulses.

Once the time-zero stage position has been located, the user is ready to acquire time-resolved ion-yield data on the molecule of interest. One initially defines the pump-probe limits over which data should be attained, and in what incremental steps, before deciding whether to include a number of additional exponential steps to

the end of the scan.

The inclusion of exponential steps at the end of a scan's linear time range is useful as it allows one to observe the long and short-time dynamics of a molecule within a single measurement. Other, more laborious, methods to collect data on an extended timescale would require either excessively long, linearly stepping measurements or collection of data over multiple experimental runs, interrogating the molecules over varying time ranges. The number of scans may then be chosen, as well as how many oscilloscope traces are to be taken and averaged at each translation stage position. These functions are required so as to limit the effects of statistical fluctuation within the data, which may be introduced by fluctuations in the laser power or sample density. At this point, the main routine of the GUI for data collection may be started.

For each translation stage position, a pump-probe oscilloscope trace/average trace is obtained and plotted in the box labelled 'Pump-Probe' to the top left of Figure 3.2. If background readings are required, additional pump-alone and probe-alone plots are also presented. The data is then inverted, such that ion peaks are represented as a positive voltage response, and plotted as a line on a 2D graph of 'time-of-flight'/'m/z' vs. pump-probe separation. The plot to the left of this 2D data in Figure 3.2 presents the total ion-yield for each pump-probe position, a summation over all 'time-of-flight'/'m/z', whilst the plots beneath the 2D data are representations of the total ion signal for each individual measurement. Monitoring the total ion signal with time is important in the experimental set-up utilised, so as to ensure sample concentration is not significantly decaying through use of the thermal desorption source. Each of these plots are updated within the GUI as each new set of measurements is recorded. If multiple scans are to be obtained, the 2D plot and total ion-yield vs. pump-probe separation plot will sum all traces taken at the same translation stage position. An example time-resolved ion-yield trace may be seen in the main plot of Figure 3.2. At the end of each scan, pump, probe and pump-probe data is saved to a text file which may then be analysed through the TOFANALYSE2 GUI, as will be discussed presently.

3.3 TOFANALYSE2

The final GUI developed, TOFANALYSE2, may be utilised for the analysis of time-resolved photoion yield data post acquisition, with the capability to carefully calibrate time-of-flight data to m/z values, remove background signals from pump-probe data, perform cross-correlation Gaussian fitting of data to obtain instrument response functions and to fit various parallel and/or sequential exponential decay models to obtain molecular-decay time constants. The interface for the TOFANALYSE2 programme may be seen in Figure 3.3.

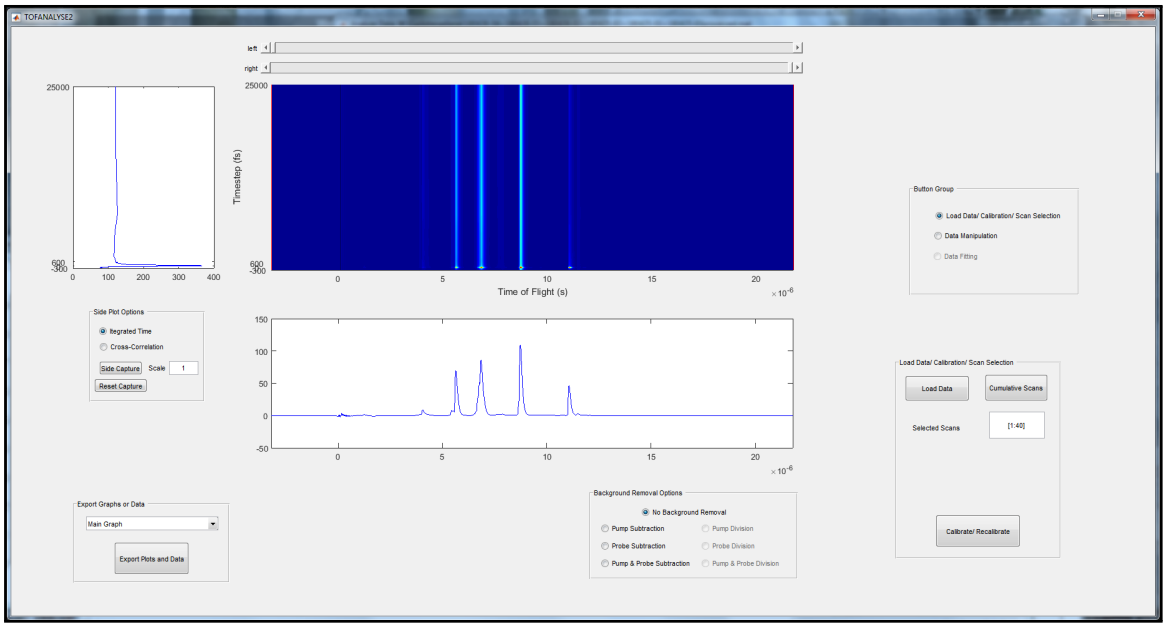

Fig. 3.3: TOFANALYSE2 graphical user interface displaying a time-resolved ion-yield trace of uracil, following 267 nm pump excitation and a 400 nm probe.

The main panel of Figure 3.3 initially displays the time-resolved ion-yield spectra experimentally obtained, whilst a plot to the left side shows total ion-yield vs. pump-probe separation. A particular ion-yield region may be monitored on this left-hand plot by positioning cursors, controlled by a pair of horizontal scroll bars above the 2D graph, over a mass region of interest. A final plot of note, below the 2D plot, presents the ion-yield data summated over all times sampled.

One of the first requirements for analysis of TRIY data is to first accurately calibrate the time-of-flight axis to a mass-to-charge ratio. This is performed through a sub-GUI developed within TOFANALYSE2 and is known as 'Calibration', the interface of which may be seen in Figure 3.4. Once initialised, operation of TOFANALYSE2 is suspended and the interface displays a plot of the experimental ion-yield time-of-flight

mass spectrum. Two known m/z peak positions (or one peak and a zero time position) are required for axis calibration, in conjunction with Equation (3.1). Use of the inbuilt MATLAB cursor function allows one to carefully select the centre of a known mass peak, before confirming the position as a calibration point by clicking either 'Left Peak' or 'Right Peak'. Once two peaks are chosen and m/z values are specified, the 'Calibrate/Recalibrate' button may be used to calibrate the time-of-flight axis and can be reset through re-pressing. Once an acceptable calibration is achieved, the 'Export Calibration' button allows one to save the calibration parameters to a text file and implement the calibration to the data in TOFANALYSE2.

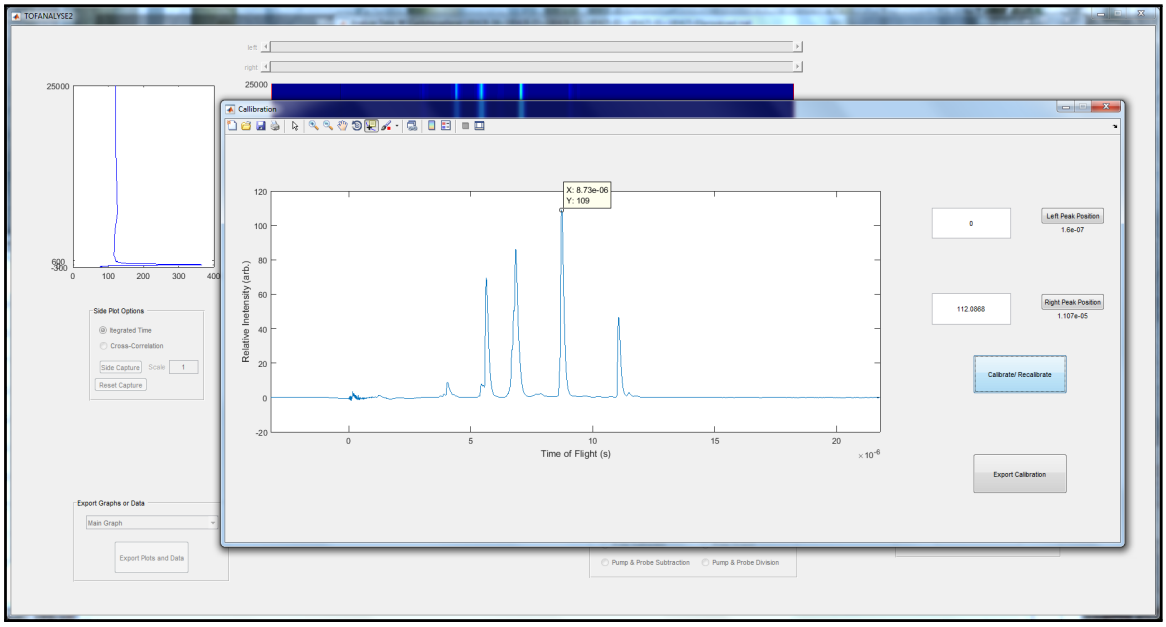

Fig. 3.4: Calibrate graphical user interface displaying an uncalibrated uracil TOF trace.

Numerous forms of data manipulation have been incorporated into TOFANALYSE2 for display purposes and to achieve publication-ready image outputs. These may be accessed through the data manipulation button within the button group on the right side of the GUI.

Key features include the ability to set m/z and pump-probe separation limits to zoom in on key areas of the data and being able to plot the pump-probe separation on a mixed linear-logarithmic axis, with a user optional linear-logarithmic step increment ratio, for easy observation of short and long time dynamics simultaneously. Further capabilities include the ability to plot TRIY data in 2D or 3D format with rotatable and reproducible viewing angles, performing 3- or 5-point running average data smoothing and plotting data intensity on a log-scale. It is also possible to display

the TRIY data from specific scans, observe 2D pump-alone or probe-alone transient data or one can subtract these background transients from the pump-probe data. Examples of some of these features are presented in Figure 3.5.

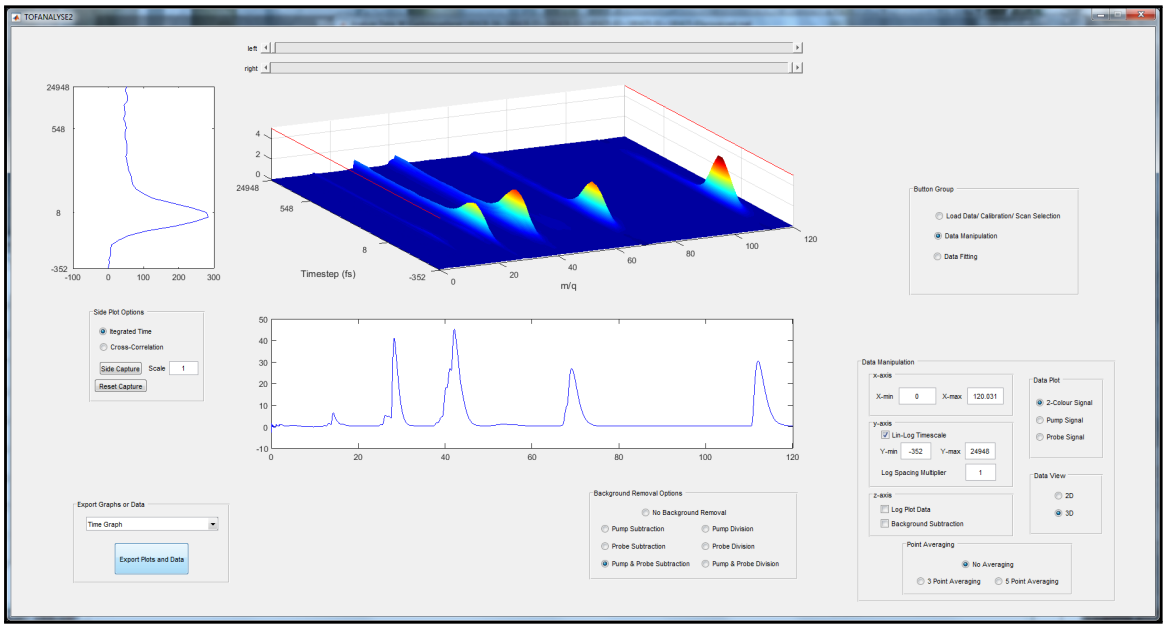

Fig. 3.5: Example data presentation options available through use of the TOFANALYSE2 programme. The data presented within the main panel shows a 3D plot of uracil from a 267-400 nm pump-probe experiment. Individual pump-alone and probe-alone signals have been subtracted and the temporal data is presented on a mixed linear-logarithmic plot. Data has also been truncated between m/z = 0 - 120 for ease of viewing.

In order to fit this TRIY data, it is important to first know the time-zero offset between the pump and probe beam as well as the instrument response of the spectrometer for the wavelengths utilised. These may be obtained by performing a Gaussian fitting routine on cross-correlation data from a molecule with a zero lifetime. The output parameters obtained provide the the central position of the data peak (time-zero position) and the Gaussian width (instrument response function). The Gaussian fit, *cc(t)*, was performed using an inbuilt Levenberg-Marquardt non-linear least squares fitting routine and was of the form Equation (3.3)

$$cc(t) = A * exp\left[-\frac{(t-t_0)^2}{\frac{\sigma^2}{4ln(2)}}\right] + Y_0 \tag{3.3}$$

Here, A is the Gaussian peak amplitude, t is pump probe separation, t_0 is the peak time-offset, σ is the Gaussian peak variance and Y_0 is the baseline offset. A 4ln(2) factor is required for conversion of the Gaussian variance into a full width at half

maximum value, representative of the instrument response function from the spectrometer. An example cross-correlation and Gaussian fit of the molecule diethylether may be seen on the left of Figure 3.6.

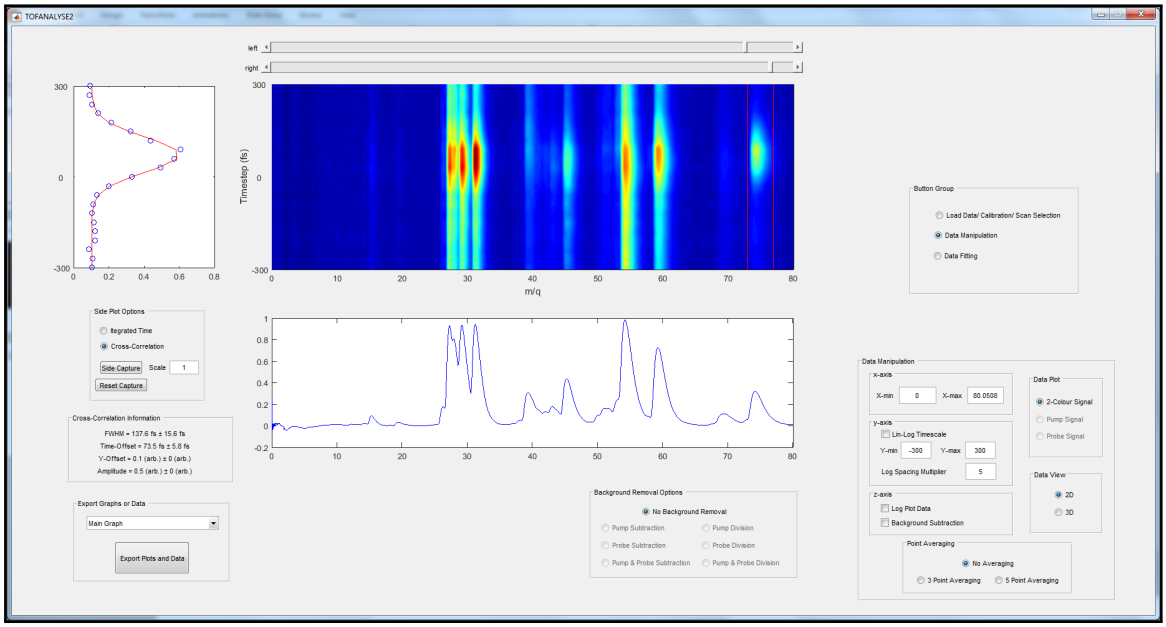

Fig. 3.6: Example cross-correlation measurement on the molecule diethylether following 267-400 nm pump-probe ionisation, analysed with a Gaussian fitting routine. The fit itself may be seen on the left plot within the GUI with details of the fit seen in the 'Cross-Correlation Information' panel.

Once the time-zero offset and Gaussian full width at half maximum values have been attained, it is possible to implement them as constants within the main fitting routine for obtaining molecular decay time constants from time-resolved ion-yield data. The interface for the data fitting is presented in Figure 3.7. Cursors, controlled by the two horizontal scroll bars positioned above the 2D TRIY data, are utilised to select an ion-yield region to sum over, which form the ion transients to be fitted. The code allows for the observation of up to seven dynamical time constants with an inbuilt Levenberg-Marquardt fitting routine. The fitting function utilised to describe the transient ionisation signal, ΔS, is initially described in the simplest form by Equation (3.4)

$$S(\Delta t) = \sum_{i=1}^{n} P_i(\Delta t) \otimes cc(\Delta t) \tag{3.4}$$

Here, $cc(\Delta t)$ denotes the experimentally determined Gaussian cross-correlation (as previously described in Equation (3.3)) and is convoluted with $P_i(\Delta t)$, a series of n exponentially decaying functions. $P_i(\Delta t)$ is extremely multifunctional within the GUI

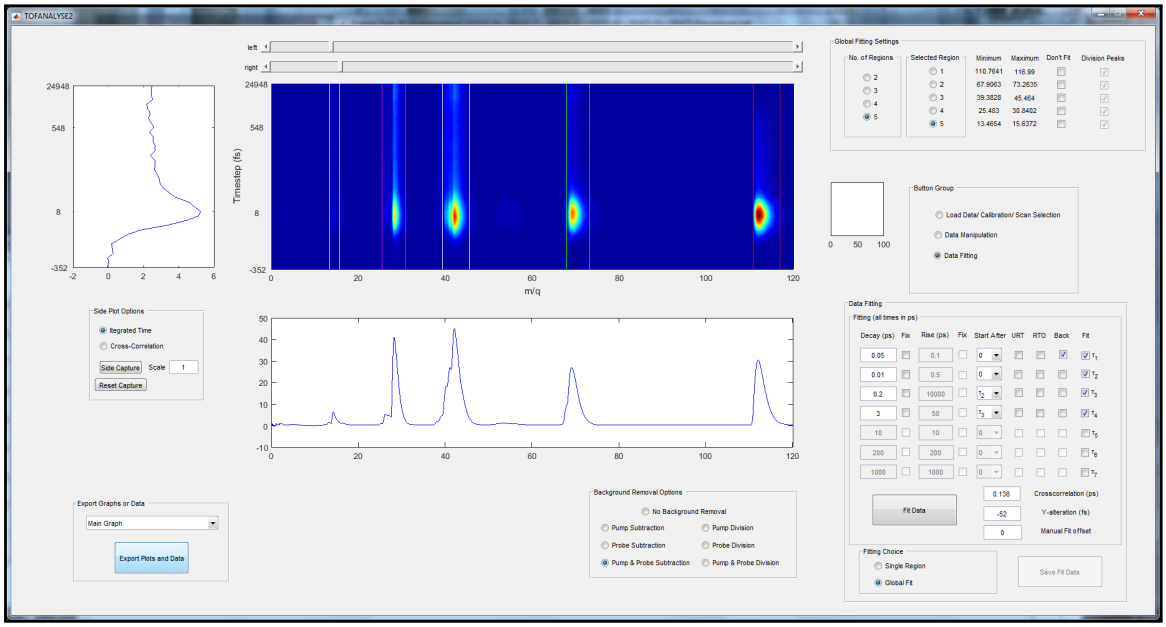

Fig. 3.7: TOFANALYSE2 GUI interface presenting the fitting options for uracil 267-400 nm pump-probe time-resolved ion-yield data.

framework presented here, with it possible to investigate a wide variety of molecular decay models utilising a simple set of tick boxes and drop-down menus presented in the bottom right of Figure 3.7. Options include propagation of molecular time constants in both pump-probe and probe-pump directions and fitting of both sequential and parallel molecular decay models, with additional options to include features which may have an unknown independent rise time or a rise time only feature, which does not decay relative to the times sampled. A number of example fitting models which may be implemented for determining two dynamical features are presented in Equation (3.5).

$$P(\Delta t) = \begin{cases} a_1 exp(\frac{-t}{\tau_{d1}}) + a_2 exp(\frac{-t}{\tau_{d2}})(1 - exp(\frac{-t}{\tau_{d1}})), & \text{Sequential forward fit} \\ a_1 exp(\frac{-t}{\tau_{d1}}) + a_2 exp(\frac{-t}{\tau_{d2}}), & \text{Parallel forward fit} \\ a_{(-)1} exp(\frac{t}{\tau_{d(-)1}}) + a_1 exp(\frac{-t}{\tau_{d1}}), & \text{Counter-propagating parallel fit} \\ a_1 exp(\frac{-t}{\tau_{d1}}) + a_2 exp(\frac{-t}{\tau_{d2}})(1 - exp(\frac{-t}{\tau_{r2}})), & \text{Unknown rise time feature} \\ a_1 exp(\frac{-t}{\tau_{d1}}) + a_2 (1 - exp(\frac{-t}{\tau_{r2}})), & \text{Unique rise time only feature} \end{cases} \tag{3.5}$$

Here, τ_{dn} and $\tau_{d(-)n}$ represent pump-probe and probe-pump decay time constants respectively, whilst τ_{rn} denotes a rise time time constant and a_n represents the fit amplitude associated with a particular dynamical decay. For ease of understanding, a graphical representation of each of these fitting models may be seen in Figure 3.8.

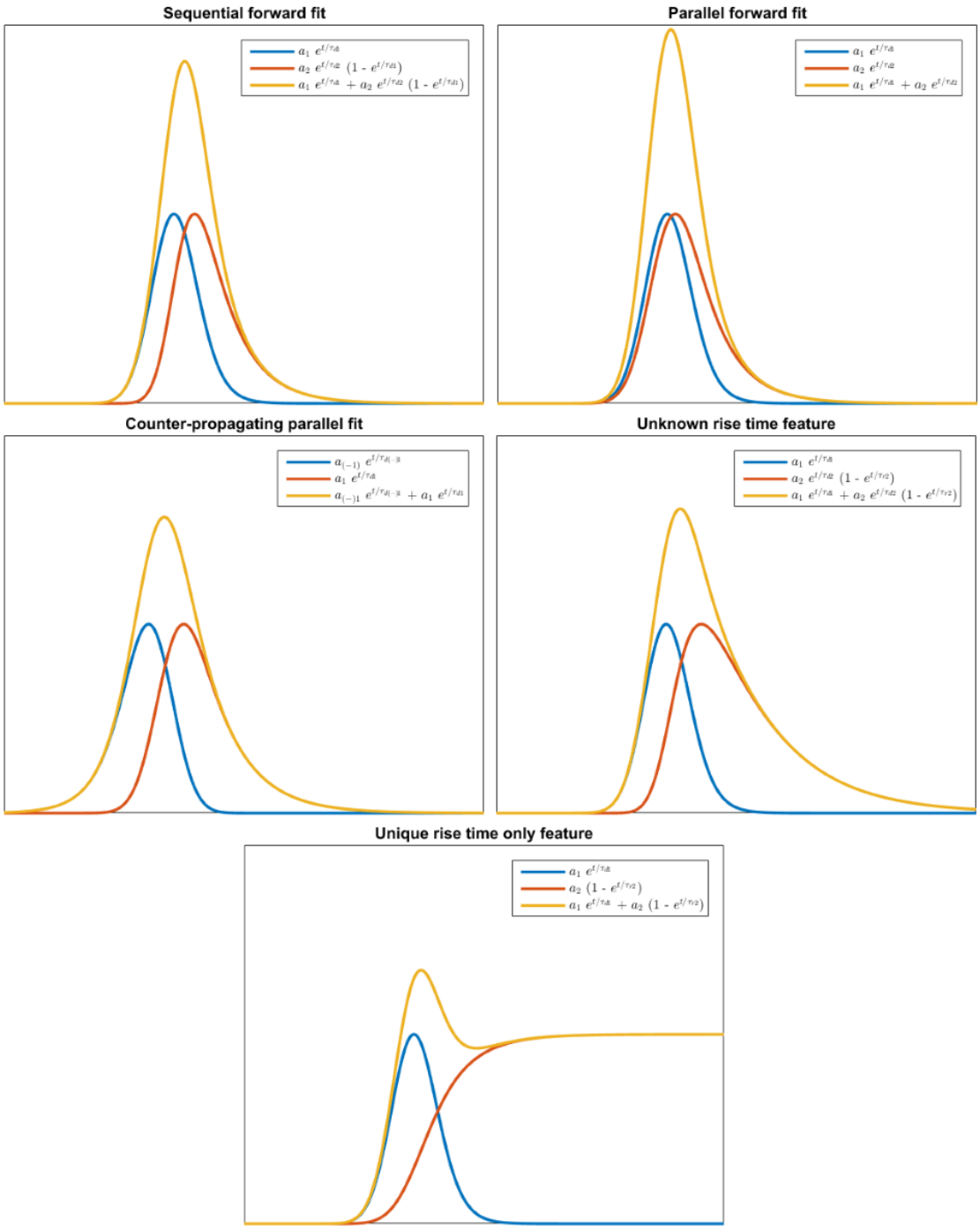

Fig. 3.8: Fitting models available employing the TOFANALYSE2 code for a 2 component fit. Examples include sequential and parallel fitting, counter-propagating parallel fitting and fitting models involving unknown rise time or rise time only features.

An example output from the fitting routine for a backwards probe-pump fit and a three-sequential pump-probe fit of the uracil parent ion is presented in Figure 3.9.

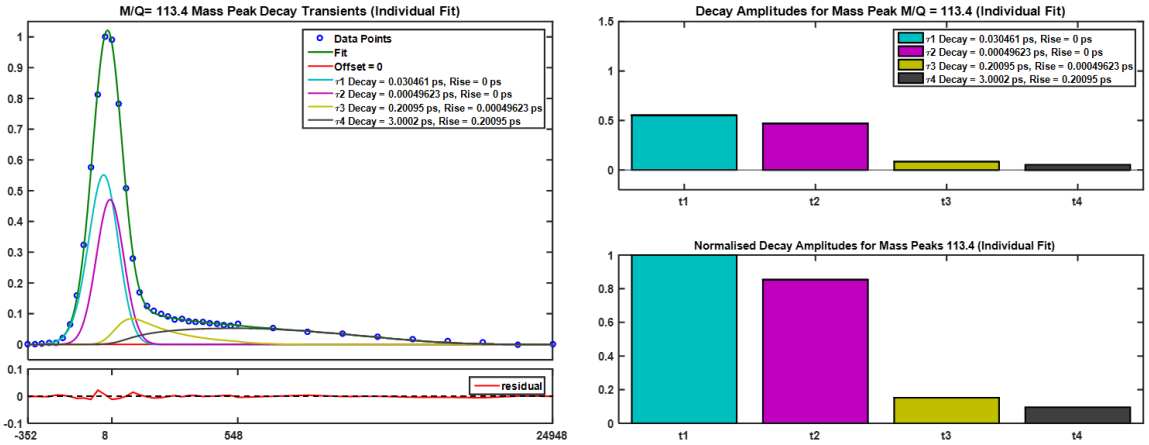

Fig. 3.9: Example of a single fit output from the TOFANALYSE2 programme for the uracil parent ion following a 267-400 nm pump-probe experiment. Left: transient parent ion-yield fit and trace for uracil. Right: decay amplitudes.

The left of Figure 3.9 presents the experimental transient ion data as points on a mixed linear-logarithmic timescale, with solid lines representing the overall fit and fit components. Below this plot, a smaller graph is presented of the fit residual, displaying the difference between each experimental data point and its corresponding fitted value. The right of Figure 3.9 displays the decay amplitudes in the form of a bar chart, an intrinsic way to compare the relative influence of the various dynamical processes.

A further fitting feature incorporated into the TOFANALYSE2 software is the capability to perform global fitting of up to five separate ions. Global fitting means that the time constants attained from the fitting function are consistent for all ions analysed, however the relative decay amplitudes are varied for the individual transients. Transient amplitudes are also normalised so lifetimes observed are not weighted due to the relative ion abundance. This is a useful tool as it allows one to investigate if comparable dynamics are operating in the different fragments formed in a time-resolved ion-yield measurement within a single fitting procedure. Transients are generated in a similar manner to that of an individual fit, utilising cursors operated by the horizontal scroll bars, however up to five pairs of cursors may now be operated in this manner for the global fitting option. Choosing how many transients one wishes to investigate and control of a particular cursor pair is selected through use of the button panels presented in the top right of Figure 3.7. Tick boxes also allow for a particular chosen fragment not to be fitted during the global fitting routine, allowing for fast analysis of ion transient subsets. An example fitting output for the four main uracil fragment ions, which will be discussed at length in Section 4.3.3, is presented

in Figure 3.10.

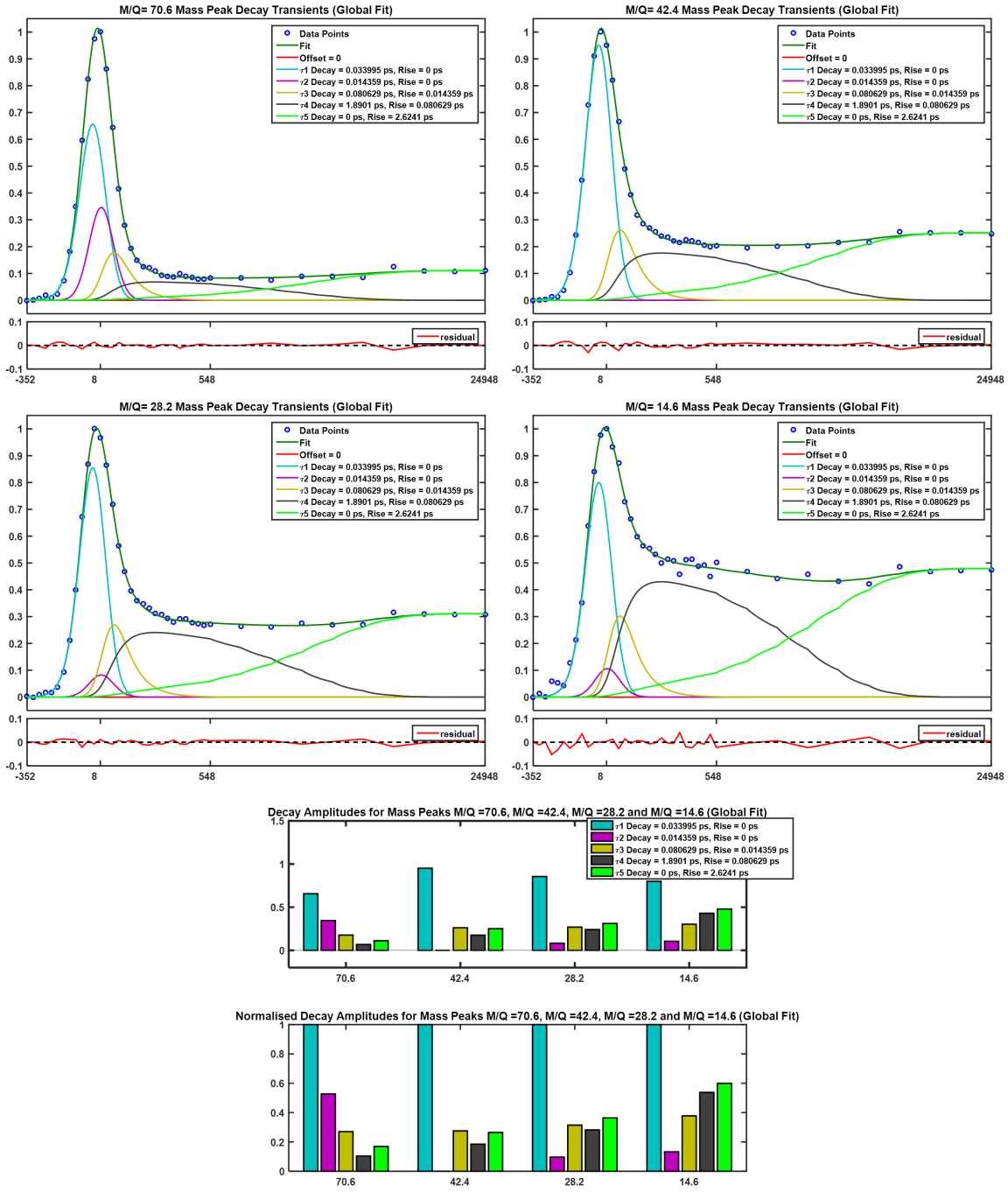

Fig. 3.10: Example of a global fit output from the TOFANALYSE2 programme showing four transient fragment ion-yield fits and traces for uracil following 267 nm excitation and probed with a 400 nm pulse. Also shown are the associated decay amplitudes.

A final feature of the TOFANALYSE2 GUI to discuss is that of a background division feature for compensation of a decaying sample. Due to the use of a thermal

desorption source, some TRIY measurements displayed sample concentration reducing throughout the acquisition time of the experiment. This is a problem for the analysis of molecular lifetimes, as what may be discerned as a decay lifetime may actually be a signature of lower sample concentrations. This can be monitored within the GUI through observation of pump-alone or probe-alone signal plotted for each experimental data point. In such a case, simple subtraction of the pump-alone and probe-alone data will not be sufficient for background removal and a more refined background compensation is required for pump-probe transient retrieval.

The first step to this background removal is to create a decay transient by averaging the pump-alone, probe-alone, or an average of both pump- and probe-alone at each timestep. Each of the transient peaks of interest may then be divided by this decay transient so as to form a flat baseline for the pump-probe data of interest, removing the effects of sample depletion. One can also choose to use only a subset of the background decay transients for this division removal through use of the tick boxes in the top right of Figure 3.7. Due to this being a division technique, the baseline of the transient trace will not be zero, thus when fitting a small manual offset may be included as a baseline.

3.4 Conclusion

The construction of the experimental set-up described in Chapter 2 and development of spectroscopic software discussed in this chapter has formed a huge part of this PhD. The spectrometer is now fully functioning and code is fully developed for data acquisition and analysis. Initial results obtained from this set-up are provided in the proceeding chapters, with further experiments employing the new spectrometer and developed time-resolved photoion yield software planned.

CHAPTER 4

Uracil and 2-Thiouracil:

Relaxation Dynamics of Non-Volatile UV Chromophores

The sections preceding this chapter have provided a valuable insight into how and why one would perform spectroscopic studies, with discussions of the experimental set-ups utilised and computational acquisition and analysis software developed. The following chapter will discuss the first results produced from the new time-resolved photoion-yield spectrometer, presenting results on the UV excitation of uracil across the 200-267 nm region, as well as a comparative study of the molecule 2-thiouracil following 267 nm excitation.

4.1 Motivation and Previous Studies

Ribonucleic acid (RNA) is a vital nucleic acid to all living matter and is essential to various biological roles including in coding, decoding, regulating, and the expression of genes[344]. Given the biological relevance of RNA, it is desirable to investigate the ultrafast relaxation dynamics of such a molecule post-UV excitation to understand its photo-protection mechanisms, however, given the size of the macromolecule, analysis of the relaxation process would be challenging. One approach is to utilise a gas-phase 'bottom-up' approach where one investigates the relaxation dynamics of a UV chromophore within the macromolecule, providing an instructive initial insight to the relaxation dynamics in an environment free from background perturbations and cluster effects. The nucelobases of the RNA macromolecule (uracil, adenine, guanine and cytosine) are prime candidates for such studies and are a rich area for spectroscopic study.

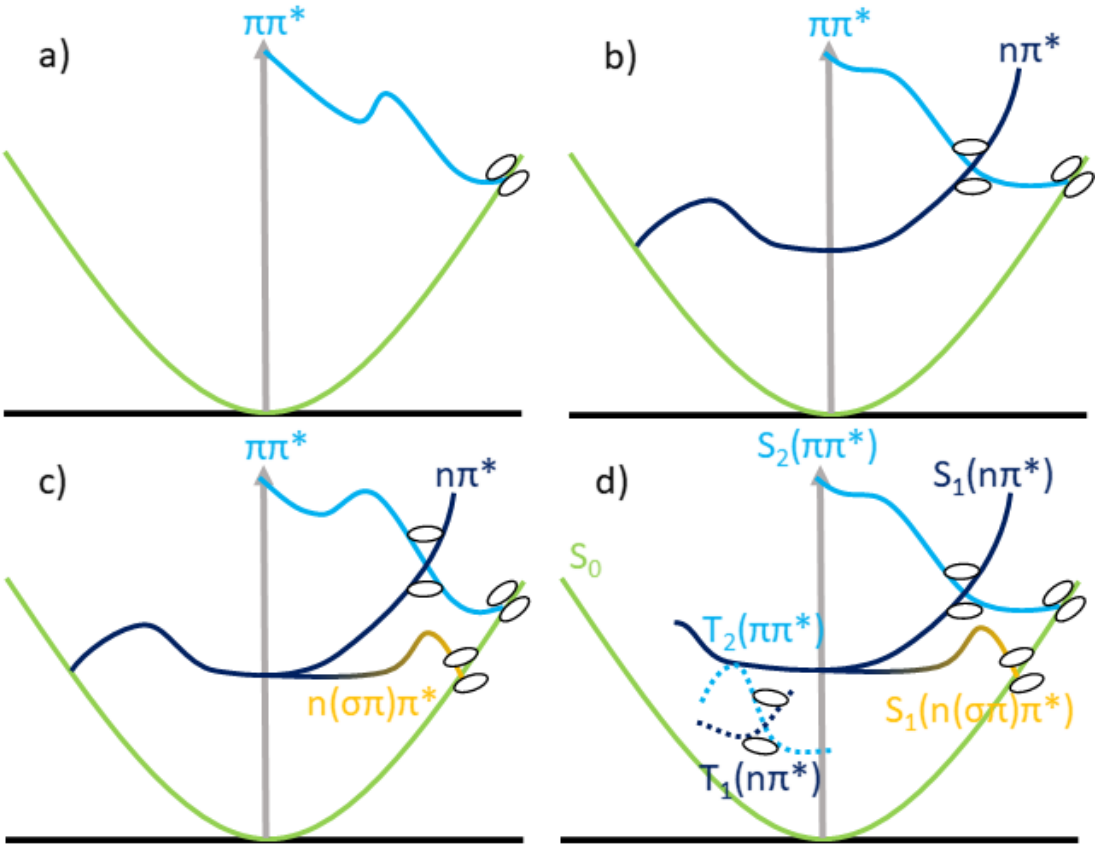

Fig. 4.1: A graphical summary of the various ultrafast relaxation mechanisms predicted for uracil predicted by a) Nieber et al.[345], b) Lan et al.[346] and Fingerhut et al.[347;348], c) Nachtigallová et al.[349] and d) Richter et al.[350]. Image adapted from Richter et al.[350]

The RNA nucleobase uracil ($C_4H_4N_2O_2$) has been extensively investigated across the ∼220-270 nm UV absorption region through numerous gas-phase spectroscopy and dynamics studies[351–360], as well as in various theoretical works[346;349;350;361–372]. These previous studies reveal the complex nature of relaxation dynamics in the uracil molecule, with various competing non-radiative decay pathways occurring on the femtosecond to nanosecond timescales. Key pathways include those of internal conversion (IC) from an excited $S_2(^1\pi\pi^*)$ either to the energetically lower $S_1(^1n\pi^*)$ state or, alternatively, directly to the S_0 ground state, as predicted by Nieber *et al.*[345]. Subsequent relaxation from the S_1 state has been theorised to occur through various schemes, including via intersystem crossing to the triplet manifold, as calculated by Richter *et al.*[350] or through a further IC to the S_0 ground state, as found by Lan *et al.*[346] and Fingerhut *et al.*[347;348]. A final theoretically predicted relaxation route from the S_1 state theorised is that of a ring-opening conical intersection of (σ(n-π)π^* character suggested by Nachtigallová *et al.*[349], connecting the S_1 state to the S_0 ground state. For simplicity, Figure 4.1 provides a graphical summary of these various ultrafast relaxation mechanisms for uracil.

The theoretical prediction of a possible ring-opening mechanism is of particular interest in the uracil molecule, given this would suggest a destructive and potentially harmful energy dissipation mechanism which would be detrimental to the molecule's photostability. Predictions of both S_2/S_1 (Nachtigallová *et al.*[349]) and S_1/S_0 (Nachtigallová *et al.*[349] and Richter *et al.*[350]) ring-opening conical intersections have been found computationally via cleavage of the N_3C_4 bond in the uracil molecule, as depicted in Figure 4.2.

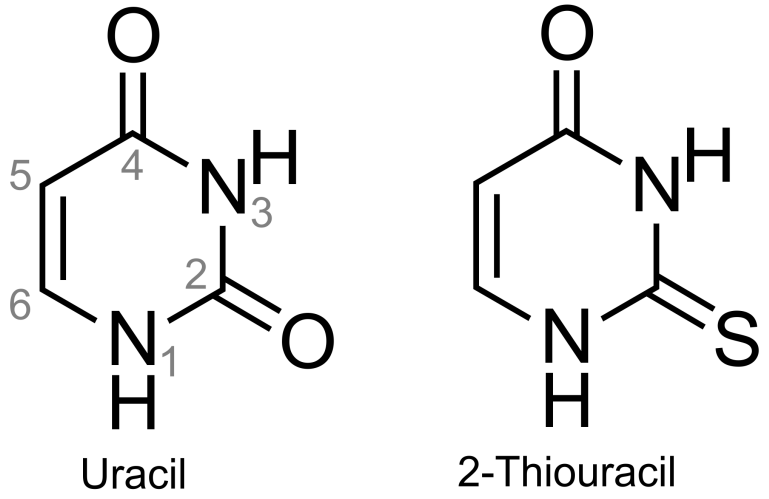

Fig. 4.2: Schematic structures of the lowest energy tautomers of uracil and 2-thiouracil.

In addition to this, Nachtigallová *et al.*[349] further suggested that the presence of such a ring-opening mechanism would almost certainly produce new photoproducts on an ultrafast timescale (predicted 700 fs). Potential experimental evidence of a ring opening channel has been suggested in nanosecond (1 +1) resonantly-enhanced multi-photon ionisation (REMPI) experiments on uracil across the 220 - 270 nm absorption region performed by Barc *et al.*[358]. In these experiments, the formation of a $m/z = 84$ peak at wavelengths below 232 nm was attributed to an S_2/S_1 ring-opening conical intersection, with further deuterated measurements[373] identifying the fragment as $C_3H_4N_2O^+$. Critically, this $m/z = 84$ fragment is absent in both single-photon ionisation and collision experiments, which may directly access the excited ionic states[374], and is also energetically consistent with the energies of all three predicted ring-opening conical intersections[349;350]. Furthermore, cleavage of the N_3-C_4 bond results in an exposed CO group at one end of the molecule and elimination of this moiety following photoionisation would yield the observed $C_3H_4N_2O^+$ fragment. The prediction of this ring-opening mechanism and m/z =84 fragment appearance was one of the key motivations for performing time-resolved ion-yield (TRIY) measurements on the uracil molecule, with the intention of further characterising the dynamical origin of this specific fragmentation channel. For this purpose, uracil was interrogated utilising 220 nm and 200 nm pump pulses, in conjunction with an intense 400 nm probe.

Although TRIY measurements are not as sensitive or differential as some other spectroscopic techniques, such as photoelectron spectroscopy or imaging studies, they are ideally suited to these mass-selective fragment appearance studies given the separation of ions on an m/z scale. This leads to a final key motivation for the study of uracil, as well as a further study of the sulfated equivalent 2-thiouracil (the structure of which may be seen in Figure 4.2), which is the direct comparison of excited state time constants produced via volatilisation from a soft thermal desorption source to those of traditional volatilisation methods and more differential studies[360;375]. To this end, further TRIY measurements on the uracil and 2-thiouracil molecules were performed in order to benchmark the newly designed spectrometer, utilising a 267 - 400 nm excitation-ionisation scheme. The works discussed in this chapter were completed in collaboration with the group of Dr Sam Eden at the Open University.

4.2 Experimental Set-up

A full description of the optical set-up, chamber design, sample preparation techniques and data acquisition software and methods utilised to perform these measurements have been previously described at length in Chapter 2 and Chapter 3 and the reader is encouraged to revisit these sections for further information.

Uracil and 2-thiouracil were purchased from Sigma-Aldrich (≥99% purity) and were used without further purification. Molecular samples were deposited on a 10 μm thick 316 stainless steel foil (ϕ = 32 mm) using application of methanol to ensure a uniform coating 300-500 μm thick. Production of gas-phase species was accomplished via the soft-thermal desorption technique discussed in Section 2.3.2, with a desorption laser power typically of ∼330 mW and a spot on the foil ∼1 mm in diameter. Due to sample burn-off during the volatilisation process, the foil was rotated to a new position every 45 - 60 minutes with data acquisition temporarily suspended.

The optical set-ups for generation of 400 nm (20 μJ/pulse), 267 nm (1.6 μJ/pulse), 220 nm (0.3 μJ/pulse) and 200 nm (0.2 μJ/pulse) pulses utilised in these measurements are described at length in Section 2.2.5 and should be referred to for a full overview.

The Gaussian instrument response function was determined using diethylether backfilled into the interaction region, utilising non-resonant multiphoton ionisation. Diethylether is an ideal choice for determining the temporal resolution of this experiment as uracil (vertical ∼9.5 eV, adiabatic 9.34 eV)[343;376] and diethylether (vertical ∼9.6 eV)[377;378] have very similar ionisation potentials. This will result in both parent ion signals arising predominantly from the same photon order process in each of the investigations undertaken, an important consideration as the instrument response function is dependent upon the photon order of the ionisation process. Further to this, although 2-thiouracil has a considerably lower ionisation potential (vertical 8.80 eV)[379], for the case of the 267 nm pump investigated here, it too will predominantly ionise on the same photon order as diethylether. Cross-correlation measurements of the parent ion were recorded, with resolution optimised though varying the thickness of BK7 windows (anti-reflection coated for the near-IR) in which the probe beam of the set-up was incident to prior to the UV generation. Utilisation of this technique allows one to compensate for the residual (negative) spectral dispersion induced due to optimisation of the laser amplifier grating compressor for nonlinear conversion in the pump arm. Numerical cross-correlation values obtained were 140 ± 10 fs, 175 ± 15 fs and 170 ± 15 fs when using the 267 nm, 220 nm and 200 nm pump wavelengths, respectively.

4.3 Results and Discussion

The following section will discuss the main results found from our study on the dynamics of uracil and 2-thiouracil. Section 4.3.1 will discuss the thermal effects one must consider due to the use of a soft laser desorption source for sample volatilisation. An analysis of the parent and fragment transients of uracil and 2-thiouracil after 267 nm excitation will follow in Section 4.3.2 and Section 4.3.3 respectively. An examination of the 220 nm and 200 nm uracil studies will be then described in Section 4.3.4 before a final discussion of some REMPI nanosecond uracil measurements at 220 nm in Section 4.3.5. The results discussed in Section 4.3.5 also utilised a soft thermal laser desorption source for sample volatilisation and were performed by Jana Bocklova and Andre Robelo at the Open university.

4.3.1 Thermal Desorption Source Characterisation

Prior to discussing the dynamical molecular signatures observed within the uracil data, it is imperative to first consider the sample temperature. One must consider the thermal effects which could be induced through use of a laser desorption source, as well as to ensure that there is no risk of thermal decomposition of the sample pre-photoexcitation. To investigate the thermal stability of the sample, the ratio of fragment-to-parent ions was investigated over a range of desorption laser power settings using one-color multi-photon ionisation at 267 nm, the results of which are presented in Figure 4.3

As is demonstrated in Figure 4.3, the parent/fragment ion ratios remain steady for all of the major fragments produced during the photoionisation of uracil. This strongly suggests that there is no significant thermal decomposition of the sample through use of the desorption laser over the range of settings investigated.

Estimates of the localised temperature of the stainless steel substrate foil under various desorption laser power and focussing conditions were made possible through use of a K-type (chromel-alumel) thermocouple contact which was carefully positioned at the center of the 1 mm beam focus. Use of such a thermocouple may be justified when one considers that the thermal conductivities of both chromel and alumel are both very low ($\sim$18 $Wm^{-1}K^{-1}$ and $\sim$30 $Wm^{-1}K^{-1}$ respectively)[380] and are comparable to that of stainless steel itself ($\sim$16 $Wm^{-1}K^{-1}$)[381]. Further supporting arguments may be made when one considers the respective reflectivities of both alumel and chromel. Both materials consist of >90% nickel, which shows a comparable reflectivity to that of stainless steel at the 445 nm desorption laser wavelength (while utilising the reasonable

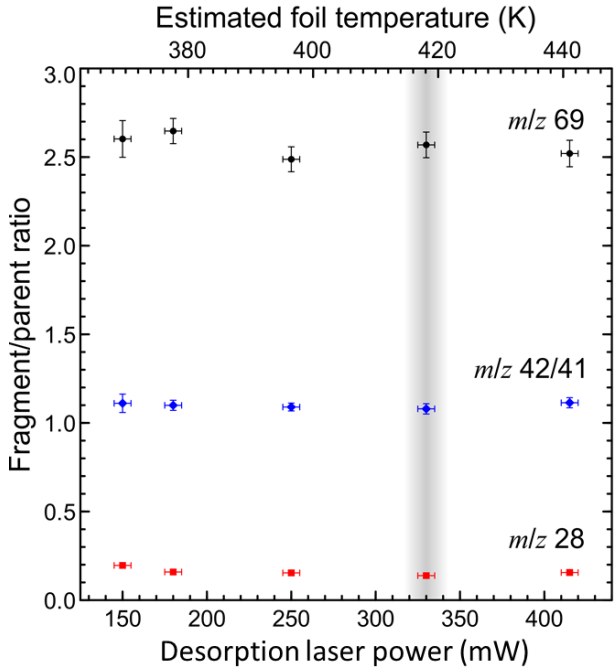

Fig. 4.3: Parent/fragment ion ratios obtained from uracil following 267 nm irradiation through variation of desorption laser power (for fragments m/z = 69, 42/41 & 28). Shaded region indicates the operating conditions used in the time-resolved ion yield measurements and an estimated foil temperature is also included along the upper x-axis. Error bars denote 1σ uncertainties. Horizontal bars represent error in desorption laser power. Corresponding uncertainties in foil temperature are significantly larger (∼ ×3).

assumption that both the alumel-chromel and stainless steel have a similar surface finish quality)[382]. Utilisation of this approach therefore allows for a rudimentary estimation of the foil substrate temperature which, as shown by the shaded region in Figure 4.3, is predicted to be of the order ∼420 ± 30 K for the experiments performed in this study. This may also be considered as the maximum temperature possible for the molecular sample. As uracil and 2-thiouracil are chemically stable species, and also considering the fragment ratio data previously discussed, such a temperature would seem insufficient to induce significant thermal decomposition of the samples. Furthermore, such a thermal desorption approach has previously been shown to successfully volatilise intact DNA nucleosides[287], which are far more thermally unstable than the uracil and 2-thiouracil molecules in this present study.

Although thermal decomposition of the sample may be considered a negligible effect, there are further implications to heating one must contemplate, including the presence of multiple tautomeric forms and thermal excitation of ground state vibrational modes. Computational calculations[383–385] on both uracil and 2-thiouracil

would suggest that all excited tautomers lie >1500 cm^{-1} higher than the di-keto (uracil) and oxo-thione (2-thiouracil) structures displayed in Figure 4.2 and would not be present to any great extent in the desorption plume at a temperature of 420 K. However, such an argument may not be made when considering vibrational modes accessible from the ground electronic state at such a temperature, where calculations[386;387] show vibrational modes are present with very low frequencies (<500 cm^{-1}) in both uracil and 2-thiouracil and thus a non-negligible excited state population would be present in the gaseous sample. This is a potentially important consideration given that out-of-plane bending vibrations of the aromatic ring system have previously been implicated in helping to access conical intersections, which mediate the electronically excited state dynamics[346;349;350;361;370;371;388].

4.3.2 Parent Ion Transients of Uracil and 2-Thiouracil Following 267 nm Excitation

As previously discussed in Section 4.1, it is important to compare the dynamical signatures of molecules volatilised by employing the new laser desorption source with those of previous studies utilising more conventional molecular beam methods[351–353;355–357;360;375]. This benchmarking was achieved through performing time-resolved ion-yield measurements on uracil and 2-thiouracil, using a 267 nm excitation pump and 400 nm ionisation probe, interrogating the $S_2(^1\pi\pi^*)$ state in both systems. A 3D depiction of the transient mass-spectra attained for the uracil and 2-thiouracil molecules may be seen in Figure 4.4.

The uracil data displays a fragmentation pattern comprising 4 main peaks, which have previously been assigned[358;373], consisting of the parent ion ($m/z = 112$) and 3 main fragments at $m/z = 69$ ($C_3H_3NO^+$), 42/41 (mostly $C_2H_2O^+$) and 28 (CH_2N^+), as well as a somewhat less intense peak at $m/z = 14$ (predominantly $CH_2{}^+$). The fragmentation pattern observed is in good accord with numerous previous studies on the uracil molecule investigated with a range of different techniques such as one-color single- and multi-photon ionisation[358;373;374], proton impact[389–391] and electron impact[343;389;392–394] ionisation and, of particular importance, a series of time-resolved studies by Weinacht and co-workers that employed a resonant 260 nm excitation pulse followed by an intense 780 nm ionising probe[355–357;395].

2D cuts though the uracil and 2-thiouracil data at pump-probe delay times of $\Delta t = 0$ and 5 ps, as well as pump-alone and probe-alone fragment distributions, are presented in Figure 4.5. On inspection of Figure 4.5, it becomes clear that the experimental apparatus has good signal-to-noise, with it possible to observe extremely weak

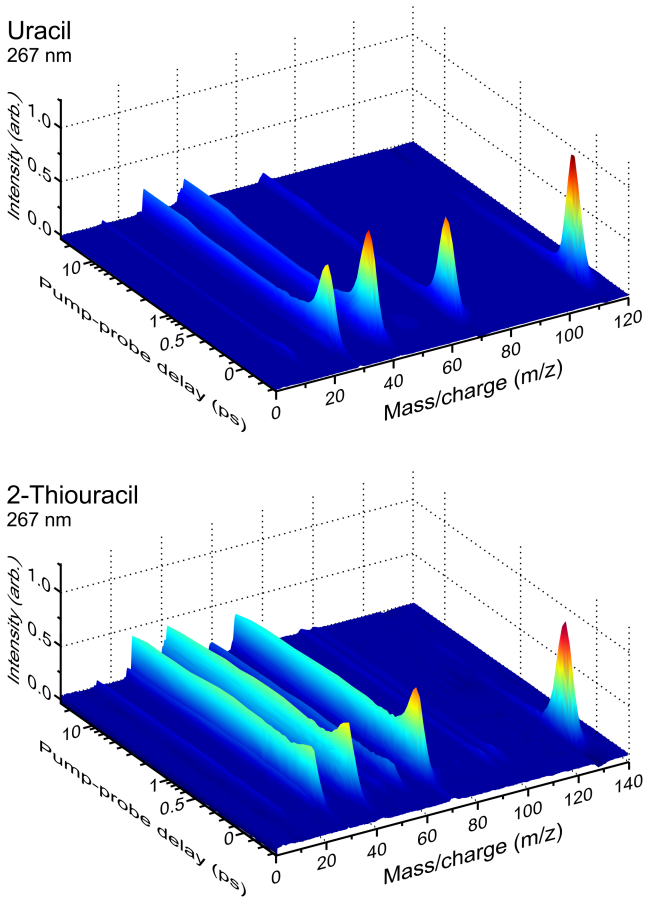

Fig. 4.4: TRIY plots for uracil and 2-thiouracil utilising a 267 nm pump and an intense 400 nm probe. Data collection runs scanned the translation stage repeatedly between -300 fs to +600 fs in 30 fs steps and +600 fs to +25 ps over 9 exponentially increasing increments.

features, including fragments at $m/z = 53/54$, 26 and 1. The presence of $m/z = 26$ in particular demonstrates the good signal-to-noise achieved in these experiments, given that it was not discernible in a number of previous mass spectrometry studies[391]. It is also evidence that these measurements should be sensitive to the presence of weak photoproducts, including $m/z = 84$, should they be produced in the latter 220 nm and 200 nm investigations of uracil. In 2-thiouracil, a wider range of ion peaks were observed, including strong features at $m/z = 128$ (parent ion), 69, 42/41 and 28, which may also be seen in Figure 4.5.

If one wishes to analyse the excited state dynamics observed in a TRIY experiment, a logical first step is to consider the dynamical signatures produced by the parent ion transients with respect to pump-probe delay time Δt. This consists of fitting a series of sequential exponential rises and decays to the parent ions, each convoluted with the instrument response function for the given experimental conditions. A full

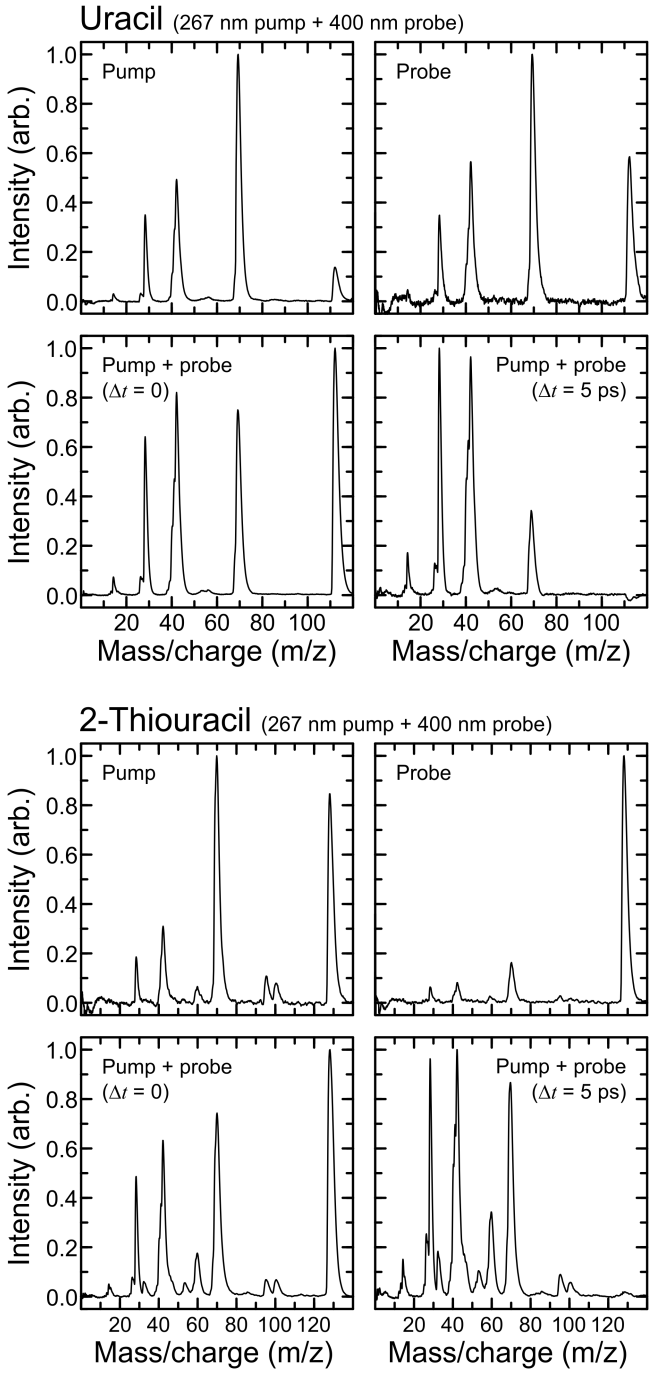

Fig. 4.5: Mass spectra observed for uracil and 2-thiouracil for 267 nm pump-alone signal, 400 nm probe-alone signal and with a 0 ps and 5 ps pump-probe delay time

description of the fitting procedure has been previously provided in Chapter 3 and so will not be discussed in greater detail here. Four exponential decaying functions were required to adequately fit to the parent ion transients of both uracil and 2-thiouracil. An extremely rapid 'probe-pump' feature was present in both data sets

in the negative time direction due to the high propensity to absorb at 200 nm in both molecules, energetically equivalent to a 2-photon absorption of 400 nm light. This will be labelled as τ_{-1}. In the forward direction, both molecules required a 3 sequential exponential decay fit, which may be considered as a molecule initially optically prepared to an excited state (A), prior to excited state geometry relaxation and/or population transfers to lower energy states (B-D) as a result of non-radiative decay processes. These forward propagating time constants will be referred to as $\tau_{1\text{-}3}$ throughout the remainder of this section. The application of this fitting analysis to the parent transients is presented in Figure 4.6

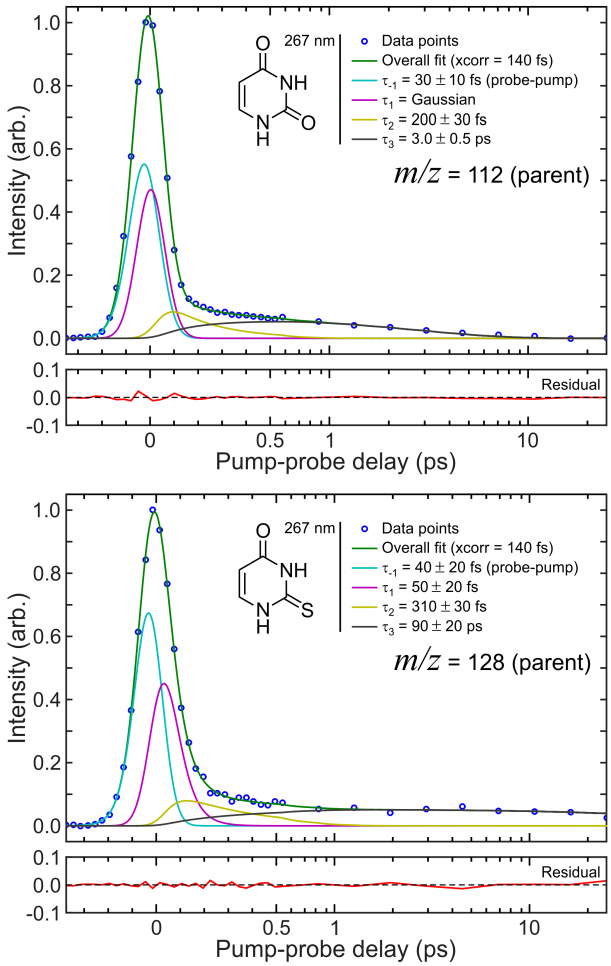

Fig. 4.6: Parent ion transients and fits for uracil (top) and 2-thiouracil (bottom) following 267/400 nm pump/probe ionisation on a mixed linear-logarithmic timescale. Also shown are the associated fit residuals (i.e., the overall fit subtracted from the raw data).

The forward-evolving time constants presented in Figure 4.6 for the uracil molecule (τ_1 = Gaussian,τ_2 = 200 ± 30 fs and τ_3 = 3.0 ± 0.5 ps), compare favourably to a number of previous TRIY studies which utilise similar excitation wavelengths and

multi-photon probes[351;356;357]. Generally in these investigations an initial <100 fs decay is observed prior to a longer lifetime on the order of 2.2-3.2 ps, comparable to the time constants τ_1 and τ_3 found in this present study. An exception to this is an investigation by Canuel *et al.*[353] in 2005, where decays of 130 fs and 1.1 ps were observed. Further evidence for the longer time constant in uracil has been shown when utilising the more differential time-resolved photoelectron imaging technique, in an experiment performed by Yu *et al.*[360]. In this study, a 260 nm pump pulse was employed in conjunction with a two-photon 290 nm probe. Time constants of 170 ± 35 fs and 2.35 ± 0.47 ps were extracted. An additional comparison which may be drawn from the results of Yu *et al.* and this present study is the presence of the τ_2 = 170 ± 35 fs time constant in the photoelectron measurements, which is remarkably similar to the second time constant, τ_2 = 200 ± 30 fs, for uracil presented here.

A time constant of this duration has not generally been observed in previous TRIY studies, however this may be rationalised when one considers the possibility of coherent processes occurring around the time zero position through use of intense multi-photon probes[351]. The necessity for two ultrafast time constants in this present work, τ_1 and τ_2, may allude to two distinct dynamical process occurring which may not always have been fully distinguishable in previous studies. One can have confidence in the requirement for two time constants in the present study given the good signal-to-noise in the attained data transients.

Although alternative relaxation schemes have previously been proposed[350], we assign the dynamical signatures observed in this study similarly to that of Yu *et al.*. The physical origin of the Gaussian feature in the uracil data, τ_1, is interpreted as a geometry reoptimisation of the optically prepared $S_2(^1\pi\pi^*)$ to its minimum energy configuration (with the additional possibility that some fraction of population may also decay directly to the S_0 ground state). Subsequent internal conversion of the geometry relaxed excited $S_2(^1\pi\pi^*)$ state to the energetically lower lying $S_1(^1n\pi^*)$ state may then be assigned to the second time constant, τ_2 = 200 ± 30 fs, before the final decay of this $S_1(^1n\pi^*)$ state is modelled by the third time constant τ_3 = 3.0 ± 0.5 ps.

The most important result from this investigation, however, is the demonstration that the use of a laser-based thermal desorption approach does not significantly alter the dynamical signatures observed when compared to results attained with more traditional molecular beam methods. This leads to the conclusion that any low-frequency out-of-plane vibrational modes which may have been excited due to elevated experimental temperatures do not significantly alter the dynamical timescales and mechanisms operating in uracil at this excitation energy. This may be rationalised when

one considers that use of 267 nm (4.64 eV) pulses to excite uracil will prepare it well above the $S_2(^1\pi\pi^*)$ origin (4.48 eV[365]) and, theory has predicted conical intersections accessing lower lying electronic states will be essentially barrierless[346;350;364;370;371].

The previously discussed photoelectron imaging study of Yu *et al.* also reports a further long-lived dynamical component with a lifetime of >1 ns and is assigned to intersystem crossing to the triplet manifold from the $S_1(^1n\pi^*)$ state. Absence of this feature in the present work may be attributed to the two photon probe energy in our investigation (6.2 eV) being significantly lower than that of the previous photoelectron imaging study (8.4 eV) and thus it is not possible to project sufficiently deep into the ionisation continuum to observe this long-lived component. This is further confirmed through observation of the binding energy spectrum for uracil produced in the photoelectron imaging study[360] and also leads to the conclusion that our detected parent ion signals arise predominantly from $1 + 2'$ ionisation. The lack of $1 + 3'$ signal would suggest that either it is not a significant factor in the present ion-yield measurements or that the parent ion is so internally excited upon $1 + 3'$ absorption that it rapidly fragments with a probability close to unity.

Similarly to the uracil results discussed thus far, the pump-probe time constants attained for the 2-thiouracil parent ion, $\tau_1 = 50 \pm 20$ fs, $\tau_2 = 310 \pm 30$ fs, and $\tau_3 = 90 \pm 20$ ps, are in excellent agreement to those of a recent time-resolved photoelectron imaging study performed by Sánchez-Rodríguez *et al.*[375]. In this investigation, 2-thiouracil was interrogated over a range of pump wavelengths spanning 292-249 nm, with time constants observed with 271 nm excitation of particular interest for data comparison ($\tau_1 < 50$ fs, $\tau_2 = 333$ fs, and $\tau_3 = 109$ ps). Again, due to the similarity of numerical time constants attained utilising traditional molecular beam methods and through use of a thermal desorption source, one can argue that the elevated sample temperatures are not sufficient to significantly modify the relaxation dynamics probed in this investigation.

Given the similarity in the dynamical behaviours observed, the present study assumes the relaxation mechanisms suggested by Sánchez-Rodríguez *et al.*, which are consistent with recent theoretical predictions[396]. Accordingly, τ_1 is assigned to the decay of the initially excited $S_2(^1\pi\pi^*)$ state to the energetically lower $S_1(^1n\pi^*)$ state, τ_2 relates to intersystem crossing to the triplet manifold and finally τ_3 is a signature of the decay of the lowest energy triplet state back to the S_0 ground state. An interesting note is that, in contrast to the study of uracil, observation of a long-lived component in 2-thiouracil, τ_3, is feasible when employing a 2-photon 400 nm probe. This is due to 2-thiouracil having a significantly lower ionisation potential than uracil ($\sim$0.8 eV) and, thus, it is possible to project deeper into the ionisation continuum. This is

further supported by the photoelectron binding energy spectrum at 271 nm presented in the work of Sánchez-Rodríguez *et al.*[375].

4.3.3 Fragment Ion Transients of Uracil and 2-Thiouracil Following 267 nm Excitation

In contrast to the dynamical behaviour of the uracil parent ion in Figure 4.4 and Figure 4.6, the fragment transients investigated (m/z = 69, 41/42, 28 and 14) clearly present a distinctly different dynamical picture. Although all the fragment ions appear to display a broadly similar temporal evolution, much longer-lived dynamical processes appear to be revealed than those observed in the uracil parent ion, extending well beyond the sampled pump-probe delay range of 25 ps. Furthermore, one also observes a slight rise in signal level at pump-probe delays beyond ~8 ps, which is in stark contrast to the behaviour observed in the uracil parent ion. Individual fragment ion transients obtained from uracil following 267 nm excitation are presented in Figure 4.7. Similar behaviour is also observed in 2-thiouracil, as can be discerned in the 3D mass spectrum presented in Figure 4.4.

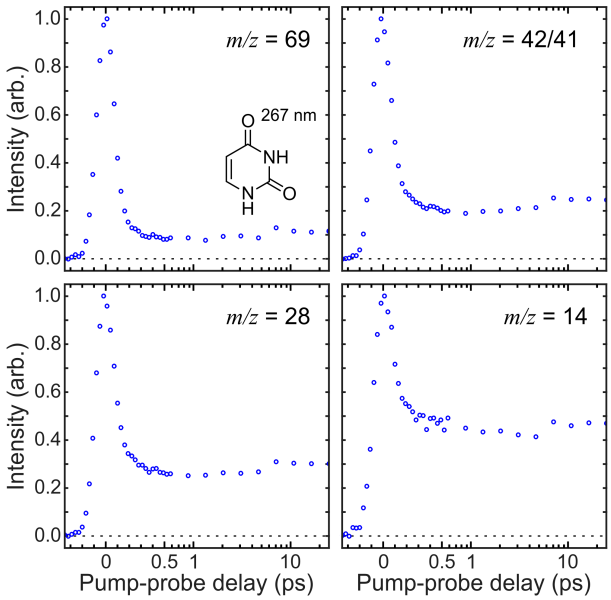

Fig. 4.7: Transients obtained from various uracil fragment ions following 267/400 nm pump/probe ionisation, plotted with a mixed linear-logarithmic timescale.

Although one may initially assume that it is possible to glean additional information about the neutral molecule from this dynamical behaviour, there is, however, also the caveat that the signal observed may be the superposition of a number of unrelated

dynamical processes. One possibility is that the decay signature may arise from direct excitation to the cation. Under these conditions, ionisation is achieved exclusively via the 267 nm pump beam, with subsequent absorption of a 400 nm photon probing the cation dynamics, which may include additional, prompt fragmentation in a $(3 + 1')$ scheme. Complications arise, however, as the signal may also reflect dynamical processes as a result of higher-order $(1 + 3')$ processes. This may take the form of photoionisation of low-lying vibrationally excited states in the parent molecule, leading to the formation of highly vibrationally excited cations which will readily fragment, or, alternatively, as a result of photofragment ionisation following photodissociation of the neutral parent. Presence of such behaviour would make extraction of meaningful dynamical information from these fragment transients challenging, as excited states in the neutral parent molecule and parent cation would evolve dynamically on different timescales. Deconvolution and analysis of such data would not be possible within the one-dimensional (i.e. non-differential) measurement framework of a simple pump-probe TRIY experiment. Recent theoretical calculations on the non-adiabatic relaxation dynamics of the uracil cation predict extremely rapid internal conversion to the D_0 ground state occurs prior to any significant fragmentation occurring[397;398].

The theory that cation dynamics make a non-negligible contribution to the overall fragment dynamics observed is supported by three independent pieces of evidence. Firstly, the appearance time of the fragments with respect to the parent ion show no discernible offset, which one would not expect for the case of neutral dynamics given that two uracil ring bonds must break to form any of the fragment species discussed. It would be expected that the time resolution in our TRIY measurement would be good enough to discern nascent formation of photofragments, which would lead to the conclusion that ionisation of neutral photofragments cannot be the sole dynamical process observed in this study. Furthermore, previous works have suggested that fragment formation occurs sequentially[374;392;395], with the appearance of $m/z = 42/41$ and 28 a consequence of $m/z = 69$ fragmentation through successive bondbreaking. The successive bondbreaking consists of a two-stage process in which two bonds are initially broken in the parent ion to form the $m/z = 69$ fragment, with a further bond broken within this fragment required subsequently for the formation of $m/z = 41/42$ and $m/z = 28$ respectively. Secondly, although numerous attempts were made to fit the data utilising various numbers of exponential functions and a number of different sequential and/or parallel models, it was not possible to extract numerical time constants resembling those observed in the parent ion. This result is quite significant, as if the fragments are a reflection of the neutral parent dynamics, one should observe time constants on a similar timescale in both the parent and frag-

ment ions, with possible additional longer lived processes also seen in the fragments. The final piece of evidence considered here is the energetic appearance energies of the fragment ions. Previous theoretical[395] and experimental[343;374;389] studies have reported the energetic appearance thresholds for several uracil fragments, a summary of which may be seen in Table 4.1.

Fragment (m/z)	Appearance Energy (eV)
112	9.34[a]
69	10.85 - 10.87[b]
41/42	12.95 - 13.41[b]
28	13.75 - 13.83[b]
14	-

Table 4.1: Summary of the uracil fragment appearance energies reported by a) Choi et al.[376] and b) Coupier et al.[389], Denifl et al.[343] and Jochims et al.[374] respectively.

A further summary of the possible total available energies generated in a 267 nm pump, 400 nm probe experiment is also provided in Table 4.2.

Ionisation Process	Total Photon Energy (eV)
1 × 267 nm + 2 × 400 nm	10.85
1 × 267 nm + 3 × 400 nm	13.95
2 × 267 nm	9.30
3 × 267 nm	13.95
3 × 400 nm	9.30
4 × 400 nm	12.40

Table 4.2: Summary of the total available energies in a 267 nm pump and 400 nm probe experiment.

What may be gleaned from Table 4.1 and Table 4.2 is that although it may be possible to access the $m/z = 69$ fragment through a $(1 + 2')$ photoionisation process, observation of the $m/z = 41/42$ and 28 fragments should require a higher photon order (minimum $1 + 3'$) in the present study. Given that it has already been established that the parent ion arises from predominantly $1 + 2'$ photoionisation, it is highly

unlikely that the relatively large fragment peaks observed (particularly at $\Delta t. = 0$) would be exclusively the result of a $1 + 3'$ process. One would expect that dynamics from a higher photon-order process would represent a much smaller fraction of the overall signal. An additional lower probe photon order process is likely to also be contributing (e.g. a $3 + 1'$ process observing cation dynamics).

In order to establish the origin of the fragment ions observed in this experiment, and further investigate the role of competing neutral vs. cation dynamics, a series of power dependence measurements were undertaken for the fragments $m/z = 69$, 42/41, 28 and 14, in addition to the parent ion. These measurements were performed at $\Delta t = 0$ and 5 ps (only at $\Delta t = 0$ for the parent ion due to insufficient signal at later times) and the 400 nm probe power was varied between 4 and 10 μJ/pulse, limited so as to avoid reaching a saturation regime. Furthermore, background signals arising from one-colour ionisation (pump-alone and probe-alone signals) were subtracted from the total recorded ion signal. The number of probe photons absorbed (α_{probe}) may then be estimated using Equation (4.1).

$$I = cP^{\alpha_{probe}} \tag{4.1}$$

Here, I is the ion intensity, c is a constant and P is the 400 nm photon fluence. The gradient of a probe laser power vs. pump-probe ion signal, plotted on a log-log scale, then yields the desired probe photon order, the results of which may be observed in Figure 4.8.

The results drawn from this power dependence study present a complex picture of the ensuing dynamics at the two time periods investigated ($\Delta t = 0$ and 5 ps). Around the time-zero position, the parent ion exhibits close to the expected behaviour of 2-photon probe absorption, with photon order (α_{probe}) found to be 1.7. The α_{probe} found for the other fragments investigated, however, lie much lower than the expected 3-photon absorption anticipated for their given expected appearance energies (summarised in Table 4.1), with photon-orders ranging between 1.4 ($m/z = 69$) and 2.1 ($m/z = 14$) respectively. This leads to the conclusion that close to $\Delta t = 0$, it is highly likely that cation dynamics make a strong contribution to the fragmentation signals observed, probed with a low photon order 400 nm pulse.

However, when considering the power dependence studies at more extended timeframes ($\Delta t = 5$ ps), the dynamics observed align much more closely to the 3-photon dependence expected energetically, with all fragments having an α_{probe} value within the range 2.6-3.2. This result is more in keeping with the theory that fragments are produced following predominantly $(1 + 3')$ ionisation of neutral excited states rather than post-ionisation via optically induced electronic transitions within the cation.

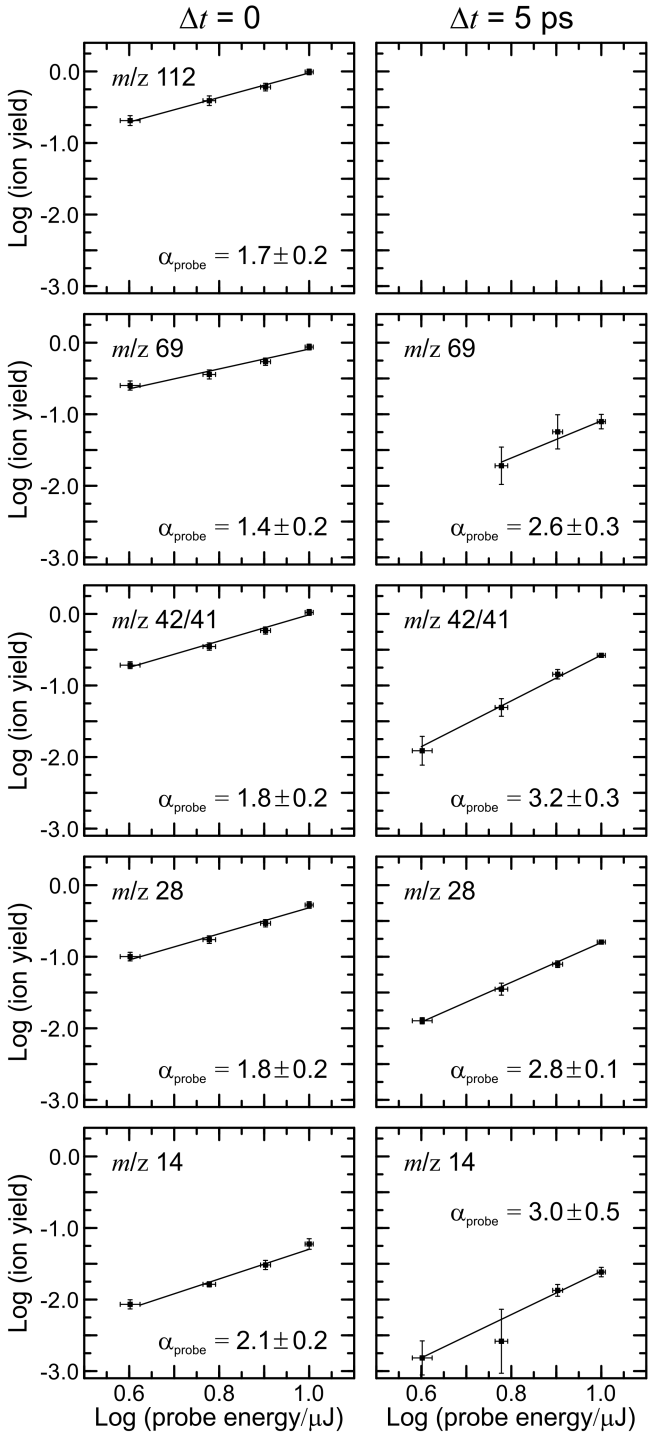

Fig. 4.8: 400 nm probe power dependence plots showing the photon order (α_{probe}) for the uracil parent ion (m/z = 112) and various fragment ions at pump-probe delay times of 0 ps and 5 ps.

Further to this, the long-time dynamics observed in these fragment transients would be consistent with the timescales seen for the uracil triplet manifold in the time-

resolved photoelectron study by Yu *et al.*[360]. Given that the present analysis supports the theory that both neutral and cation excited state dynamics are occurring simultaneously (particularly at $\Delta t = 0$), and it would not be possible to deconvolute the individual components, the fragment transients will not be quantitatively considered further in the current study. It should be also noted that these issues are also expected to be prevalent in the subsequent 200 nm and 220 nm studies presented in Section 4.3.4.

Although the 220 nm and 200 nm pump intensities were significantly reduced relative to the 267 nm study (an order of magnitude lower), only a $(2 + 1')$ photoionisation scheme would be required to induce cation dynamics here and thus would still be prevalent. A summary of the total available energies in 200/220 nm pump - 400 nm probe excitation schemes is presented in Table 4.3.

Ionisation Process	Total Photon Energy (eV)
1×220 nm + 2×400 nm	11.83
1×220 nm + 3×400 nm	14.93
2×220 nm	11.27
3×220 nm	16.91
1×200 nm + 2×400 nm	12.40
1×200 nm + 3×400 nm	15.50
2×200 nm	12.40
3×400 nm	9.30
4×400 nm	12.40

Table 4.3: Summary of the total available energies in a 220/200 nm pump and 400 nm probe experiment.

In a more general sense, utilising greatly reduced pump powers when recording fragment transients (where all pump-alone signal is fully suppressed) opens the possibility to additional quantitative insights into the excited state dynamics operating in the neutral uracil molecule. Conversely, however, this will result in a dramatic reduction in ion counts which would be detrimental to the signal-to-noise ratio achieved.

4.3.4 Parent Ion Transients of Uracil Following 220 nm and 200 nm Excitation

Having successfully demonstrated the thermal stability of molecular samples (Section 4.3.1) and benchmarked the new spectrometer (Section 4.3.2), it is now possible to consider excitation in uracil at shorter wavelengths. As discussed previously in Section 4.1, the formation of photofragments would provide compelling evidence for the existence of an ultrafast ring-opening pathway in uracil. Of particular interest would be the rise of a $m/z = 84$ peak, which has previously been suggested as a by-product of a ring-opening mechanism by Barc *et al.*[358]. In order to investigate this further, a 220/400 nm pump-probe scheme was employed. This wavelength was chosen as Barc *et al.* reported the greatest abundance of this specific fragment at 220 nm using nanosecond (1 + 1) REMPI measurements (the shortest excitation wavelength investigated in that particular work). However, as seen in the transient data presented in Figure 4.9, there is no evidence in the current measurements to support the appearance of any additional photoproducts to those seen in the 267 nm experiments.

As dynamical simulations predicted the nascent formation of photoproducts on the ultrafast timescale (< 1 ps)[349;350], cut-throughs of the transient mass-spectra in the $m/z = 65$ - 90 region at delay times $\Delta t = 0$ and 1 ps are presented in Figure 4.10. This again shows no evidence of an $m/z = 84$ fragment peak.

Although the main fragment peaks that are observed in this study are comparable to those of previous work reported for uracil, higher mass resolution experiments[358;373] reveal that the peaks have a finer substructure which cannot be discerned in this present study. This is a consequence of the phosphor screen decay time (>100 ns), which has a limited resolution for closely spaced features. This concern, however, may be mitigated when one considers that there are no significant ion signals in the $m/z = 80$ - 90 region of the mass spectrum and thus if an $m/z = 84$ peak were present at these excitation energies it should be observable. Furthermore, contrast should not be an issue for $m/z = 84$ detection given that previous power dependence studies have shown that the energetic onset for the formation of this fragment is 11.28 eV[358]. This is the equivalent of absorbing 2 photons of 220 nm, which is well below the total energy supplied from the (1 + 2′) 220 nm pump - 400 nm probe scheme (11.83 eV total energy) employed in the present study. Our present work was further expanded to investigate longer delay times, in order to ascertain if slower processes may be responsible for production of the $m/z = 84$ mass peak. These included extending the pump-probe scan range of the experiment out to 100 ps (the limit of our

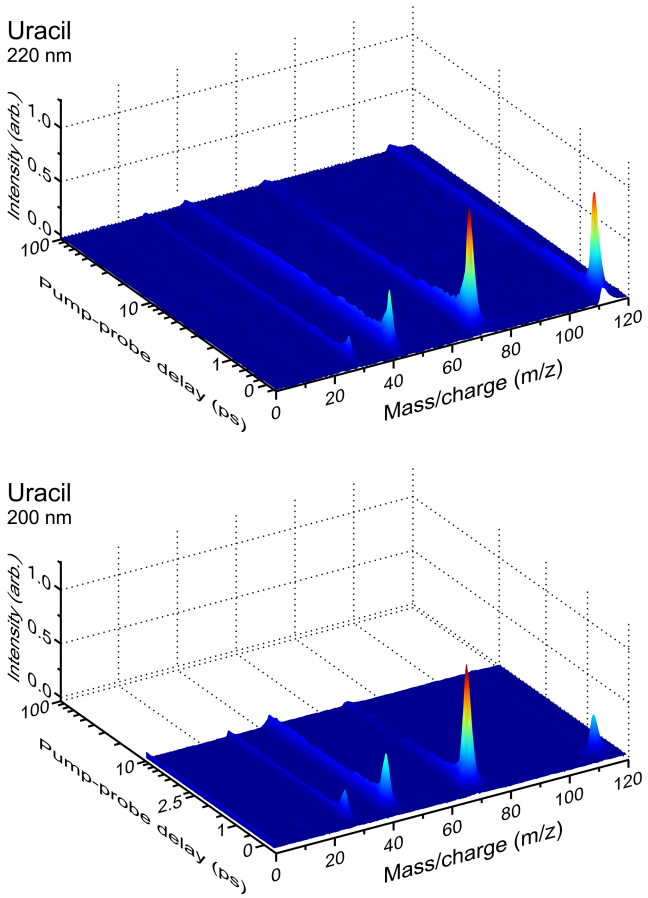

Fig. 4.9: TRIY plots for uracil when excited at 220 nm (top) or 200 nm (bottom) and probed by an intense 400 nm pulse. Data collection runs scanned the translation stage between -330 fs to +1.2 ps in 30 fs steps and +1.2 ps to +100 ps over 59 exponentially increasing increments (220 nm) and between -400 fs to +2450 fs in 30 fs steps and +2450 fs to +10 ps over 59 exponentially increasing increments (200 nm). As was observed with the 267 nm pump, fragment ions display longer lived transient signals than that of the parent ion.

translation stage) and an additional measurement at a fixed pump-probe delay of ∼ 330 ps. These studies, however, still provided no evidence for the formation of any additional photoproducts and, thus, does not support the theory of a ring-opening mechanism in uracil.

Given that the maximum wavelength in the REMPI study of Barc *et al.* was 220 nm and that the $m/z = 84$ fragment had been steadily rising between 232 nm - 220 nm in their work, it was then postulated that the relative size of this fragment signal could possibly increase as the excitation wavelength is further shortened. Moreover, the plausibility of this theory was further supported by considering the vapour-phase absorption spectrum of uracil[399]. A second $\pi\pi^*$ absorption band is present in the

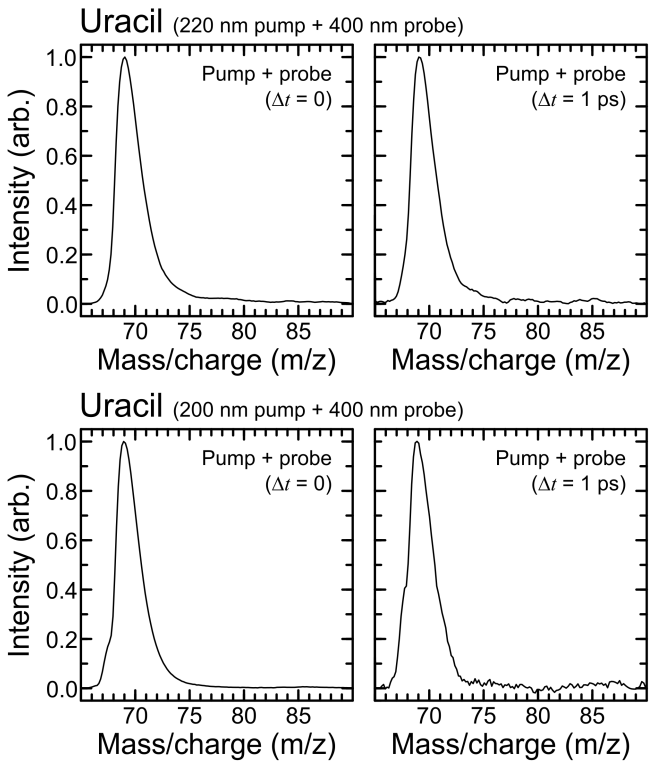

Fig. 4.10: Mass spectra obtained for uracil over the m/z = 65 - 90 mass region at two selected pump-probe delay times (Δt = 0 and 1 ps) following excitation at 220 nm (top) and 200 nm (bottom).

uracil molecule, denoted as $S_3(^1\pi\pi^*)$ for the remainder of this study, which begins to supersede the $S_2(^1\pi\pi^*)$ at $\sim$ 220 nm and peaks at 190 nm. It was therefore speculated as an alternative origin of the m/z = 84 peak. A further TRIY study was therefore performed utilising a pump wavelength of 200 nm and 400 nm probe. Again, however, there was no evidence of any nascent photofragments forming over the 10 ps pump-probe range scanned, as may be seen in both Figure 4.9 and Figure 4.10.

Although a lack of support for an ultrafast ring-opening mechanism in this data is perhaps an unexpected result, there is still significant merit in the analysis of m/z = 112 parent ion transients given that this is the first reported time-resolved experimental study of uracil at excitation wavelengths < 250 nm. A similar fitting model was utilised to that described in Section 4.3.2, however only 2 forward-propagating sequential decays, in addition to the ultrafast backwards component, were required to fit the transients satisfactorily. A small additional constant baseline offset was also included in this model as a result of imperfect pump-alone and probe-alone signal subtraction in this data. The resultant parent transients and fits are presented in Figure 4.11.

In contrast to the extended lifetimes observed in the uracil parent ion when util-

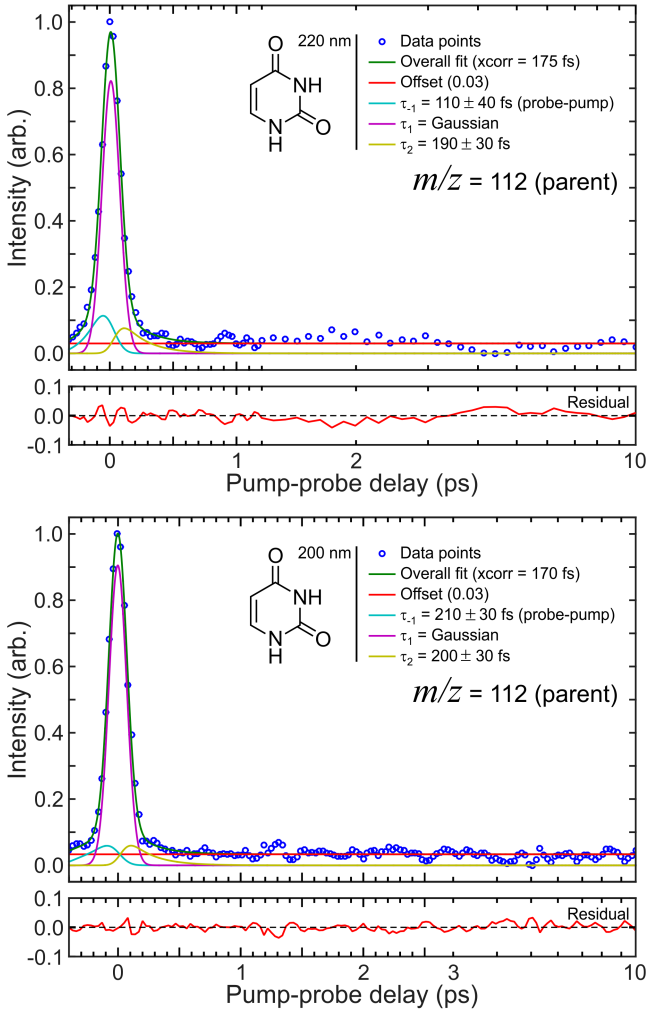

Fig. 4.11: Parent ion transients and fits for uracil following 220/400 nm (top) and 200/400 nm (bottom) pump/probe ionisation on a mixed linear-logarithmic timescale. Also shown are the associated fit residuals (i.e., the overall fit subtracted from the raw data).

ising a 267 nm pump, in the cases of 220 nm and 200 nm excitation the dynamics of uracil appear to occur at a faster rate. In both of these shorter wavelength studies one observes an initial, essentially Gaussian feature (τ_1) prior to a much lower intensity feature of lifetime 190 - 200 fs (τ_2). Relaxation of the excited $S_3(^1\pi\pi^*)$ state, which is known to be optically accessible at both of these wavelengths, has been theoretically suggested to proceed via extremely rapid internal conversion to $S_2(^1\pi\pi^*)$[349]. Subsequent relaxation from the $S_2(^1\pi\pi^*)$ state proceeds via the same mechanism as described in Section 4.3.2, with population transferring to the $S_1(^1n\pi^*)$ state prior to intersystem crossing to the triplet manifold. Utilising a 220 nm pump, it is expected that uracil will have both an $S_2(^1\pi\pi^*)$ and an $S_3(^1\pi\pi^*)$ excited state population, whereas for the case of a 200 nm pump population will almost exclusively be prepared

in $S_3(^1\pi\pi^*)$ state[399]. Observation of the very similar dynamics when using either a 220 nm or 200 nm pump therefore leads to the conclusion that the decay of the $S_3(^1\pi\pi^*)$ is extremely rapid and is not resolvable within the current measurements. Furthermore, it is also concluded that the $S_2(^1\pi\pi^*)$ state is extremely short-lived. It is, however, not possible to determine whether these parent ion transients also provide an insight into the fate of the $S_1(^1n\pi^*)$ state, which is expected to be a significantly faster decay process than the 3.0 ps observed in the 267 nm study.

An alternative consideration is that the measurement may be effectively blind to the $S_1(^1n\pi^*)$ state. The Franck-Condon factors associated with these particular pump and probe energies may be poor and, thus, efficient ionisation of the highly vibrationally excited $S_1(^1n\pi^*)$ state may not be possible. Further to this, following ionisation from highly vibrationally excited $S_1(^1n\pi^*)$ there will be a high propensity for extremely rapid dissociation of the parent ion. It is possible, therefore, that the $\sim$200 fs decay observed in the parent transient data is only a reflection of the $S_2(^1\pi\pi^*)$ lifetime. As previously discussed in Section 4.3.2, due to potential contributions from cation states, it is not possible to glean additional insights into the neutral uracil molecules dynamics through analysis of the fragment ion transients. This is further reinforced through observation of the non-consistent fragment dynamics operating at these wavelengths, as may be seen in Figure 4.9, where it is clear that the $m/z = 69$ channel has a much more rapid decay than those of $m/z = 41/42$ or 28. As such, the data presented here only permits the assignment of an upper bound on the $S_2(^1\pi\pi^*)$ lifetime of $\sim$200 fs.

4.3.5 Nanosecond REMPI Thermal Desorption Studies at 220 nm

Although the dynamical timescales observed in the 267 nm studies presented in Section 4.3.2 have been found to be comparable to those of previous works utilising cold molecular beams, it is possible that thermal influences may still be contributing to the 220/200 nm measurements and could be the reason why no $m/z = 84$ peak is observed in the present data. In order to investigate this postulation further, complimentary nanosceond REMPI measurements were performed by Jana Bockova and Andre Rebelo at the Open University. This investigation used the same instrument employed in the original study by Barc *et al.*[358], however a laser-based thermal desorption source was employed for sample volatilisation rather than the original supersonic molecular beam nozzle. The only difference of note between the thermal sources at Heriot-Watt and the Open University is that the latter set-up did not employ a rotatable foil

mount, thus sample replenishment was more limited in this experimental arrangement. A (1 + 1) REMPI mass-spectra was recorded at the OU utilising 220 nm nanosecond pulses and may be seen in Figure 4.12.

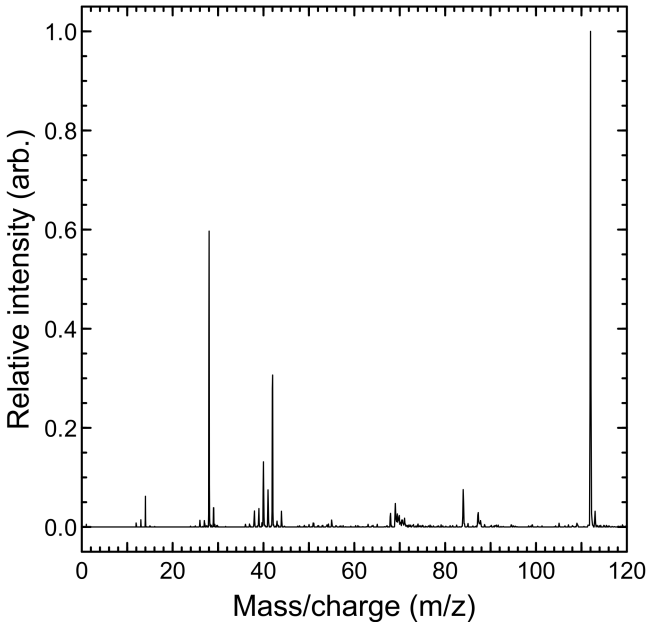

Fig. 4.12: REMPI mass spectrum obtained from uracil utilising a thermal desorption source for volatilisation, recorded using nanosecond 220 nm laser pulses. An m/z = 84 peak is clearly visible, as observed in previous molecular beam experiments[358]. The broad peak centred at m/z = 87.6 and additional tail feature observed on the m/z = 69 peak are signatures of metastable HNCO loss from excited uracil ions.[358].

What is evident in Figure 4.12 is that a prominent peak at $m/z = 84$ is still clearly apparent, which leads to the conclusion that elevated sample temperatures are not responsible for the lack of an $m/z = 84$ mass peak in our TRIY measurements. A further point of note is that the relative fragment intensities observed in this nanosecond study contrasts significantly to that of the previous femtosecond work discussed in this chapter. In particular, when comparing Figure 4.12 and Figure 4.9, it becomes clear that the nanosecond data $m/z = 69$ peak is a much smaller feature than that observed in the femtosecond TRIY measurements. A potential explanation is that the higher total photon energy in the femtosecond experiments (0.56 - 1.13 eV, as seen in Table 4.3) may lead to a higher propensity for fragmentation in the TRIY measurements. However, similar discrepancies arise when utilising photons of identical energy, as is evident through comparison of our 267 nm pump-alone uracil data and the 266 nm REMPI mass spectrum reported by Barc *et al.*[358] and presented in Figure 4.13.

In this nanosecond study, the $m/z = 28$ and 14 channels appear considerably

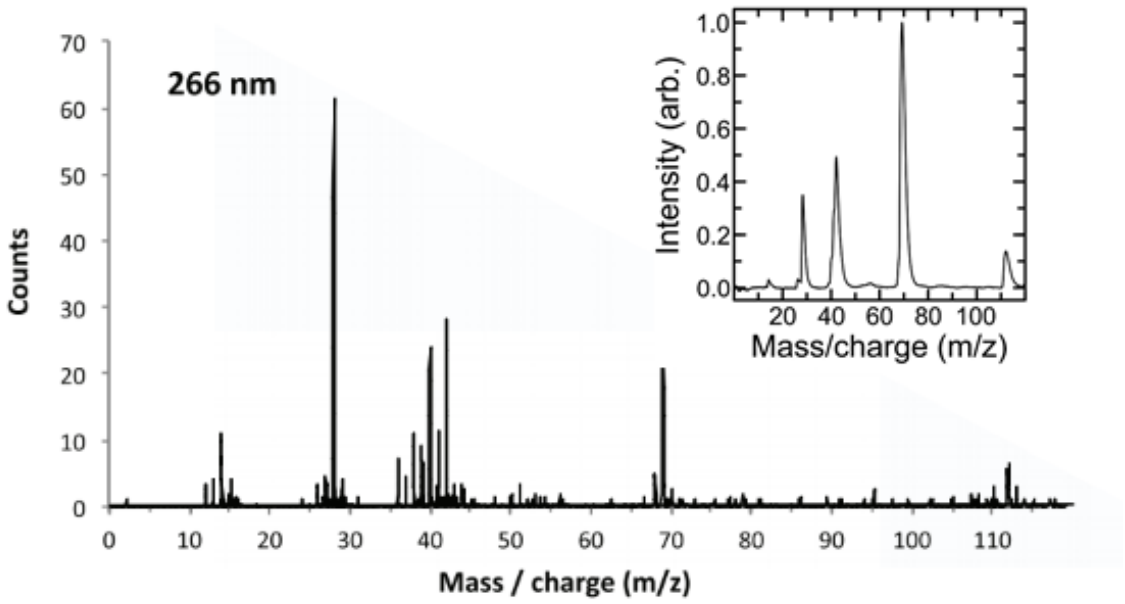

Fig. 4.13: REMPI mass spectrum of uracil recorded using 266 nm nanosecond laser pulses. Plot taken from Barc et al.[358]. Inset shows one colour 267 data from the present study.

enhanced whereas the $m/z = 69$ fragment is somewhat suppressed. Making strong comparisons in terms of total absorbed energy is challenging, however, as both sets of measurements contain different relative combinations of ionisation schemes associated with the various product ions. Furthermore, comparisons between femtosecond and nanosecond ionisation measurements have previously shown significant differences in ion production patterns, with fragmentation less prevalent when utilising femtosecond pulses. One may rationalise this by considering the propensity for ionisation via ladder-climbing or ladder-switching with respect to laser pulse duration[400–404]. In a ladder-climbing mecahanism, photon absorption occurs exclusively in the parent molecule with the formation of all smaller fragment species as a direct or indirect consequence, whilst in a ladder-switching scheme it is also possible for fragment ions to absorb photons, leading to further subsequent dissociation. The propensity for additional photon absorption in fragment ions, as in the ladder-switching mechanism, becomes favoured with longer laser pulses, as fragmentation of the parent ion may then occur within the temporal duration of the laser pulse. Utilisation of a pump-probe scheme, as in that of the TRIY measurements presented in this chapter, effectively enhances the ladder-switching pathway when compared to one-colour femtosecond ionisation measurements. This is because the temporal delay between pump and probe pulses may be longer than the dissociation of the parent molecule and, thus,

increases the likelihood of probe absorption by subsequently produced fragments. Even so, the 100 ps delay range sampled in this present study is extremely small in comparison to the 7 ns pulses utilised in the REMPI experiments of Barc *et al.*[358]. To suggest that the production of $m/z = 84$ mass fragments in the nanosecond study is a direct consequence of a ladder-switching ionisation mechanism, however, is an inadequate conclusion. This is because a minimum of three 220 nm photons would then be required for the production of $m/z = 84$ fragments, whereas previous power dependence studies have shown only two photons are necessary for formation of this fragment[358]. This leads to the suggestion that formation of the $m/z = 84$ species is a result of dynamics operating on a longer timescale in the neutral uracil molecule than those sampled in this present study. Natural candidates for this are long-lived triplet states and/or the highly vibrationally excited S_0 ground state.

4.4 Conclusion

This chapter has presented the first results from the newly designed gas-phase spectrometer, utilising a laser-based thermal desorption source for volatilisation of low-vapor pressure molecular samples. A series of time-resolved ion-yield measurements have been undertaken on the RNA nucleobase uracil, using pump wavelengths of 267 nm, 220 nm and 200 nm and ionising with an intense multiphoton 400 nm probe. Complimentary measurements on the related sulfated species 2-thiouracil are also presented for 267 nm excitation. Dynamical signatures observed in the 267 nm studies of uracil and 2-thiouracil are in good agreement with previous time-resolved studies and thus provide a useful benchmark for the newly commissioned instrument. In addition, ultrafast time-resolved studies of uracil have not previously been reported for excitation wavelengths <250 nm, thus studies at 220 nm and 200 nm provide a valuable new insight into the relaxation mechanism operating in this UV-regime. Extremely rapid relaxation of the $S_3(^1\pi\pi^*)$ state is observed on a timescale of <200 fs. A further point of note is that within the first few hundred picoseconds of pump-probe delay, there is no evidence for the appearance of $m/z = 84$ fragment ions. This leads to the conclusion that the presence of this fragment is not directly linked to theoretically predicted ultrafast ring opening processes at S_2/S_1 or S_1/S_0 conical intersections as previously attributed in nanosecond studies. It does, however, leave open the possibility that the appearance of an $m/z = 84$ peak may be associated with an excited state process operating on a much more extended timescale, an interesting avenue of future investigation.

CHAPTER 5

5,6-Dihydroxyindole:
A Wavelength Dependent Study

With the newly designed time-resolved mass spectrometer and soft thermal desorption source benchmarked using uracil and 2-thiouracil in Chapter 4, Chapter 5 will discuss the energy dissipation signatures of another significant biologically relevant molecule, 5,6-dihydroxyindole. This molecule has not previously been investigated in the gas-phase due to its low vapour pressure. Time-resolved photoion yield measurements have again been utilised to investigate the excited state dynamics of this molecule. Photoexcitation was achieved through employing pump wavelengths across the 241 - 296 nm region and the molecule was ionised using with an intense 800 nm probe. A comparative study with deuterated 5,6-dihydroxyindole at a pump wavelength of 260 nm provides a further valuable insight into the ongoing structure-dynamics-function relationships within this molecule.

5.1 Motivation and Relevant Works

Skin, the largest organ of the human body, serves as our first point of contact with the external environment. Various biological and physical characteristics of the skin dictate its ability to resist repeated exposure to various damaging environmental stimuli, including ultraviolet light. Examples include increasing epidermal thickness, shedding of epidermal squamous layers, programmed cell death of damaged cells, DNA repair activity and, importantly, production of skin pigments[405]. Melanin[406] is an important class of naturally occurring pigments found in the hair, eyes and skin of mammals, in addition to other animals and plants[407]. Melanin has a broad absorption across the UV region[408], however the mechanism by which this occurs is not well known or understood. Furthermore, epidemiological studies have shown that the relative levels of the two main melanin pigments found in skin, pheomelanin and eumelanin, may be significant to UV self-protection. These investigations concluded that people with fairer skin colours, and a higher proportion of pheomelanin, are more prone to tumor formation and UV-induced damage than those of a darker complexion, with greater levels of eumelanin[409]. A full investigation of the UV-dissipation mechanisms of the eumelanin pigments would therefore be desirable, however eumellanin has a large and ill-defined amorphous structure. Using the rationale outlined in Section 4.1 for the case of RNA, deconvolution of the various energy redistribution mechanisms would be complex for a system such as this. Again, a gas-phase bottom-up approach may be employed, investigating one of the UV-chromophores of the eumelanin pigment. This gives a background-free insight into the dynamics of this eumelanin building block, providing key new benchmarks for theory. To this end, eumelanin has two main subunits[410] which could be considered as candidates for such studies, 5,6-dihydroxyindole (5,6-DHI)[411] and 5,6-dihydroxyindole-2-carboxylic acid (5,6-DHICA), with 5,6-DHI chosen for investigation within this present study. The structures of 5,6-DHI and 5,6-DHICA, may be seen in Figure 5.1.

5.1.1 Previous Studies

Eumelanin

The photo-properties of eumelanin have been the subject of numerous spectroscopic studies over the past two decades[412–418], with several investigations showing an interest in the excited state lifetimes of solvated melanin[419–427]. Theoretical investigations into the non-radiative relaxation mechanisms of this melanin, however, have been far more sparse. A recent publication by Marchetti *et al.*[428], provided a first the-

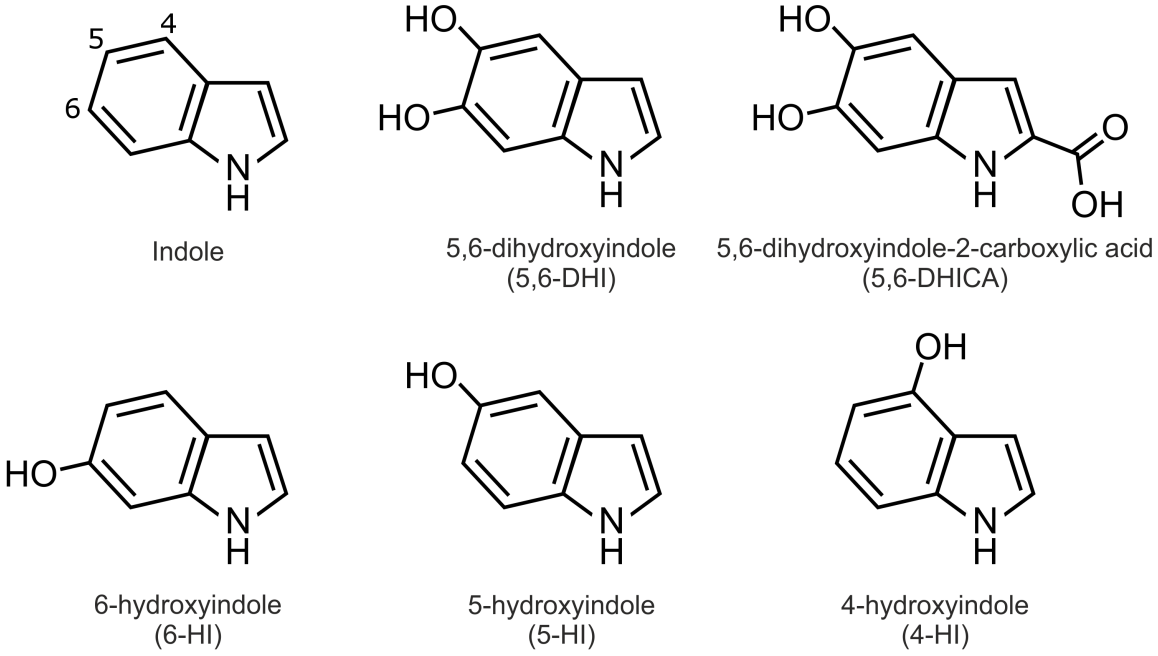

Fig. 5.1: Schematic structures of the eumelanin building blocks 5,6-dihydroxyindole and 5,6-dihydroxyindole-2-carboxylic acid, the mono-hydroxyindoles 4-, 5- and 6-hydroxyindole and the bare UV chromophore indole. For clarity, the 4, 5 and 6 carbon positions are shown on the indole structure.

oretical insight into elucidating these complex dynamics, investigating the relaxation processes in a selection of dimers and trimer combinations made from a combination of eumelanin building blocks. This study concluded the presence of a barrierless ultrafast electron driven proton transfer pathway from the initially excited $S_1(^1\pi\pi^*)$ state to an S_1/S_0 crossing, however further theoretical investigations are required to more fully understand the relaxation schemes in operation.

5,6-dihydroxyindole: Theoretical Investigations

5,6-DHI ($C_8H_7NO_2$) has been the subject of a number of theoretical studies, investigating the molecular structure and photo-properties of the molecular monomer [429–436], and, more recently, an increasing body of work on the oligomer systems [430;434;437–439]. Bolívar-Marinez *et al.* [429] undertook the first *ab initio* and semiempirical calculations of 5,6-DHI. This study revealed the molecule is a good electron acceptor, which is speculated as the basis for a protection mechanism against damage by free radicals, as well as the first simulations of the 5,6-DHI absorption spectrum. Ilichev *et al.* [431] calculated the minimum energy tautomer of the 5,6-DHI system when in the gas-phase and when solvated. All tautomers were found to lie > 1300 cm^{-1} energetically

higher than the ground state geometry. Given that only modest teperature elevation of the sample due to use of a thermal desorption is seen in our present investigation, only the lowest energy tautomer of 5,6-DHI is accessible and present in the sample plume. In addition, vertical excitation energies of various 5,6-DHI tautomers dispersed in vacuum and in solvent were calculated using combined density functional theory (DFT), as well as self-consistent reaction field (SCRF) and conductor-like polarisable continuum model (CPCM) methods. A further publication by Stark *et al.*[430] calculated the bond distances and angles of the minimum energy tautomer, in addition to simulations of the gas-phase absorption spectrum. An investigation by Powell *et al.*[432] used DFT to also calculate the bond lengths and angles of the 5,6-DHI structure. Additional findings in this study include calculations of the HOMO-LUMO energy difference of 5,6-dihydroxyindole via the ΔSCF method as well as simulations of the infrared and Raman spectra of the the 5,6-DHI redox form from first principles. A further publication by Mandal *et al.*[434] employed equation of motion ionisation potential coupled cluster with single and double excitations (EOM-IP-CCSD) to calculate the vertical and adiabatic ionisation energies of 5,6-DHI (7.31 eV and 7.00 eV respectively).

Of particular interest to the present study of 5,6-dihydroxyindole are a small selection of studies focussed upon the non-adiabatic excited state deactivation routes in the 5,6-DHI molecule. An *ab initio* study on the photochemistry of 5,6-DHI by Sobolewski *et al.*[433] investigated the dynamical behaviour of the molecule following excitation to the first $S_1(^1\pi\pi^*)$ state. These authors proposed a non-adiabatic relaxation route via the $S_2(^1\pi\sigma^*)$ state mediated along the O_5H coordinate. Furthermore, a hydrogen migration is predicted from the O_5H to the neighbouring C_4 atom forming the photoproduct 6-hydroxy-4-dihydro-indol-5-one (HHI). This photoproduct is predicted to absorb strongly in the visible region of the spectrum, transitioning to a $^1\pi\pi^*$ state prior to rapid relaxation to the HHI ground state.

A more recent study employing multireference methods on the deactivation mechanisms operating in 5,6-DHI by Datar *et al.*[435] provides an alternative insight into the molecule's energy dissipation routes. Geometry optimization of the first two excited states S_1 and S_2, conical intersections in the plane of the molecule, and non-radiative decay pathways were calculated using state averaged complete active space self-consistent field (SA-CASSCF) method with explicit use of C_s symmetry. The authors state that following excitation to the $S_1(^1\pi\pi^*)$ state, the molecule undergoes internal conversion to $S_2(^1\pi\sigma^*)$ via a conical intersection. In contrast to the suggestions of Sobolewski *et al.*, however, this publication suggests the $S_2(^1\pi\sigma^*)$ state has a minimum energy geometry rather than a barrierless hydrogen migration from

the O_5H to the neighbouring C_4 atom. Furthermore, energy cuts along the O_5H and NH stretching coordinates showed non-radiative conical intersections accessible along the two possible ($^1\pi\sigma^*$) deactivation routes. Both mechanisms display an energetic barrier for energy dissipation, however this barrier is found to be smaller along the O_5H coordinate (0.3 eV compared to 0.63 eV along the NH coordinate). An additional ring-puckered conical intersection was found for direct deactivation from the $S_1(^1\pi\pi^*)$ state to the S_0 ground state, however a barrier is again present for this energy dissipation mechanism. Deactivation from the second bright $^1\pi\pi^*$ state is also suggested to occur via a barrierless conical intersection to the $S_1(^1\pi\pi^*)$ state. A final conclusion drawn from this study is that the antibonding σ^* orbital, corresponding to the hydrogen-bonded O_6H, was shown to be much higher in energy than the O_5H σ^* orbital. This can be rationalised when one considers the interaction of the σ^* molecular orbital along the O_6H coordinate with the non-bonding orbital on the hydrogen bond acceptor, O_5H coordinate. A sketch of the potential energy cuts taken from this publication may be seen in Figure 5.2.

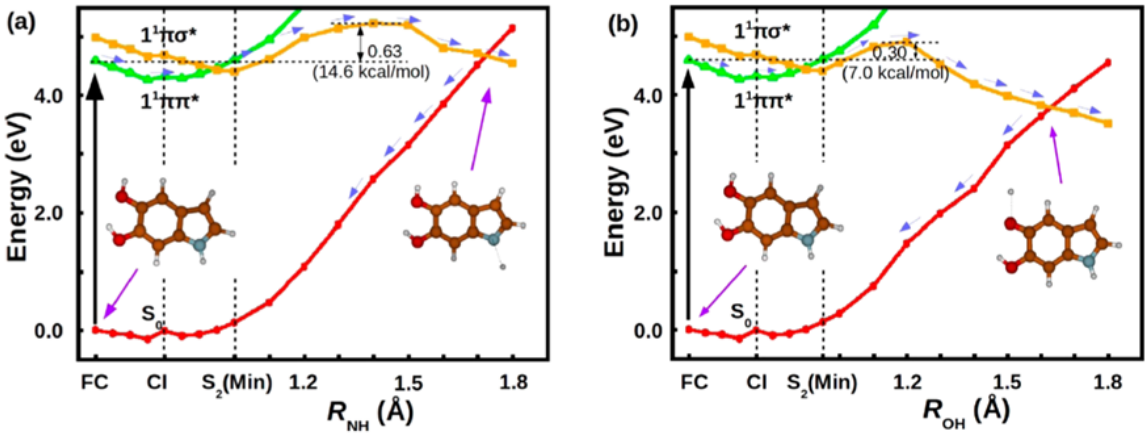

Fig. 5.2: Potential energy cuts along the (a) NH and (b) O_5H coordinates of 5,6-DHI. Inset molecule schematics show the O_6H hydrogen bonded structure of 5,6-DHI. Figure taken from Datar et al.[435]

A final publication considered here is the work of Ghosh *et al.*[436] who employed SA-CASSCF and multistate complete active space second-order perturbation theory (MS-CASPT2) calculations to understand the nonradiative decay pathways in 5,6-DHI. In this study the authors calculated potential energy cuts comparable to Datar *et al.*[435] along the O_5H and NH stretching coordinates of 5,6-DHI, drawing a similar conclusion to the fate of the $S_1(^1\pi\pi^*)$ state. The $S_1(^1\pi\pi^*)$ state was found to nonradiatively decay to the $S_2(^1\pi\sigma^*)$ state via a conical intersection, prior to encountering a further conical intersection with the S_0 ground state. A barrier is again present

between the $S_2(^1\pi\sigma^*)$ state and the S_0 ground state along the O_5H and NH stretching coordinates, with that along O_5H found to be energetically lower. Calculations along the O_6H stretching coordinate yielded no deactivation mechanism for the 5,6-DHI molecule to the S_0 ground state. Furthermore, the authors also investigated the morphology of the potential energy surfaces produced through elongation of the O_5H and NH coordinates. The study analysed the tilt of the cone in the $\vec{g}$ and $\vec{h}$ branching plane between the $S_2(^1\pi\sigma^*)$ state and S_0 ground state for elongation of both the O_5H and NH stretching coordinates. Due to the symmetric nature of the cone in the case of O_5H elongation, it was concluded that there is an equal propensity for non-radiative decay to the ground state and H-atom elimination/radical formation. The cone formed along the NH stretching coordinate was found to be tilted along the $\vec{g}$, corresponding to a higher likelihood of radical 5,6-DHI formation and H elimination, with only a small probability of returning non-radiatively to the ground state minima.

5,6-dihydroxyindole: Experimental Studies

Experimental studies on the excited state lifetime of 5,6-DHI following UV irradiation have thus far been restricted to the liquid phase. These investigations have been performed within the group of Villy Sundström at Lund University, employing both transient absorption and time-resolved fluorescence spectroscopies, respectively. Both of these techniques have been described previously in Section 1.3.1 and Section 1.3.1 and the reader is encouraged to revisit these sections for further information.

Sundström and co-workers[440] undertook transient absorption studies of the 5,6-DHI system. Here, a 267 nm pump and white light probe were employed, monitoring absorption changes over the 440-715 nm region at pH 3 and pH 7. A three-component overall lifetime was observed in both cases, with picosecond time constants of 10 ps and 140 ps at pH 3 and 5 ps and 180 ps at pH 7, respectively, with both displaying a further long-lived non-decaying component. The shortest time constant (5/10 ps) was assigned to vibrational energy redistribution and dissipation to form the equilibrated $S_1(^1\pi\pi^*)$ excited state, whilst the middle time constant (140/180 ps) was attributed to the lifetime of the S_1 state, with sequential population transfer to both the ground state (both radiatively and non-radiatively) and the triplet manifold. The non-decaying component is assigned as a spectral signature of the 5,6-DHI cation, formed through direct photoionisation from the equilibrated S_1 state, with a lifetime far longer than that of the experimentally sampled pump-probe window.

The first time-resolved fluorescence measurements on the 5,6-DHI molecule were performed by Huijser *et al.*[441], with the system dispersed in a 0.02 M pH 7.0 sodium phosphate buffer solution. The data presented utilised pump wavelengths of 266 nm

and 280 nm, with fluorescence emission observed between 320 nm and 460 nm. Results showed two main excited state deactivation routes for 5,6-DHI, dependent upon excitation to the first $S_1(^1\pi\pi^*)$ or second $S_4(^1\pi\pi^*)$ state. Following excitation to $S_4(^1\pi\pi^*)$, an ultrafast electron transfer to the solvent competes with internal conversion to the S_1 state on a sub-picosecond timescale. A 110 ps lifetime observed from the 3.75 eV emission band is attributed to the excited state lifetime of the radical cation formed. Energy redistribution from the $S_1(^1\pi\pi^*)$ takes place on a far more extended timescale of 1.7 ns, with deactivation occurring through internal conversion to the S_0 ground state, fluorescence emission of 3.20 eV or via intersystem crossing to the triplet manifold.

A follow up publication by Corani *et al.*[442] presented the same 266 nm time-resolved fluorescence data as Huijser *et al.*[441], however this work included further measurements of 5,6-DHI in a poly(vinyl alcohol)/sodium phosphate buffer solution. The short time constant was shown to elongate to 130 ps, whilst the long-lived component occurred on the same 1.7 ns timescale. The interpretation of the UV-dissipation mechanisms of 5,6-DHI presented by Corani *et al.*[442] are very similar to that of Huijser *et al.*[441]. Following excitation to the $S_4(^1\pi\pi^*)$ state, internal conversion to the $S_1(^1\pi\pi^*)$ state is expected to occur on a sub-picosecond timescale, with $S_3(^1\pi\sigma^*)$ and $S_2(^1\pi\sigma^*)$ states possibly also implicated in the relaxation route. The middle lifetime (130 ps in sodium phosphate buffer and 110 ps in poly(vinyl alcohol)/sodium phosphate buffer) is again attributed to the lifetime of a radical 5,6-DHI cation following ultrafast electron transfer to the solvent. The 1.7 ns long-lived component is assigned to fluorescence decay of the $S_1(^1\pi\pi^*)$ state.

A final publication from the Sundström group considered here is that of a further time-resolved fluorescence study of 5,6-DHI dispersed in a water/methanol mixture[443]. These measurements employed a 280 nm pump and monitored fluorescence emission at 340 nm. The study found that the excited state lifetime of 5,6-DHI was dependent upon solvent and the lifetime increased from 103 ± 10 ps in aqueous buffer solution to 2.2 ± 0.1 ns in neat methanol. Analysis of the time-resolved fluorescence data in conjunction with quantum-chemical calculations, which included explicit solvent molecules, revealed a proton-coupled electron transfer deactivation pathway. A reorganisation of the solvent molecules facilitates the formation of a solvated electron and subsequently induces a further proton transfer from one of the OH groups to the surrounding solvent, with both OH groups involved in the process. It is further suggested that multiple proton transfers are likely along solvent wires, driven by the electrostatic interaction between the proton and the solvated electron. Lifetimes observed within the time-resolved fluorescence data are attributed to internal conver-

sion to the molecular ground state, with the solvated electron recombining with the deprotonated 5,6-DHI molecule.

5,6-dihydroxyindole-2-carboxylic Acid

The related sub-unit of eumelanin, 5,6-DHICA, has also been the subject of a small number of theoretical and experimental investigations. A theoretical study by Powell[444] provided the first insights into the structure of the 5,6-DHICA molecule using density functional theory. Furthermore, the study provided the first calculations of the seperation between the highest occupied molecular orbital and the lowest unoccupied molecular orbital (HOMO-LUMO) using the difference of self consistant fields (ΔSCF) method for 5,6-DHICA and its oxidised forms. An experimental study by Olsen *et al.*[445] investigated the absorption and fluorescence of the molecular anion (hydrogen eliminated from the O_6H position) in a borax buffer solution, pH = 9.0, and suggest deactivation via a excited-state intramolecular proton transfer. Following excitation to either the S_1 or S_2 states, the mechanism for energy dissipation predicts a non-adiabatic proton transfer between the O_5H hydroxyl group and O_6^- anion position, with radiative decay to the ground state from the S_1 state of this new photoproduct.

Huijser *et al.*[446] performed time-resolved fluorescence studies on 5,6-DHICA dispersed in both acidic (pH = 2.5/3.0) and neutral (pH = 7.0) sodium phosphate buffer solutions. The molecule was excited at 280 nm and fluorescence emission was monitored over the 380 nm - 540 nm region. Under neutral conditions, a 5,6-DHICA anion is formed, with a loss of hydrogen on the carboxylate group. Excitation of the anion leads to dual fluorescence with bands peaking at λ_{max} = 378 nm and 450 nm respectively. The first band (378 nm) is assigned to emission from the excited initial geometry, whilst the second band is attributed to the probable complex formation between the carboxylate anion and a sodium ion of the buffer. In the absence of complex formation, the carboxylate anion solely decays non-radiatively or by emission, with a lifetime of about 2.1 ns, whilst in the presence of buffer ions lifetimes of 1.1 ns and 2.4 ns are observed for the two bands respectively. The situation is quite different when utilising an acidic buffer solution as the 5,6-DHICA molecule if fully hydrogenated. Similar 1.1 ns and 2.4 ns lifetimes are again observed under acidic conditions, however the second band is red-shifted to 427 nm. In addition to this, the 427 nm emission displays a 240 ps lifetime, attributed to zwitterionic species formation following rapid excited-state intramolecular proton transfer from the COOH group toward the NH group.

A follow-up publication by Corani *et al.*[447] utilising fluorescence up-conversion

provided an extension to the findings of Huijser *et al.*[446]. Here the authors state that the mechanism for relaxation of the 5,6-DHICA anion in neutral buffer solution (pH = 7) is a consequence of a excited-state intramolecular proton transfer to form the 5,6-DHICA double-anion on a timescale of 2.5 ns, with a proton lost at the O_6H position. Relaxation from the S_1 state of the double-anion to its ground state occurs of a timescale of 2.4 ps, prior to reprotonation to form the 5,6-DHICA mono-anion. Furthermore, this publication states that excited-state intramolecular proton transfer under acidic conditions then occurs in 300 fs. A further conclusion drawn from this publication is that the proton transfer mechanism is solvent dependent, with studies in methanol inhibiting this relaxation pathway.

A final publication by Corani *et al.*[448] provides an additional insight into not only the excited state lifetime of the 5,6-DHICA molecule, but also a number of its dimers and trimers. Fluorescence up-conversion and streak camera studies following 267 nm excitation found that dimers and trimers of the 5,6-DHICA molecule showed a far more rapid excited state lifetime. Under neutral conditions, pH = 7, the dimer lifetime was found to be 300 fs in comparison to the 1.6 ns of the monomer. When in a more acidic solution, the lifetime reduction is more modest, with the dimer and momomer having having 190 fs and 300 fs lifetimes respectively. This rate increase is attributed to the increased proton accepting capacity of the several OH-groups of a 5,6-DHICA oligomer, with the O_5H and O_6H positions seen to be key to the proton transfer process. Again, these dynamics are shown to be solvent dependent however, with monomer and dimer samples in methanol showing more extended lifetimes.

Mono-Hydroxyindoles

A further set of molecules one may use to compare with 5,6-DHI are the monohydroxyindoles, 4-, 5- and 6-hydroxyindole, the structures of which may be seen in Figure 5.1. By far the most prevalently studied of the three molecules is 5-hydroxyindole (5-HI), a key analogue to 5,6-DHI.

Theoretical studies by Catalán *et al.*[449] and Robinson *et al.*[450] discovered that the two lowest lying optically excited states of 5-HI are the $S_1(^1\pi\pi^*)$ state and the $S_4(^1\pi\pi^*)$ state.

Experimentally, Oeltermann *et al.*[451] performed a rotationally resolved electronic spectroscopy study on gas-phase 5-HI, where it was possible to assign the band origins to the molecule to the syn- and anti-conformers. Studies of the H-atom photofragment distributions of 4- and 5-HI where investigated by Oliver *et al.*[452], employing excitation wavelengths between 303.9 nm and 193.3 nm. In the case of 4-hydroxyindole, it was found that high kinetic energy H atoms were produced at all

excitation wavelengths studied, formed predominantly from O-H bond fission. 5-HI displayed a markedly different behaviour, with a wavelength-dependent H-atom photofragment production. High kinetic energy H atoms were produced at excitation wavelengths below 255 nm, originating predominantly from N-H bond fission, with only a small contribution from O-H dissociation becoming apparent at wavelengths shorter than 235 nm. Employing wavelengths longer that 255 nm resulted in the production of only low kinetic energy H atom fragments. Fluorescence lifetime investigations of the mono-hydroxyindoles in a helium jet have also been reported, with 4-hydroxyindole[453] displaying a far shorter lifetime (0.2 ± 0.05 ns), to that of 5-[454] and 6-hydroxyindole[455] (11.1 ± 0.1 ns and 2.8 ± 0.2 ns respectively)[456].

A final investigation to discuss with regard to the 5-HI molecule is that of a time-resolved photoelectron study by Livingstone *et al.*[6], a publication produced within the Townsend group. Employing excitation wavelengths of 249 nm and 273 nm and probing with a 320 nm pulse, it was concluded that the molecule exhibited a lifetime which may be modelled by three components. An ultrafast lifetime, $\tau_1 = < 100$ fs, was attributed to the decay of the initially prepared $S_4(^1\pi\pi^*)$ state via either the $S_1(^1\pi\pi^*)$ or $S_2(^1\pi\sigma^*)$ state. The lifetimes of the second and third time constants, $\tau_2 = 0.8$ ps/1.4 ps and $\tau_3 = \infty$ (defined as > 1 ns in the study), are assigned to the decay of the $S_2(^1\pi\sigma^*)$ and $S_1(^1\pi\pi^*)$ states respectively. Here, the authors agree with Oliver *et al.*[452] and state that excess energy is mainly dissipated along the NH coordinate. The OH bond is considered to act as a spectator in this study, supported by complementary measurements on indole at the same experimental wavelengths displaying extremely similar dynamics.

5.1.2 Experimental Outline

As is evident from each of the discussed studies, the environment in which the 5,6-DHI molecules are dispersed plays a key role in the excited state deactivation pathways. Using the rationale outlined in Section 4.1, it would be of interest to understand the excess energy dissipation mechanisms of the bare molecule, free from perturbations induced by the surrounding solvent molecules, providing new benchmarks for theoretical study.

The results discussed within this chapter present the first gas-phase spectroscopic investigation of the 5,6-DHI monomer molecule. Previous detection of 5,6-DHI in the gas-phase has been limited to oligomer ions, consisting of dimers or larger, following MALDI investigations of synthetic melanins[457;458], dihydroxyphenylalanine and dopamine[459], tyrosine[460] or 5,6-DHI following autoxidation in acetone[461]. A

key reason for the lack of gas-phase spectroscopic studies on this molecule is due to its extremely low vapour pressure, further showing the importance of our soft laser desorption technique for sample volatilisation. Pump wavelengths across the 241 - 296 nm region have been employed in conjunction with an intense 800 nm probe to investigate the UV-redistribution mechanisms of the 5,6-DHI monomer via time-resolved photoion yield measurements. A comparative study with deuterated 5,6-DHI at a pump wavelength of 260 nm provides a further valuable insight into the ongoing structure-function-dynamic relationship ongoing within this molecules.

5.2 Experimental Set-up

Similarly to the preceding chapter, descriptions of the equipment utilised for data acquisition and codes developed for data collection and analysis have been extensively described previously in Chapter 2 and Chapter 3. For further information on the experiment in this regard, the reader is encouraged to revisit these sections.

5,6-DHI samples were synthesised by Thomas Cowie, within the research group of Dr Magnus Bebbington, at Heriot-Watt University. Samples were produced employing the synthesis scheme developed by Novellino *et al.*[462;463]. Deuterated samples were synthesised by dissolving 5,6-DHI in deuterated water, boiling for 3 - 4 hours and recrystallising. The resultant deuterated samples were found to show 90 % deuterium substitution at the O_5D and O_6D positions. 4-HI (99% purity), 5-HI (97% purity), 6-HI (>99% purity) and indole (99% purity) samples were purchased from Sigma-Aldrich and were used without further purification in preliminary UV absorption spectra experiments.

Samples were deposited onto a 10 μm thick 316 stainless steel foil in the same manner as described in Section 4.2 previously. The molecular plume was produced employing a desorption laser power typically of ~150 mW, which relates to an estimated foil temperature on the order of 370 ± 30 K. This is deduced from our previous foil temperature studies on uracil in Section 4.3.1, with Figure 4.3 showing this desorption laser/ temperature relationship.

Generation of the pump wavelengths employed in these experiments (241 nm - 296 nm) have previously been described at length in Section 2.2.5, with Table 2.2 and Table 2.1 providing an overview of the generation schemes. In brief, either the signal or idler output of an OPA-800C (depending on the particular pump wavelength generated) was sum-frequency mixed with a portion of the 800 nm output from the regeneratively amplified Ti-sapphire laser system. The output of this generation process was then frequency doubled in order to produce pulses of the required pump wavelength. Pump powers used in experiments were dependent upon wavelength generation efficiency, with powers ranging 0.2 μJ/pulse - 1 μJ/pulse typical. Systems were ionised with an 800 nm probe of either 130 μJ/pulse or 220 μJ/pulse, with similar dynamics detected in both instances when compared at the same pump wavelengths. Pump and probe beams were individually focussed into the spectrometer through use of 63 cm and 50 cm focal length lenses respectively.

1,3-butadiene was backfilled into the interaction region in order to perform cross-correlation measurements, provide time-of-flight callibration and also to determine the experimental time-zero positions prior to starting experiments. Although 1,3-

butadiene has a higher ionisation potential (9.082 ± 0.004 eV)[464] and thus a different ionisation photon order ($1 + 3'$ or $1 + 4'$ depending on wavelength) than 5,6-DHI (predicted 7.31 eV vertical and 7.00 eV adiabatic ionisation potentials[434] and photon order $1 + 2'$ respectively), utilisation of this molecule for cross-correlation purposes is still valid. The cross-correlations are temporally limited by the broader UV excitation pulses employed in these experiments rather than the much shorter ionisation pulse. The 800 nm ionisation pulse was found to be temporally short from autocorrelation measurements ($\approx$ 70 fs), thus the absorption of 1 - 2 additional photons will have only a minimal effect on the Gaussian instrument response function. Numerical cross-correlation values obtained were dependent upon wavelength and generation scheme, but were found to lie between 90 fs - 160 fs for the 241 nm - 296 nm range investigated, with a summary provided in Table 5.1 below.

λ_{pump} (nm)	Energy (eV)	Power (μJ/pulse)	XCorr (fs)
241	5.15	0.3	120
250	4.97	0.4	130
260	4.78	0.5	150
*260**	*4.78*	*0.5*	*160*
267	4.65	1.0	135
273	4.54	0.4	125
278	4.47	0.8	160
282	4.40	0.8	110
287	4.32	0.8	110
292	4.26	0.4	125
296	4.20	0.2	90

*Table 5.1: Pump powers and cross-correlation measurements for each 5,6-dihydroxyindole excitation wavelength. Cross-correlations were performed on 1,3-butadiene in conjunction with an 800 nm probe. Associated errors in power and cross-correlation values are $\pm$ 0.1 μJ/pulse and $\pm$ 10 fs respectively. *Experiments performed on deuterated 5,6-dihydroxyindole.*

5.3 Results and Discussion

The proceeding section will present the main results and findings from our dynamical study of 5,6-DHI. Section 5.3.1 will examine preliminary UV absorption specta of the 5,6,-DHI molecule, in addition to the mono-hydroxyindoles 4-, 5- and 6-HI, as well as the hydroxyl-free indole chromophore. These spectra were collected by Dr James Thompson. A discussion of the time-resolved mass spectra and assignment of 5,6-DHI fragment species will be presented in Section 5.3.2, whilst an analysis of the excited state parent lifetimes and assignment of their origins will be discussed in Section 5.3.3.

5.3.1 UV Absorption Spectra

The first data sets to be considered here are UV absorption spectra collected for 5,6-DHI, the mono-hydroxyindoles 4-, 5- and 6-hydroxyindole and the hydroxyl-free UV-chromophore indole. Spectra were recorded for all molecules using a commercial bench-top UV/visible spectrophotometer (Shimadzu UV-2550, 0.2 nm scan interval/1 mm slit width) over the wavelength range 225 nm - 325 nm. Due to the relatively low vapor pressures of some of these molecules, in particular 5,6-DHI which has a predicted vapor pressure on the order of 10^{-6} - 10^{-7} mmHg at 25 °C[465], all samples were dispersed in cyclohexane. Cyclohexane is an ideal solvent for this application as it is very non-polar, thus will have minimal interaction with the dispersed molecules and the obtained spectra should be analagous to vapor-phase results. Furthermore, cyclohexane has minimal UV absorption at wavelengths greater than 195 nm[466] and will therefore not show absorption over the sampled wavelength range (225 nm - 325 nm). The collected spectra may be seen in Figure 5.3.

The first point of note from observing these spectra is that indole and 5-HI are very similar to previous vapor-phase spectra reported by Livingstone *et al.*[6]. This provides support to the notion that use of cyclohexane as a solvent results in minimal perturbation to absorption data, with the resultant spectra comparable to the vapor-phase equivalent. In addition, by comparison to the UV absorption spectrum of the bare indole chromophore, 4-HI, 5-HI and 6-HI all display red-shifted absorption bands. The introduction of a hydroxyl group at the C_4 position only slightly perturbs the onset of the first absorption band with respect to indole, whereas adding a hydroxyl group to the C_6 position displays a more pronounced red shift in the absorption spectrum. The presence of a hydroxyl group at the C_5 position produces the most pronounced spectral red-shift of the three molecules, in addition to the first absorption band displaying a more diffuse feature than those seen in the other systems.

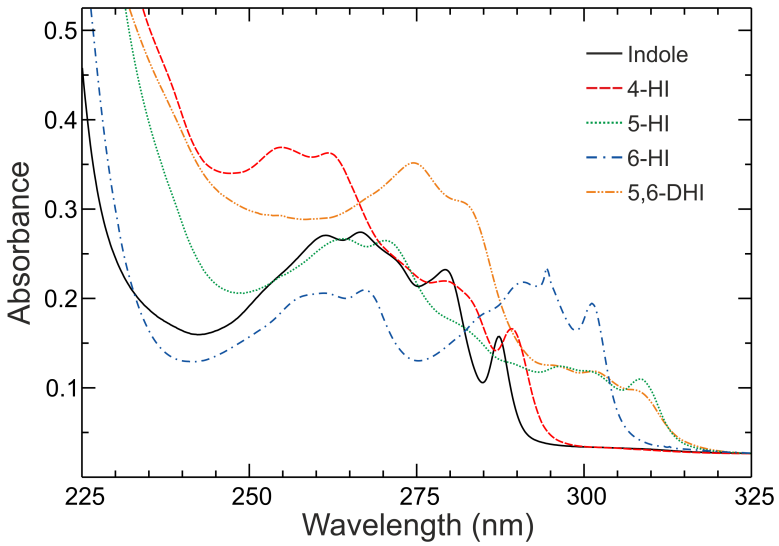

Fig. 5.3: UV absorption spectra of 5,6-dihydroxyindole, the monohydroxyindoles 4-, 5- and 6-hydroxyindole, as well as the UV chromophore indole. Samples dispersed in cyclohexane providing spectra analogous to the gas-phase. Absorption spectra were collected by Dr James Thompson.

A further piece of information gained from the 5,6-DHI UV-absorption spectra is the approximation of the onsets for the first excited states of the molecule. This is an important requirement for the analysis of this data, as the state a molecule is excited to will play a key role in its energy redistribution mechanism. Furthermore, it is noted that the UV absorption spectra for 5,6-DHI shows very similar features to that of 5-HI, thus comparisons between 5-HI and 5,6-DHI at the same pump wavelength are valid. To this end, a similar assignment of the optically bright excited states is made. The absorption onset of the first excited band of 5,6-DHI begins to appear at approximately 310 nm and is attributed to excitation to the $S_1(^1\pi\pi^*)$ state. The second excited band begins to rise at approximately 285 nm and extends to approximately 265 nm. This state is assigned as the second $\pi\pi^*$ state, $S_4(^1\pi\pi^*)$, the next available optically accessible state.

5.3.2 5,6-dihydroxyindole Time-Resolved Photoion Yield Mass Spectra

With the excitation bands of 5,6-DHI having been preliminarily characterised and preliminarily assigned through the UV absorption spectra in Section 5.3.1, it is now possible to investigate the excited state deactivation mechanisms of the molecule following UV excitation. The time-resolved photoion-yield technique was employed to interrogate the energy dissipation schemes of 5,6-DHI, using UV pump excitation

wavelengths between 241 nm and 296 nm and an intense 800 nm ionisation probe. A representative 3D plot of the transient mass-spectra attained for 5,6-DHI employing pump and probe wavelengths of 250 nm and 800 nm respectively may be seen at the top of Figure 5.4.

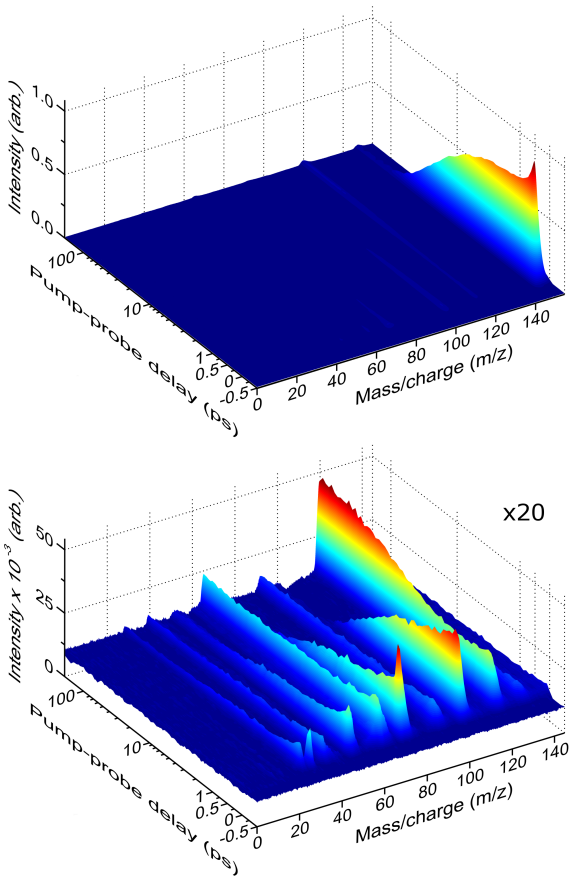

Fig. 5.4: Top: TRIY plots for 5,6-DHI utilising a 250 nm pump and an intense 800 nm probe. Data collection runs scanned the translation stage repeatedly between -600 fs to +1000 fs in 100 fs steps and +1000 fs to +190 ps over 49 exponentially increasing increments. Bottom: ×20 zoomed in view of the 5,6-DHI fragments, displaying various dynamical features.

On first inspection of Figure 5.4, it is clear that there is a prominent parent ion (m/z = 149) and very minimal fragmentation. This same lack of significant fragmentation is seen for all pump photon energies investigated, suggesting that photoionisation is achieved via the same photon-order process for all measurements. If a higher photon-order ionisation scheme were to be required as the pump photon energy is reduced (i.e becomes redder), it would be expected that the relative intensity of the fragments would increase significantly as the total excess energy in the cation is greater. What may be concluded here is that the 5,6-DHI parent ion is produced

via a 1 + 2′ ionisation scheme at all pump wavelengths investigated. This puts an upper limit on the ionisation potential of the molecule to the energetic equivalent of one 296 nm photon (4.189 eV) and two 800 nm photons (1.55 eV), which equates to 7.2 eV - 7.3 eV (within pulse bandwith considerations). This latter finding is in good agreement with previous theoretical calculations of the ionisation potential of 5,6-DHI performed by Mandal *et al.*[434] (predicted 7.31 eV vertical and 7.00 eV adiabatic ionisation potentials).

By zooming in on the mass spectra by a factor of 20, as is the case in the bottom plot of Figure 5.4, it is possible to see a rich variety of dynamics present in the low intensity fragments. The fragments present an array of dynamical signatures, including both ultrafast and extended decays, long-lived components and even a rising feature in the case of $m/z = 120$. Furthermore the observed fragments produced and the relative dynamics appear to be consistent at all wavelengths studied. An additional small Gaussian feature seen at $m/z = 32$ is the dynamic signature of contaminant methanol parent ion signal. Trace amount of methanol were observed as it is utilised when depositing sample onto stainless steel foils in preparation for soft thermal desorption. This, however, is a useful signal as it provides a real-time time-zero lock in the experiment. A summary of the various fragments observed in these experiments and some assignments are presented in Table 5.2.

It is tempting to try to glean additional information relating to the dynamics operating in the neutral excited states of 5,6-DHI using the fragment transients, however much like in the case of uracil and 2-thiouracil in Section 4.3.3 this is not possible. The produced fragments could be the signature of higher-order 1 + 3′ multiphoton ionisation, producing highly internally excited cations which readily fragment, or via the multiphoton ionisation of photofragments, formed following dissociation of the neutral parent species, both of which would be useful signals. Once again, however, the temporal evolution of fragment ions may also reflect independent dynamical processes operating solely in the parent cation, for example in a 2 + 1′ ionisation/excitation process. In this instance, ionisation is achieved solely through two-photon absorption of the pump and dynamics within the cation produced may evolve on a different timescale to that of the neutral species. Absorption of an 800 nm photon probes the dynamical signatures of the photocation, inducing additional prompt fragmentation. As with uracil and 2-thiouracil, it is concluded that within the one-dimensional framework of a time-resolved photoion yield measurement, it is impossible to deconvolve the various unconnected neutral and cation dynamical processes. As such, further analysis of the transient fragment ion data will not be considered further within this present study.

m/z	Molecular Formula
1	H^+
27	??
28	??
32	CH_3OH^+ (Methanol contaminant)
39	??
43	??
51/52	??
65/66	??
75	$C_8H_7NO_2{}^{2+}$
93	??
103	$C_7H_5N^+$
120	$C_7H_6NO^+$
132	$C_8H_6NO^+$

Table 5.2: A tabulation of the various fragment ions produced from 5,6-dihydroxyindole following UV excitation over the 241 nm - 296 nm region and ionisation with an 800 nm probe.

5.3.3 Parent Ion Transients of 5,6-dihydroxyindole

Fitting Model

In order to understand the energy redistribution mechanisms operating in neutral 5,6-DHI, analysis of the molecule's transient nature following photoexcitation and ionisation must be performed. Having established the unreliability in the analysis of fragment ion transients as a reflection of neutral dynamics in Section 5.3.2, temporal fits to the parent ion are the limit to this study. Figure 5.5 presents representative fits to the 5,6-DHI parent ion, utilising pump wavelengths of 292 nm (top) and 250 nm (bottom) in conjunction with an intense 800 nm probe.

A fitting model similar to that of uracil, as described in Section 4.3.2, was required to adequately fit the parent ion transients of 5,6-DHI. Data fitting was performed using the in-house built TOFANALYSE2 code, discussed previously in Section 3.3. The transients required either a one, two or three exponential decay fit (convoluted with the Gaussian instrument response function), which was dependent upon the excitation wavelength employed. Ion transients which required more than one time constant

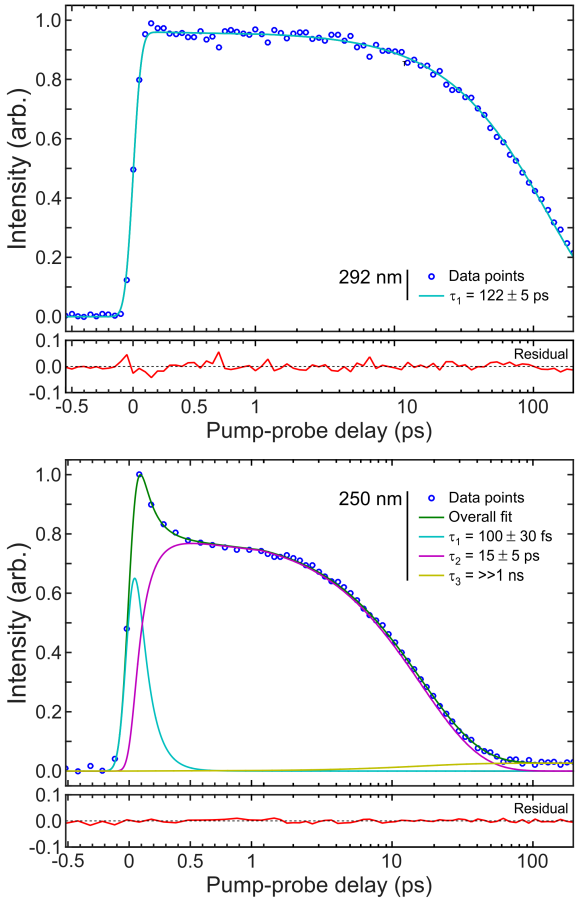

Fig. 5.5: Representative parent ion transients and fits for 5,6-DHI presented on a mixed linear-logarithmic timescale. Also shown are the associated fit residuals. Top: 292/800 nm pump/probe. Bottom: 250/800 nm pump/probe.

were modelled to occur sequentially, whereby the lifetime of the previous exponential decay served as the rise time for the next function as in the form of Equation (3.5) in Section 3.3. In the case of wavelengths $\leq$278 nm, a function containing three exponential lifetimes (τ_1, τ_2 and τ_3 respectively) was required to adequately fit the parent transient. Here τ_1 is considered as a short-time component with numerical values of $\leq$1 ps, τ_2 is a picosecond component with lifetimes ranging tens to hundreds of picoseconds and τ_3 is a long-lived component with lifetimes $>$1 ns. This model considers the molecule to be initially prepared in an excited state (A) prior to geometry relaxation and/or population redistribution to states of lower energy (B-D) via non-radiative decay mechanisms. In the case of a pump wavelength of 282 nm, only a two exponential sequential fit is employed to model the lifetimes of the parent transient (τ_1 and τ_2). This is a result of the signal arising from the middle time constant, τ_2, extending beyond the limit of the sampled pump and probe time window, thus a long-lived component could not be fitted. Although not expressly included in the

fitting procedure, it is assumed that this long-lived component will still exist at pump wavelengths ≥282 nm given its presence at shorter wavelengths. When considering the excited state lifetime of 5,6-DHI following pump excitation of ≥287 nm, only a single time constant was required to model the decay of the parent ion. This lifetime reflects the dynamics of the second time constant, τ_2, with reasons for this presented later in this section. A summary of the fitted time constants at each pump wavelength is shown in Table 5.3.

λ_{pump} (nm)	Energy (eV)	τ_1 (fs)	τ_2 (ps)	τ_3
241	5.15	20 ± 20	10 ± 5	>1 ns
250	4.97	100 ± 30	15 ± 5	>1 ns
260	4.78	200 ± 50	22 ± 5	>1 ns
*260**	*4.78*	*320 ± 100*	*37 ± 5*	*>1 ns*
267	4.65	275 ± 100	30 ± 5	>1 ns
273	4.54	325 ± 100	36 ± 5	>1 ns
278	4.47	600 ± 150	51 ± 5	>1 ns
282	4.40	990 ± 150	73 ± 5	n/a
287	4.32	-	95 ± 5	n/a
292	4.26	-	122 ± 5	n/a
296	4.20	-	132 ± 5	n/a

*Table 5.3: Experimental decay times of 5,6-dihydroxyindole following UV excitation over the 241 nm - 296 nm region and ionisation with an 800 nm probe. Cross-correlations for these decay fits may be seen in Table 5.1. τ_3 lifetimes labelled 'n/a' indicate signals beyond the experimental time window, however are assumed to still be present. *Experiments performed on deuterated 5,6-dihydroxyindole.*

τ_1 Lifetime Assignment

Assignment and understanding the origin of the time constants in Table 5.3 is a non-trivial process with various potential reasons for the observed decay signatures. Considered here first is the decay of the short time component τ_1, with two preliminary suggestions for its dynamical behaviour. One possible origin for the τ_1 lifetime is an intramolecular vibrational energy redistribution (IVR) response to photoexcitation in the $S_1(^1\pi\pi^*)$ state. The molecule may be prepared vibrationally hot following the absorption of a pump photon, with vibrational redistribution of energy the origin of

this short time component. However, this potential assignment is not wholly supported when comparing the onset threshold for τ_1 in Table 5.3, with the UV absorption measurements discussed in Section 5.3.1. Since the origin of the $S_1(^1\pi\pi^*)$ state was found at approximately 310 nm (see Figure 5.3) and the first appearance of the τ_1 time constant occurred with a pump photon of 278 nm, this would suggest that the threshold for IVR would lie >3550 cm^{-1} above the band origin. As a threshold for IVR onset, this value would seem too large[467–469], escpecially for a relatively large molecule with low symmetry such as 5,6-DHI. Therefore, to suggest that τ_1 is a decay signature of IVR would seem unlikely. An alternate possibility is that the decay of τ_1 is a signature of the second $^1\pi\pi^*$ state, $S_4(^1\pi\pi^*)$. This assignment aligns well with interpretations from the UV absorption spectrum, with the origin of the $S_4(^1\pi\pi^*)$ state seen at approximately 285 nm (see Figure 5.3). In addition, it has also been predicted that a barrierless conical intersection exists between the $S_4(^1\pi\pi^*)$ state and the energetically lower $S_1(^1\pi\pi^*)$ state[435], adding further support to this assignment. Given the supporting evidence considered here, it appears that attributing τ_1 to the decay of the $S_4(^1\pi\pi^*)$ - $S_1(^1\pi\pi^*)$ state would appear reasonable.

τ_2 Lifetime Assignment

The logical next step would be to consider the second lifetime, τ_2, as the decay of the first $\pi\pi^*$ state, $S_1(^1\pi\pi^*)$. More detailed analysis, however, reveals that a more subtle picture is required. This time constant does not show a similar lifetime to that seen in indole and 5-HI at similar wavelengths[6], with decay of this state appearing to occur far more rapidly. This suggests that the presence of O_6H in this system opens up new dynamical pathways for energy redistribution, with it possibly more appropriate to draw comparisons to systems such as phenol/catechol[189;470;471] (the structures of which may be seen in Figure 5.7) and the interplay between the two hydroxyl groups. Furthermore, an unexpected relationship is observed in the lifetime of the second time constant when τ_2 is plotted with respect to the pump photon energy, as may be seen in Figure 5.6.

On inspection of Figure 5.6, it becomes apparent that the excited state lifetimes display a non-linear behaviour with respect to the energy of the pump photon. In the case of direct population transfer, a linear relationship might reasonably be expected between excited state lifetimes and pump photon energy. It is not possible to definitively ascertain whether this relationship is a bi-linear or exponential in nature, however speculations as to how it arises may be made. If the relationship is perceived as bi-linear, this would suggest that there is a pump-energy dependent threshold in the energy dissipation within 5,6-DHI at 282 nm. This, however, would suggest that

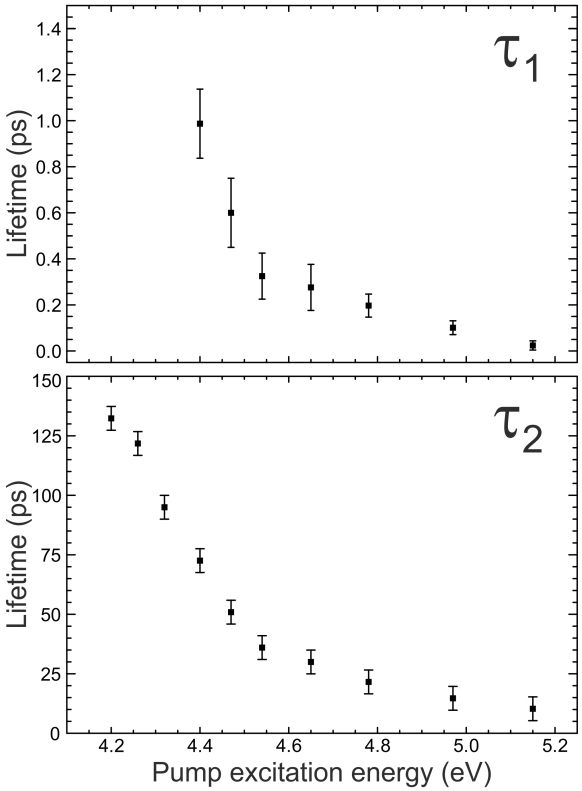

Fig. 5.6: Plots of the τ_1 (top) and τ_2 (bottom) lifetimes of 5,6-DHI fitted for the various pump energies employed.

the molecule can more efficiently redistribute excess energy for pump energies $\leq\sim$ 4.55 eV, with it to be expected that a molecule would more efficiently redistribute excess energy as the pump energy is increased. This behaviour is reflected in Figure 5.6 as at high pump photon energies there is a significantly more shallow gradient than at low pump photon energies. This would therefore suggest that a bi-linear function is not the behaviour observed in this time constant.

If considered as an exponential relationship, a very different conclusion may be drawn as to the origin of τ_2. Drawing on the possible similarities of 5-HI/5,6-DHI to phenol/catechol systems, as mentioned earlier, it is possible that the observed behaviour of τ_2 may reflect H-atom tunnelling through a barrier along the O_5H coordinate. This behaviour has been observed in both the phenol[189;470] and catechol[189;471] systems. Potential energy cuts along the OH coordinate displaying this tunnelling behaviour are presented in Figure 5.7.

On observation of Figure 5.7, it can be seen that there are only minimal perturbations to the shape of the S_1 and S_0 states when comparing phenol and catechol. The major differences in the potential energy cuts relate to the shape of the S_2 state. The reduction in the H-tunnelling barrier height/volume seen in catechol is mainly

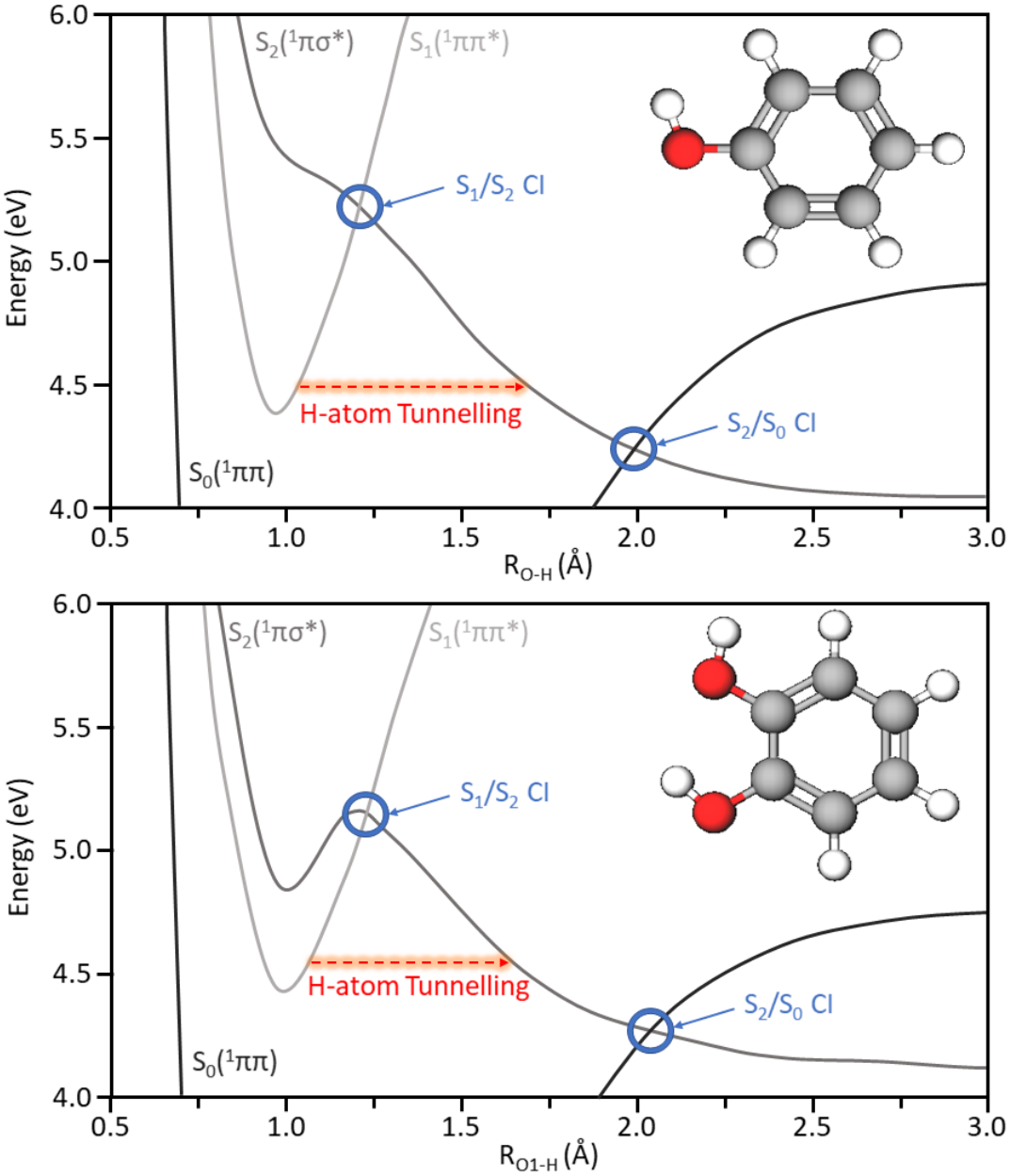

Fig. 5.7: Potential energy cuts along the OH coordinate of phenol (top) and catechol (bottom), displaying a H-atom tunnelling dynamic. Adapted from Roberts et al.[470] and Chatterley et al.[471] respectively.

attributed to the conical intersection crossing point between the S_1 and S_2 states lying energetically lower when compared to phenol. Although the reduction in barrier height may seem modest from Figure 5.7, given the exponential dependence of the H-atom tunnelling rate on barrier height [470], a small reduction leads to a significant increase in the energy dissipation rate. Investigations of phenol and catechol performed at equivalent excitation wavelengths appear to confirm this theory, with

Livingstone *et al.*[189] having studied both molecules with a 267/300 nm pump-probe ionisation scheme. Here the authors found the $S_1(^1\pi\pi^*)$ lifetime of phenol (980 ps) to be significantly more extended than that seen in catechol (12.1 ps), with change in barrier height along the OH coordinate cited as a key reason for this finding. This work, in addition to the study of Chatterley *et al.*[471], concluded that the introduction of the additional hydroxyl group in catechol reduced the barrier for tunnelling along the non-hydrogen bonded OH coordinate, induced by $S_1(^1\pi\pi^*)/S_2(^1\pi\sigma^*)$ state mixing. This consequently gives rise to more efficient energy dissipation in catechol than that seen in the phenol system. This would be a significantly different situation when compared with 5-HI, where both Oliver *et al.*[452] and Livingstone *et al.*[6] concluded that the O_5H coordinate acted as a spectator in energy dissipation schemes. Furthermore, a tunnelling interpretation aligns well with predictions made by Datar *et al.*[435] and Ghosh *et al.*[436] as to the nature of energy dissipation within 5,6-DHI. As discussed in Section 5.1.1, both authors conclude that there is a lower barrier for energy dissipation along the $S_2(^1\pi\sigma^*)$ O_5H coordinate than the NH coordinate, following a barrierless conical intersection connecting the $S_1(^1\pi\pi^*)/S_2(^1\pi\sigma^*)$ states.

Deuterated 5,6-dihydroxyindole Measurement

In order to further investigate whether a phenol/catechol H-atom tunnelling behaviour (mediated by the OH coordinate) is seen in this data rather than behaviour similar to indole/5-HI (mediated by the NH coordinate), a study on deuterated 5,6-DHI was performed. Here, the 5,6-DHI molecule was deuterated at the O_5D and O_6D positions and measurements were taken employing a 260 nm pump. This investigation showed a marked difference in the dynamical time constants when compared to those found for standard 5,6-DHI under the same conditions. Upon deuteration there was a significant increase in the observed excited state lifetimes, with τ_1 increasing from 200 fs to 320 fs and similarly τ_2 extending from 22 ps to 37 ps. From this result it may therefore be concluded that the energy redistribution mechanism in 5,6-DHI relies upon dissipation via interaction of the two OH coordinates. As previously discussed, this is drastically different to the dynamics observed in other indolic systems such as 5-HI, where the OH coordinate was found to act as a spectator with energy redistribution mediated via the NH coordinate.

τ_3 Lifetime Assignment

From our time-resolved photoion yield studies it is not possible to determine the fate of the state associate with the final time constant, τ_3, however speculations may again

be made as to its origin. Following the decay of the $S_1(^1\pi\pi^*)$ state following H-atom barrier tunnelling induced by interaction between $S_1(^1\pi\pi^*)$ and $S_2(^1\pi\sigma^*)$, there are two active routes for energy redistribution. One route is the population of the triplet manifold, indicated as a key dissipation route in the deactivation of indole by Park *et al.*[472]. Alternatively, τ_3 may reflect repopulation of the S_0 ground state, supported by the studies of Datar *et al.*[435] and Ghosh *et al.*[436]. Here both authors performed calculations on 5,6-DHI which showed the presence of an S_2/S_0 barrierless conical intersection, accessible along both the O_5H and NH coordinates. It is postulated, within the bounds of this present study, that the signal arising from τ_3 is a signature of triplet manifold population. This conclusion is drawn as we consider it less likely that two 800 nm photons would probe deep enough into the ionisation continuum to pick-up dynamical signatures from the vibrationally hot S_0 ground state. It is considered more likely the signal will arise from the less vibrationally excited triplet manifold, which should be more easily accessible under the experimental conditions employed. Furthermore, the previous theoretical studies of Datar *et al*[435] and Ghosh *et al.*[436]did not consider the role of triplet states within their calculations, thus further theoretical work is required. Finally, it is also important to note that further dynamical processes will undoubtedly also be operating within this system on similar timescales, however this present measurement is blind to their dynamical fingerprint. Possible further operating mechanisms include H-atom dissociation along the O_5H coordinate, as seen in studies of 5-HI by Oliver *et al.*[452], as well as H-atom migration as theorised by Sobolewski *et al.*[433] for the formation of 6-hydroxy-4-dihydro-indol-5-one.

5.4 Conclusion

This chapter has presented the first ever gas-phase spectroscopic study of the eumelanin sub-unit 5,6-DHI, with sample volatilisation achieved via a laser-based thermal desorption source. A series of time-resolved ion-yield measurements have been undertaken employing pump wavelengths across the 241 nm - 296 nm excitation region and ionisation achieved with an intense multiphoton 800 nm probe. An upper limit on the ionisation threshold of 5,6-DHI is assigned as 7.2 - 7.3 eV, given that the relative intensity of fragment transients are equal at all pump wavelengths investigated and is in good agreement with theoretical predictions. Relaxation of the $S_4(^1\pi\pi^*)$ state to the $S_1(^1\pi\pi^*)$ state is observed at wavelengths $\leq$282 nm on a timescale of $\tau_1 = <1$ ps. Drawing on comparisons with phenol/catechol systems, H-atom barrier tunnelling along the O_5H coordinate following $S_1(^1\pi\pi^*)/S_2(^1\pi\sigma^*)$ state mixing mediates the decay of $S_1(^1\pi\pi^*)$ on a timescale of τ_2 = 10 ps - 132 ps. Complimentary measurements of 5,6-DHI deuterated at the OH positions utilising a 260 nm pump showed a significant elongation of the excited state lifetimes, confirming that the OH coordinates play a key role in the energy dissipation mechanisms in 5,6-DHI. This is in contrast to the related 5-HI system, where the OH coordinate is considered a spectator and the NH coordinate is key to energy redistribution. A final long-lived component $\tau_3 = >1$ ns, is attributed to intersystem crossing and population of the triplet manifold. The results from this study provide a good illustration of how subtle changes to a molecular structure can lead to significant modification of the observed dynamics.

CHAPTER 6

Conclusions and Future Work:

What To Do Now?

As can easily be imagined, when working on a continuous project with various aims there are numerous avenues along which work continues following one's working time frame coming to an end. This section aims to summarise the various partially completed projects and intended future endeavours of the experimental set-up. Furthermore, a final conclusion to the thesis is discussed, providing an overview of the work undertaken.

6.1 Future Work

6.1.1 Characterisation of a Molecular Nozzle

One key aim for further development of the laser desorption source presented in this thesis is the ability to entrain the desorption plume into a molecular beam set-up. The benefits of such a design would include increasing sample density, as molecules would have a more restricted directionality once within the molecular beam. Use of a carrier gas would provide partial molecular cooling through collisions. Initial design ideas considered the use of a modified pulsed valve set-up, similar to that presented in Figure 6.1.

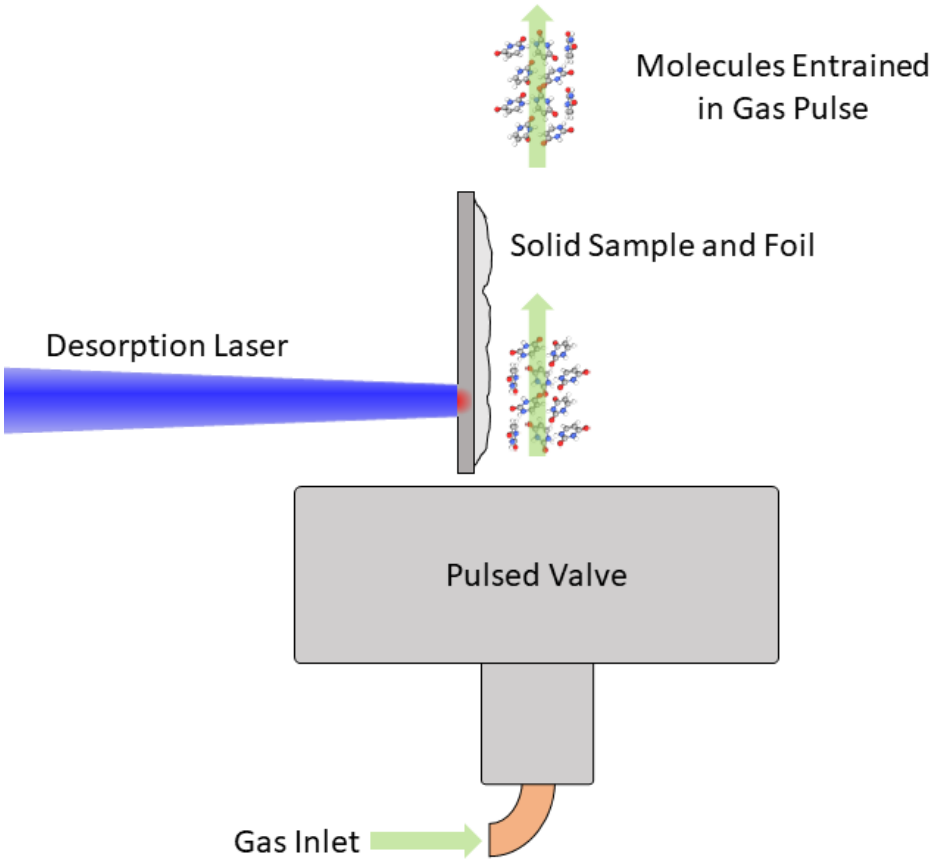

Fig. 6.1: A schematic of a potential laser desorption molecular beam source. The laser desorbed plume interacts with a gas pulse from a pulsed molecular valve creating an entrained sample beam.

Although this set-up would provide the desired molecular cooling, this design is not ideal for this intended application. Such a set-up would not entrain the entire sample plume following laser desorption, lowering potential sample concentration.

Furthermore, due to the low temperature and speed of the desorbed plume, it is believed the molecules may not be able to penetrate into the molecular beam pulse to any great extent. The gas pulse would therefore have poor sample pick-up and thus would not be a successful molecular carrier.

An alternate idea for sample collimation considered the use of aerodynamic lenses[473;474]. A typical aerodynamic lens system consists of three sections: a flow control opening, a series of mass flow lenses, and an accelerating nozzle output. A schematic of an example aerodynamic lens system cut-through may be seen in Figure 6.2.

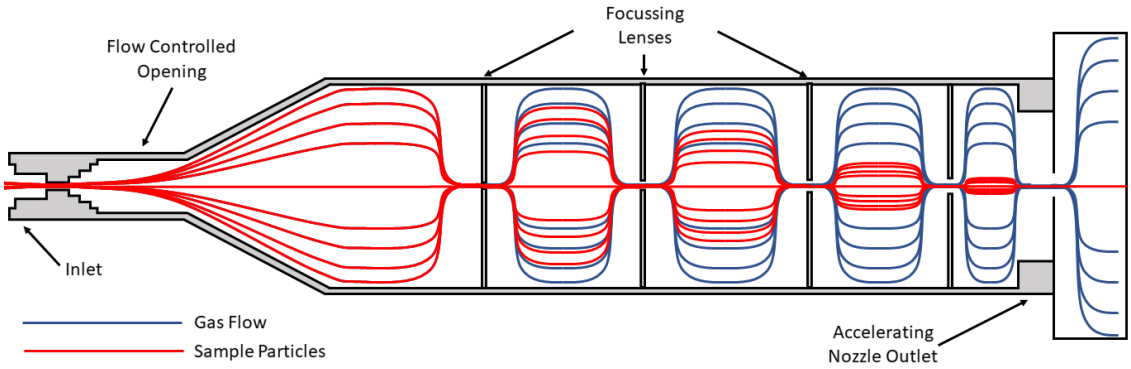

Fig. 6.2: A schematic of an aerodynamic lens system cut-through. Blue lines represent the flow of the carrier gas whereas red lines show the particle trajectories when successfully collimating.

After entering the aerodynamic lens system, the gas streamlines are forced to the axial center at each focussing lens aperture. A gas expansion occurs on the opposite side of the orifice, however inertia maintains the sample particles closer to the centreline axis[475]. The separation between focussing lenses is key to sample collimation, with particles that are too large or too small not effectively aligning. For particles that are above a certain size, their inertia is greater than the drag imparted by the carrier gas and thus do not follow gas streamlines to the central axis. In the case of particles below a critical size limit, focussing is unsuccessful as the particles either diffuse away from the center axis due to Brownian motion or follow the gas streamlines due to a lack of inertia[476].

Aerodynamic lenses are traditionally utilised when focussing particles that are in the nanometre regime, thus to deduce the feasibility of using such a technique for molecular samples an aerodynamic lens calculator[477], designed by Xiaoliang Wang and Peter H. McMurry, was used to investigate ideal focussing conditions. Calculations showed the expected behaviour, with use of multiple focussing lenses resulting in very low transmission rates due to the molecules being too light. The simulation

suggested use of only a single focussing lens would be possible and would still suffer from the loss effects of Brownian motion.

A final design idea considered is similar to that of the focussing nozzle of Piseri *et al.*[478–480], utilised for the production of supersonic cluster beams. The basic principle of this set-up relies upon the fact that a sample is already within a gas pulse before entering the focuser. The focuser consists of a circular disk with eight evenly spaced holes sitting an adjustable distance in front of a smaller exit nozzle. Variation of the disk-nozzle distance allows for mass selectivity along the exit nozzle central axis, due to inertial changes between the gas and particles travelling through two tight bends. A schematic of this design may be seen in Figure 6.3.

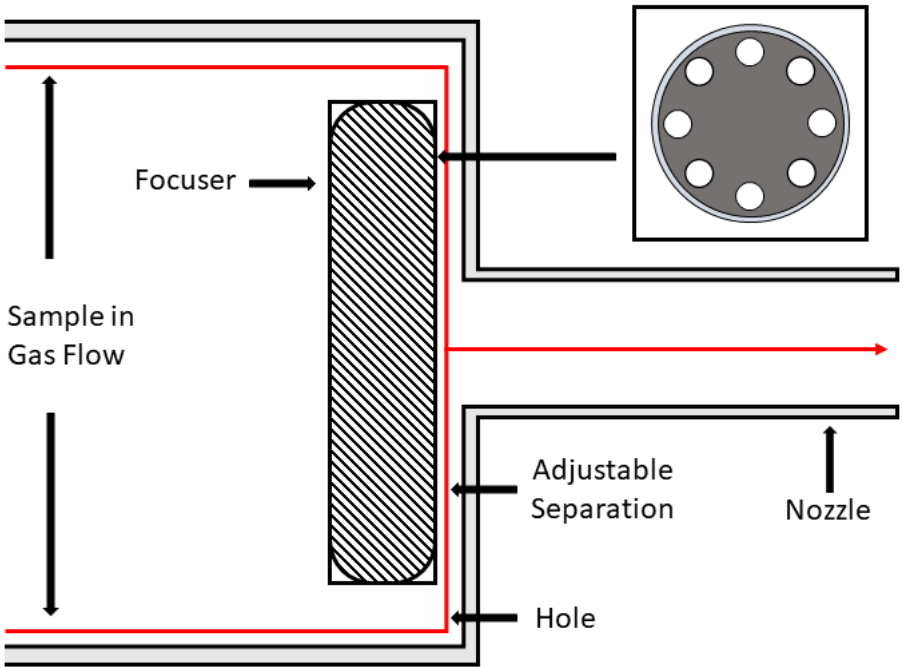

Fig. 6.3: A schematic cut-through of an supersonic cluster beam focuser as designed by Piseri et al.[478]. Mass selectivity is achieved through variation of the focuser position with respect to the nozzle outlet. Inset: Front facing view of the focuser.

Inspiration was taken from these previously described set-ups for a final Heriot-Watt molecular nozzle design which will be implemented and tested in the near future. A molecular nozzle, similar to that of the Piseri *et al.*[478] set-up, has been designed for sample pick-up and cooling in a molecular beam. The focuser is replaced with the laser desorption foil and sample penetration into the gas flow is facilitated through a series of 'saw-teeth' in the region between foil and nozzle. The increased pressure in the 100 μm gaps at the foil surface allow for targeted regions of sample pick-

up. 2D axis-symmetric helium gas velocity and pressure profiles have been simulated for the intended design using the commercial modelling software package COMSOL Multiphysics, the results of which may be seen in Figure 6.4.

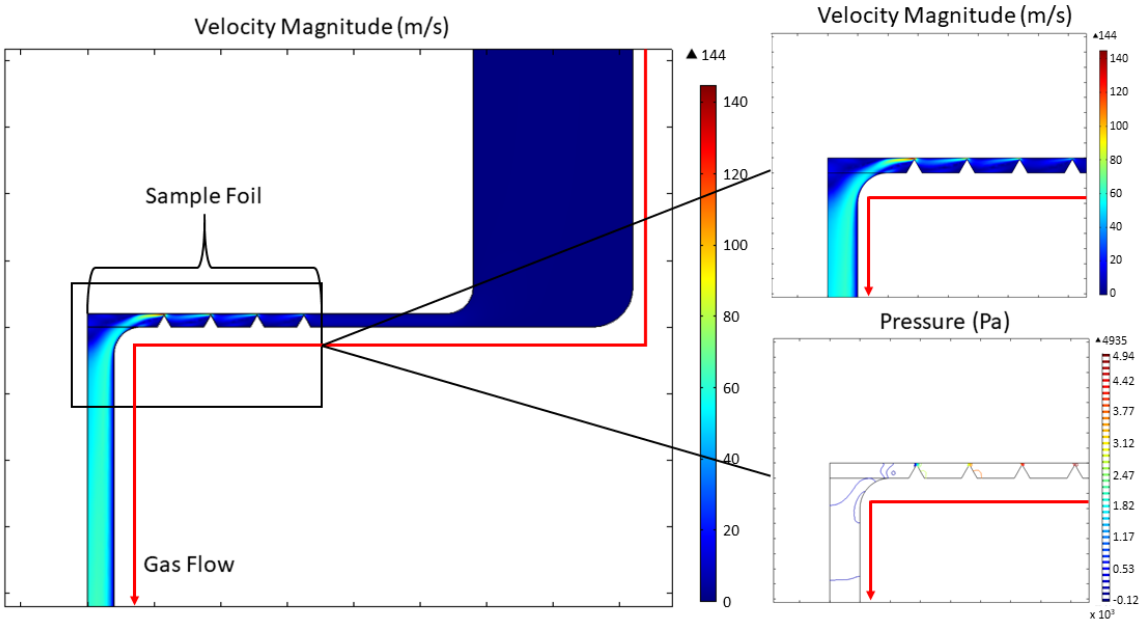

Fig. 6.4: Steady-state 2D axis-symmetric gas velocity and pressure profiles for the intended molecular nozzle design. Initial inlet pressure was set to 5000 Pa and outlet pressure was set as 10^{-3} Pa and helium was the chosen carrier gas simulated.

Here, an input pressure of 5000 Pa was assumed and an outlet pressure of 10^{-3} Pa was chosen. As can be seen from Figure 6.4, the use of the saw-tooth design creates a region of high velocity and pressure at the sample surface which will allow molecules to penetrate into the gas flow. Furthermore, a time-dependent study of the sample pick-up and collimation has been simulated over a 3 ms time-region using the same modelling software. A subset of these results may be seen in Figure 6.5.

The final molecular nozzle design was developed using the AutoCAD software package. This allowed for the construction of each of the individual pieces as a 3D structure, with the ability to export the various components dimensions with ease for design layouts. The nozzle has been designed to sit on a flange within the CF160 cross of the new spectrometer and may be positioned in x, y and z dimensions through use of a series of sliders. Gas flow for molecular pick-up may be achieved either by coupling with an attotech GR001 pulse valve or via a continuous flow. The final nozzle design has also now been constructed by the Heriot-Watt University mechanical engineering workshop. The final AutoCAD design and construction may be seen in Figure 6.6.

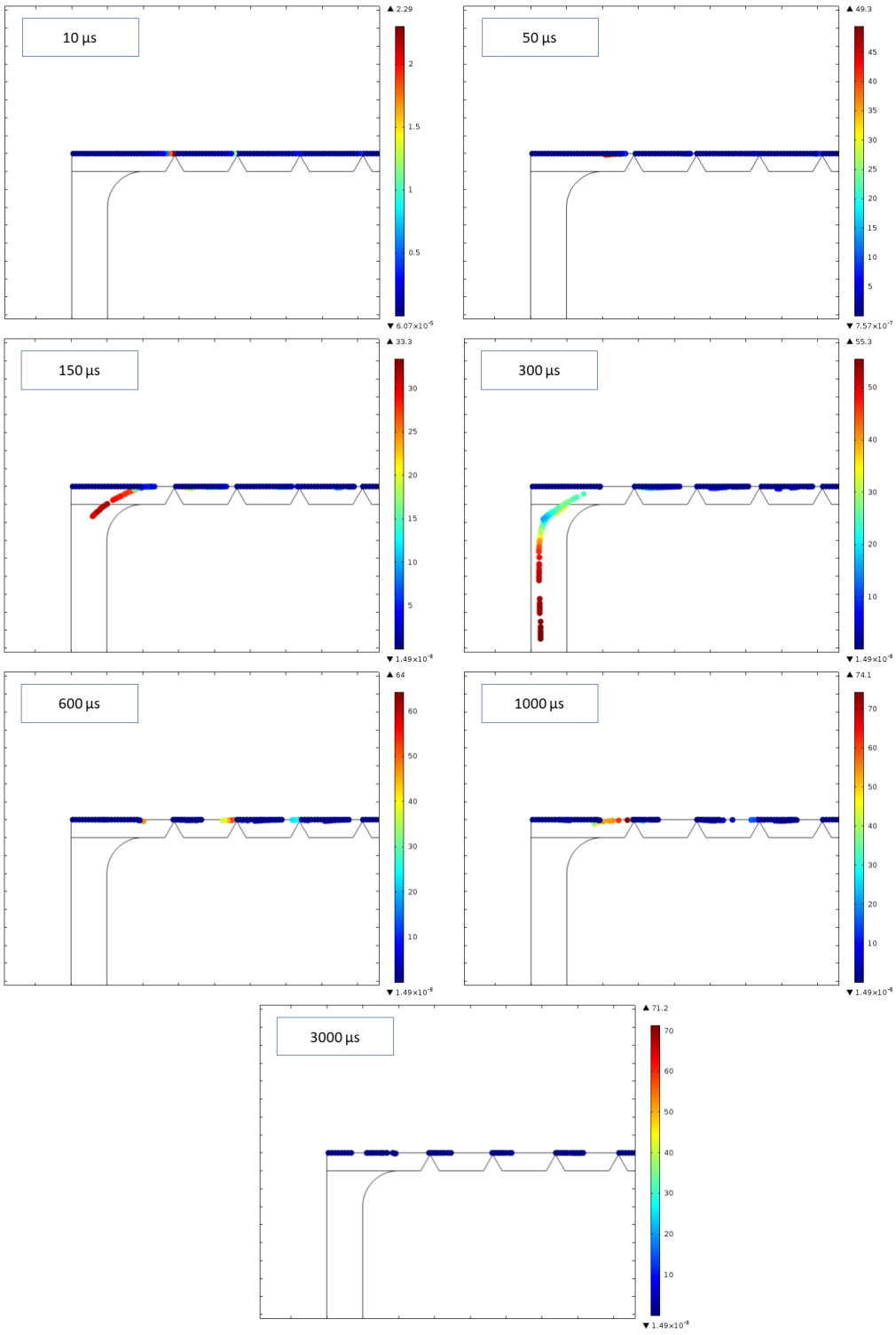

Fig. 6.5: Time-dependent study of the sample pick-up and collimation following laser desorption. A time-range of 3 ms was sampled and particles are born with an initial velocity of 200 ms^{-1} and assumed as 1 nm spheres and density 2200 kgm^{-3}. Pressure conditions are the same as described previously.

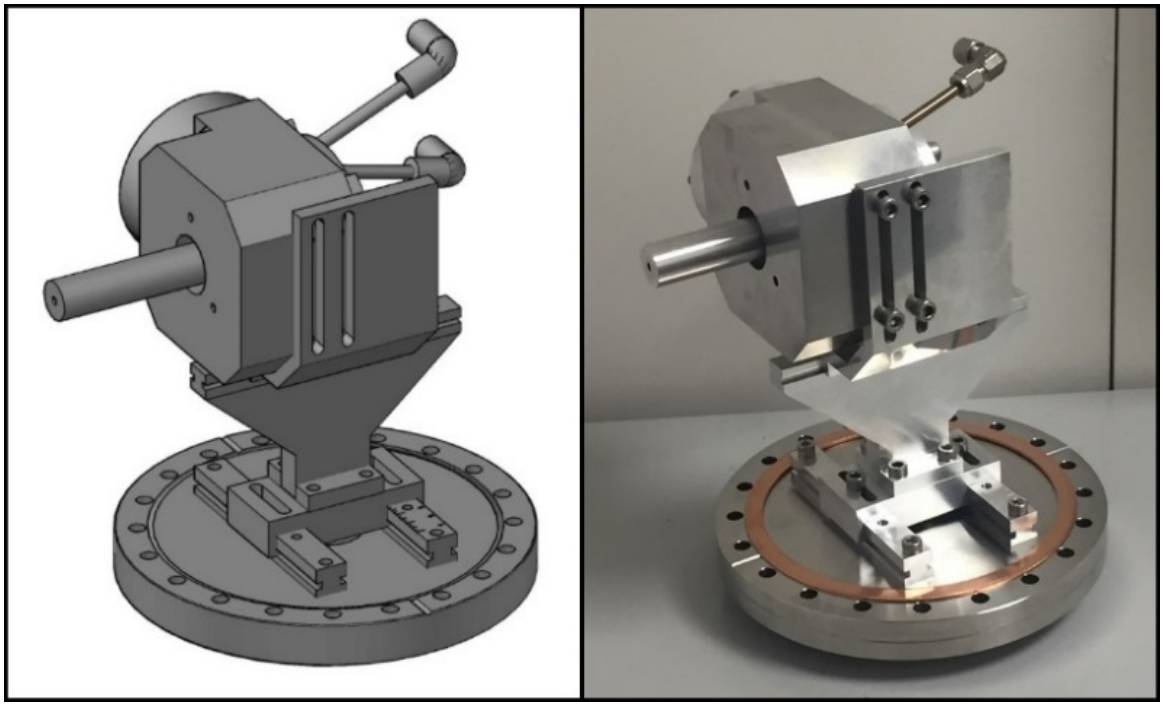

Fig. 6.6: Left: Final AutoCAD design of the molecular nozzle. Right: Constructed molecular nozzle for comparison. Molecular nozzle parts made by Heriot-Watt University mechanical engineering workshop.

An additional z-axis cut-through of the molecular nozzle is provided for clarity of the design in Figure 6.7.

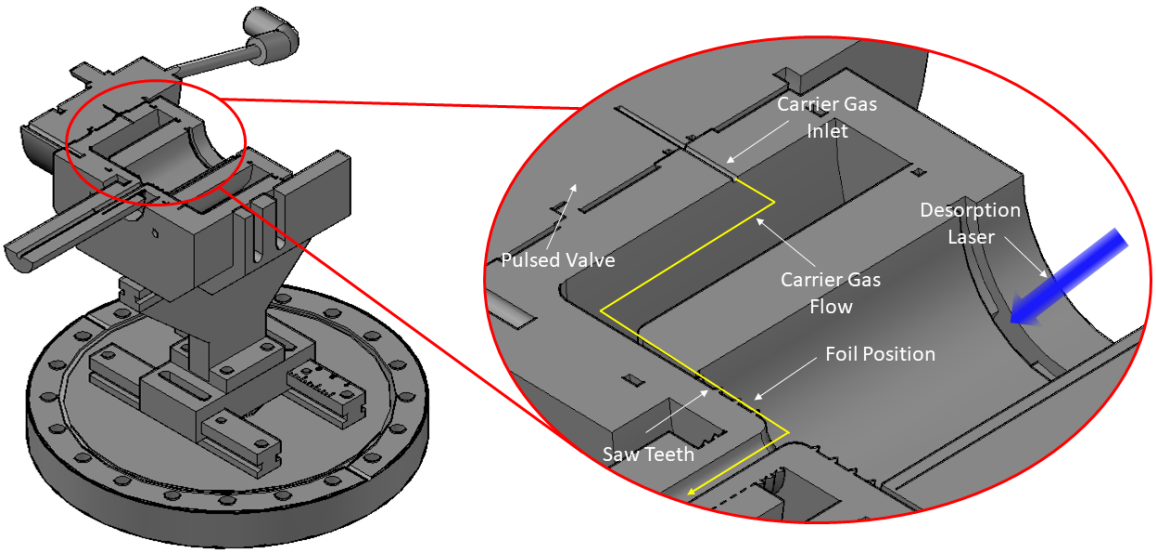

Fig. 6.7: A z-axis cut-through of the molecular nozzle. Inset: An annotated zoomed in view of the foil holding position and gas inlet. Yellow arrow shows carrier gas flow direction. Sample foil not included in image for clarity.

Future work associated with this project initially consists of testing the performance of this molecular nozzle in conjunction with the mass spectrometer utilised for the experiments throughout this thesis. This potential molecular beam source will need to be characterised to ensure an increase in sample density has been achieved at the nozzle outlet and to investigate whether any molecular cooling is exhibited in the desorbed sample.

6.1.2 Velocity Map Imaging Spectroscopy

Velocity map imaging is a powerful spectroscopic acquisition technique which can provide a wealth of dynamical information through both energy- and angle-resolved measurements. An extensive literature review and the benefits of utilising this technique have been discussed previously in Section 1.3.1, and the reader is encouraged to revisit this section for further information to this regard.

As discussed in Section 2.3.3, the ion optics incorporated into the mass spectrometer, utilised for measurements throughout this thesis, have been designed to also perform velocity map imaging. In order to investigate the capabilities of the spectrometer, a series of 267 nm one-colour photoelectron images were collected for the molecules 2-thiouracil, DL-phenylalanine and guanine, utilising the laser desorption source for sample volatilisation. The obtained photoelectron images may be seen in Figure 6.8.

Collection of these photoelectron images is in itself a noteworthy result, with no imaging studies having previously been reported when employing a soft thermal desorption source. Utilisation of this volatilisation method opens up a wealth of new opportunities, with it now possible to produce a gaseous molecular sample of significant density for detailed spectroscopic investigations.

Going forward, there are two exciting potential research avenues considered for future experimental investigations utilising the velocity map imaging technique, time-resolved photoelectron spectroscopy and photoelectron circular dichroism studies, with each discussed in the proceeding subsections.

Time-resolved Photoelectron Spectroscopy

Time-resolved photoelectron spectroscopy [187] is an established technique for the study of molecular dynamics and has been utilised within the Townsend group for the last decade [6;148;189–196]. An extensive description of the technique and the benefits of utilising this differential measurement have been detailed previously in Section 1.3.1 and thus will only be discussed briefly here.

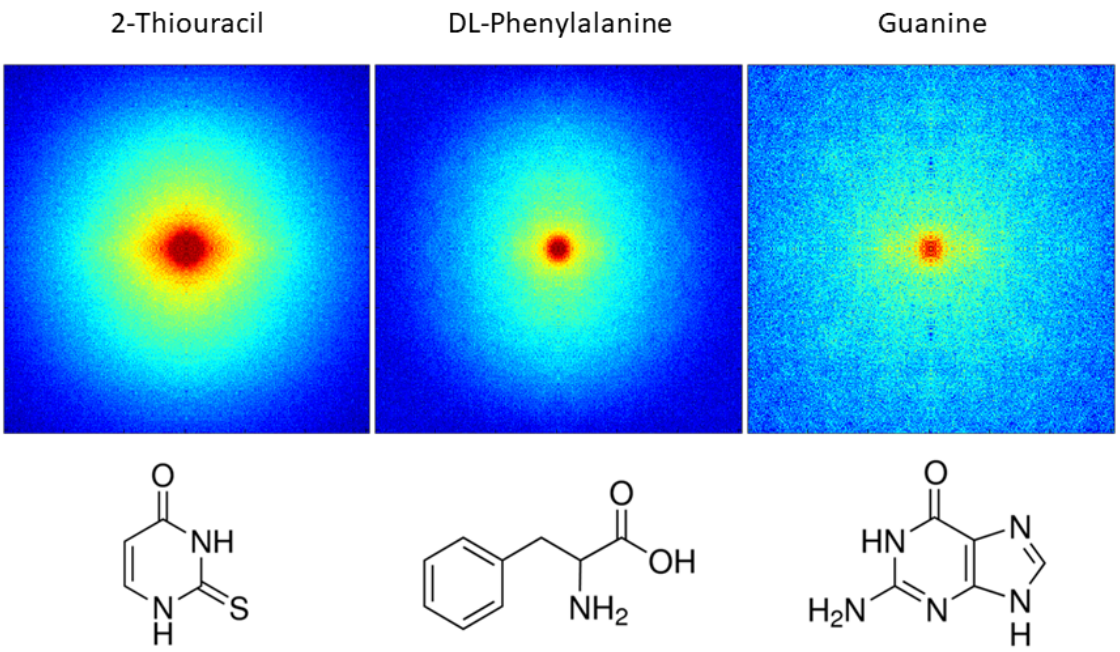

Fig. 6.8: Symmetrised one-colour 267 nm photoelectron images of 2-thiouracil, DL-phenylalanine and guanine obtained using the laser desorption source for sample volatilisation.

The technique itself relies on the use of a pump-probe scheme, in which two laser pulses excite and ionise the molecules of interest respectively, with a controlled time separation, Δt, between the interactions. Photoelectron images are collected as a function of this pump-probe delay, providing time-, energy- and angle-resolved data. An example strip of time-resolved photoelectron images for the molecule N,N-dimethylisopropylamine (DMIPA) following 200 nm excitation and 267 nm ionisation may be seen in Figure 6.9[193].

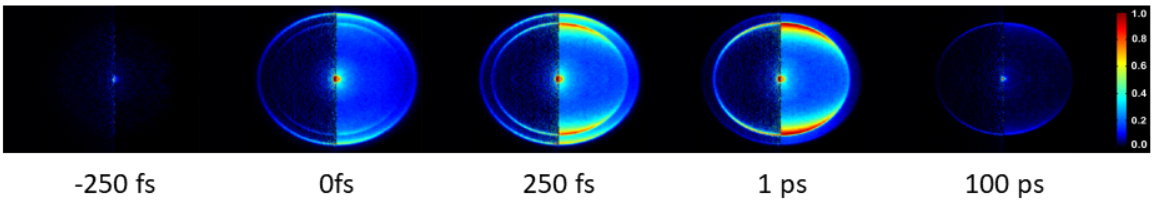

Fig. 6.9: Time-resolved photoelectron images of the molecule N,N-dimethylisopropylamine (DMIPA) utilising a 200 nm pump/ 267 nm probe ionisation scheme. Image taken from Thompson et al.[193].

The avenue of interest for future work is the utilisation of the thermal desorption source as a method of sample volatilisation in conjunction with the VMI set-up. Time-resolved photoelectron studies utilising a desorption source such as that presented

here have not previously been reported, thus in itself would be a beneficial endeavour. The time-resolved photoelectron imaging technique is vastly more differential than the time-resolved ion yield measurements presented within this body of work, and thus could provide an array of new spectroscopic information on these systems. Furthermore, the range of molecules which would become accessible to investigate is a key motivation. Molecules which may previously have been considered non-viable for studies of this form due to a low vapour pressure may now be investigated with relative ease thanks to this volatilisation scheme.

Photoelectron Circular Dichroism Studies

An alternate avenue for further research is to image the photoelectron emission from chiral molecules following excitation with circularly polarised light, an effect known as photoelectron circular dichroism (PECD) imaging. PECD was first predicted by Ritchie *et al.* in 1976[481], however experimental demonstrations were not shown until the 21st century[482–484]. In a non-chiral molecule, photoelectron emissions are symmetric parallel and anti-parallel to the direction of laser propagation. In the case of chiral molecules, however, an asymmetry is present due to scattering of the emitted electron from the chiral potential of the molecule. Coupled with the velocity mapping technique it is possible to obtain PECD angular distributions. This is achieved by performing a difference measurement following excitation with left ($p = +1$) and right ($p =$ -1) circularly polarised light respectively, with the resultant image representative of the molecules PECD. An example of PECD data for (S)-(-)-camphor excited with 398 nm light, produced by Lux *et al.*[485], may be seen in Figure 6.10.

Furthermore, it is possible to extract the normalised angular distribution of emitted photoelectrons, $I_p(\theta)$, from this difference image using an equation of the form Equation (6.1)[481].

$$I_p(\theta) = b_0 + \sum_{i=1}^{2N} b_i{}^{(p)} P_i(cos\theta) \tag{6.1}$$

Here, N is the number of excitation photons, b_i are the anisotropy parameters, P_i are the Legendre polynomials and θ is the photoelectron emission angle relative to the propagation direction. The odd coefficients b_1, b_3, b_5, etc., are normally zero unless the molecule is chiral and the light is circularly polarised. These odd coefficients also exhibit a change in sign when either the polarisation helicity is switched or the opposite enantiomer is investigated. If the PECD image distribution is integrated over all forwards $F_p(\theta =$ 0deg - 90deg) and backward $B_p(\theta =$ 90deg - 180deg) angles, the overall asymmetry may be expressed conveniently by a single parameter, G, which

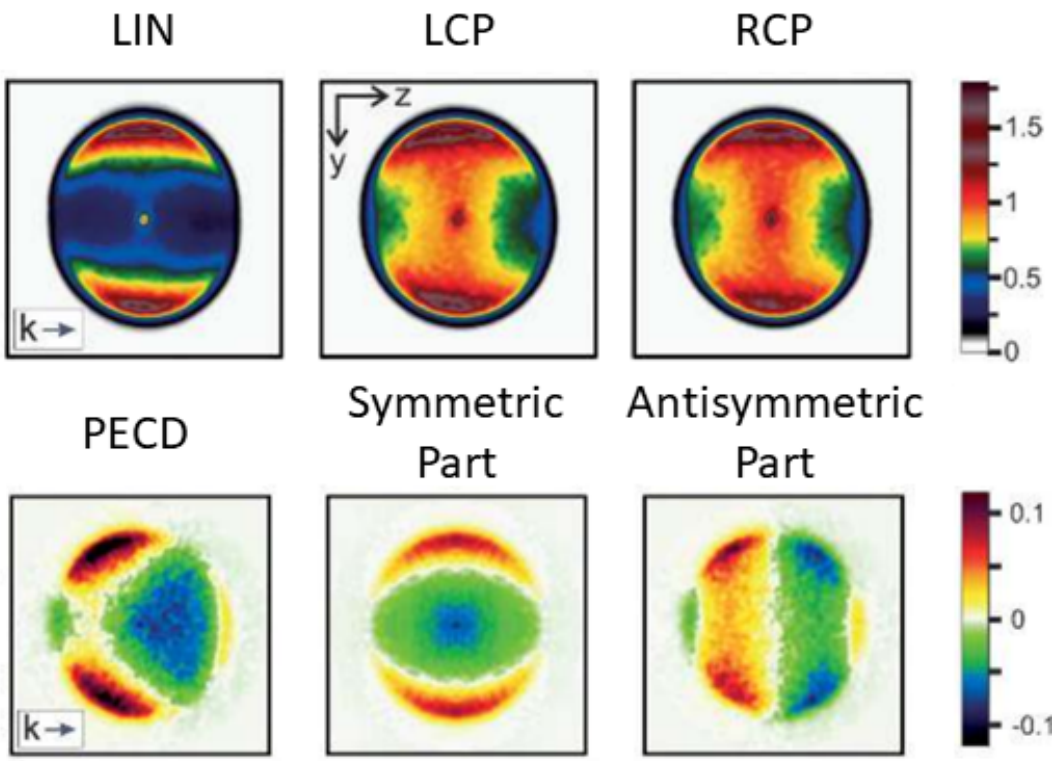

Fig. 6.10: Photoelectron images of (S)-(-)-camphor excited with linear (LIN) left circularly-polarised (LCP) and right circularly-polarised (RCP) 398 nm light. PECD shows the difference image (LCP-RCP), with symmetric and anti-symmetric components of the PECD image presented in the final two panels. Image adapted from Lux et al.[485].

may be calculated as shown in Equation (6.2)[486].

$$G = \frac{(F_{+1} - F_{-1})}{(F_{+1} + F_{-1})/2} - \frac{(B_{+1} - B_{-1})}{(B_{+1} + B_{-1})/2} = \frac{1}{b_0}\left(2b_1 - \frac{1}{2}b_3 + \frac{1}{4}b_5 - ...\right) \tag{6.2}$$

Although measurements such as these were originally only performed utilising synchrotron radiation for single photon PECD, more recently studies of multiphoton PECD have been demonstrated utilising femtosecond laser systems[486–488]. This is an exciting avenue for future research within the Townsend group, with use of the laser desorption source offering the opportunity to investigate an array of previously unstudied molecules. Moreover, there is also the potential to investigate the transient nature of these PECD responses through time-resolved studies[489–491], a further exciting avenue of future research.

6.2 Conclusion

In this thesis, the non-adiabatic dynamics of non-volatile biologically relevant molecular species have been investigated following the absorption of UV radiation. Time-resolved photoion-yield spectroscopy has been employed for data acquisition, with sample volatilisation facilitated through use of a newly developed thermal desorption source, producing neutral plumes of low vapour pressure systems.

At the beginning of this thesis, Chapter 1 provided an extensive review of spectroscopic techniques, considering methods both in the frequency- and time-domain, in addition to a further review of the various volatilisation methods available to produce gas-phase samples of low vapour pressure molecules. Furthermore, the various radiative and non-radiative energy dissipation mechanisms for molecular relaxation were discussed as well as an overview of the various principles and approximations which are assumed in spectroscopic studies.

An outline of the experimental set-up utilised for data collection was presented in Chapter 2. A description of how femtosecond laser pulses are produced and amplified was followed by an extensive discussion on the theory of non-linear optical frequency conversion as well as how it was implemented in the work for this thesis. A further description of the new state-of-the-art time-of-flight mass spectrometer, employed with a soft thermal desorption source, was provided as well as a background to the various vacuum components required to construct such a machine.

Chapter 3 discussed the extensive spectroscopic software developed in MATLAB for the acquisition and analysis of time-resolved photoion-yield data. This required interfacing with various pieces of hardware, including an oscilloscope, home-built arduino shutters and a translation stage, for automation of the data acquisition process. Furthermore, extensive code development was required for the production of a universal data transient fitting function to determine molecular excited state lifetimes. All software produced are operated through graphical user interfaces for ease of use.

Chapter 4 presented the first results obtained from the newly designed spectrometer, investigating the RNA base uracil, as well as its sulfated equivalent 2-thiouracil, across the 267 - 200 nm excitation region and employing an intense 400 nm probe. Benchmark studies of the two molecules at 267 nm show good agreement with previous time-resolved studies of excited state lifetimes. Furthermore, studies of uracil at 220 nm and 200 nm showed extremely rapid relaxation of the $S_3(^1\pi\pi^*)$ state on a timescale of <200 fs. A further point of note is that within the first few hundred picoseconds of pump-probe delay, there is no evidence for the appearance of an m/z = 84 fragment ion, the presence of which in previous nanosecond REMPI studies had

been attributed to theoretically predicted ultrafast ring opening processes at S_2/S_1 or S_1/S_0 conical intersections. This leads to the conclusion that production of *m/z* = 84 is not associated with any ultrafast ring-opening process, however, this leaves open the possibility that the appearance of this fragment may be associated with an excited state process operating on a much more extended timescale.

The first ever gas-phase spectroscopic study of the eumelanin sub-unit 5,6-DHI was presented in Chapter 5, with sample volatilisation again achieved via a laser-based thermal desorption source. Investigations were performed across the 241 - 296 nm excitation region in conjunction with an 800 nm ionising probe. An upper limit on the ionisation threshold of 5,6-DHI is assigned as 7.2 - 7.3 eV which is in good agreement with theoretical predictions. Relaxation of the $S_4(^1\pi\pi^*)$ state to the $S_1(^1\pi\pi^*)$ state was observed at wavelengths $\leq$282 nm on a timescale of τ_1 = <1 ps. Drawing on comparisons with phenol/catechol systems, H-atom barrier tunnelling along the O_5H coordinate following $S_1(^1\pi\pi^*)/S_2(^1\pi\sigma^*)$ state mixing mediated the decay of $S_1(^1\pi\pi^*)$ on a timescale of τ_2 = 10 ps - 132 ps. Complimentary measurements of deuterated 5,6-DHI employing a 260 nm pump showed a significant elongation of the excited state lifetimes, confirming that the OH coordinates play a key role in energy dissipation. This is in contrast to the related 5-HI system, where the OH coordinate is considered a spectator and the NH coordinate is key to energy redistribution. A final long-lived component τ_3 = >1 ns, is attributed to intersystem crossing and population of the triplet manifold. The results from this study provide a good illustration of how subtle changes to a molecular structure can lead to significant modification of the observed dynamics.

Finally, Chapter 6 has discussed the various avenues of future work being actively pursued within the Townsend group building on the work presented within this thesis. A particular area of interest is the testing of a molecular nozzle, which will be employed to concentrate sample plume density and provide an aspect of molecular cooling. Further projects will include investigating molecular dynamical and chiral signatures using the time-resolved photoelectron technique and photoelectron circular dichroism imaging respectively, both in conjunction with the thermal desorption source. A final summary of the work presented within this thesis has been provided within the present subsection.

References

[1] S. Boldissar and M. S. de Vries. How nature covers its bases. *Physical Chemistry Chemical Physics*, 20(15):9701–9716, 2018.

[2] A. N. Pisarevskii, S. N. Cherenkevich and V. T. Andrianov. Fluorescence spectrum and quantum yield of DNA in solution. *Journal of Applied Spectroscopy*, 5(5):452–454, 1966.

[3] J. C. Tully. Perspective : Nonadiabatic dynamics theory. *The Journal of Chemical Physics*, 137(22):22A301, 2012.

[4] P. R. Stannard and W. M. Gelbart. Intramolecular Vibrational Energy Redistribution. *The Journal of Physical Chemistry*, 85(24):3592–3599, 1981.

[5] S. Ullrich, N. L. Evans, H. Yu and A. N. Brouillette. The Photoprotective Properties of Adenine : Time-resolved Photoelectron Spectroscopy at Different Excitation Wavelengths. In *International Conference on Ultrafast Phenomena*, page WB7, Snowmass, CO, 2010.

[6] R. Livingstone, O. Schalk, A. E. Boguslavskiy, G. Wu, L. T. Bergendahl, A. Stolow, M. J. Paterson and D. Townsend. Following the excited state relaxation dynamics of indole and 5-hydroxyindole using time-resolved photoelectron spectroscopy Following the excited state relaxation dynamics of indole and 5-hydroxyindole using time-resolved photoelectron spectroscopy. *The Journal of Chemical Physics*, 135(19): 194307, 2011.

[7] C. V. Shank and E. P. Ippen. Subpicosecond kilowatt pulses from a mode-locked cw dye laser. *Applied Physics Letters*, 24(8):373–375, 1974.

[8] A. H. Zewail. Femtochemistry : Recent Progress in Studies of Dynamics and Control of Reactions and Their Transition States. *The Journal of Physical Chemistry*, 100 (21):12701–12724, 1996.

[9] A. H. Zewail. Femtochemistry: AtomicScale Dynamics of the Chemical Bond Using Ultrafast Lasers (Nobel Lecture). *Angewandte Chemie International Edition*, 39(15): 2586–2631, 2000.

[10] V. S. Antonov, I. N. Knyazev, V. S. Letokhov, V. M. Matiuk, V. G. Movshev and V. K. Potapov. Stepwise laser photoionization of molecules in a mass spectrometer: a new method for probing and detection of polyatomic molecules. *Optics letters*, 3(2): 37–39, 1978.

[11] E. Schrödinger. An undulatory theory of the mechanics of atoms and molecules. *Physical Review*, 28(6):1049–1070, 1926.

[12] M. Born and R. Oppenheimer. Zur Quantentheorie der Molekeln. *Annalen der Physik*, 389(20):457–484, 1927.

[13] M. R. Marcelin. Contribution à l'étude de la cinétique physico-chimique. *Annales De Physique*, 9(3):120–231, 1915.

[14] H. Eyring and M. Polanyi. Über Einfache Gasreaktionen. *Zeitschrift fur Physikalische Chemie B*, 12:279–311, 1931.

[15] H. Eyring. The Activated Complex in Chemical Reactions. *The Journal of Chemical Physics*, 3(2):107–115, 1935.

[16] J. Franck. Elementary Processes of Photochemical Reactions. *Transactions of the Faraday Society*, 21:536–542, 1926.

[17] E. Condon. A theory of intensity distribution in band systems. *Physical Review*, 28 (6):1182–1201, 1926.

[18] A. S. Coolidge, H. M. James and R. D. Present. A study of the franck-condon principle. *The Journal of Chemical Physics*, 4(3):193–211, 1936.

[19] F. Hund. Zur Deutung der Molekelspektren. I. *Zeitschrift für Physik*, 40(10):742–764, 1927.

[20] J. von Neumann and E. Wigner. Über das Verhalten von Eigenwerten bei adiabatischen Prozessen. *Physikalische Zeitschrift*, 30:467–470, 1929.

[21] H. A. Jahn and E. Teller. Stability of Polyatomic Molecules in Degenerate Electronic States. I. Orbital Degeneracy. *Proceedings of the Royal Society A: Mathematical, Physical and Engineering Sciences*, 161(905):220–235, 1937.

[22] E. Teller. The crossing of potential surfaces. *The Journal of Physical Chemistry*, 41 (1):109–116, 1937.

[23] R. S. Mulliken. Electronic structures of polyatomic molecules and valence. II. General considerations. *Physical Review*, 41(1):49–71, 1932.

[24] E. Schrödinger. Quantisierung als Eigenwertproblem. *Annalen der Physik*, 384(6): 489–527, 1926.

[25] W. Pauli. Über den Zusammenhang des Abschlusses der Elektronengruppen im Atom mit der Komplexstruktur der Spektren. *Zeitschrift für Physik*, 31(1):765–783, 1925.

[26] F. Hund. Zur Deutung einiger Erscheinungen in den Molekelspektren. *Zeitschrift für Physik*, 36(9-10):657–674, 1926.

[27] R. S. Mulliken. Electronic States and Band Spectrum Structure in Diatomic Molecules. IV. Hund's Theory; Second Positive Nitrogen and Swan Bands; Alternating Intensities. *Physical Review*, 29(5):637–649, 1927.

[28] R. S. Mulliken. The assignment of quantum numbers for electrons in molecules. I. *Physical Review*, 32(2):186–222, 1928.

[29] G. Herzberg and H. C. Longuet-Higgins. Intersection of potential energy surfaces in polyatomic molecules. *Discussions of the Faraday Society*, 35:77–82, 1963.

[30] Z. Gengeliczki, M. P. Callahan, N. Svadlenak, C. I. Pongor, B. Sztáray, L. Meerts, D. Nachtigallová, P. Hobza, M. Barbatti, H. Lischka and M. S. de Vries. Effect of substituents on the excited-state dynamics of the modified DNA bases 2,4-diaminopyrimidine and 2,6-diaminopurine. *Physical Chemistry Chemical Physics*, 12(20):5375–5388, 2010.

[31] K. Kosma, C. Schröter, E. Samoylova, I. V. Hertel and T. Schultz. Excited-state dynamics of cytosine tautomers. *Journal of the American Chemical Society*, 131(46): 16939–16943, 2009.

[32] A. Jabłoński. Efficiency of Anti-Stokes Fluorescence in Dyes. *Nature*, 131:839–840, 1933.

[33] R. A. Marcus and O. K. Rice. The Kinetics of the Recombination of Methyl Radicals and Iodine Atoms. *The Journal of Physical Chemistry*, 55(6):894–908, 1951.

[34] M. A. El-Sayed. Spin-orbit coupling and the radiationless processes in nitrogen heterocyclics. *The Journal of Chemical Physics*, 38(12):2834–2838, 1963.

[35] M. Kasha. Collisional perturbation of spin-orbital coupling and the mechanism of fluorescence quenching. a visual demonstration of the perturbation. *The Journal of Chemical Physics*, 20(1):71–74, 1952.

[36] O. Yushchenko, G. Licari, S. Mosquera-Vazquez, N. Sakai, S. Matile and E. Vauthey. Ultrafast intersystem-crossing dynamics and breakdown of the Kasha-Vavilov's rule of naphthalenediimides. *The Journal of Physical Chemistry Letters*, 6(11):2096–2100, 2015.

[37] A. Bhattacherjee, C. D. Pemmaraju, K. Schnorr, A. R. Attar and S. R. Leone. Ultrafast Intersystem Crossing in Acetylacetone via Femtosecond X-ray Transient Absorption at the Carbon K-Edge. *Journal of the American Chemical Society*, 139(46): 16576–16583, 2017.

[38] J. P. Zobel, J. J. Nogueira and L. González. Mechanism of Ultrafast Intersystem Crossing in 2-Nitronaphthalene. *Chemistry - A European Journal*, 24(20):5379–5387, 2018.

[39] J. S. Brodbelt and J. J. Wilson. Infrared multiphoton dissociation in quadrupole ion traps. *Mass Spectrometry Reviews*, 28(3):390–424, 2009.

[40] J. P. Reilly. Ultraviolet photofragmentation of biomolecular ions. *Mass Spectrometry Reviews*, 28(3):425– 447, 2009.

[41] G. G. Stokes. XXX . On the change of refrangibility of light. *Philosophocal Transactions*, 142:463–562, 1852.

[42] F. Perrin. La Fluorescence des solutions, induction moléculaire, polarisation et durée d'émission, photochimie. *Annales De Physique*, 10:169–275, 1929.

[43] J. R. Lakowicz. *Principles of Fluorescence Spectroscopy*. Springer US, New York, NY, 3rd edition, 2006.

[44] A. Einstein. Über einen die Erzeugung und Verwandlung des Lichtes betreffenden heuristischen Gesichtspunkt. *Annalen der Physik*, 322(6):132–148, 1905.

[45] J. de Vries, H. Steger, B. Kamke, C. Menzel, B. Weisser, W. Kamke and I. V. Hertel. Single-photon ionization of C60- and C70-fullerene with synchrotron radiation: determination of the ionization potential of C60. *Chemical Physics Letters*, 188(3): 159–162, 1992.

[46] F. Wuilleumier, M. Y. Adam, N. Sandner and V. Schmidt. Photoionization of helium above the n = 2 photoionization threshold. *Journal de Physique Lettres*, 41(16):373–378, 1980.

[47] M. Göppert-Mayer. Uber Elementarakte mit zwei Quantensprungen. *Annalen der Physik*, 401(3):273–294, 1931.

[48] P. Kusch. Some Observations of Double-and Triple-Quantum Transitions'. *Physical Review*, 93(5):1022–1025, 1954.

[49] P. M. Johnson, M. R. Berman and D. Zakheim. Nonresonant multiphoton ionization spectroscopy: The four-photon ionization spectrum of nitric oxide. *The Journal of Chemical Physics*, 62(6):2500–2502, 1975.

[50] P. M. Johnson. Multiphoton ionization spectroscopy: A new state of benzene. *The Journal of Chemical Physics*, 62(11):4562–4563, 1975.

[51] G. Reiser, W. Habenicht, K. Müller-Dethlefs and E. W. Schlag. The ionization energy of nitric oxide. *Chemical Physics Letters*, 152(2-3):119–123, 1988.

[52] M. C. R. Cockett, K. Muller-Dethlefs and T. G. Wright. Chapter 9. Recent applications and developments in ZEKE spectroscopy. *Annual Reports on the Progress of Chemistry, Section C: Physical Chemistry*, 94:327–373, 1998.

[53] L. Zhu and P. Johnson. Mass analyzed threshold ionization spectroscopy. *The Journal of Chemical Physics*, 94(8):5769–5771, 1991.

[54] G. Lembach and B. Brutschy. Fragmentation energetics and dynamics of the neutral and ionized fluorobenzene center dot Ar cluster studied by mass analyzed threshold ionization spectroscopy. *The Journal of Physical Chemistry*, 100(51):19758–19763, 1996.

[55] L. Schnieder, W. Meier, K. H. Welge, M. N. R. Ashfold and C. M. Western. Photodissociation dynamics of H2S at 121.6 nm and a determination of the potential energy function of SH(A2Σ+). *The Journal of Chemical Physics*, 92(12):7027–7037, 1990.

[56] M. N. Ashfold, I. R. Lambert, D. H. Mordaunt, G. P. Morley and C. M. Western. Photofragment translational spectroscopy. *The Journal of Physical Chemistry*, 96(7): 2938–2949, 1992.

[57] X. Yang. State-to-state dynamics of elementary chemical reactions using Rydberg H-atom translational spectroscopy. *International Reviews in Physical Chemistry*, 24 (1):37–98, 2005.

[58] T. P. Softley. Applications of molecular Rydberg states in chemical dynamics and spectroscopy. *International Reviews in Physical Chemistry*, 23(1):1–78, 2004.

[59] B. Cronin, M. G. Nix, A. L. Devine, R. N. Dixon and M. N. Ashfold. High resolution photofragment translational spectroscopy studies of the near ultraviolet photolysis of 2,5-dimethylpyrrole. *Physical Chemistry Chemical Physics*, 8:599–612, 2006.

[60] P. M. Regan, S. R. Langford, A. J. Orr-Ewing and M. N. R. Ashfold. The ultraviolet photodissociation dynamics of hydrogen bromide. *The Journal of Chemical Physics*, 110(1):281–288, 1999.

[61] C. Lin, M. F. Witinski and H. F. Davis. Oxygen atom Rydberg time-of-flight spectroscopy. *The Journal of Chemical Physics*, 119(1):251–255, 2003.

[62] B. Jones, J. Zhou, L. Yang and C. Y. Ng. High-resolution Rydberg tagging time-of-flight measurements of atomic photofragments by single-photon vacuum ultraviolet laser excitation. *Review of Scientific Instruments*, 79(12):123106, 2008.

[63] R. Lipert and S. D. Colson. Persistent Spectral Hole Burning of Molecular Clusters in a Supersonic Jet. *The Journal of Physical Chemistry*, 93(2):3894–3896, 1989.

[64] T. S. Zwier. The Spectroscopy of Solvation in Hydrogen-Bonded Aromatic Clusters. *Annual Review of Physical Chemistry*, 47:205–241, 1996.

[65] E. Nir, C. Janzen, P. Imhof, K. Kleinermanns and M. S. De Vries. Guanine tautomerism revealed by UV-UV and IR-UV hole burning spectroscopy. *The Journal of Chemical Physics*, 115(10):4604–4611, 2001.

[66] J. A. Dickinson, M. R. Hockridge, E. G. Robertson and J. P. Simons. Molecular and Supramolecular Structures of N -Phenyl Formamide and its Hydrated Clusters. *The Journal of Physical Chemistry A*, 103(35):6938–6949, 1999.

[67] J. R. Carney and T. S. Zwier. The Infrared and Ultraviolet Spectra of Individual Conformational Isomers of Biomolecules: Tryptamine. *The Journal of Physical Chemistry A*, 104(38):8677–8688, 2000.

[68] M. Schmitt, H. Müller, U. Henrichs, M. Gerhards, W. Perl, C. Deusen and K. Kleinermanns. Structure and vibrations of phenol·CH3OH (CD3OD) in the electronic ground and excited state, revealed by spectral hole burning and dispersed fluorescence spectroscopy. *The Journal of Chemical Physics*, 103(2):584–594, 1995.

[69] M. Schmitt, U. Henrichs, H. Müller and K. Kleinermanns. Intermolecular vibrations of the phenol dimer revealed by spectral hole burning and dispersed fluorescence spectroscopy Intermolecular vibrations of the phenol dimer revealed by spectral hole burning and dispersed fluorescence spectroscopy. *The Journal of Chemical Physics*, 103(23):9918–9928, 1995.

[70] S. Ezekiel and R. Weiss. Laser-Induced Fluorescence in a Molecular Beam of Iodine. *Physical Review Letters*, 20(3):91–93, 1968.

[71] W. J. Tango, J. K. Link and R. N. Zare. Spectroscopy of K2 Using Laser-Induced Fluorescence. *The Journal of Chemical Physics*, 49(10):4264–4268, 1968.

[72] P. S. H. Fitch, L. Wharton and D. H. Levy. The fluorescence spectrum of free base phthalocyanine cooled in a supersonic free jet. *The Journal of Chemical Physics*, 70 (4):2018–2019, 1979.

[73] J. Tellinghuisen, A. Ragone, M. S. Kim, D. J. Auerbach, R. E. Smalley, L. Wharton and D. H. Levy. The dispersed fluorescence spectrum of NaAr: Ground and excited state potential curves. *The Journal of Chemical Physics*, 71(3):1283–1291, 1979.

[74] R. E. Smalley, B. L. Ramakrishna, D. H. Levy and L. Wharton. Laser spectroscopy of supersonic molecular beams: Application to the NO 2 spectrum. *The Journal of Chemical Physics*, 61(10):4363–4364, 1974.

[75] R. E. Smalley, L. Wharton and D. H. Levy. The fluorescence excitation spectrum of rotationally cooled NO2. *The Journal of Chemical Physics*, 63(11):4977–4989, 1975.

[76] H. Kasahara, N. Mikami, M. Ito, S. Iwata and I. Suzuki. Excitation and dispersed fluorescence spectra of the 1B2(V)-1Σg+(X) transition of jet-cooled CS2. *Chemical Physics*, 86(1):173–188, 1984.

[77] X. Zhu, M. M. Kamal and P. Misra. Laser-induced excitation and dispersed fluorescence spectra of the ethoxy radical. *Pure and Applied Optics: Journal of the European Optical Society Part A*, 5:1021–1029, 1996.

[78] T. C. Tsai, C. W. Chen and B. C. Chang. Laser excitation and dispersed fluorescence spectra of the HCBr $\tilde{A}X$ vibronic transition. *The Journal of Chemical Physics*, 115 (2):766–770, 2001.

[79] S. Leach, H.-W. Jochims and H. Baumgärtel. VUV photodissociation of ammonia: a dispersed fluorescence excitation spectral study. *Physical chemistry chemical physics*, 7(5):900–911, 2005.

[80] G. M. Breuer and E. K. C. Lee. Fluorescence Decay Times of Photoexcited Benzene and Toluene in the Gas Phase. *The Journal of Chemical Physics*, 51:3130–3132, 1969.

[81] F. Piuzzi, M. Mons, I. Dimicoli, B. Tardivel and Q. Zhao. Ultraviolet spectroscopy and tautomerism of the DNA base guanine and its hydrate formed in a supersonic jet. *Chemical Physics*, 270(1):205–214, 2001.

[82] W. Chin, M. Mons, I. Dimicoli, F. Piuzzi, B. Tardivel and M. Elhanine. Tautomer contributions to the near UV spectrum of guanine: Towards a refined picture for the spectroscopy of purine molecules. *European Physical Journal D*, 20(3):347–355, 2002.

[83] K. G. Spears, L. E. Cramer and L. D. Hoffland. Subnanosecond time-correlated photon counting with tunable lasers. *Review of Scientific Instruments*, 49(2):255–262, 1978.

[84] B. Valeur. *Molecular Fluorescence: Princeples And Applications*. Wiley-VCH Verlag, Weinheim, 2002.

[85] T. J. Kang, J. Yu and M. Berg. Limitations on measuring solvent motion with ultrafast transient hole burning. *The Journal of Chemical Physics*, 94(4):2413–2424, 1991.

[86] H. Murakami, S. Kinoshita, Y. Hirata, T. Okada and N. Mataga. Transient hole-burning and time-resolved fluorescence spectra of dye molecules in solution: Evidence for ground-state relaxation and hole-filling effect. *The Journal of Chemical Physics*, 97(11):7881–7888, 1992.

[87] S. A. Kovalenko, A. L. Dobryakov, J. Ruthmann and N. P. Ernsting. Femtosecond spectroscopy of condensed phases with chirped supercontinuum probing. *Physical Review A*, 59(3):2369–2384, 1999.

[88] U. Megerle, I. Pugliesi, C. Schriever, C. F. Sailer and E. Riedle. Sub-50 fs broadband absorption spectroscopy with tunable excitation: putting the analysis of ultrafast molecular dynamics on solid ground. *Applied Physics B: Lasers and Optics*, 96(2-3): 215–231, 2009.

[89] R. Berera, R. van Grondelle and J. T. M. Kennis. Ultrafast transient absorption spectroscopy: principles and application to photosynthetic systems. *Photosynthesis Research*, 101(2-3):105–118, 2009.

[90] S. A. Kovalenko, J. Ruthmann and N. P. Ernsting. Femtosecond hole-burning spectroscopy with stimulated emission pumping and supercontinuum probing. *The Journal of Chemical Physics*, 109(5):1894–1900, 1998.

[91] F. D. Lewis, T. Wu, Y. Zhang, R. L. Letsinger, S. R. Greenfield and M. R. Wasielewski. Distance-dependent electron transfer in DNA hairpins. *Science*, 277(5326):673–676, 1997.

[92] N. P. Ernsting, S. A. Kovalenko, T. Senyushkina, J. Saam and V. Farztdinov. Wave-Packet-Assisted Decomposition of Femtosecond Transient UltravioletVisible Absorption Spectra: Application to Excited-State Intramolecular Proton Transfer in Solution. *The Journal of Physical Chemistry A*, 105(14):3443–3453, 2001.

[93] C. L. Thomsen, J. Thøgersen and S. R. Keiding. Ultrafast Charge-Transfer Dynamics: Studies of p -Nitroaniline in Water and Dioxane. *The Journal of Physical Chemistry A*, 102(7):1062–1067, 1998.

[94] F. Schlosser, J. Sung, P. Kim, D. Kim and F. Würthner. Excitation energy migration in covalently linked perylene bisimide macrocycles. *Chemical Science*, 3:2778–2785, 2012.

[95] S. Schenkl, F. van Mourik, N. Friedman, M. Sheves, R. Schlesinger, S. Haacke and M. Chergui. Insights into excited-state and isomerization dynamics of bacteriorhodopsin from ultrafast transient UV absorption. *Proceedings of the National Academy of Sciences of the United States of America*, 103(11):4101–4106, 2006.

[96] H.-Y. Chen, I.-R. Lee and P.-Y. Cheng. Gas-phase femtosecond transient absorption spectroscopy. *Review of Scientific Instruments*, 77(7):076105, 2006.

[97] C. Schriever, S. Lochbrunner, E. Riedle and D. J. Nesbitt. Ultrasensitive ultraviolet-visible 20 fs absorption spectroscopy of low vapor pressure molecules in the gas phase. *Review of Scientific Instruments*, 79(1):013107, 2008.

[98] E. Goulielmakis, Z. H. Loh, A. Wirth, R. Santra, N. Rohringer, V. S. Yakovlev, S. Zherebtsov, T. Pfeifer, A. M. Azzeer, M. F. Kling, S. R. Leone and F. Krausz. Real-time observation of valence electron motion. *Nature*, 466:739–743, 2010.

[99] A. R. Beck, D. M. Neumark and S. R. Leone. Probing ultrafast dynamics with attosecond transient absorption. *Chemical Physics Letters*, 624:119–130, 2015.

[100] J. E. Bækhøj and L. B. Madsen. Attosecond transient-absorption spectroscopy on aligned molecules. *Physical Review A*, 94(4):043414, 2016.

[101] I. Noda. Generalized two-dimensional correlation method applicable to infrared, Raman, and other types of spectroscopy. *Applied Spectroscopy*, 47(9):1329–1336, 1993.

[102] S. Mukamel. Multidimensional Femtosecond Correlation Spectroscopies of Electronic and Vibrational Excitations. *Annual Review of Physical Chemistry*, 51:691–729, 2000.

[103] D. M. Jonas. Two-Dimensional Femtosecond Spectroscopy. *Annual Review of Physical Chemistry*, 54:425–463, 2003.

[104] I. Noda. Two-Dimensional Infrared Spectroscopy. *Journal of the American Chemical Society*, 111(21):8116–8118, 1989.

[105] J. D. Hybl, A. W. Albrecht, S. M. Gallagher Faeder and D. M. Jonas. Complete Electric Field of Femtosecond Photon Echoes at Their Point of Origin. In T. Elsaesser, J. G. Fujimoto, D. A. Wiersma and W. Zinth, editors, *Ultrafast Phenomena XI*, pages 127–129, Berlin, 1998. Springer.

[106] P. Hamm, M. Lim and R. M. Hochstrasser. Structure of the Amide I Band of Peptides Measured by Femtosecond Nonlinear-Infrared Spectroscopy. *The Journal of Physical Chemistry B*, 102(31):6123–6138, 1998.

[107] J. D. Hybl, A. A. Ferro and D. M. Jonas. Two-dimensional Fourier transform electronic spectroscopy. *The Journal of Chemical Physics*, 115(14):6606–6622, 2001.

[108] J. Bredenbeck, J. Helbing, R. Behrendt, C. Renner, L. Moroder, J. Wachtveitl and P. Hamm. Transient 2D-IR Spectroscopy: Snapshots of the Nonequilibrium Ensemble during the Picosecond Conformational Transition of a Small Peptide. *The Journal of Physical Chemistry B*, 107(33):8654–8660, 2003.

[109] H. S. Chung, Z. Ganim, K. C. Jones and A. Tokmakoff. Transient 2D IR spectroscopy of ubiquitin unfolding dynamics. *Proceedings of the National Academy of Sciences of the United States of America*, 104(36):14237–14242, 2007.

[110] S.-H. Shim and M. T. Zanni. How to turn your pumpprobe instrument into a multidimensional spectrometer: 2D IR and Vis spectroscopies via pulse shaping. *Physical Chemistry Chemical Physics*, 11(5):748–761, 2009.

[111] N. T. Hunt. 2D-IR spectroscopy: ultrafast insights into biomolecule structure and function. *Chemical Society Reviews*, 38(7):1837–1848, 2009.

[112] V. Cervetto, J. Helbing, J. Bredenbeck and P. Hamm. Double-resonance versus pulsed Fourier transform two-dimensional infrared spectroscopy: An experimental and theoretical comparison. *The Journal of Chemical Physics*, 121(12):5935–5942, 2004.

[113] J. P. Ogilvie and K. J. Kubarych. Multidimensional Electronic and Vibrational Spectroscopy: An Ultrafast Probe of Molecular Relaxation and Reaction Dynamics. In E. Arimondo, P. Berman and C. Lin, editors, *Advances in Atomic, Molecular and Optical Physics*, volume 57, pages 249–321. Elsevier Inc., 2009.

[114] L. P. DeFlores, R. A. Nicodemus and A. Tokmakoff. Two-dimensional Fourier transform spectroscopy in the pump probe geometry. *Optics Letters*, 32(20):2966–2968, 2007.

[115] J. D. Hybl, A. W. Albrecht, S. M. Gallagher Faeder and D. M. Jonas. Two-dimensional electronic spectroscopy. *Chemical Physics Letters*, 297(3-4):307–313, 1998.

[116] N. T. Hunt. Transient 2D-IR spectroscopy of inorganic excited states. *Dalton Transactions*, 43:17578–17589, 2014.

[117] S. M. Gallagher, A. W. Albrecht, J. D. Hybl, B. L. Landin, B. Rajaram and D. M. Jonas. Heterodyne detection of the complete electric field of femtosecond four-wave mixing signals. *Journal of the Optical Society of America B*, 15(8):2338–2345, 1998.

[118] F. Milota, J. Sperling, A. Nemeth, T. Mancal and H. F. Kauffmann. Two-dimensional electronic spectroscopy of molecular excitons. *Accounts of Chemical Research*, 42(9): 1364–1374, 2009.

[119] C.-H. Tseng, P. Sándor, M. Kotur, T. C. Weinacht and S. Matsika. Two-dimensional Fourier transform spectroscopy of adenine and uracil using shaped ultrafast laser pulses in the deep UV. *The Journal of Physical Chemistry A*, 116(11):2654–2661, 2012.

[120] C. Kolano, J. Helbing, M. Kozinski, W. Sander and P. Hamm. Watching hydrogen-bond dynamics in a β-turn by transient two-dimensional infrared spectroscopy. *Nature*, 444:469–472, 2006.

[121] K. C. Jones, C. S. Peng and A. Tokmakoff. Folding of a heterogeneous β-hairpin peptide from temperature-jump 2D IR spectroscopy. *Proceedings of the National Academy of Sciences of the United States of America*, 110(8):2828–2833, 2013.

[122] A. I. Stewart, J. A. Wright, G. M. Greetham, S. Kaziannis, S. Santabarbara, M. Towrie, A. W. Parker, C. J. Pickett and N. T. Hunt. Determination of the photolysis products of [FeFe]hydrogenase enzyme model systems using Ultrafast multidimensional infrared spectroscopy. *Inorganic Chemistry*, 49(20):9563–9573, 2010.

[123] C. S. Peng, C. R. Baiz and A. Tokmakoff. Direct observation of ground-state lactam-lactim tautomerization using temperature-jump transient 2D IR spectroscopy. *Proceedings of the National Academy of Sciences of the United States of America*, 110 (23):9243–9248, 2013.

[124] G. M. Greetham, I. P. Clark, D. Weidmann, M. N. R. Ashfold, A. J. Orr-Ewing and M. Towrie. Waveguide-enhanced 2D-IR spectroscopy in the gas phase. *Optics letters*, 38(18):3596–3599, 2013.

[125] H. Mark and R. Wierl. Über Elektronenbeugung am einzelnen Molekül. *Naturwissenschaften*, 18(9):205, 1930.

[126] L. O. Brockway. Electron diffraction by gas molecules. *Reviews of Modern Physics*, 8 (3):231–266, 1936.

[127] R. L. Hilderbrandt and R. A. Bonham. Structure Determination by Gas Electron Diffraction. *Annual Review of Physical Chemistry*, 22:279–312, 1971.

[128] K. Hedberg, L. Hedberg, D. S. Bethune, C. A. Brown, H. C. Dorn, R. D. Johnson and M. D. Vries. Bond Lengths in Free Molecules of Buckminsterfullerene, C60 from Gas-Phase Electron Diffraction. *Science*, 254(5030):410–412, 1991.

[129] H. Fleischer, D. A. Wann, S. L. Hinchley, K. B. Borisenko, J. R. Lewis, R. J. Mawhorter, E. Robertson and D. W. H. Rankin. Molecular structures of Se(SCH3)2 and Te(SCH3)2 using gas-phase electron diffraction and. *Dalton Transactions*, 0(19): 3221–3228, 2005.

[130] D. A. Wann, R. J. Less, F. Rataboul, P. D. McCaffrey, A. M. Reilly, H. E. Robertson, P. D. Lickiss and D. W. H. Rankin. Accurate Gas-Phase Experimental Structures of Octasilsesquioxanes (Si8O12X8; X = H, Me). *Organometallics*, 27(16):4183–4187, 2008.

[131] J. Yang and M. Centurion. Gas-phase electron diffraction from laser-aligned molecules. *Structural Chemistry*, 26(5-6):1513–1520, 2015.

[132] I. Hargittai. Gas-Phase Electron Diffraction for Molecular Structure Determination. In T. E. Weirich, J. L. Lábár and X. Zou, editors, *Electron crystallography: novel approaches for structure determination of nanosized materials*, pages 197–206. Springer, Dordrecht, 2006.

[133] J. C. Williamson, M. Dantus, S. B. Kim and A. H. Zewail. Ultrafast diffraction and molecular structure. *Chemical Physics Letters*, 196(6):529–534, 1992.

[134] J. C. Williamson, J. Cao, H. Ihee, H. Frey and A. H. Zewail. Clocking transient chemical changes by ultrafast electron diffraction, 1997.

[135] R. Srinivasan, V. a. Lobastov, C.-Y. Ruan and A. H. Zewail. Ultrafast Electron Diffraction (UED) A New Development for the 4D Determination of Transient Molecular Structures. *Helvetica Chimica Acta*, 86(6):1761–1799, 2003.

[136] B. J. Siwick, J. R. Dwyer, R. E. Jordan and R. J. D. Miller. Ultrafast electron optics: Propagation dynamics of femtosecond electron packets. *Journal of Applied Physics*, 92(3):1643–1648, 2002.

[137] M. Dantus, S. B. Kim, J. C. Williamson and A. H. Zewail. Ultrafast electron diffraction. 5. Experimental time resolution and applications. *The Journal of Physical Chemistry*, 98(11):2782–2796, 1994.

[138] J. Yang, M. Guehr, T. Vecchione, M. S. Robinson, R. Li, N. Hartmann, X. Shen, R. Coffee, J. Corbett, A. Fry, K. Gaffney, T. Gorkhover, C. Hast, K. Jobe, I. Makasyuk, A. Reid, J. Robinson, S. Vetter, F. Wang, S. Weathersby, C. Yoneda, M. Centurion and X. Wang. Diffractive imaging of a rotational wavepacket in nitrogen molecules with femtosecond megaelectronvolt electron pulses. *Nature Communications*, 7(5): 11232, 2016.

[139] J. Yang, M. Guehr, T. Vecchione, M. S. Robinson, R. Li, N. Hartmann, X. Shen, R. Coffee, J. Corbett, A. Fry, K. Gaffney, T. Gorkhover, C. Hast, K. Jobe, I. Makasyuk, A. Reid, J. Robinson, S. Vetter, F. Wang, S. Weathersby, C. Yoneda, X. Wang and M. Centurion. Femtosecond gas phase electron diffraction with MeV electrons. *Faraday Discussions*, 194:563–581, 2016.

[140] O. Zandi, K. J. Wilkin, Y. Xiong and M. Centurion. High current table-top setup for femtosecond gas electron diffraction. *Structural Dynamics*, 4:044022, 2017.

[141] D. W. Chandler and P. L. Houston. Twodimensional imaging of stateselected photodissociation products detected by multiphoton ionization. *The Journal of Chemical Physics*, 87(2):1445–1447, 1987.

[142] J. W. Thoman, D. W. Chandler, D. H. Parker and M. H. M. Janssen. Two-dimensional Imaging of Photofragments. *Laser Chemistry*, 9(1-3):27–46, 1988.

[143] W. K. Kang, Y. S. Kim and K.-H. Jung. Two-dimensional photoelectron imaging of state-selected iodine atom by (2 + 1) resonance-enhanced multiphoton ionization. *Chemical Physics Letters*, 244(1-2):183–187, 1995.

[144] D. W. Chandler, J. W. Thoman Jr, M. H. Janssen and D. H. Parker. Photofragment imaging: The 266 nm photodissociation of CH3I. *Chemical Physics Letters*, 156(2-3): 151–158, 1989.

[145] D. W. Chandler, M. H. Janssen, S. Stolte, R. N. Strickland, J. W. Thoman Jr and D. H. Parker. Photofragment imaging: The 266-nm photolysis of CD3I. *The Journal of Physical Chemistry*, 94(12):4839–4846, 1990.

[146] A. T. Eppink and D. H. Parker. Velocity map imaging of ions and electrons using electrostatic lenses: Application in photoelectron and photofragment ion imaging of molecular oxygen. *Review of Scientific Instruments*, 68(9):3477–3484, 1997.

[147] D. H. Parker and A. T. Eppink. Photoelectron and photofragment velocity map imaging of state-selected molecular oxygen dissociation/ionization dynamics. *The Journal of Chemical Physics*, 107(7):2357–2362, 1997.

[148] S. W. Crane, M. M. Zawadzki, J. O. Thompson, N. Kotsina, O. Ghafur and D. Townsend. Caveats in the interpretation of time-resolved photoionization measurements: A photoelectron imaging study of pyrrole. *The Journal of Chemical Physics*, 145(23): 234304, 2016.

[149] R. N. Strickland and D. W. Chandler. Reconstruction of an axisymmetric image from its blurred and noisy projection. *Applied Optics*, 30(14):1811–1819, 1991.

[150] C. Bordas, F. Paulig, H. Helm and D. L. Huestis. Photoelectron imaging spectrometry: Principle and inversion method. *Review of Scientific Instruments*, 67(6):2257–2268, 1996.

[151] M. J. J. Vrakking. An iterative procedure for the inversion of two-dimensional ion/photoelectron imaging experiments. *Review of Scientific Instruments*, 72(11): 4084–4089, 2001.

[152] M. J. Bass, M. Brouard, A. P. Clark and C. Vallance. Fourier moment analysis of velocity-map ion images. *The Journal of Chemical Physics*, 117(19):8723–8735, 2002.

[153] S. Manzhos and H.-P. Loock. Photofragment image analysis via pattern recognition. *Review of Scientific Instruments*, 75(7):2435–2445, 2004.

[154] Y. T. Cho and S.-J. Na. Application of Abel inversion in real-time calculations for circularly and elliptically symmetric radiation sources. *Measurement Science and Technology*, 16(3):878–884, 2005.

[155] F. Renth, J. Riedel and F. Temps. Inversion of velocity map ion images using iterative regularization and cross validation. *Review of Scientific Instruments*, 77(3):033103, 2006.

[156] J. Cooper and R. N. Zare. Angular Distribution of Photoelectrons. *The Journal of Chemical Physics*, 48(2):942–943, 1976.

[157] D. P. Baldwin, M. A. Buntine and D. W. Chandler. Photodissociation of acetylene: Determination of D00 (HCCH) by photofragment imaging. *The Journal of Chemical Physics*, 93(9):6578–6584, 1990.

[158] P. C. Samartzis, B. L. G. Bakker, D. H. Parker and T. N. Kitsopoulos. Photoelectron and Photofragment Velocity Imaging Following the Excitation of CH 3 I to the A-Band Using fs , ps , and ns Laser Pulses. *The Journal of Physical Chemistry A*, 103 (31):6106–6113, 1999.

[159] Y. Sato, Y. Matsumi, M. Kawasaki, K. Tsukiyama and R. Bersohn. Ion imaging of the photodissociation of OCS near 217 and 230 nm. *The Journal of Physical Chemistry*, 99(44):16307–16314, 1995.

[160] B. L. G. Bakker, T. J. B. Eppink, D. H. Parker, M. L. Costen, G. Hancock and G. A. D. Ritchie. The sequential two photon dissociation of NO as a source of aligned N(2D), N(4S) and O(3P) atoms. *Chemical Physics Letters*, 283(5-6):319–325, 1998.

[161] M. J. Cooper, P. J. Jackson, L. J. Rogers, A. J. Orr-ewing, M. N. R. Ashfold, J. Whitaker, M. J. Cooper, P. J. Jackson, L. J. Rogers, A. J. Orr-ewing, M. N. R. Ashfold and B. J. Whitaker. Ion imaging studies of the Cl(2PJ) and Br(2PJ) atomic products resulting from BrCl photodissociation in the wavelength range 235540 nm. *The Journal of Chemical Physics*, 109(11):4367–4377, 1998.

[162] A. T. J. B. Eppink and D. H. Parker. Methyl iodide A-band decomposition study by photofragment velocity imaging. *The Journal of Chemical Physics*, 109(12):4758–4767, 1998.

[163] S.-T. Tsai, C.-K. Lin, Y. T. Lee and C.-K. Ni. Multimass ion imaging detection: Application to photodissociation. *Review of Scientific Instruments*, 72(4):1963–1969, 2001.

[164] C.-K. Ni and Y. T. Lee. Photodissociation of simple aromatic molecules in a molecular beam. *International Reviews in Physical Chemistry*, 23(2):187–218, 2004.

[165] C.-K. Ni, C.-M. Tseng, M.-F. Lin and Y. A. Dyakov. Photodissociation dynamics of small aromatic molecules studied by multimass ion imaging. *The Journal of Physical Chemistry B*, 111(44):12631–12642, 2007.

[166] R. Forbes, V. Makhija, K. Veyrinas, A. Stolow, J. W. Lee, M. Burt, M. Brouard, C. Vallance, I. Wilkinson, R. Lausten and P. Hockett. Time-resolved multi-mass ion imaging: Femtosecond UV-VUV pump-probe spectroscopy with the PImMS camera. *The Journal of Chemical Physics*, 147(1):013911, 2017.

[167] M. Brouard, E. K. Campbell, A. J. Johnsen, C. Vallance, W. H. Yuen and A. Nomerotski. Velocity map imaging in time of flight mass spectrometry. *Review of Scientific Instruments*, 79(12):123115, 2008.

[168] A. Nomerotski, S. Adigun-Boaye, M. Brouard, E. Campbell, A. Clark, J. Crooks, J. J. John, A. J. Johnsen, C. Slater, R. Turchetta, C. Vallance, E. Wilman and W. H. Yuen. Pixel imaging mass spectrometry with fast silicon detectors. *Nuclear Instruments and Methods in Physics Research Section A: Accelerators, Spectrometers, Detectors and Associated Equipment*, 633(Supplement 1):S243–S246, 2011.

[169] A. T. Clark, J. P. Crooks, I. Sedgwick, R. Turchetta, J. W. Lee, J. J. John, E. S. Wilman, L. Hill, E. Halford, C. S. Slater, B. Winter, W. H. Yuen, S. H. Gardiner, M. L. Lipciuc, M. Brouard, A. Nomerotski and C. Vallance. Multimass velocity-map imaging with the pixel imaging mass spectrometry (PImMS) sensor: An ultra-fast event-triggered camera for particle imaging. *The Journal of Physical Chemistry A*, 116(45):10897–10903, 2012.

[170] M. Brouard, E. Halford, A. Lauer, C. Slater, B. Winter, W. Yuen, J. J. John, L. Hill, A. Nomerotski, A. Clark, J. Crooks, R. Turchetta, J. Lee and E. Wilman. The application of multi-hit pixel sensors to spatial imaging mass spectrometry. *Review of Scientific Instruments*, 83(11):114101, 2012.

[171] R. A. Ingle, C. S. Hansen, E. Elsdon, M. Bain, S. J. King, J. W. Lee, M. Brouard, C. Vallance, R. Turchetta and M. N. Ashfold. Ultraviolet photochemistry of 2-bromothiophene explored using universal ionization detection and multi-mass velocity-map imaging with a PImMS2 sensor. *The Journal of Chemical Physics*, 147(1):013914, 2017.

[172] C. S. Slater, S. Blake, M. Brouard, A. Lauer, C. Vallance, J. J. John, R. Turchetta, A. Nomerotski, L. Christensen, J. H. Nielsen and H. Stapelfeldt. Covariance imaging experiments using a pixel-imaging mass-spectrometry camera. *Physical Review A*, 89 (1):011401(R), 2014.

[173] C. S. Slater, S. Blake, M. Brouard, A. Lauer, C. Vallance, C. S. Bohun, L. Christensen, J. H. Nielsen, M. P. Johansson and H. Stapelfeldt. Coulomb-explosion imaging using a pixel-imaging mass-spectrometry camera. *Physical Review A*, 91(5):053424, 2015.

[174] L. Christensen, J. H. Nielsen, C. S. Slater, A. Lauer, M. Brouard and H. Stapelfeldt. Using laser-induced Coulomb explosion of aligned chiral molecules to determine their absolute configuration. *Physical Review A*, 92(3):033411, 2015.

[175] K. Amini, R. Boll, A. Lauer, M. Burt, J. W. Lee, L. Christensen, F. Brauβe, T. Mullins, E. Savelyev, U. Ablikim, N. Berrah, C. Bomme, S. Düsterer, B. Erk, H.

Höppner, P. Johnsson, T. Kierspel, F. Krecinic, J. Küpper, M. Müller, E. Müller, H. Redlin, A. Rouzée, N. Schirmel, J. Thøgersen, S. Techert, S. Toleikis, R. Treusch, S. Trippel, A. Ulmer, J. Wiese, C. Vallance, A. Rudenko, H. Stapelfeldt, M. Brouard and D. Rolles. Alignment, orientation, and Coulomb explosion of difluoroiodobenzene studied with the pixel imaging mass spectrometry (PImMS) camera. *The Journal of Chemical Physics*, 147(1):013933, 2017.

[176] D. E. Pooley, J. W. L. Lee, M. Brouard, R. Farrow, J. J. John, W. Kockelmann, R. B. Nickerson, N. J. Rhodes, E. M. Schooneveld, I. Sedgwick, R. Turchetta and C. Vallance. GP2 ' An Energy Resolved Neutron Imaging Detector using a Gd Coated CMOS Sensor. In *2015 IEEE Nuclear Science Symposium and Medical Imaging Conference (NSS/MIC)*, pages 1–3, Sandiego, CA, 2015.

[177] T. Shibata and T. Suzuki. Photofragment ion imaging with femtosecond laser pulses. *Chemical Physics Letters*, 262(1-2):115–119, 1996.

[178] T. Shibata, H. Li, H. Katayanagi and T. Suzuki. Dissociation of Metastable CH 3 CO Radical Observed by Subpicosecond Time-Clocked Photofragment Imaging. *The Journal of Physical Chemistry A*, 102(21):3643–3647, 1998.

[179] J. J. Larsen, N. J. Mørkbak, J. Olesen, N. Bjerre, M. Machholm, S. R. Keiding and H. Stapelfeldt. Femtosecond photodissociation dynamics of I2 studied by ion imaging. *The Journal of Chemical Physics*, 109(20):8857–8863, 1998.

[180] L. Wang, H. Kohguchi and T. Suzuki. Femtosecond time-resolved photoelectron imaging. *Faraday Discussions*, 113:37–46, 1999.

[181] T. Suzuki, L. Wang and H. Kohguchi. Femtosecond time-resolved photoelectron imaging on ultrafast electronic dephasing in an isolated molecule. *The Journal of Chemical Physics*, 111(11):4859–4861, 1999.

[182] J. A. Davies, J. E. LeClaire, R. E. Continetti and C. C. Hayden. Femtosecond time-resolved photoelectron photoion coincidence imaging studies of dissociation dynamics Femtosecond time-resolved photoelectron photoion coincidence imaging studies of dissociation dynamics. *The Journal of Chemical Physics*, 111(1):1–4, 1999.

[183] M. Burt, R. Boll, J. W. Lee, K. Amini, H. Köckert, C. Vallance, A. S. Gentleman, S. R. Mackenzie, S. Bari, C. Bomme, S. Düsterer, B. Erk, B. Manschwetus, E. Müller, D. Rompotis, E. Savelyev, N. Schirmel, S. Techert, R. Treusch, J. Küpper, S. Trippel, J. Wiese, H. Stapelfeldt, B. C. de Miranda, R. Guillemin, I. Ismail, L. Journel, T. Marchenko, J. Palaudoux, F. Penent, M. N. Piancastelli, M. Simon, O. Travnikova, F. Brausse, G. Goldsztejn, A. Rouzée, M. Géléoc, R. Geneaux, T. Ruchon, J. Underwood, D. M. Holland, A. S. Mereshchenko, P. K. Olshin, P. Johnsson, S. Maclot, J. Lahl, A. Rudenko, F. Ziaee, M. Brouard and D. Rolles. Coulomb-explosion imaging of concurrent CH2 BrI photodissociation dynamics. *Physical Review A*, 96(4):043415, 2017.

[184] S. A. Aseyev, Y. Ni, L. J. Frasinski, H. G. Muller and M. J. Vrakking. Attosecond angle-resolved photoelectron spectroscopy. *Physical Review Letters*, 91(22):223902, 2003.

[185] G. Sansone, F. Kelkensberg, J. F. Pérez-Torres, F. Morales, M. F. Kling, W. Siu, O. Ghafur, P. Johnsson, M. Swoboda, E. Benedetti, F. Ferrari, F. Lépine, J. L. Sanz-Vicario, S. Zherebtsov, I. Znakovskaya, A. L'Huillier, M. Y. Ivanov, M. Nisoli, F. Martín and M. J. J. Vrakking. Electron localization following attosecond molecular photoionization. *Nature*, 465:763–766, 2010.

[186] M. J. J. Vrakking. Attosecond imaging. *Physical Chemistry Chemical Physics*, 16(7): 2775–2789, 2014.

[187] A. Stolow, A. E. Bragg and D. M. Neumark. Femtosecond time-resolved photoelectron spectroscopy. *Chemical Reviews*, 104(4):1719–1757, 2004.

[188] T. Suzuki. Femtosecond Time-Resolved Photoelectron Imaging. *Annual Review of Physical Chemistry*, 57:555–592, 2006.

[189] R. A. Livingstone, J. O. F. Thompson, M. Iljina, R. J. Donaldson, B. J. Sussman, M. J. Paterson and D. Townsend. Time-resolved photoelectron imaging of excited state relaxation dynamics in phenol, catechol, resorcinol, and hydroquinone. *The Journal of Chemical Physics*, 137(18):184304, 2012.

[190] J. O. F. Thompson, R. A. Livingstone and D. Townsend. Following the relaxation dynamics of photoexcited aniline in the 273-266 nm region using time-resolved photoelectron imaging. *The Journal of Chemical Physics*, 139(3):034316, 2013.

[191] J. O. F. Thompson, L. Saalbach, S. W. Crane, M. J. Paterson and D. Townsend. Ultraviolet relaxation dynamics of aniline, N, N-dimethylaniline and 3,5- dimethylaniline at 250 nm. *The Journal of Chemical Physics*, 142(11):114309, 2015.

[192] M. M. Zawadzki, J. O. F. Thompson, E. A. Burgess, M. J. Paterson and D. Townsend. Time-resolved photoionization spectroscopy of mixed Rydberg-valence states: indole case study. *Physical Chemistry Chemical Physics*, 17(40):26659–26669, 2015.

[193] J. O. F. Thompson, L. B. Klein, T. I. Sølling, M. J. Paterson and D. Townsend. The role of novel Rydberg-valence behaviour in the non-adiabatic dynamics of tertiary aliphatic amines. *Chemical Science*, 7(3):1826–1839, 2016.

[194] L. B. Klein, T. J. Morsing, R. A. Livingstone, D. Townsend and T. I. Sølling. The effects of symmetry and rigidity on non-adiabatic dynamics in tertiary amines: A time-resolved photoelectron velocity-map imaging study of the cage-amine ABCO. *Physical Chemistry Chemical Physics*, 18(14):9715–9723, 2016.

[195] L. B. Klein, J. O. F. Thompson, S. W. Crane, L. Saalbach, T. I. Sølling, M. J. Paterson and D. Townsend. Ultrafast relaxation dynamics of electronically excited piperidine: ionization signatures of Rydberg/valence evolution. *Physical Chemistry Chemical Physics*, 18(36):25070–25079, 2016.

[196] M. M. Zawadzki, M. Candelaresi, L. Saalbach, S. W. Crane, M. J. Paterson and D. Townsend. Observation of multi-channel non-adiabatic dynamics in aniline derivatives using time-resolved photoelectron imaging. *Faraday Discussions*, 194:185–208, 2016.

[197] M. A. Duncan, T. G. Dietz, M. G. Liverman and R. E. Smalley. Photoionization measurement of the triplet lifetime of benzene. *The Journal of Physical Chemistry*, 85(1):7–9, 1981.

[198] V. G. Stavros and J. R. Verlet. Gas-Phase Femtosecond Particle Spectroscopy: A Bottom-Up Approach to Nucleotide Dynamics. *Annual Review of Physical Chemistry*, 67:211–232, 2016.

[199] R. Fröchtenicht and M. Hartmann. Time-Resolved REMPI Detection of Methyl Radicals Generated in Laser-Induced Unimolecular Reactions. *The Journal of Physical Chemistry*, 99(44):16290–16295, 1995.

[200] D. Zhong and A. H. Zewail. Femtosecond real-time probing of reactions. 23. Studies of temporal, velocity, angular, and state dynamics from transition states to final products by femtosecond-resolved mass spectrometry. *The Journal of Physical Chemistry A*, 102(23):4031–4058, 1998.

[201] H. Lippert, H. H. Ritze, I. V. Hertel and W. Radloff. Femtosecond time-resolved hydrogen-atom elimination from photoexcited pyrrole molecules. *ChemPhysChem*, 5 (9):1423–1427, 2004.

[202] A. Iqbal, L. J. Pegg and V. G. Stavros. Direct versus indirect H atom elimination from photoexcited phenol molecules. *The Journal of Physical Chemistry A*, 112(39): 9531–9534, 2008.

[203] T. G. Dietz, M. A. Duncan and R. E. Smalley. Time evolution studies of triplet toluene by two-color photoionization. *The Journal of Chemical Physics*, 76(3):1227–1232, 1982.

[204] J. W. Perry, N. F. Scherer and A. H. Zewail. Picosecond pump-probe multiphoton ionization of isolated molecules: IVR and coherence. *Chemical Physics Letters*, 103 (1):1–8, 1983.

[205] B. I. Greene and R. C. Farrow. Subpicosecond time resolved multiphoton ionization: Excited state dynamics of cis-stilbene under collision free conditions. *The Journal of Chemical Physics*, 78(6):3336–3338, 1983.

[206] J. M. Wiesenfeld and B. I. Greene. Femtosecond relaxation dynamics of molecular rydberg states using time-resolved multiphoton ionization. *Physical Review Letters*, 51(19):1745–1748, 1983.

[207] M. Uiberacker, T. Uphues, M. Schultze, A. J. Verhoef, V. Yakovlev, M. F. Kling, J. Rauschenberger, N. M. Kabachnik, H. Schröder, M. Lezius, K. L. Kompa, H. G. Muller, M. J. J. Vrakking, S. Hendel, U. Kleineberg, U. Heinzmann, M. Drescher and F. Krausz. Attosecond real-time observation of electron tunnelling in atoms. *Nature*, 446:627–632, 2007.

[208] T. Baumert, B. Bühler, M. Grosser, R. Thalweiser, V. Weiss, E. Wiedenmann and G. Gerber. Femtosecond time-resolved wave packet motion in molecular multiphoton ionization and fragmentation. *The Journal of Physical Chemistry*, 95(21):8103–8110, 1991.

[209] M. Dantus, M. H. M. Janssen and A. H. Zewail. Femtosecond Probing of Molecular-Dynamics by Mass-Spectrometry in a Molecular-Beam. *Chemical Physics Letters*, 181 (4):281–287, 1991.

[210] J. D. Young, M. Staniforth, J. C. Dean, G. M. Roberts, F. Mazzoni, T. N. Karsili, M. N. Ashfold, T. S. Zwier and V. G. Stavros. Towards understanding photodegradation pathways in lignins: The role of intramolecular hydrogen bonding in excited states. *The Journal of Physical Chemistry Letters*, 5(12):2138–2143, 2014.

[211] J. D. Young, M. Staniforth, M. J. Paterson and V. G. Stavros. Torsional motion of the chromophore catechol following the absorption of ultraviolet light. *Physical Review Letters*, 114(23):233001, 2015.

[212] L. R. Khundkar and A. H. Zewail. Picosecond MPI mass spectrometry of CH3I in the process of dissociation. *Chemical Physics Letters*, 142(5):426–432, 1987.

[213] T. S. Rose, M. J. Rosker and A. H. Zewail. Femtosecond real-time observation of wave packet oscillations (resonance) in dissociation reactions. *The Journal of Chemical Physics*, 88(10):6672–6673, 1988.

[214] M. J. Rosker, T. S. Rose and A. H. Zewail. Femtosecond real-time dynamics of photofragment-trapping resonances on dissociative potential energy surfaces. *Chemical Physics Letters*, 146(3-4):175–179, 1988.

[215] T. Uphues, M. Schultze, M. F. Kling, M. Uiberacker, S. Hendel, U. Heinzmann, N. M. Kabachnik and M. Drescher. Ion-charge-state chronoscopy of cascaded atomic Auger decay. *New Journal of Physics*, 10:025009, 2008.

[216] M. Krikunova, T. Maltezopoulos, A. Azima, M. Schlie, U. Frühling, H. Redlin, R. Kalms, S. Cunovic, N. M. Kabachnik, M. Wieland and M. Drescher. Time-resolved ion spectrometry on xenon with the jitter-compensated soft x-ray pulses of a free-electron laser. *New Journal of Physics*, 11:123019, 2009.

[217] F. J. Vastola, A. J. Pirone and B. E. Knox. Proceedings of the ASTM Committee E-14, 14th Annual Conference on Mass Spectrometry and Allied Topics. page 78, 1966.

[218] F. J. Vastola and A. J. Pirone. Ionization of organic solids by laser irradiation. In E. Kendrick, editor, *Advances in Mass Spectrometry*, volume 4, pages 107–111, Institute of Petroleum, London, 1968.

[219] J. R. Cable, M. J. Tubergen and D. H. Levy. Laser Desorption Molecular Beam Spectroscopy: The Electronic Spectra of Tryptophan Peptides in the Gas Phase. *Journal of the American Chemical Society*, 109(20):6198–6199, 1987.

[220] R. Cohen, B. Brauer, E. Nir, L. Grace and M. S. de Vries. Resonance-Enhanced Multiphoton Ionization Spectroscopy of Dipeptides. *The Journal of Physical Chemistry A*, 104(27):6351–6355, 2000.

[221] F. Piuzzi, I. Dimicoli, M. Mons, B. Tardivel and Q. Zhao. A simple laser vaporization source for thermally fragile molecules coupled to a supersonic expansion: application to the spectroscopy of tryptophan. *Chemical Physics Letters*, 320(3-4):282–288, 2000.

[222] E. Nir, K. Kleinermanns, L. Grace and M. S. De Vries. On the photochemistry of purine nucleobases. *The Journal of Physical Chemistry A*, 105(21):5106–5110, 2001.

[223] M. A. Posthumus, P. G. Kistemaker, H. L. Meuzelaar and M. C. Ten Neover de Brauw. Laser Desorption-Mass Spectrometry of Polar Nonvolatile Bio-Organic Molecules. *Analytical Chemistry*, 50(7):985–991, 1978.

[224] D. V. Davis, R. G. Cooks, B. N. Meyer and J. L. McLaughlin. Identification of Naturally Occurring Quaternary Compounds by Combined Laser Desorption and Tandem Mass Spectrometry. *Analytical Chemistry*, 55(8):1302–1305, 1983.

[225] L. G. Wright, R. G. Cooks and K. V. Wood. Matrix enhanced laser desorption in mass spectrometry and tandem mass spectrometry. *Biomedical Mass Spectrometry*, 12(4):159–162, 1985.

[226] M. Karas, D. Bachmann, U. Bahr and F. Hillenkamp. Matrix-assisted ultraviolet laser desorption of non-volatile compounds. *International Journal of Mass Spectrometry and Ion Processes*, 78:53–68, 1987.

[227] K. Tanaka, H. Waki, Y. Ido, S. Akita, Y. Yoshida and T. Yoshida. Protein and polymer analyses up to m/z 100 000 by laser ionization time-of-flight mass spectrometry. *Rapid Communications in Mass Spectrometry*, 2(8):151–153, 1988.

[228] M. Karas and R. Krüger. Ion formation in MALDI: The cluster ionization mechanism. *Chemical Reviews*, 103(2):427–439, 2003.

[229] K. Dreisewerd. The desorption process in MALDI. *Chemical Reviews*, 103(2):395–425, 2003.

[230] R. C. Beavis and B. T. Chait. Cinnamic Acid Derivatives as Matrices for Ultraviolet Laser Desorption Mass Spectrometry of Proteins. *Rapid Communications in Mass Spectrometry*, 3(12):432–435, 1989.

[231] R. C. Beavis, T. Chaudhary and B. T. Chait. α-Cyano-4hydroxycinnamic Acid as a Matrix for Matrix-assisted Laser Desorption Mass Spectrometry. *Organic Mass Spectrometry*, 27:156–158, 1992.

[232] M. Karas, H. Ehring, E. Nordhoff, B. Stahl, K. Strupat, F. Hillenkamp, M. Grehl and B. Krebs. Matrixassisted laser desorption/ionization mass spectrometry with additives to 2, 5dihydroxybenzoic acid. *Organic Mass Spectrometry*, 28:1476–1481, 1993.

[233] R. C. Beavis and B. T. Chait. Matrix-assisted Laser-desorption Mass Spectrometry Using 355 nm Radiation. *Rapid Communications in Mass Spectrometry*, 3(12):436–439, 1989.

[234] K. Strupat, M. Karas and F. Hlllenkamp. 2,5-Dihydroxybenzoic acid: a new matrix for laser desorptionionization mass spectrometry. *International Journal of Mass Spectrometry and Ion Processes*, 111:89–102, 1991.

[235] B. Spengler, U. Bahr, M. Karas and F. Hillenkamp. Postionization of laser-desorbed organic and inorganic compounds in a time of flight mass spectrometer. *Instrumentation Science & Technology*, 17(1-2):173–193, 1988.

[236] C. W. Liang, C. H. Lee, Y.-J. Lin, Y. T. Lee and C. K. Ni. MALDI mechanism of dihydroxybenzoic acid isomers: Desorption of neutral matrix and analyte. *Journal of Physical Chemistry B*, 117(17):5058–5064, 2013.

[237] R. Knochenmuss, F. Dubois, M. J. Dale and R. Zenobi. The matrix suppression effect and ionization mechanisms in matrix-assisted laser desorption/ionization. *Rapid Communications in Mass Spectrometry*, 10(8):871–877, 1996.

[238] X. Tang, M. Sadeghi, Z. Olumee and A. Vertes. Matrix-assisted Laser Desorption/Ionization by Two Collinear Subthreshold Laser Pulses. *Rapid Communications in Mass Spectrometry*, 11(5):484–488, 1997.

[239] R. Knochenmuss and A. Vertes. Time-delayed 2-Pulse Studies of MALDI Matrix Ionization Mechanisms. *The Journal of Physical Chemistry B*, 104(23):5406–5410, 2000.

[240] E. Moskovets and A. Vertes. Fast dynamics of ionization in ultraviolet matrix-assisted laser desorption ionization of biomolecules. *Journal of Physical Chemistry B*, 106(12): 3301–3306, 2002.

[241] M. W. Little, J.-K. Kim and K. K. Murray. Two-laser infrared and ultraviolet matrix-assisted laser desorption/ionization. *Journal of Mass Spectrometry*, 38(7):772–777, 2003.

[242] Y. Minegishi, J. Matsumoto, H. Shiromaru, K. Hashimoto and T. Fujino. Femtosecond time-resolved laser desorption/ionization mass spectrometry of perylene crystals using Raman-induced vibrational excitation. *Chemical Physics Letters*, 584:14–17, 2013.

[243] M. Dole, L. L. Mack, R. L. Hines, R. C. Mobley, L. D. Ferguson and M. B. Alice. Molecular beams of macroions. *The Journal of Chemical Physics*, 49(5):2240–2249, 1968.

[244] M. Yamashita and J. B. Fenn. Electrospray ion source. Another variation on the free-jet theme. *The Journal of Physical Chemistry*, 88(20):4451–4459, 1984.

[245] J. B. Fenn, M. Mann, C. K. Meng, S. F. Wong and C. M. Whitehouse. Electrospray Ionization for Mass Spectrometry of Large Biomolecules. *Science*, 246(4926):64–71, 1989.

[246] J. Fernández de la Mora. The Fluid Dynamics of Taylor Cones. *Annual Review of Fluid Mechanics*, 39:217–243, 2007.

[247] S. J. Gaskell. Electrospray: Principles and practice. *Journal of Mass Spectrometry*, 32(7):677–688, 1997.

[248] J. V. Iribarne and B. A. Thomson. On the evaporation of small ions from charged droplets. *The Journal of Chemical Physics*, 64(6):2287–2294, 1976.

[249] J. Fernandez De La Mora. Electrospray ionization of large multiply charged species proceeds via Dole's charged residue mechanism. *Analytica Chimica Acta*, 406(1):93–104, 2000.

[250] O. T. Ehrler, J. P. Yang, C. Hättig, A.-N. Unterreiner, H. Hippler and M. M. Kappes. Femtosecond pump/probe photoelectron spectroscopy of isolated C 60 negative ions. *The Journal of Chemical Physics*, 125(7):074312, 2006.

[251] J. Lecointre, G. M. Roberts, D. A. Horke and J. R. R. Verlet. Ultrafast relaxation dynamics observed through time-resolved photoelectron angular distributions. *The Journal of Physical Chemistry A*, 114(42):11216–11224, 2010.

[252] D. A. Horke and J. R. R. Verlet. Time-resolved photoelectron imaging of the chloranil radical anion: ultrafast relaxation of electronically excited electron acceptor states. *Physical Chemistry Chemical Physics*, 13(43):19546–19552, 2011.

[253] D. A. Horke, A. S. Chatterley and J. R. R. Verlet. Femtosecond photoelectron imaging of aligned polyanions: Probing molecular dynamics through the electron-anion Coulomb repulsion. *The Journal of Physical Chemistry Letters*, 3(7):834–838, 2012.

[254] D. A. Horke and J. R. R. Verlet. Photoelectron spectroscopy of the model GFP chromophore anion. *Physical Chemistry Chemical Physics*, 14(24):8511–8515, 2012.

[255] D. A. Horke, Q. Li, L. Blancafort and J. R. Verlet. Ultrafast above-threshold dynamics of the radical anion of a prototypical quinone electron-acceptor. *Nature Chemistry*, 5 (8):711–717, 2013.

[256] C. R. S. Mooney, D. A. Horke, A. S. Chatterley, A. Simperler, H. H. Fielding and J. R. R. Verlet. Taking the green fluorescence out of the protein: dynamics of the isolated GFP chromophore anion. *Chemical Science*, 4(3):921–927, 2013.

[257] A. S. Chatterley, C. W. West, V. G. Stavros and J. R. R. Verlet. Time-resolved photoelectron imaging of the isolated deprotonated nucleotides. *Chemical Science*, 5 (10):3963–3975, 2014.

[258] C. W. West, J. N. Bull, A. S. Hudson, S. L. Cobb and J. R. R. Verlet. Excited state dynamics of the isolated green fluorescent protein chromophore anion following UV excitation. *The Journal of Physical Chemistry B*, 119(10):3982–3987, 2015.

[259] A. V. Bulgakov, N. Goodfriend, O. Nerushev, N. M. Bulgakova, S. V. Starinskiy, Y. G. Shukhov and E. E. B. Campbell. Laser-induced transfer of nanoparticles for gas-phase analysis. *Journal of the Optical Society of America B*, 31(11):C15–C21, 2014.

[260] N. T. Goodfriend, S. V. Starinskiy, O. A. Nerushev, N. M. Bulgakova, A. V. Bulgakov and E. E. Campbell. Laser pulse duration dependence of blister formation on back-radiated Ti thin films for BB-LIFT. *Applied Physics A: Materials Science and Processing*, 122(3):154, 2016.

[261] T. V. Kononenko, P. Alloncle, V. I. Konov and M. Sentis. Laser transfer of diamond nanopowder induced by metal film blistering. *Applied Physics A: Materials Science and Processing*, 94(3):531–536, 2009.

[262] T. V. Kononenko, I. A. Nagovitsyn, G. K. Chudinova and I. N. Mihailescu. Application of clean laser transfer for porphyrin micropatterning. *Applied Surface Science*, 256 (9):2803–2808, 2010.

[263] T. V. Kononenko, I. A. Nagovitsyn, G. K. Chudinova and I. N. Mihailescu. Clean, cold, and liquid-free laser transfer of biomaterials. *Laser Physics*, 21(4):823–829, 2011.

[264] T. V. Kononenko, P. Alloncle, V. I. Konov and M. Sentis. Shadowgraphic imaging of laser transfer driven by metal film blistering. *Applied Physics A: Materials Science and Processing*, 102(1):49–54, 2011.

[265] N. T. Kattamis, N. D. McDaniel, S. Bernhard and C. B. Arnold. Laser direct write printing of sensitive and robust light emitting organic molecules. *Applied Physics Letters*, 94(10):103306, 2009.

[266] M. S. Brown, N. T. Kattamis and C. B. Arnold. Time-resolved study of polyimide absorption layers for blister-actuated laser-induced forward transfer. *Journal of Applied Physics*, 107(8):083103, 2010.

[267] N. Goodfriend, S. Y. Heng, O. A. Nerushev, A. V. Gromov, A. V. Bulgakov, M. Okada, R. Kitaura, J. Warner, H. Shinohara and E. Campbell. Blister-based-laser-induced-forward-transfer: A non-contact, dry laserbased transfer method for nanomaterials. *Nanotechnology*, 29:385031, 2018.

[268] B. Lindner and U. Seydel. Laser Desorption Mass Spectrometry of Nonvolatiles under Shock Wave Conditions. *Analytical Chemistry*, 57(4):895–899, 1985.

[269] B. Lindner. On the desorption of electrosprayed organic compounds from supporting metal foils by laser induced pressure waves. *International Journal of Mass Spectrometry and Ion Processes*, 103:203–218, 1991.

[270] A. V. Zinovev, I. V. Veryovkin, J. F. Moore and M. J. Pellin. Laser-Driven Acoustic Desorption of Organic Molecules from Back-Irradiated Solid Foils. *Analytical Chemistry*, 79(21):8232–8241, 2007.

[271] R. C. Shea, S. C. Habicht, W. E. Vaughn and H. I. Kenttämaa. Design and characterization of a high-power laser-induced acoustic desorption probe coupled with a fourier transform ion cyclotron resonance mass spectrometer. *Analytical Chemistry*, 79(7):2688–2694, 2007.

[272] A. V. Zinovev, I. V. Veryovkin and M. J. Pellin. Laser-induced desorption of organic molecules from front- and back- irradiated metal foils. *AIP Conference Proceedings*, 1104(1):200, 2009.

[273] A. Zinovev, I. Veryovkin and M. Pellin. Molecular Desorption by LaserDriven Acoustic Waves: Analytical Applications and Physical Mechanisms. In M. G. Beghi, editor, *Acoustic Waves - From Microdevices to Helioseismology*, pages 343–368. IntechOpen, 2011.

[274] Z. Huang, T. Ossenbrüggen, I. Rubinsky, M. Schust, D. A. Horke and J. Küpper. Development and Characterization of a Laser-Induced Acoustic Desorption Source. *Analytical Chemistry*, 90(6):3920–3927, 2018.

[275] V. V. Golovlev, S. L. Allman, W. R. Garrett, N. I. Taranenko and C. H. Chen. Laser-induced acoustic desorption. *International Journal of Mass Spectrometry and Ion Processes*, 169/170:69–78, 1997.

[276] L. Nyadong, J. P. Quinn, C. S. Hsu, C. L. Hendrickson, R. P. Rodgers and A. G. Marshall. Atmospheric Pressure Laser-Induced Acoustic Desorption Chemical Ionization Mass Spectrometry for Analysis of Saturated Hydrocarbons. *Analytical Chemistry*, 84(16):7131–7137, 2012.

[277] S. C. Habicht, L. M. Amundson, P. Duan, N. R. Vinueza and H. I. Kenttämaa. Laser-Induced Acoustic Desorption Coupled with a Linear Quadrupole Ion Trap Mass Spectrometer. *Analytical Chemistry*, 82(2):608–614, 2010.

[278] J. Gao, D. J. Borton II, B. C. Owen, Z. Jin, M. Hurt, L. M. Amundson, J. T. Madden, K. Qian and H. I. Kenttämaa. Laser-Induced Acoustic Desorption / Atmospheric Pressure Chemical Ionization Mass Spectrometry. *Journal of the American Society for Mass Spectrometry*, 22(16):531–538, 2011.

[279] J. Pérez, L. E. Ramírez-Arizmendi, C. J. Petzold, L. P. Guler, E. D. Nelson and H. I. Kenttämaa. Laser-induced acoustic desorption/chemical ionization in Fourier-transform ion cyclotron resonance mass spectrometry. *International Journal of Mass Spectrometry*, 198(3):173–188, 2000.

[280] R. C. Shea, C. J. Petzold, J. L. Campbell, S. Li, D. J. Aaserud and H. I. Kenttämaa. Characterization of laser-induced acoustic desorption coupled with a Fourier transform ion cyclotron resonance mass spectrometer. *Analytical Chemistry*, 78(17):6133–6139, 2006.

[281] U. Sezer, L. Wörner, J. Horak, L. Felix, J. Tüxen, C. Götz, A. Vaziri, M. Mayor and M. Arndt. Laser-induced acoustic desorption of natural and functionalized biochromophores. *Analytical Chemistry*, 87(11):5614–5619, 2015.

[282] W.-P. Peng, Y.-C. Yang, M.-W. Kang, Y.-K. Tzeng, Z. Nie, H.-C. Chang, W. Chang and C.-H. Chen. Laser-Induced Acoustic Desorption Mass Spectrometry of Single Bioparticles. *Angewandte Chemie International Edition*, 45(9):1423–1426, 2006.

[283] N. Zhang, K. Zhu, C. Xiong, Y. Jiang, H.-C. Chang and Z. Nie. Mass Measurement of Single Intact Nanoparticles in a Cylindrical Ion Trap. *Analytical Chemistry*, 88(11): 5958–5962, 2016.

[284] C. R. Calvert, L. Belshaw, M. J. Duffy, O. Kelly, R. B. King, A. G. Smyth, T. J. Kelly, J. T. Costello, D. J. Timson, W. A. Bryan, T. Kierspel, P. Rice, I. C. E. Turcu, C. M. Cacho, E. Springate, I. D. Williams and J. B. Greenwood. LIAD-fs scheme for studies of ultrafast laser interactions with gas phase biomolecules. *Physical Chemistry Chemical Physics*, 14(18):6289–6297, 2012.

[285] L. Belshaw, F. Calegari, M. J. Duffy, A. Trabattoni, L. Poletto, M. Nisoli and J. B. Greenwood. Observation of ultrafast charge migration in an amino acid. *The Journal of Physical Chemistry Letters*, 3(24):3751–3754, 2012.

[286] F. Calegari, D. Ayuso, A. Trabattoni, L. Belshaw, S. D. Camillis, S. Anumula, F. Frassetto, L. Poletto, A. Palacios, P. Decleva, J. B. Greenwood, F. Martín and M. Nisoli. Ultrafast electron dynamics in phenylalanine initiated by attosecond pulses. *Science*, 346(6207):336–339, 2014.

[287] S. D. Camillis, J. Miles, G. Alexander, O. Ghafur, I. D. Williams, D. Townsend and J. B. Greenwood. Ultrafast non-radiative decay of gas-phase nucleosides. *Physical Chemistry Chemical Physics*, 17(36):23643–23650, 2015.

[288] F. Calegari, A. Trabattoni, A. Palacios, D. Ayuso, M. C. Castrovilli, J. B. Greenwood, P. Decleva, F. Martín and M. Nisoli. Charge migration induced by attosecond pulses in bio-relevant molecules. *Journal of Physics B: Atomic, Molecular and Optical Physics*, 49(14):142001, 2016.

[289] E. P. Månsson, S. De Camillis, M. C. Castrovilli, M. Galli, M. Nisoli, F. Calegari and J. B. Greenwood. Ultrafast dynamics in the DNA building blocks thymidine and thymine initiated by ionizing radiation. *Physical Chemistry Chemical Physics*, 19(30): 19815–19821, 2017.

[290] T. H. Maiman. Stimulated Optical Radiation in Ruby. *Nature*, 187(4736):493, 1960.

[291] T. Gaumnitz, A. Jain, Y. Pertot, M. Huppert, I. Jordan, F. Ardana-Lamas and H. J. Wörner. Streaking of 43-attosecond soft-X-ray pulses generated by a passively CEP-stable mid-infrared driver. *Optics Express*, 25(22):27506–27518, 2017.

[292] C. Rullière. *Femtosecond Laser Pulses*. Springer-Verlag, New York, NY, 2 edition, 2005.

[293] A. E. Siegman. *Lasers*. University Science Books, Mill Valley, CA, 1986.

[294] S. Backus, C. G. Durfee, M. M. Murnane and H. C. Kapteyn. High power ultrafast lasers. *Review of Scientific Instruments*, 69(3):1207–1223, 1998.

[295] W. Koechner. *Solid-State Laser Engineering*. Springer, New York, NY, 6 edition, 2006.

[296] O. Svelto. *Principles of Lasers*. Springer, New York, NY, 5 edition, 2010.

[297] W. E. Lamb. Theory of an Optical Maser. *Physical Review*, 134:A1429–A1450, 1964.

[298] L. E. Hargrove, R. L. Fork and M. A. Pollack. Locking of {H}e-{N}e laser modes ninduced by synchronous intracavity modulatio. *Applied Physics Letters*, 5(1):4–5, 1964.

[299] D. E. Spence, P. N. Kean and W. Sibbett. 60-fsec pulse generation from a self-mode-locked Ti: sapphire laser. *Optics Letters*, 16(1):42–44, 1991.

[300] T. Brabec, C. Spielmann, P. F. Curley and F. Krausz. Kerr lens mode locking. *Optics Letters*, 17(18):1292–1294, 1992.

[301] A. Yariv. *Quantum Electronics*. John Wiley & Sons, New York, NY, 3 edition, 1989.

[302] M. Piché and F. Salin. Self-mode locking of solid-state lasers without apertures. *Optics Letters*, 18(13):1041–1043, 1993.

[303] T. Brabec, P. F. Curley, C. Spielmann, E. Wintner and A. J. Schmidt. Hard-aperture Kerr-lens mode locking. *Journal of the Optical Society of America B*, 10(6):1029–1034, 1993.

[304] Spectra-Physics. Tsunami-Mode-locked Ti:sapphire Laser User's Manual, 2002.

[305] Spectra-Physics. Millennia Pro s-Series Diode-Pumped, CW Visible Laser Systems User's Manual, 2007.

[306] Spectra-Physics. Spitfire Pro Ti:Sapphire Regenerative Amplifier Systems User Manual, 2004.

[307] Spectra-Physics. Empower Intercavity-Doubled, Diode-Pumped Nd:YLF Laser Systems User's Manual, 2005.

[308] D. Strickland and G. Mourou. Compression of amplified chirped optical pulses. *Optics Communications*, 56(3):219–221, 1985.

[309] P. Maine, D. Strickland, P. Bado, M. Pessot and G. Mourou. Generation of Ultrahigh Peak Power Pulses by Chirped Pulse Amplification. *IEEE Journal of Quantum Electronics*, 24(2):398–403, 1988.

[310] The International Commission on Non-Ionizing Radiation Protection. Giudelines on Limits of Exposure to Ultraviolet Radiation of Wavelengths Between 180 nm and 400 nm (Incoherent Optical Radiation). *Health Physics*, 87(2):171–186, 2004.

[311] R. H. Kingston. Parametric Amplification and Oscillation at Optical Frequencies. *Proceedings of the IRE*, 50(4):472, 1962.

[312] J. A. Giordmaine and R. C. Miller. Tunable Coherent Parametric Oscillation in LiNbO3 at Optical Frequencies. *Physical Review Letters*, 14(24):973–976, 1965.

[313] N. M. Kroll. Parametric amplification in spatially extended media and application to the design of tuneable oscillators at optical frequencies. *Physical Review*, 127(4): 1207–1211, 1962.

[314] C. C. Wang and G. W. Racette. Measurement of Parametric Gain Accompanying Optical Difference Frequency Generation. *Applied Physics Letters*, 6(8):169–171, 1965.

[315] M. Bass, P. A. Franken, A. E. Hill, C. W. Peters and G. Weinreich. Optical mixing. *Physical Review Letters*, 8(1):18, 1962.

[316] P. A. Franken, A. E. Hill, C. W. Peters and G. Weinreich. Generation of optical harmonics. *Physical Review Letters*, 7(4):118–119, 1961.

[317] W. T. Silvfast. *Laser Fundamentals*. Cambridge University Press, New York, NY, 2 edition, 2004.

[318] C. Li. *Nonlinear Optics: Principles and Applications*. Springer, Singapore, 2017.

[319] G. New. *Introduction to Nonlinear Optics*. Cambridge University Press, Cambridge, 2011.

[320] A. W. Smith and N. Braslau. Observation of an Optical Difference Frequency. *Journal of Applied Physics*, 34:2105–2106, 1963.

[321] J. H. Simmons and K. S. Potter. *Optical Materials*, volume 1. Academic Press, San Diego, CA, 2000.

[322] P. E. Powers. *Fundamentals of Nonlinear Optics*. CRC Press\ Taylor and Francis Group, Boca Raton, FL, 2011.

[323] J. A. Armstrong, N. Bloembergen, J. Ducuing and P. S. Pershan. Interactions between light waves in a nonlinear dielectric. *Physical Review*, 127(6):1918–1939, 1962.

[324] R. C. Miller, G. D. Boyd and A. Savage. Nonlinear optical interactions in LiNbO3 without double refraction. *Applied Physics Letters*, 6(4):77–79, 1965.

[325] P. D. Maker, R. W. Terhune, M. Nisenoff and C. M. Savage. Effects of Dispersion and Fosusing on the Production of Optical Harmonics. *Physical Review Letters*, 8(1): 21–22, 1962.

[326] G. D. Boyd, R. C. Miller, K. Nassau, W. L. Bond and A. Savage. LiNbO3: An efficient phase matchable nonlinear optical material. *Applied Physics Letters*, 5(11):234–236, 1964.

[327] G. R. Fowles. *Introduction to Modern Optics.pdf*. Dover, New York, NY, 2 edition, 1989.

[328] Spectra-Physics. OPA-800C Ultrafast Optical Parametric Amplifier User's Manual, 2003.

[329] D. N. Nikogosyan. Beta barium borate (BBO) - A review of its properties and applications. *Applied Physics A*, 52(6):359–368, 1991.

[330] K. Naganuma, K. Mogi and H. Yamada. Group-delay measurement using the Fourier transform of an interferometric cross correlation generated by white light. *Optics Letters*, 15(7):393–395, 1990.

[331] R. W. Boyd. *Nonlinear Optics*. Academic Press, London, 3 edition, 2008.

[332] W. E. Stephens. A Pulsed Mass Spectrometer with Time Dispersion. *Physical Review*, 69(12):691, 1946.

[333] A. E. Cameron and D. F. Eggers. An Ion "Velocitron". *Review of Scientific Instruments*, 19(9):605–607, 1948.

[334] R. W. Engstrom. *Photomultiplier Handbook: Theory, Design, Application*. RCA Corporation, Princeton, NJ, 1980.

[335] K. L. Brown and G. W. Tautfest. Faraday-Cup Monitors for High-Energy Electron Beams Faraday-Cup Monitors for High-Energy Electron Beams*. *Review of Scientific Instruments*, 27(9):696–702, 1956.

[336] N. R. Daly. Scintillation type mass spectrometer ion detector. *Review of Scientific Instruments*, 31(3):264–267, 1960.

[337] J. L. Wiza. Microchannel plate detectors. *Nuclear Instruments and Methods*, 162: 587–601, 1979.

[338] H. N. Sharma, E. A. Sangalang, C. K. Saw, G. A. Cairns, W. Mclean, R. S. Maxwell and L. N. Dinh. Volatility of the catalytic hydrogenation products of 1,4-bis(phenylethynyl)benzene. *The Journal of Chemical Physics*, 147:194701, 2017.

[339] PubChem. DL-phenylalanine vapor pressure, 2010. URL `https://pubchem.ncbi.nlm.nih.gov/compound/dl-phenylalanine{#}section=Vapor-Pressure`.

[340] B. C. Yadav. Structure, properties and applications of fullerenes. *International Journal of Nanotechnology and Applications*, 2(1):15–24, 2008.

[341] NIST. DL-Phenylalanine Electron Impact Ionisation Mass Spectrum, 2014. URL `https://webbook.nist.gov/cgi/cbook.cgi?ID=C150301{&}Mask=200{#}Mass-Spec`.

[342] NIST. Buckminsterfullerene Electron Impact Ionisation Mass Spectrum, 2014. URL `https://webbook.nist.gov/cgi/cbook.cgi?ID=C99685968{&}Mask=200{#}Mass-Spec`.

[343] S. Denifl, B. Sonnweber, G. Hanel, P. Scheier and T. D. Märk. Threshold electron impact ionization studies of uracil. *International Journal of Mass Spectrometry*, 238 (1):47–53, 2004.

[344] H. Lodish, A. Berk, P. Matsudaira, C. A. Kaiser, M. Krieger, M. P. Scott, L. Zipursky and J. Darnell. Basic Molecular Genetic Mechanisms. In *Molecular Cell Biology*, chapter 4, pages 101–145. W.H.Freeman & Co Ltd, New York, NY, 5th edition, 2004.

[345] H. Nieber and N. L. Doltsinis. Elucidating ultrafast nonradiative decay of photoexcited uracil in aqueous solution by ab initio molecular dynamics. *Chemical Physics*, 347(1-3):405–412, 2008.

[346] Z. Lan, E. Fabiano and W. Thiel. Photoinduced nonadiabatic dynamics of pyrimidine nucleobases: On-the-fly surface-hopping study with semiempirical methods. *The Journal of Physical Chemistry B*, 113(11):3548–3555, 2009.

[347] B. P. Fingerhut, K. E. Dorfman and S. Mukamel. Monitoring nonadiabatic dynamics of the RNA base uracil by UV pump-IR probe spectroscopy. *The Journal of Physical Chemistry Letters*, 4(11):1933–1942, 2013.

[348] B. P. Fingerhut, K. E. Dorfman and S. Mukamel. Probing the conical intersection dynamics of the RNA base uracil by UV-pump stimulated-raman-probe signals; Ab initio simulations. *Journal of Chemical Theory and Computation*, 10(3):1172–1188, 2014.

[349] D. Nachtigallová, A. J. Aquino, J. J. Szymczak, M. Barbatti, P. Hobza and H. Lischka. Nonadiabatic dynamics of uracil: Population split among different decay mechanisms. *The Journal of Physical Chemistry A*, 115(21):5247–5255, 2011.

[350] M. Richter, S. Mai, P. Marquetand and L. González. Ultrafast intersystem crossing dynamics in uracil unravelled by ab initio molecular dynamics. *Physical Chemistry Chemical Physics*, 16(44):24423–24436, 2014.

[351] H. Kang, K. T. Lee, B. Jung, Y. J. Ko and S. K. Kim. Intrinsic lifetimes of the excited state of DNA and RNA bases. *Journal of the American Chemical Society*, 124(44): 12958–12959, 2002.

[352] S. Ullrich, T. Schultz, M. Z. Zgierski and A. Stolow. Electronic relaxation dynamics in DNA and RNA bases studied by time-resolved photoelectron spectroscopy. *Physical Chemistry Chemical Physics*, 6(10):2796–2801, 2004.

[353] C. Canuel, M. Mons, F. Piuzzi, B. Tardivel, I. Dimicoli and M. Elhanine. Excited states dynamics of DNA and RNA bases: Characterization of a stepwise deactivation pathway in the gas phase. *The Journal of Chemical Physics*, 122(7):074316, 2005.

[354] M. Schneider, C. Schon, I. Fischer, L. Rubio-Lago and T. Kitsopoulos. Photodissociation of uracil. *Physical Chemistry Chemical Physics*, 9(45):6021–6026, 2007.

[355] S. Matsika, C. Zhou, M. Kotur and T. C. Weinacht. Combining dissociative ionization pumpprobe spectroscopy and ab initio calculations to interpret dynamics and control through conical intersections. *Faraday Discussions*, 153:247–260, 2011.

[356] M. Kotur, T. C. Weinacht, C. Zhou and S. Matsika. Following ultrafast radiationless relaxation dynamics with strong field dissociative ionization: A comparison between adenine, uracil, and cytosine. *IEEE Journal on Selected Topics in Quantum Electronics*, 18(1):187–194, 2012.

[357] S. Matsika, M. Spanner, M. Kotur and T. C. Weinacht. Ultrafast relaxation dynamics of uracil probed via strong field dissociative ionization. *The Journal of Physical Chemistry A*, 117(48):12796–12801, 2013.

[358] B. Barc, M. Ryszka, J. Spurrell, M. Dampc, P. Limão-Vieira, R. Parajuli, N. J. Mason and S. Eden. Multi-photon ionization and fragmentation of uracil: Neutral excited-state ring opening and hydration effects. *The Journal of Chemical Physics*, 139(24): 244311, 2013.

[359] M. Ligare, F. Siouri, O. Bludsky, D. Nachtigallová and M. S. de Vries. Characterizing the dark state in thymine and uracil by double resonant spectroscopy and quantum computation. *Physical Chemistry Chemical Physics*, 17(37):24336–24341, 2015.

[360] H. Yu, J. A. Sánchez-Rodríguez, M. Pollum, C. E. Crespo-Hernández, S. Mai, P. Marquetand, L. González and S. Ullrich. Internal conversion and intersystem crossing pathways in UV excited, isolated uracils and their implications in prebiotic chemistry. *Physical Chemistry Chemical Physics*, 18(30):20168–20176, 2016.

[361] S. Matsika. Radiationless decay of excited states of uracil through conical intersections. *The Journal of Physical Chemistry A*, 108(37):7584–7590, 2004.

[362] S. Matsika. Three-State Conical Intersections in Nucleic Acid Bases. *The Journal of Physical Chemistry A*, 109(33):7538–7545, 2005.

[363] M. Z. Zgierski, S. Patchkovskii, T. Fujiwara and E. C. Lim. On the origin of the ultrafast internal conversion of electronically excited pyrimidine bases. *The Journal of Physical Chemistry A*, 109(42):9384–9387, 2005.

[364] M. Merchán, R. González-Luque, T. Climent, L. Serrano-Andrés, E. Rodríguez, M. Reguero and D. Peláez. Unified model for the ultrafast decay of pyrimidine nucleobases. *The Journal of Physical Chemistry B*, 110(51):26471–26476, 2006.

[365] T. Climent, R. González-Luque, M. Merchán and L. Serrano-Andrés. On the intrinsic population of the lowest triplet state of uracil. *Chemical Physics Letters*, 441(4-6): 327–331, 2007.

[366] H. R. Hudock, B. G. Levine, A. L. Thompson, H. Satzger, D. Townsend, N. Gador, S. Ullrich, A. Stolow and T. J. Martínez. Ab Initio molecular dynamics and time-resolved photoelectron spectroscopy of electronically excited uracil and thymine. *The Journal of Physical Chemistry A*, 111(34):8500–8508, 2007.

[367] E. Epifanovsky, K. Kowalski, P.-D. Fan, M. Valiev, S. Matsika and A. I. Krylov. On the Electronically Excited States of Uracil. *The Journal of Physical Chemistry A*, 112 (40):9983–9992, 2008.

[368] M. Etinski, T. Fleig and C. M. Marian. Intersystem crossing and characterization of dark states in the pyrimidine nucleobases uracil, thymine, and 1-methylthymine. *The Journal of Physical Chemistry A*, 113(43):11809–11816, 2009.

[369] M. Barbatti, A. J. A. Aquino and H. Lischka. Molecular mechanisms of the photostability of life. *Physical Chemistry Chemical Physics*, 12(19):4959–4967, 2010.

[370] M. Barbatti, A. J. A. Aquino, J. J. Szymczak, D. Nachtigallová, P. Hobza and H. Lischka. Relaxation mechanisms of UV-photoexcited DNA and RNA nucleobases. *Proceedings of the National Academy of Sciences of the United States of America*, 107 (50):21453–21458, 2010.

[371] V. B. Delchev, A. L. Sobolewski and W. Domcke. Comparison of the non-radiative decay mechanisms of 4-pyrimidinone and uracil: an ab initio study. *Physical Chemistry Chemical Physics*, 12(19):5007–5015, 2010.

[372] P. Carbonniere, C. Pouchan and R. Improta. Intramolecular vibrational redistribution in the non-radiative excited state decay of uracil in the gas phase: an ab initio molecular dynamics study. *Physical Chemistry Chemical Physics*, 17(17):11615–11626, 2015.

[373] M. Ryszka, R. Pandey, C. Rizk, J. Tabet, B. Barc, M. Dampc, N. J. Mason and S. Eden. Dissociative multi-photon ionization of isolated uracil and uracil-adenine complexes. *International Journal of Mass Spectrometry*, 396:48–54, 2016.

[374] H.-W. Jochims, M. Schwell, H. Baumgärtel and S. Leach. Photoion mass spectrometry of adenine, thymine and uracil in the 6-22 eV photon energy range. *Chemical Physics*, 314(1-3):263–282, 2005.

[375] J. A. Sánchez-Rodríguez, A. Mohamadzade, S. Mai, B. Ashwood, M. Pollum, P. Marquetand, L. González, C. E. Crespo-Hernández and S. Ullrich. 2-Thiouracil intersystem crossing photodynamics studied by wavelength-dependent photoelectron and transient absorption spectroscopies. *Physical Chemistry Chemical Physics*, 19(30): 19756–19766, 2017.

[376] K.-W. Choi, J.-H. Lee and S. K. Kim. Vacuum-ultraviolet ionization spectroscopy of the jet-cooled RNA-base uracil. *Chemical Communications*, pages 78–79, 2006.

[377] K. Watanabe, T. Nakayama and J. Mottl. Ionization potentials of some molecules. *Journal of Quantitative Spectroscopy and Radiative Transfer*, 2(4):369–382, 1962.

[378] B. J. Cocksey, J. H. D. Eland and C. J. Danby. The effect of alkyl substitution on ionisation potential. *Journal of Chemical Society B : Physical Organic*, 0:790–792, 1971.

[379] A. R. Katritzky, G. Baykut, S. Rachwal, M. Szafran, K. C. Caster and J. Eyler. The tautomeric equilibria of thio analogues of nucleic acid bases. Part 1. 2-Thiouracil: background, preparation of model compounds, and gas-phase proton affinities. *Journal of the Chemical Society, Perkin Transactions 2*, 0:1499–1506, 1989.

[380] B. Sundqvist. Thermal diffusivity and thermal conductivity of Chromel, Alumel, and Constantan in the range 100-450 K. *Journal of Applied Physics*, 72(2):539–545, 1992.

[381] M. J. Assael and K. Gialou. Measurement of the Thermal Conductivity of Stainless Steel AISI 304L up to 550 K. *International Journal of Thermophysics*, 24(4):1145–1153, 2003.

[382] G. B. Sabine. Refiectivities of Evaporated Metal Films in the Near and Far Ultraviolet. *Physical Review*, 55(11):1064–1069, 1939.

[383] J. Rejnek, M. Hanus, M. Kabeláč, F. Ryjáček and P. Hobza. Correlated ab initio study of nucleic acid bases and their tautomers in the gas phase, in a microhydrated environment and in aqueous solution. Part 4. Uracil and thymine. *Physical Chemistry Chemical Physics*, 7(9):2006–2017, 2005.

[384] B. M. Giuliano, V. Feyer, K. C. Prince, M. Coreno, L. Evangelisti, S. Melandri and W. Caminati. Tautomerism in 4-Hydroxypyrimidine , S -Methyl-2-thiouracil , and 2-Thiouracil. *The Journal of Physical Chemistry A*, 114(48):12725–12730, 2010.

[385] C. Puzzarini, M. Biczysko, V. Barone, I. Peña, C. Cabezas and J. L. Alonso. Accurate molecular structure and spectroscopic properties of nucleobases: a combined computationalmicrowave investigation of 2-thiouracil as a case study. *Physical Chemistry Chemical Physics*, 15(39):16965–16975, 2013.

[386] C. Puzzarini, M. Biczysko and V. Barone. Accurate anharmonic vibrational frequencies for uracil: The performance of composite schemes and hybrid CC/DFT model. *Journal of Chemical Theory and Computation*, 7(11):3702–3710, 2011.

[387] M. A. Palafox, V. K. Rastogi, R. P. Tanwar and L. Mittal. Vibrational frequencies and structure of 2-thiouracil by Hartree-Fock, post-Hartree-Fock and density functional methods. *Spectrochimica Acta - Part A: Molecular and Biomolecular Spectroscopy*, 59 (11):2473–2486, 2003.

[388] L. Serrano-Andrés and M. Merchán. Are the five natural DNA/RNA base monomers a good choice from natural selection?. A photochemical perspective. *Journal of Photochemistry and Photobiology C: Photochemistry Reviews*, 10(1):21–32, 2009.

[389] B. Coupier, B. Farizon, M. Farizon, M. J. Gaillard, F. Gobet, N. V. de Castro Faria, G. Jalbert, S. Ouaskit, M. Carré, B. Gstir, G. Hanel, S. Denifl, L. Feketeova, P. Scheier and T. D. Märk. Inelastic interactions of protons and electrons with biologically relevant molecules. *The European Physical Journal D - Atomic, Molecular, Optical and Plasma Physics*, 20(3):459–468, 2002.

[390] A. Le Padellec, P. Moretto-Capelle, M. Richard-Viard, J. P. Champeaux and P. Cafarelli. Ionization and fragmentation of DNA, RNA bases induced by proton impact. *Journal of Physics: Conference Series*, 101:1 012007, 2008.

[391] J. Tabet, S. Eden, S. Feil, H. Abdoul-Carime, B. Farizon, M. Farizon, S. Ouaskit and T. D. Märk. 20-150-keV proton-impact-induced ionization of uracil: Fragmentation ratios and branching ratios for electron capture and direct ionization. *Physical Review A - Atomic, Molecular, and Optical Physics*, 81(1):012711, 2010. ISSN 10502947.

[392] J. M. Rice, G. O. Dudek and M. Barber. Mass Spectra of Nucleic Acid Derivatives. Pyrimidines. *Journal of the American Chemical Society*, 87(20):4569–4576, 1965.

[393] S. M. Hecht, A. S. Gupta and N. J. Leonard. Position of uridine thiation: The identification of minor nucleosides from transfer RNA by mass spectrometry. *Biochimica et Biophysica Acta (BBA) - Nucleic Acids and Protein Synthesis*, 182(2):444–448, 1969.

[394] M. Imhoff, Z. Deng and M. A. Huels. Ionizing fragmentation of uracil and 5-bromouracil by electron impact in gas phase and hyperthermal Ar+ ion irradiation in condensed phase. *International Journal of Mass Spectrometry*, 262(1-2):154–160, 2007.

[395] C. Zhou, S. Matsika, M. Kotur and T. C. Weinacht. Fragmentation pathways in the uracil radical cation. *The Journal of Physical Chemistry A*, 116(37):9217–9227, 2012.

[396] S. Mai, P. Marquetand and L. González. Intersystem Crossing Pathways in the Noncanonical Nucleobase 2-Thiouracil: A Time-Dependent Picture. *The Journal of Physical Chemistry Letters*, 7(11):1978–1983, 2016. ISSN 19487185.

[397] M. Assmann, H. Köppel and S. Matsika. Photoelectron spectrum and dynamics of the uracil cation. *The Journal of Physical Chemistry A*, 119(5):866–875, 2015. ISSN 15205215.

[398] M. Assmann, T. Weinacht and S. Matsika. Surface hopping investigation of the relaxation dynamics in radical cations. *Journal of Chemical Physics*, 144(3):034301, 2016.

[399] L. B. Clark, G. G. Peschel and I. Tinoco. Vapor Spectra and Heats of Vaporization of Some Purine and Pyrimidine Bases 1. *The Journal of Physical Chemistry*, 69(10): 3615–3618, 1965.

[400] R. Weinkauf, P. Aicher, G. Wesley, J. Grotemeyer and E. W. Schlag. Femtosecond versus nanosecond multiphoton ionization and dissociation of large molecules. *The Journal of Physical Chemistry*, 98(34):8381–8391, 1994.

[401] K. P. Aicher, U. Wilhelm and J. Grotemeyer. Multiphoton ionization of molecules: A comparison between femtosecond and nanosecond laser pulse ionization efficiency. *Journal of the American Society for Mass Spectrometry*, 6(11):1059–1068, 1995.

[402] K. W. D. Ledingham and R. P. Singhal. High intensity laser mass spectrometry - A review. *International Journal of Mass Spectrometry and Ion Processes*, 163:149–168, 1997.

[403] J. Matsumoto, C.-H. Lin and T. Imasaka. Supersonic jet multiphoton ionization mass spectrometry using nanosecond and femtosecond pulse lasers. *Analytica Chimica Acta*, 343(1-2):129–133, 1997.

[404] N. Lockyer and J. Vickerman. Multiphoton ionization mass spectrometry of small biomolecules with nanosecond and femtosecond laser pulses. *International Journal of Mass Spectrometry*, 176(1-2):77–86, 1998.

[405] T. H. Nasti and L. Timares. MC1R, eumelanin and pheomelanin: Their role in determining the susceptibility to skin cancer. *Photochemistry and Photobiology*, 91 (1):188–200, 2015.

[406] F. Solano. Photoprotection versus photodamage: updating an old but still unsolved controversy about melanin. *Polymer International*, 65(11):1276–1287, 2016.

[407] K. Takeuchi, Y. Satou, H. Yamamoto and N. Satoh. A genome-wide survey of genes for enzymes involved in pigment synthesis in an ascidian, Ciona intestinalis. *Zoological Science*, 22(7):723–734, 2005.

[408] A. L. Kadekaro, R. J. Kavanagh, K. Wakamatsu, S. Ito, M. A. Pipitone and Z. A. Abdel-Malek. Cutaneous photobiology. The melanocyte vs. the sun: Who will win the final round? *Pigment Cell Research*, 16(5):434–447, 2003.

[409] M. Brenner and V. J. Hearing. The Protective Role of Melain Against UV Damage in Human Skin. *Photochemistry and Photobiology*, 84(3):539–549, 2008.

[410] H. S. Raper. THE AEROBIC OXIDASES. *Physiological Reviews*, 8(2):245–282, 1928.

[411] M. D'Ischia, A. Napolitano and A. Pezzella. 5,6-dihydroxyindole chemistry: Unexplored opportunities beyond eumelanin. *European Journal of Organic Chemistry*, 2011 (28):5501–5516, 2011.

[412] J. B. Nofsinger, S. E. Forest and J. D. Simon. Explanation for the Disparity among Absorption and Action Spectra of Eumelanin. *The Journal of Physical Chemistry B*, 103(51):11428–11432, 1999.

[413] J. D. Simon. Spectroscopic and dynamic studies of the epidermal chromophores trans-urocanic acid and eumelanin. *Accounts of Chemical Research*, 33(5):307–313, 2000.

[414] P. Meredith and J. Riesz. Radiative Relaxation Quantum Yields for Synthetic Eumelanin. *Photochemistry and Photobiology*, 79(2):211–216, 2004.

[415] P. Meredith, B. J. Powell, J. Riesz, S. P. Nighswander-Rempel, M. R. Pederson and E. G. Moore. Towards structure-property-function relationships for eumelanin. *Soft Matter*, 2(1):37–44, 2006.

[416] J. Riesz, J. Gilmore and P. Meredith. Quantitative scattering of melanin solutions. *Biophysical Journal*, 90(11):4137–4144, 2006.

[417] L. Sangaletti, S. Pagliara, P. Vilmercati, C. Castellarin-Cudia, P. Borghetti, P. Galinetto, R. Gebauer and A. Goldoni. Electronic excitations in synthetic eumelanin aggregates probed by soft X-ray spectroscopies. *The Journal of Physical Chemistry B*, 111(19):5372–5376, 2007.

[418] G. Perna, M. Lasalvia and V. Capozzi. Vibrational spectroscopy of synthetic and natural eumelanin. *Polymer International*, 65(11):1323–1330, 2016.

[419] S. E. Forest, W. C. Lam, D. P. Millar, J. B. Nofsinger and J. D. Simon. A Model for the Activated Energy Transfer within Eumelanin Aggregates. *The Journal of Physical Chemistry B*, 104(4):811–814, 2000.

[420] J. B. Nofsinger and J. D. Simon. Radiative relaxation of Sepia eumelanin is affected by aggregation. *Photochemistry and Photobiology*, 74(1):31–37, 2001.

[421] J. B. Nofsinger, T. Ye and J. D. Simon. Ultrafast Nonradiative Relaxation Dynamics of Eumelanin. *The Journal of Physical Chemistry B*, 105(14):2864–2866, 2001.

[422] Y. Liu and J. D. Simon. Isolation and Biophysical Studies of Natural Eumelanins : Applications of Imaging Technologies and Ultrafast Spectroscopy. *Pigment Cell Research*, 16(6):606–618, 2003.

[423] T. Ye and J. D. Simon. Comparison of the Ultrafast Absorption Dynamics of Eumelanin and Pheomelanin. *The Journal of Physical Chemistry B*, 107(40):11240–11244, 2003.

[424] P. Meredith and T. Sarna. The physical and chemical properties of eumelanin. *Pigment Cell Research*, 19(6):572–594, 2006.

[425] S. P. Nighswander-Rempel, I. B. Mahadevan, H. Rubinsztein-Dunlop and P. Meredith. Time-Resolved and Steady-State Fluorescence Spectroscopy of Eumelanin and Indolic Polymers. *Photochemistry and Photobiology*, 83(6):1449–1454, 2007.

[426] I. R. Piletic, T. E. Matthews and W. S. Warren. Probing Near-Infrared Photorelaxation Pathways in Eumelanins and Pheomelanins. *The Journal of Physical Chemistry A*, 114(43):11483–11491, 2010.

[427] A. Aloi, A. Brunetti, G. Perna, V. Capozzi and R. Tommasi. Ultrafast transient absorption of eumelanin suspensions : the role of inverse Raman scattering. *Biomedical Optics Express*, 6(10):4000–4013, 2015.

[428] B. Marchetti and T. N. Karsili. Theoretical insights into the photo-protective mechanisms of natural biological sunscreens: Building blocks of eumelanin and pheomelanin. *Physical Chemistry Chemical Physics*, 18(5):3644–3658, 2016.

[429] L. E. Bolívar-Marinez, D. S. Galvão and M. J. Caldas. Geometric and Spectroscopic Study of Some Molecules Related to Eumelanins . 1 . Monomers. *The Journal of Physical Chemistry B*, 103(15):2993–3000, 1999.

[430] K. B. Stark, J. M. Gallas, G. W. Zajac, M. Eisner and J. T. Golab. Spectroscopic Study and Simulation from Recent Structural Models for Eumelanin: I. Monomer, Dimers. *The Journal of Physical Chemistry B*, 107(13):3061–3067, 2003.

[431] Y. V. Il'ichev and J. D. Simon. Building Blocks of Eumelanin : Relative Stability and Excitation Energies of Tautomers of. *The Journal of Physical Chemistry B*, 107(29): 7162–7171, 2003.

[432] B. J. Powell, T. Baruah, N. Bernstein, K. Brake, R. H. McKenzie, P. Meredith and M. R. Pederson. A first-principles density-functional calculation of the electronic and vibrational structure of the key melanin monomers. *The Journal of Chemical Physics*, 120(18):8608–8615, 2004.

[433] A. L. Sobolewski and W. Domcke. Photophysics of Eumelanin : Ab Initio Studies on the Electronic Spectroscopy and Photochemistry of 5 , 6-Dihydroxyindole. *ChemPhysChem*, 8(5):756–762, 2007.

[434] M. Mandal, T. Das, B. K. Grewal and D. Ghosh. Feasibility of Ionization-Mediated Pathway for Ultraviolet-Induced Melanin Damage. *The Journal of Physical Chemistry B*, 119(42):13288–13293, 2015.

[435] A. Datar and A. Hazra. Pathways for Excited-State Nonradiative Decay of 5,6-Dihydroxyindole, a Building Block of Eumelanin. *The Journal of Physical Chemistry A*, 121(14):2790–2797, 2017.

[436] P. Ghosh and D. Ghosh. Elucidating the Photoprotection Mechanism of Eumelanin Monomers. *The Journal of Physical Chemistry B*, 121(24):5988–5994, 2017.

[437] M. D'Ischia, O. Crescenzi, A. Pezzella, M. Arzillo, L. Panzella, A. Napolitano and V. Barone. Structural effects on the electronic absorption properties of 5,6-dihydroxyindole oligomers: The potential of an integrated experimental and DFT approach to model eumelanin optical properties. *Photochemistry and Photobiology*, 84(3):600–607, 2008.

[438] G. Prampolini, I. Cacelli and A. Ferretti. Intermolecular interactions in eumelanins: A computational bottom-up approach. I. small building blocks. *RSC Advances*, 5(48): 38513–38526, 2015.

[439] D. Tuna, A. Udvarhelyi, A. L. Sobolewski, W. Domcke and T. Domratcheva. Onset of the Electronic Absorption Spectra of Isolated and π-Stacked Oligomers of 5,6-Dihydroxyindole: An Ab Initio Study of the Building Blocks of Eumelanin. *The Journal of Physical Chemistry B*, 120(14):3493–3502, 2016.

[440] M. Gauden, A. Pezzella, L. Panzella, A. Napolitano, M. D'Ischia and V. Sundström. Ultrafast excited state dynamics of 5,6-dihydroxyindole, a key eumelanin building block: nonradiative decay mechanism. *The Journal of Physical Chemistry B*, 113(37): 12575–12580, 2009.

[441] A. Huijser, A. Pezzella and V. Sundström. Functionality of epidermal melanin pigments : current knowledge on UV-dissipative mechanisms and research perspectives. *Physical Chemistry Chemical Physics*, 13(20):9119–9127, 2011.

[442] A. Corani, A. Huijser, A. Iadonisi, A. Pezzella, V. Sundström and M. D'Ischia. Bottom-Up approach to eumelanin photoprotection: Emission dynamics in parallel sets of water-soluble 5,6-dihydroxyindole-based model systems. *The Journal of Physical Chemistry B*, 116(44):13151–13158, 2012.

[443] J. J. Nogueira, A. Corani, A. El Nahhas, A. Pezzella, M. D'Ischia, L. González and V. Sundström. Sequential Proton-Coupled Electron Transfer Mediates Excited-State Deactivation of a Eumelanin Building Block. *The Journal of Physical Chemistry Letters*, 8(5):1004–1008, 2017.

[444] B. J. Powell. 5,6-Dihydroxyindole-2-carboxylic acid: A first principles density functional study. *Chemical Physics Letters*, 402(1-3):111–115, 2005.

[445] S. Olsen, J. Riesz, I. Mahadevan, A. Coutts, J. P. Bothma, B. J. Powell, R. H. McKenzie, S. C. Smith and P. Meredith. Convergent proton-transfer photocycles violate mirror-image symmetry in a key melanin monomer. *Journal of the American Chemical Society*, 129(21):6672–6673, 2007.

[446] A. Huijser, A. Pezzella, J. K. Hannestad, L. Panzella, A. Napolitano and V. Sundström. UV-Dissipation Mechanisms in the Eumelanin Building Block DHICA. *ChemPhysChem*, 11(11):2424–2431, 2010.

[447] A. Corani, A. Pezzella, T. Pascher, T. Gustavsson, D. Markovitsi, A. Huijser, M. D'Ischia and V. Sundstrom. Excited-State Proton-Transfer Processes of DHICA Resolved: From Sub-Picoseconds to Nanoseconds. *The Journal of Physical Chemistry Letters*, 4(9):1383–1388, 2013.

[448] A. Corani, A. Huijser, T. Gustavsson, D. Markovitsi, P.-Å. Malmqvist, A. Pezzella, M. D'Ischia and V. Sundstrom. Superior Photoprotective Motifs and Mechanisms in Eumelanins Uncovered. *Journal of the American Chemical Society*, 136(33):11626–11635, 2014.

[449] J. Catalán, P. Perez and A. U. Acuña. Indole spectroscopy: The location of the 1La and 1Lb electronic states and the absorption spectrum. *Journal of Molecular Structure*, 142:179–182, 1986.

[450] D. Robinson, N. A. Besley, E. A. Lunt, P. O'Shea and J. D. Hirst. Electronic structure of 5-hydroxyindole: from gas phase to explicit solvation. *The Journal of Physical Chemistry B*, 113(8):2535–2541, 2009.

[451] O. Oeltermann, C. Brand, M. Wilke and M. Schmitt. Ground and electronically excited singlet state structures of the syn and anti rotamers of 5-hydroxyindole. *The Journal of Physical Chemistry A*, 116(30):7873–7879, 2012.

[452] T. A. Oliver, G. A. King and M. N. Ashfold. Position matters: Competing O-H and N-H photodissociation pathways in hydroxy- and methoxy-substituted indoles. *Physical Chemistry Chemical Physics*, 13(32):14646–14662, 2011.

[453] Y. Huang and M. Sulkes. Anomalously short fluorescence lifetimes in jet cooled 4-hydroxyindole. Evidence for excited state tautomerism and proton transfer in clusters. *Chemical Physics Letters*, 254(3-4):242–248, 1996.

[454] S. Arnold, L. Tong and M. Strikes. Fluorescence lifetimes of substituted indoles in solution and in free jets: Evidence for intramolecular charge-transfer quenching. *The Journal of Physical Chemistry*, 98(9):2325–2327, 1994.

[455] M. Sulkes and I. Borthwick. Enhanced photophysical effects in indole due to C-6 chemical group substitutions. *Chemical Physics Letters*, 279(5-6):315–318, 1997.

[456] X. Meng, T. Harricharran and L. J. Juszczak. A spectroscopic survey of substituted indoles reveals consequences of a stabilized 1Lb transition. *Photochemistry and Photobiology*, 89(1):40–50, 2013.

[457] A. Napolitano, A. Pezzella, G. Prota, R. Seraglia and P. Traldi. Structural Analysis of Synthetic Melanins from Desorption/Ionization Mass Spectrometry. *Rapid Communications in Mass Spectrometry*, 10(4):468–472, 1996.

[458] S. Reale, M. Crucianelli, A. Pezzella and F. D. Angelis. Exploring the frontiers of synthetic eumelanin polymers by high-resolution matrix-assisted laser / desorption ionization mass spectrometry . *Journal of Mass Spectrometry*, 41(1):49–53, 2012.

[459] A. Bertazzo, C. V. Costa, G. Allegri, D. Favretto and P. Traldi. Application of matrix-assisted laser desorption/ionization mass spectrometry to the detection of melanins formed from Dopa and dopamine. *Journal of Mass Spectrometry*, 34(9):922–929, 1999.

[460] A. Bertazzo, D. Favretto, C. V. Costa, G. Allegri and P. Traldi. Effects of ultraviolet irradiation on melanogenesis from tyrosine, Dopa and dopamine: a matrix-assisted laser desorption/ionization mass spectrometric study. *Rapid communications in mass spectrometry*, 14(19):1862–1868, 2000.

[461] C. Kroesche and M. G. Peter. Detection of Melanochromes by MALDI-TOF Mass Spectrometry. *Tetrahedron*, 52(11):3947–3952, 1996.

[462] L. Novellino, M. D'Ischia and G. Prota. Expedient Synthesis of 5,6-Dihydroxyindole and Derivatives via an Improved Zn(II)-Assisted 2,β-Dinitrostyrene Approach. *Synthesis*, 1999(5):793–796, 1999.

[463] G. R. Humphrey and J. T. Kuethe. Practical methodologies for the synthesis of indoles. *Chemical Reviews*, 106(7):2875–2911, 2006.

[464] W. G. Mallard, J. H. Miller and K. C. Smyth. The ns Rydberg series of 1,3-trans-butadiene observed using multiphoton ionization. *The Journal of Chemical Physics*, 79(12):5900–5905, 1983.

[465] EPA. 5,6-dihydroxyindole Predicted Vapor Pressures, 2018. URL `https://comptox.epa.gov/dashboard/dsstoxdb/results?search=DTXSID20185242{#}vp`.

[466] L. Lagesson-Andrasko and V. Lagesson. *Handbook of Ultraviolet Spectra, Vapor Phase 168 - 330 nm.* GC-UV Center, Kobergsgränd, 1 edition, 2005.

[467] G. N. Patwari, S. Doraiswamy and S. Wategaonkar. Spectroscopy and IVR in the S1 State of Jet-Cooled p-Alkoxyphenols. *The Journal of Physical Chemistry A*, 104(37): 8466–8474, 2000. ISSN 10895639.

[468] G. N. Patwari and S. Wategaonkar. Does inversion symmetry influence IVR? *Chemical Physics Letters*, 323(5-6):460–466, 2000.

[469] R. Matsumoto, K. Sakeda, Y. Matsushita, T. Suzuki and T. Ichimura. Spectroscopy and relaxation dynamics of photoexcited anisole and anisole-d3 molecules in a supersonic jet. *Journal of Molecular Structure*, 735-736:153–167, 2005.

[470] G. M. Roberts, A. S. Chatterley, J. D. Young and V. G. Stavros. Direct observation of hydrogen tunneling dynamics in photoexcited phenol. *The Journal of Physical Chemistry Letters*, 3(3):348–352, 2012.

[471] A. S. Chatterley, J. D. Young, D. Townsend, J. M. Żurek, M. J. Paterson, G. M. Roberts and V. G. Stavros. Manipulating dynamics with chemical structure: Probing vibrationally- enhanced tunnelling in photoexcited catechol. *Physical Chemistry Chemical Physics*, 15(18):6879–6892, 2013.

[472] S. T. Park, A. Gahlmann, Y. He, J. S. Feenstra and A. H. Zewail. Ultrafast electron diffraction reveals dark structures of the biological chromophore indole. *Angewandte Chemie - International Edition*, 47(49):9496–9499, 2008.

[473] J. Fernández de la Mora and P. Riesco-Chueca. Aerodynamic focusing of particles in a carrier gas. *Journal of Fluid Mechanics*, 195:1–21, 1988.

[474] J. Fernández de la Mora and J. Rosell-Llompart. Aerodynamic focusing of heavy molecules in seeded supersonic jets. *The Journal of Chemical Physics*, 91(4):2603–2615, 1989.

[475] X. Wang, F. E. Kruis and P. H. McMurry. Aerodynamic Focusing of Nanoparticles : I . Guidelines for Designing Aerodynamic Lenses for Nanoparticles. *Aerosol Science and Technology*, 39(7):611–623, 2005.

[476] P. Piseri, H. Vahedi Tafreshi and P. Milani. Manipulation of nanoparticles in supersonic beams for the production of nanostructured materials. *Current Opinion in Solid State and Materials Science*, 8(3-4):195–202, 2004.

[477] X. Wang and P. H. Mcmurry. A Design Tool for Aerodynamic Lens Systems. *Aerosol Science and Technology*, 40:320–334, 2006.

[478] P. Piseri, A. Podestà, E. Barborini and P. Milani. Production and characterization of highly intense and collimated cluster beams by inertial focusing in supersonic expansions. *Review of Scientific Instruments*, 72(5):2261–2267, 2001.

[479] H. Vahedi Tafreshi, G. Benedek, P. Piseri, S. Vinati, E. Barborini and P. Milani. A Simple Nozzle Configuration for the Production of Low Divergence Supersonic Cluster Beam by Aerodynamic Focusing. *Aerosol Science & Technology*, 36(5):593–606, 2002.

[480] H. Vahedi Tafreshi, P. Piseri, E. Barborini, G. Benedek and P. Milani. Simulation on the effect of Brownian motion on nanoparticle trajectories in a pulsed microplasma cluster source. *Journal of Nanoparticle Research*, 4(6):511–524, 2002.

[481] B. Ritchie. Theory of the angular distribution of photoelectrons ejected from optically active molecules and molecular negative ions. *Physical Review A*, 13(4):1411–1415, 1976.

[482] N. Böwering, T. Lischke, B. Schmidtke, N. Müller, T. Khalil and U. Heinzmann. Asymmetry in photoelectron emission from chiral molecules induced by circularly polarized light. *Physical Review Letters*, 86(7):1187–1190, 2001.

[483] I. Powis. Photoelectron Circular Dichroism in Gas Phase Chiral Molecules. In S. A. Rice, editor, *Advances in Chemical Physics*, volume 138, pages 267–329. Wiley-Interscience, Hoboken, NJ, 2008.

[484] L. Nahon, G. A. Garcia and I. Powis. Valence shell one-photon photoelectron circular dichroism in chiral systems. *Journal of Electron Spectroscopy and Related Phenomena*, 204(B):322–334, 2015.

[485] C. Lux, M. Wollenhaupt, C. Sarpe and T. Baumert. Photoelectron circular dichroism of bicyclic ketones from multiphoton ionization with femtosecond laser pulses. *ChemPhysChem*, 16(1):115–137, 2015.

[486] C. S. Lehmann, N. B. Ram, I. Powis and M. H. M. Janssen. Imaging photoelectron circular dichroism of chiral molecules by femtosecond multiphoton coincidence detection. *The Journal of Chemical Physics*, 139(23):234307, 2013.

[487] C. Lux, M. Wollenhaupt, T. Bolze, Q. Liang, J. Köhler, C. Sarpe and T. Baumert. Circular dichroism in the photoelectron angular distributions of camphor and fenchone from multiphoton ionization with femtosecond laser pulses. *Angewandte Chemie International Edition*, 51(20):5001–5005, 2012.

[488] S. Beaulieu, A. Ferré, R. Géneaux, R. Canonge, D. Descamps, B. Fabre, N. Fedorov, F. Légaré, S. Petit, T. Ruchon, V. Blanchet, Y. Mairesse and B. Pons. Universality of photoelectron circular dichroism in the photoionization of chiral molecules. *New Journal of Physics*, 18:102002, 2016.

[489] A. Comby, S. Beaulieu, M. Boggio-Pasqua, D. Descamps, F. Legare, L. Nahon, S. Petit, B. Pons, B. Fabre, Y. Mairesse and V. Blanchet. Relaxation Dynamics in Photoexcited Chiral Molecules Studied by Time-Resolved Photoelectron Circular Dichroism: Toward Chiral Femtochemistry. *The Journal of Physical Chemistry Letters*, 7(22):4514–4519, 2016.

[490] S. Beaulieu, A. Comby, B. Fabre, D. Descamps, A. Ferré, G. Garcia, R. Géneaux, F. Légaré, L. Nahon, S. Petit, T. Ruchon, B. Pons, V. Blanchet and Y. Mairesse. Probing ultrafast dynamics of chiral molecules using time-resolved photoelectron circular dichroism. *Faraday Discussions*, 194:325–348, 2016.

[491] S. Beaulieu, A. Comby, D. Descamps, B. Fabre, G. A. Garcia, R. Géneaux, A. G. Harvey, F. Légaré, Z. Mašín, L. Nahon, A. F. Ordonez, S. Petit, B. Pons, Y. Mairesse, O. Smirnova and V. Blanchet. Photoexcitation circular dichroism in chiral molecules. *Nature Physics*, 14(5):484–489, 2018.

APPENDIX A

Ion Optics Cut-Through

This appendix provides a cut-through view of the ion-optics in conjunction with the rotation coupler for sample replenishment.

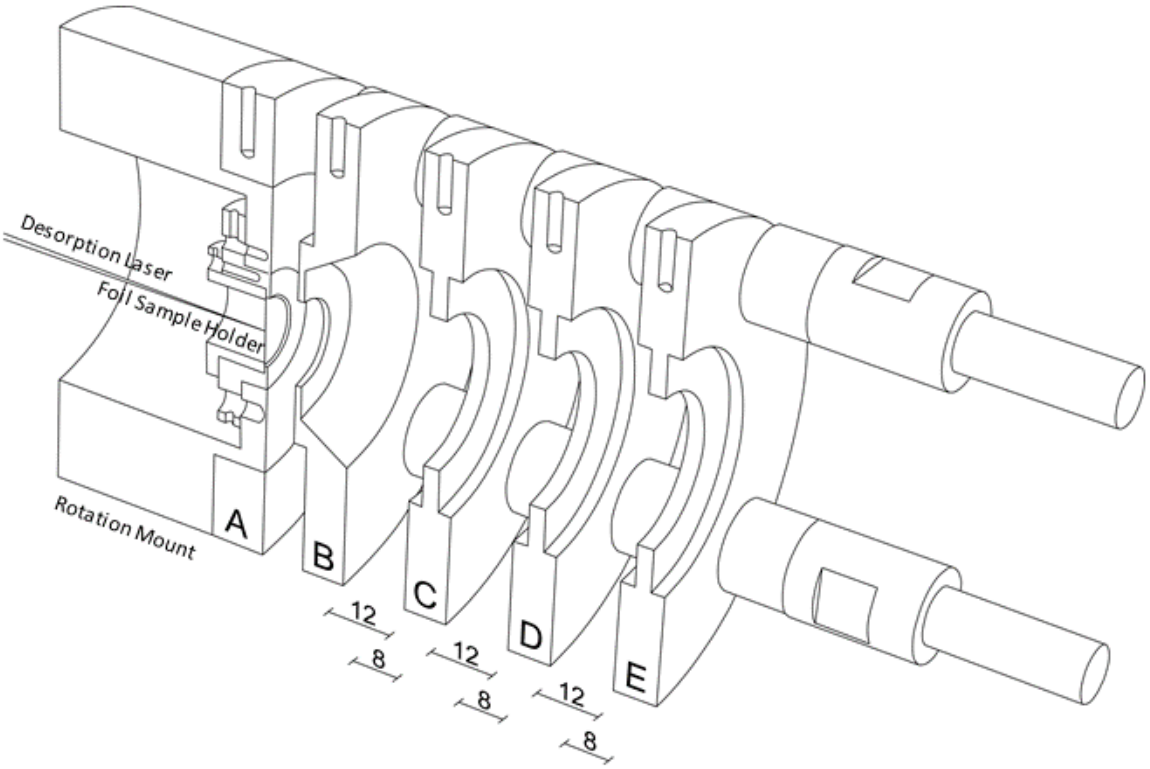

Fig. A.1: A cut-through view of the ion-optics/rotation coupler. A-C represent the repeller, extractor and grounding electrodes respectively whilst D and E are unused. The sample foil is held within the repeller electrode and is able to rotate off-axis with respect to the desorption laser beam. Sample replenishment is achieved via manually rotating the sample using an air-to-vacuum coupler.

APPENDIX B

TOFSET2 Flow Chart

This appendix provides a flow chart showing how the code behind one of the three GUIs developed during this PhD, TOFSET2.m, functions. The function of this code is to interface with a Tektronix TDS 1002B oscilloscope in order to extract and save oscilloscope traces.

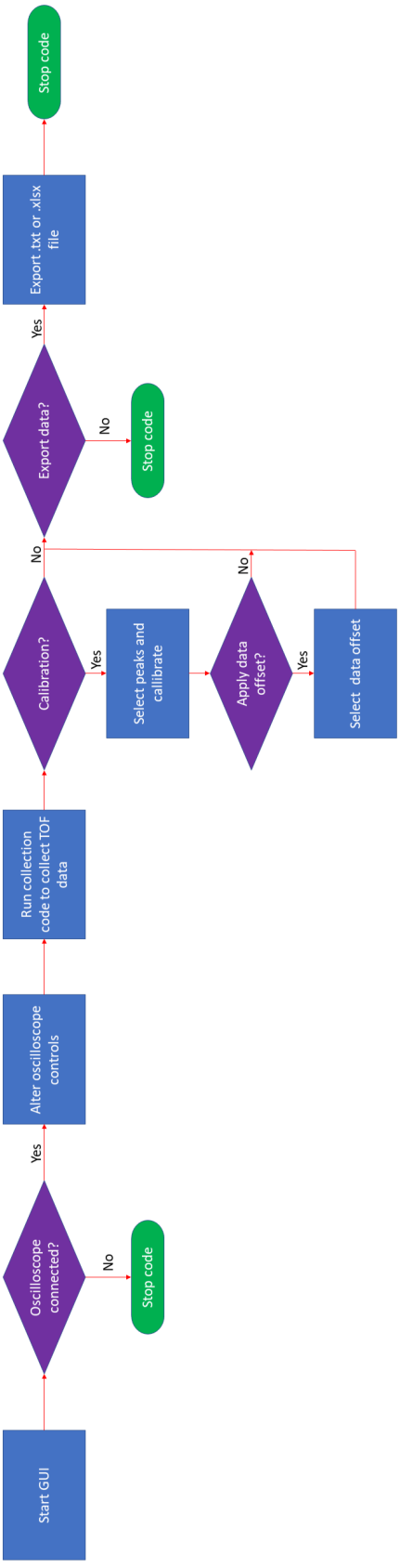

Fig. B.1: A flow chart depicting the operation of the TOFSET2 programme.

APPENDIX C

TOFRUN2 Flow Chart

This appendix provides a flow chart demonstrating the processes undertaken by the GUI for time-resolved photoion yield data acquisition, TOFRUN2.m. This code was required to interface with a Tektronix TDS 1002B oscilloscope, a PI M-403.12S linear translation stage an a pair of home-built arduino controlled stutters and allowed for automation of the data acquisition process.

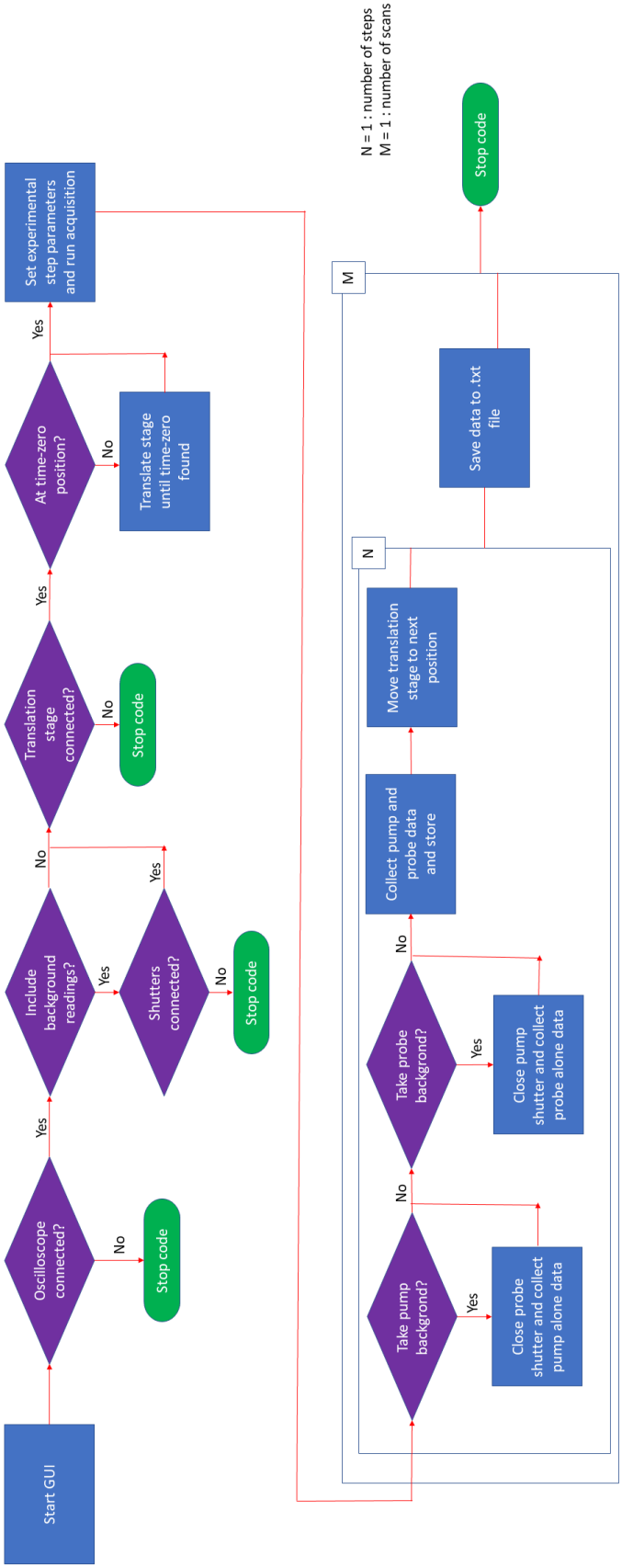

Fig. C.1: A flow chart depicting the operation of the TOFRUN2 programme.

APPENDIX D

TOFANALYSE2 Flow Chart

This appendix provides a flow chart demonstrating the processes undertaken by the main GUI for time-resolved photoion yield data analysis, TOFANALYSE2.m. This code was developed to extract molecular time constants from time-resolved photoion yield spectroscopic data, as well as to produce publication ready figures of the attained and analysed data.

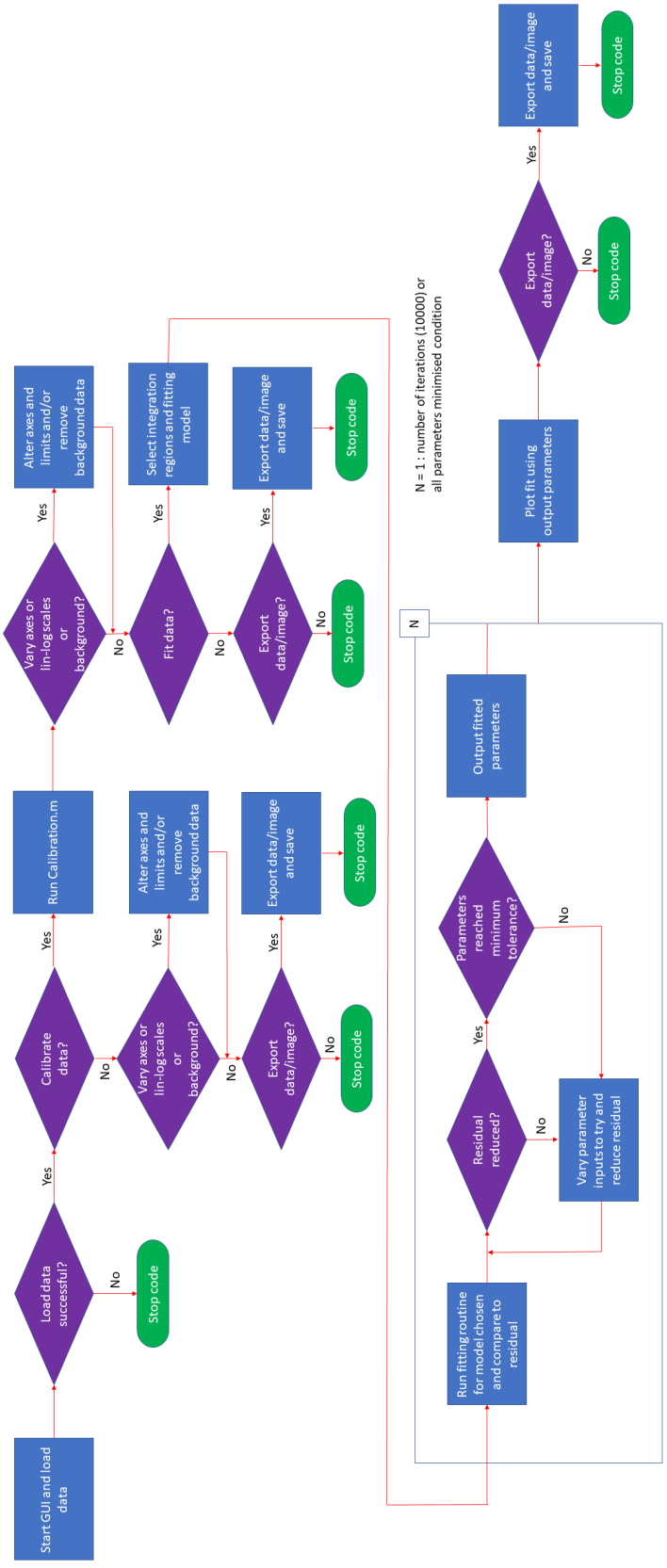

Fig. D.1: A flow chart depicting the operation of the TOFANALYSE2 programme.

APPENDIX E

Calibration Flow Chart

This appendix provides a flow chart demonstrating the processes undertaken by the the sub-GUI for calibration of time-of-flight data to mass-to-charge ratio, Calibration.m.

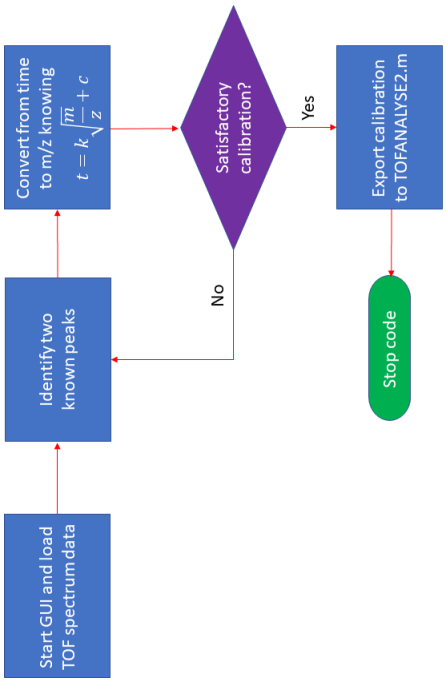

Fig. E.1: A flow chart depicting the operation of the Calibration programme.